

REPORT DOCUMENTATION PAGE				Form Approved OMB NO. 0704-0188	
<p>The public reporting burden for this collection of information is estimated to average 1 hour per response, including the time for reviewing instructions, searching existing data sources, gathering and maintaining the data needed, and completing and reviewing the collection of information. Send comments regarding this burden estimate or any other aspect of this collection of information, including suggestions for reducing this burden, to Washington Headquarters Services, Directorate for Information Operations and Reports, 1215 Jefferson Davis Highway, Suite 1204, Arlington VA, 22202-4302. Respondents should be aware that notwithstanding any other provision of law, no person shall be subject to any penalty for failing to comply with a collection of information if it does not display a currently valid OMB control number.</p> <p>PLEASE DO NOT RETURN YOUR FORM TO THE ABOVE ADDRESS.</p>					
1. REPORT DATE (DD-MM-YYYY) 27-08-2013		2. REPORT TYPE Final Report		3. DATES COVERED (From - To) 1-Jun-2010 - 31-May-2013	
4. TITLE AND SUBTITLE Shock Tube/Laser Absorption Studies of Jet Fuels at Low Temperatures (600-1200K)				5a. CONTRACT NUMBER W911NF-10-1-0125	
				5b. GRANT NUMBER	
				5c. PROGRAM ELEMENT NUMBER 611102	
6. AUTHORS R. K. Hanson, D. F. Davidson				5d. PROJECT NUMBER	
				5e. TASK NUMBER	
				5f. WORK UNIT NUMBER	
7. PERFORMING ORGANIZATION NAMES AND ADDRESSES Stanford University Office of Sponsored Research 340 Panama Street Stanford, CA 94305 -4100				8. PERFORMING ORGANIZATION REPORT NUMBER	
9. SPONSORING/MONITORING AGENCY NAME(S) AND ADDRESS(ES) U.S. Army Research Office P.O. Box 12211 Research Triangle Park, NC 27709-2211				10. SPONSOR/MONITOR'S ACRONYM(S) ARO	
				11. SPONSOR/MONITOR'S REPORT NUMBER(S) 57391-EG.29	
12. DISTRIBUTION AVAILABILITY STATEMENT Approved for Public Release; Distribution Unlimited					
13. SUPPLEMENTARY NOTES The views, opinions and/or findings contained in this report are those of the author(s) and should not be construed as an official Department of the Army position, policy or decision, unless so designated by other documentation.					
14. ABSTRACT This report describes a research program at Stanford University that focused on four areas of critical concern in the study of the combustion of jet fuels at low temperatures: the development of a fundamental kinetics database utilizing shock tubes and laser absorption for jet fuel surrogate components; the development of a new constrained-reaction-volume strategy to improve shock tube performance; the development of new laser diagnostics techniques; and the application of an aerosol shock tube to investigate low-vapor-pressure fuels.					
15. SUBJECT TERMS shock tube, jet fuel, laser absorption, constrained-reaction-volume shock tube					
16. SECURITY CLASSIFICATION OF:			17. LIMITATION OF ABSTRACT UU	15. NUMBER OF PAGES	19a. NAME OF RESPONSIBLE PERSON Ronald Hanson
a. REPORT UU	b. ABSTRACT UU	c. THIS PAGE UU			19b. TELEPHONE NUMBER 650-723-1745

Report Title

Shock Tube/Laser Absorption Studies of Jet Fuels at Low Temperatures (600-1200K)

ABSTRACT

This report describes a research program at Stanford University that focused on four areas of critical concern in the study of the combustion of jet fuels at low temperatures: the development of a fundamental kinetics database utilizing shock tubes and laser absorption for jet fuel surrogate components; the development of a new constrained-reaction-volume strategy to improve shock tube performance; the development of new laser diagnostics techniques; and the application of an aerosol shock tube to investigate low-vapor-pressure fuels.

Enter List of papers submitted or published that acknowledge ARO support from the start of the project to the date of this printing. List the papers, including journal references, in the following categories:

(a) Papers published in peer-reviewed journals (N/A for none)

ReceivedPaper

- 06/14/2011 6.00 Sung Hyun Pyun, Jungwan Cho, David F Davidson, Ronald K Hanson. Interference-free mid-IR laser absorption detection of methane, measurement science and technology, (06 2011): . doi:
- 06/14/2011 3.00 D.R. Haylett, R.D. Cook, D.F. Davidson, R.K. Hanson. OH and C₂H₄ species time-histories during hexadecane and diesel ignition behind reflected shock waves, Proceedings of the Combustion Institute, (06 2011): . doi:
- 06/14/2011 2.00 Guillaume L. Pilla, David F. Davidson, Ronald K. Hanson. Shock tube/laser absorption measurements of ethylene time-histories during ethylene and n-heptane pyrolysis, Proceedings of the Combustion Institute, (09 2010): . doi:
- 06/14/2011 1.00 D.F. Davidson, Z. Hong, G.L. Pilla, A. Farooq, R.D. Cook, R. K. Hanson. Multi-species time-history measurements during n-dodecane oxidation behind reflected shock waves, proceeding of the combustion institute, (09 2010): . doi:
- 06/14/2011 7.00 K.-Y. Lam, Z. Hong, D.F. Davidson, R.K. Hanson. Shock tube ignition delay time measurements in propane/O₂/argon mixtures at near-constant-volume conditions, Proceedings of the Combustion Institute, (08 2010): . doi:
- 07/26/2012 11.00 Daniel Haylett, David Davidson, Ronald Hanson. Second-Generation Aerosol Shock Tube: An improved Design, Shock Waves, (06 2012): 0. doi:
- 07/26/2012 12.00 Daniel Haylett, David Davidson, Ronald Hanson. Ignition Delay Times of Low-VApor-Pressure Fuels Measured Using a Aerosol Shock Tube, Combustion and Flame, (01 2012): 552. doi:
- 07/26/2012 15.00 Wei Ren, David Davidson, Ronald Hanson. IR Laser Absorption Diagnostic for C₂H₄ in Shock Tube Kinetics Studies, International Journal of Chemical Kinetics, (07 2012): 423. doi:
- 07/26/2012 16.00 Wei Ren, Aamir Farooq, David Davidson, Ronald Hanson. CO Concentration and Temperature Sensor for Combustion Gases Using Quantum-Cascade Laser Absorption near 4.7 microns, Applied Physics B: Lasers and Optics, (05 2012): 849. doi:
- 08/27/2013 18.00 Sung Hyun Pyun, Wei Ren, David F. Davidson, Ronald K. Hanson. Methane and ethylene time-history measurements in n-butane and n-heptane pyrolysis behind reflected shock waves, Fuel, (06 2013): 0. doi: 10.1016/j.fuel.2012.12.034
- 08/27/2013 19.00 A. Farooq, D. F. Davidson, W. Ren, R. K. Hanson. CO concentration and temperature sensor for combustion gases using quantum-cascade laser absorption near 4.7 μ m, Applied Physics B, (05 2012): 849. doi: 10.1007/s00340-012-5046-1
- 08/27/2013 20.00 Ronald K. Hanson, Genny A. Pang, Sreyashi Chakraborty, Wei Ren, Shengkai Wang, David Frank Davidson. Constrained reaction volume approach for studying chemical kinetics behind reflected shock waves, Combustion and Flame, (09 2013): 1550. doi: 10.1016/j.combustflame.2013.03.026
- 08/27/2013 21.00 R.D. Cook, D.F. Davidson, Z. Hong, W. Ren, S.H. Pyun, R.K. Hanson, D.R. Haylett. Multi-species time-history measurements during n-hexadecane oxidation behind reflected shock waves, Proceedings of the Combustion Institute, (01 2013): 369. doi: 10.1016/j.proci.2012.06.014

08/27/2013	22.00	Daniel R. Haylett, David F. Davidson, Ronald K. Hanson. Ignition delay times of low-vapor-pressure fuels measured using an aerosol shock tube, Combustion and Flame, (02 2012): 0. doi: 10.1016/j.combustflame.2011.08.021
08/27/2013	23.00	Yangye Zhu, David Frank Davidson, Ronald K. Hanson. 1-Butanol ignition delay times at low temperatures: An application of the constrained-reaction-volume strategy, Combustion and Flame, (07 2013): 0. doi: 10.1016/j.combustflame.2013.06.028
08/27/2013	24.00	King-Yiu Lam, Wei Ren, Sung Hyun Pyun, Aamir Farooq, David F. Davidson, Ronald K. Hanson. Multi-species time-history measurements during high-temperature acetone and 2-butanone pyrolysis, Proceedings of the Combustion Institute, (01 2013): 607. doi: 10.1016/j.proci.2012.06.009
08/27/2013	25.00	Sung Hyun Pyun, Wei Ren, King-Yiu Lam, David Frank Davidson, Ronald K. Hanson. Shock tube measurements of methane, ethylene and carbon monoxide time-histories in DME pyrolysis, Combustion and Flame, (04 2013): 747. doi: 10.1016/j.combustflame.2012.12.004

TOTAL: 17

Number of Papers published in peer-reviewed journals:

(b) Papers published in non-peer-reviewed journals (N/A for none)

<u>Received</u>	<u>Paper</u>
-----------------	--------------

08/27/2013	26.00	Y Zhu, D F Davidson, R K Hanson. Pyrolysis and Oxidation of Decalin at Elevated Pressures: A Shock-Tube Study, Combustion and Flame, (05 2013): 0. doi:
------------	-------	---

TOTAL: 1

Number of Papers published in non peer-reviewed journals:

(c) Presentations

Number of Presentations: 0.00

Non Peer-Reviewed Conference Proceeding publications (other than abstracts):

<u>Received</u>	<u>Paper</u>
-----------------	--------------

08/27/2013	27.00	R. K. Hanson, S. Chakraborty, W. Ren, D. F. Davidson . Constrained Reaction Volume: A Strategy forReflected Shock Wave Kinetics Experiments, 24th International Conference on Detonations, Explosions and Reactive Systems. 2013/07/28 03:00:00, . : ,
------------	-------	--

TOTAL:	1
---------------	----------

Number of Non Peer-Reviewed Conference Proceeding publications (other than abstracts):

Peer-Reviewed Conference Proceeding publications (other than abstracts):

<u>Received</u>	<u>Paper</u>
-----------------	--------------

08/23/2011	10.00	Matthew E. Campbell, David F. Davidson, Ronald K. Hanson. A second-generation aerosol shock tube and its use in studying ignition delay times of large biodiesel surrogates, 28th International Shock Wave Symposium. 2011/07/14 03:00:00, . : ,
------------	-------	--

08/27/2013	28.00	R. K. Hanson, S. Chakraborty, W. Ren, S. K. Wang, D. F. Davidson. Constrained Reaction Volume: A New Approach to Studying Reactive Systems in Shock Tubes, 29th International Symposium on Shock Waves. 2013/07/14 03:00:00, . : ,
------------	-------	--

TOTAL:	2
---------------	----------

Number of Peer-Reviewed Conference Proceeding publications (other than abstracts):

(d) Manuscripts

Received Paper

06/14/2011	5.00	D.R. Haylett, D.F. Davidson, R.K. Hanson. Ignition Delay Times of Low-Vapor-Pressure Fuels Measured Using an Aerosol Shock Tube, Combustion and Flame (06 2011)
07/26/2012	13.00	Daniel Hayett, David Davidson, Robert Cook, Zekai Hong, Wei Ren, Sung Pyun, Ronald Hanson. Multi-Species Time-History MEasurements during n-Hexadecane Oxidation Behind Reflected Shock Waves, Proceedings of the Combustion Institute (10 2011)
07/26/2012	14.00	Wei Ren, King-Yiu Lam, Sung Pyun, Aamir Farooq, David Davidson, Ronald Hanson. Shock Tube/Laser Absorption Studies of the Decomposition of Methyl Formate, Proceedings of the Combustion Institute (10 2011)
08/23/2011	9.00	Wei Ren, David F. Davidson, Ronald K. Hanson. IR laser absorption diagnostic for C ₂ H ₄ in shock tube kinetics studies, International Journal of Chemical Kinetics (08 2011)

TOTAL: 4

Number of Manuscripts:

Books

Received Paper

TOTAL:

Patents Submitted

Patents Awarded

Awards

6/9/2013 - Professor Hanson gave Plenary Lecture at International Conference on Chemical Kinetics (Seville, Spain)

4/30/2013 - Professor Hanson gave Edison Lecture at University of Notre Dame

July 28/2011 R. I. Soloukhin Award, International conference on detonations, explosives, and reactive systems

Graduate Students

<u>NAME</u>	<u>PERCENT SUPPORTED</u>	Discipline
Daniel Haylett	0.50	
Matthew Campbell	0.50	
Andrew Tulgetske	0.50	
Sung Hyun Pyun	0.50	
Keilan Freeman	0.50	
Subith Vasu	0.50	
FTE Equivalent:	3.00	
Total Number:	6	

Names of Post Doctorates

<u>NAME</u>	<u>PERCENT SUPPORTED</u>
FTE Equivalent:	
Total Number:	

Names of Faculty Supported

<u>NAME</u>	<u>PERCENT SUPPORTED</u>	National Academy Member
Ronald K. Hanson	0.03	Yes
FTE Equivalent:	0.03	
Total Number:	1	

Names of Under Graduate students supported

<u>NAME</u>	<u>PERCENT SUPPORTED</u>	Discipline
Andrew Lawson	0.25	Mechanical Engineering
FTE Equivalent:	0.25	
Total Number:	1	

Student Metrics

This section only applies to graduating undergraduates supported by this agreement in this reporting period

The number of undergraduates funded by this agreement who graduated during this period: 0.00

The number of undergraduates funded by this agreement who graduated during this period with a degree in science, mathematics, engineering, or technology fields:..... 0.00

The number of undergraduates funded by your agreement who graduated during this period and will continue to pursue a graduate or Ph.D. degree in science, mathematics, engineering, or technology fields:..... 0.00

Number of graduating undergraduates who achieved a 3.5 GPA to 4.0 (4.0 max scale):..... 0.00

Number of graduating undergraduates funded by a DoD funded Center of Excellence grant for Education, Research and Engineering:..... 0.00

The number of undergraduates funded by your agreement who graduated during this period and intend to work for the Department of Defense 0.00

The number of undergraduates funded by your agreement who graduated during this period and will receive scholarships or fellowships for further studies in science, mathematics, engineering or technology fields:..... 0.00

Names of Personnel receiving masters degrees

<u>NAME</u>
Keilan Freeman
Total Number:

1

Names of personnel receiving PhDs

NAME

Daniel Haylett

Sung Hyun Pyun

Total Number:

2

Names of other research staff

NAME

PERCENT SUPPORTED

David F. Davidson

0.08

FTE Equivalent:

0.08

Total Number:

1

Sub Contractors (DD882)

Inventions (DD882)

Scientific Progress

See Attached File.

Technology Transfer

Final Report

W911NF-10-1-0125

Shock Tube/Laser Absorption Studies of Jet Fuels at Low Temperatures (600-1200K)

R. K. Hanson and D. F. Davidson

Mechanical Engineering Department

Stanford University, Stanford CA 94305

rkhanon@stanford.edu

dfd@stanford.edu

August 27, 2013

Executive Summary

This research program focused on four areas of critical concern in the study of the combustion of jet fuels at low temperatures: the development of a fundamental kinetics database utilizing shock tubes and laser absorption for jet fuel surrogate components; the development of a new constrained-reaction-volume strategy to improve shock tube performance; the development of new laser diagnostics techniques; and the application of an aerosol shock tube to investigate low-vapor-pressure fuels. Attached to this Executive Summary are reprints of the major results of this work.

Jet Fuel Kinetics Database

Shock tubes and laser absorption provide unique information for the fundamental kinetics database for jet fuel surrogate components developed here. This database includes: near-constant volume ignition delay time measurements; multi-wavelength, multi-species time-history measurements; and direct measurements of elementary reaction rate constants. Near-constant volume ignition delay times provide an overall global characterization of the fuel ignition process; multi-species time-histories provide detailed information that constrains the individual species and mechanism pathways; and reaction rate constants provide fundamental input data for detailed reaction mechanisms. Representative ignition delay time and multi-species time-history data (for fuel, CH_4 , C_2H_4 , and CO) for three high-vapor-pressure surrogate components: decalin, n-butane, and n-heptane, are provided in the attached reprints.

1. Y. Zhu, D.F. Davidson and R.K. Hanson, "Pyrolysis and Oxidation of Decalin at Elevated Pressures: A Shock Tube Study," *Combustion and Flame*, in press.
2. S.H. Pyun, W. Ren, D.F. Davidson and R.K. Hanson, "Methane and Ethylene Time-History Measurements in n-Butane and n-Heptane Pyrolysis behind Reflected Shock Waves," *Fuel* 108 557-564 (2013).
3. W. Ren, D.F. Davidson and R.K. Hanson, "IR Laser Absorption Diagnostic for C_2H_4 in Shock Tube Kinetics Studies," *Int. J. Chem Kinetics* 44 423-432 (2012).
4. W. Ren, A. Farooq, D.F. Davidson, and R.K. Hanson, "CO Concentration and Temperature Sensor for Combustion Gases using Quantum-Cascade Laser Absorption near $4.7\text{ }\mu\text{m}$," *Applied Physics B* 107 849-860 (2012).

The techniques developed and described in these papers were also applied to several oxygenated fuel components. Though these fuels are not considered to be jet fuel surrogate components, development of a kinetics data base and testing and refinement of the detailed reaction sub-mechanisms that describe these fuels provide strong constraints on the oxygenate sub-mechanisms found in jet fuel surrogate mechanisms. The following oxygenate species were also studied: acetone, 2-butanone, methyl formate, dimethyl ether, and this work is described in the following papers.

5. K.-Y. Lam, W. Ren, S. H. Pyun, A. Farooq, D. F. Davidson, and R. K. Hanson, "Multi-species Time-history Measurements during High-temperature Acetone and 2-Butanone Pyrolysis," *Proceedings of the Combustion Institute* 34 607-615 (2012).
6. W. Ren, K.-Y. Lam, S. H. Pyun, A. Farooq, D.F. Davidson, and R.K. Hanson, "Shock Tube/Laser Absorption Studies of the Decomposition of Methyl Formate," *Proceedings of the Combustion Institute* 34 453-461 (2012).

7. S.H. Pyun, W. Ren, K.-Y. Lam, D.F. Davidson and R.K. Hanson, "Shock Tube Measurements of Methane, Ethylene and Carbon Monoxide Time-Histories in DME Pyrolysis," *Combustion and Flame* **160** 747-754 (2013).

Constrained-Reaction-Volume Strategy

The quality and accuracy of measurements in shock tubes are strongly dependent on the proper characterization and control of temperature and pressure behind the reflected shock wave. We have developed a new shock tube methodology, called the constrained-reaction-volume strategy, to achieve effectively near-constant pressure operation. Description of this method and an example of its application is given in the attached reprints.

8. R.K. Hanson, G.A. Pang, S. Chakraborty, W. Ren, S. Wang and D.F. Davidson, "Constrained Reaction Volume Approach for Studying Chemical Kinetics Behind Reflected Shock Waves," *Combustion and Flame* **160** 1550-1558 (2013)
9. Y. Zhu, D.F. Davidson and R.K. Hanson, "1-Butanol Ignition Delay Times at Low Temperatures: An Application of the Constrained-Reaction-Volume Strategy," *Combustion and Flame*, in press.

The development of the constrained-reaction-volume strategy was also reported in the following two conference proceedings.

10. R.K. Hanson, S. Chakraborty, G.A. Pang, W. Ren, S. Wang and D.F. Davidson, "Constrained Reaction Volume: A New Approach to Studying Reactive Systems in Shock Tubes," 29th ISSW Conference, Madison WI, 7/2013.
11. R.K. Hanson, S. Chakraborty, G.A. Pang, W. Ren, S. Wang and D.F. Davidson, "Constrained Reaction Volume: A Strategy for Reflected Shock Wave Experiments," 24th ICDERS Conference, Paper 29, Taipei, 7/2013.

Aerosol Shock Tube Studies

We have continued to develop and refine the aerosol shock tube methodology. Previous strategies to study low-vapor-fuels in shock tubes have relied on pre-heating the test gas mixtures and the shock tube facility itself. The high temperatures required to fully vaporize diesel fuels, for example, means that methods are susceptible to problems associated with pre-test oxidation, as well as partial fuel fractionation. The aerosol shock tube loading strategy developed at Stanford University avoids these problems and permits the direct gas-phase study of practical distillate fuels and large distillate archetypal surrogate components. Using this method, we have measured ignition delay times and species time-histories for the diesel surrogate n-hexadecane, bio-diesel surrogate components. Descriptions of these experiments are given in the attached reprints.

12. D. R. Haylett, D. F. Davidson, R. D. Cook, Z. Hong, W. Ren, S. H. Pyun, and R. K. Hanson, "Multi-species Time-history Measurements during n-Hexadecane Oxidation behind Reflected Shock Waves," *Proceedings of the Combustion Institute* **34** 369-376 (2012).
13. D. R. Haylett, D. F. Davidson, and R. K. Hanson, "Second-Generation Aerosol Shock Tube: an Improved Design," *Shock Waves* **22** (2012) 483-493.
14. D.R. Haylett, D.F. Davidson and R.K. Hanson, "Ignition Delay Times of Low-Vapor-Pressure Fuels Measured using an Aerosol Shock Tube," *Combustion and Flame* **159** 552-561 (2012).

15. M.A. Campbell, D.F. Davidson and R.K. Hanson, "Ignition Delay Times of Very-Low-Vapor-Pressure Biodiesel Surrogate behind Reflected Shock Waves," 8th US National Combustion Meeting, Paper 070RK-0008 Park City, UT 5/2013.

These studies provide unique and critically-needed experimental data for improving understanding of the combustion chemistry of jet fuels. Much of this data was not available before in any form and has been enabled by the accompanying developments in shock tube and laser absorption methodologies.

Pyrolysis and Oxidation of Decalin at Elevated Pressures: A Shock-Tube Study

Y. Zhu, D. F. Davidson, R. K. Hanson,
High Temperature Gasdynamics Laboratory
Department of Mechanical Engineering
Stanford University, Stanford CA 94305

Abstract

Ignition delay times and ethylene concentration time-histories were measured behind reflected shock waves during decalin oxidation and pyrolysis. Ignition delay measurements were conducted for gas-phase decalin/air mixtures over temperatures of 769 – 1202 K, pressures of 11.7 – 51.2 atm, and equivalence ratios of 0.5, 1.0, and 2.0. Negative-temperature-coefficient (NTC) behavior of decalin autoignition was observed, for the first time, at temperatures below 920 K. Current ignition delay data are in good agreement with past shock tube data in terms of pressure dependence but not equivalence ratio dependence. Ethylene mole fraction and fuel absorbance time-histories were acquired using laser absorption at 10.6 and 3.39 μm during decalin pyrolysis for mixtures of 2200 – 3586 ppm decalin/argon at pressures of 18.2 – 20.2 atm and temperatures of 1197 – 1511 K. Detailed comparisons of these ignition delay and species time-history data with predictions based on currently available decalin reaction mechanisms are presented, and preliminary suggestions for the adjustment of some key rate parameters are made.

Keywords: Shock tube, Ignition delay, Laser absorption, Pyrolysis, Decalin, Ethylene.

Introduction

Decalin is a bicyclic alkane composed of two fused six-membered rings and occurs in both *cis* and *trans* isomers. It is a primary constituent of petroleum feedstocks and found in automotive fuels, aircraft fuels and proposed additive packages for these various fuels [1]. It has also been found to be significant in the new generation of fuels derived from tar sands and oil shales [2-5]. Additionally, it is claimed that decalin has effective endothermic fuel capability particularly attractive to engine cooling [1, 6, 7], and thus a good knowledge of vapor-phase reaction kinetics of decalin pyrolysis and combustion is needed [8]. Decalin has also been chosen as an archetypical cyclo-alkane class component for surrogate jet fuels [9] and surrogate diesel fuels

[10, 59]. In spite of this, Granata *et al.*[11] stated that cyclo-alkanes, including decalin, have received scant attention and kinetic knowledge of their combustion is less defined and accurate. All of these characteristics warrant the experimental and theoretical investigations of decalin combustion reaction kinetics.

Previous experimental studies of pyrolysis and oxidation of decalin are summarized in Table 1 and 2, respectively. While these studies appear to have covered a wide range of temperature (T) and pressure (P), few studies exist for pyrolysis of decalin at high temperatures and pressures (e.g., $T > 1100$ K and $P > 17$ atm) and for oxidation of decalin at low temperatures and high pressures (e.g., $T < 1000$ K and $P > 17$ atm). Low-temperature and high-pressure oxidation of decalin is of particular interest as it holds the potential of discovery of the negative-temperature-coefficient (NTC) behavior [12-17]. To the best of our knowledge, the NTC behavior of decalin oxidation has not been reported yet. In contrast to experimental studies, surprisingly, theoretical investigations of decalin reaction kinetics are scarce. Only three relevant reaction mechanisms are available in literature and summarized in Table 3, with the one released in [18] being the only complete kinetic model that can be readily used.

The goal of current work is to extend the kinetic database of decalin at elevated pressures including low-temperature-oxidation and high-temperature-pyrolysis using reflected shock wave experiments. We first measured ignition delay time of decalin in air over a wide range of temperature, pressure, and equivalence ratio to explore potential NTC behavior. Then, we focused on decalin pyrolysis and report time-resolved laser-absorption data at $3.39\ \mu\text{m}$ and $10.6\ \mu\text{m}$ to gain kinetic insight regarding decalin decomposition and ethylene formation. Both ignition delay time and species time-histories for decalin provide needed kinetic targets for the validation and refinement of decalin reaction mechanisms.

Table 1 Previous experimental studies of pyrolysis of decalin

Refs.	<i>Cis-</i> or <i>trans</i> -decalin?	T (K)	P (atm)	Product distribution?
[19]	<i>cis</i> -	973 – 1223	0.5 (partial)	Yes
[20]	mixture(47:53 wt%)	1093	1.78	Yes
[21]	mixture	1053, 1073	1	Yes
[22]	<i>trans</i> -	973 - 1123	1	Yes
[23]	mixture(14:86 wt%)	1083	1, 2	Yes
[24]	mixture (as additive)	1083	1	Yes
[25]	mixture (40:60 v.%)	770 – 1020	1	Yes
[26]	<i>trans</i> -	300 – 1450	10^{-8}	Yes
[27]	mixture (37.6:62.4 v.%)	1015 – 1193	1	Yes
[28]	mixture	698 – 748	23 – 75	Yes
[29]	mixture	700 – 810	20 – 100	Yes
[30]	mixture	1083	3.95	Yes

Table 2 Previous experimental studies of oxidation of decalin

Refs	<i>Cis-</i> or <i>trans</i> -docalin?	T (K)	P (atm)	ϕ	Type of experiment	Type of data
[31]	mixture	1060 – 1290	0.6 – 1.5	0.1, 0.2	reflected shock wave	ignition delay time
[32]	mixture (35:65 wt%)	993 – 1305	9 – 48	0.5, 1.0	reflected shock wave	ignition delay time
[33]	<i>cis-</i> , <i>trans-</i> , mixture (35:65 wt%)	–	–	–	ignition quality tester	ignition delay, derived cetane number
[34]	mixture (35:65 wt%)	600 – 800	8	0.3	flow reactor	CO production
[27]	mixture (37.6:62.4 v.%)	1060 – 1113	1	0.65 – 0.93	flow reactor	product speciation
[35]	mixture	626 – 731	8	0.3	flow reactor	CO production
[36]	mixture (38:62 wt%)	750 – 950	5 – 17	0.25	motored engine	product speciation

Table 3 Decalin reaction mechanisms discussed in this study

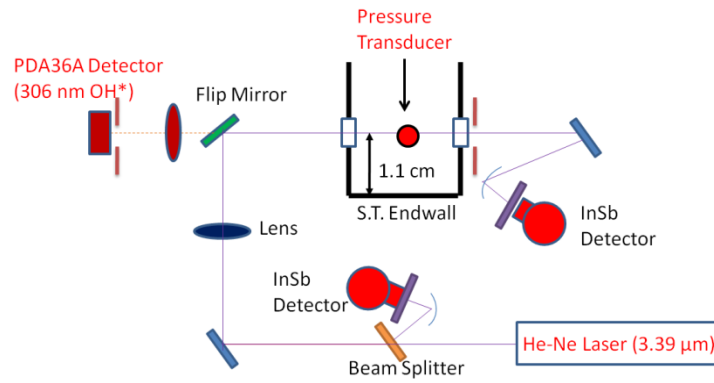
Mechanism	Year	Type	No. of species	No. of reactions
Zeppieri <i>et al.</i> [8, 27]	1997	pyrolysis sub-mechanism	179	244
Chae <i>et al.</i> [37]	2007	pyrolysis sub-mechanism	45+	132+
Dagaut <i>et al.</i> [18]	2013	complete mechanism	435	13532

Experimental Methods

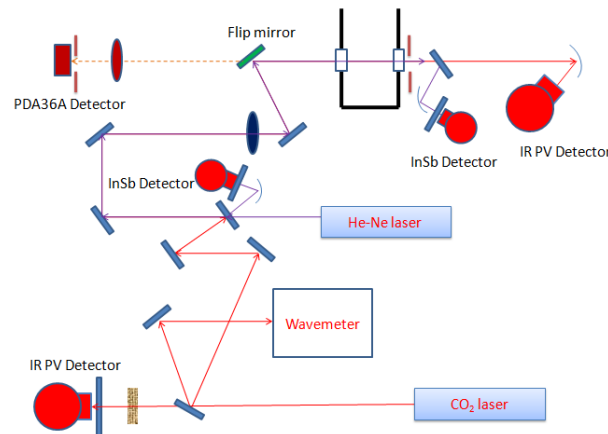
All ignition delay time and species sensing experiments were conducted in Stanford's high-purity, high-pressure shock tube (HPST). The driver section is 3 m long with a 7.5-cm internal diameter. Helium was used as the driver gas for higher-temperature experiments (2 – 3 ms test time) and 40%N₂/He tailored gas for lower-temperature ones (9 – 10 ms test time). Driver inserts were installed for all shock wave experiments to mitigate the non-ideal pressure rise (dP_s/dt) typically seen in the reflected shock region at longer test times. Incident shock attenuation rates ranged from 1.0 to 3.0 %/m. The driven section has a length of 5 m and an internal diameter of 5 cm and was heated to 100°C to prevent condensation of the test gas mixture. Overnight pumping of the shock tube produced ultimate pressures in the driven section of less than 10⁻⁶ torr and combined leak and outgassing rates of less than 10⁻⁵ torr/min. Decalin (CAS 91-17-8, a mixture of *cis*- and *trans*-decalin) provided by Sigma Aldrich was used without any further purification. Synthetic air (21% O₂/N₂) supplied from Praxair was used as the oxidizer in the autoignition studies and argon as the bath gas in the pyrolysis studies. Neat decalin was directly injected into a 12.8-liter stainless-steel mixing tank maintained at 120 °C. A test gas mixture of decalin/air or decalin/argon was then prepared manometrically and stirred using a magnetically-driven vane assembly for at least 30 minutes prior to the experiments. Further details on the shock tube facility can be found in Petersen and Hanson [38].

Multiple diagnostics were employed during the experiments: laser absorption at 3.39 μ m and 10.6 μ m, OH* emission near 306 nm, and sidewall pressure (see Figure 1). Initial fuel concentration was measured via laser absorption using a 3.39 μ m He-Ne laser. As shown in the upper frame, ignition was indicated by emission near 306 nm from the A² Σ^+ - X² Π ((0,0) band) of excited OH

radical (OH^*) and was detected by a modified PDA36A Si detector and Schott UG5 filter (not shown) with an optical arrangement that provided a temporal resolution of 10 μs or better. Ethylene species time-histories were measured during pyrolysis of decalin using a tunable Access Laser Company water-cooled LASY-4G CO_2 gas laser operated at either 10.532 μm (P14 line) or 10.675 μm (P28 line); the set-up is shown in the lower frame of Figure 1. This ethylene diagnostic will be named as “10.6 μm diagnostic” for brevity. Pressure time-histories in the test section were recorded using a KistlerTM piezoelectric pressure transducer, which also provided an alternative measurement of the ignition delay time. The measurement location of all diagnostics was 1.1 cm from the driven endwall.



(a) Ignition delay time set-up



(b) Species time-history set-up

Figure 1. Schematics of experimental set-up for (a) ignition delay time and (b) species time-history measurements.

Results and Discussion

Absorption Cross Section of Decalin

Prior to all experiments, the absorption cross section of decalin at $3.39\text{ }\mu\text{m}$ at the temperature of driven section (T_1) was needed to determine the initial fuel loading in the shock tube using the Beer-Lambert's Law. This becomes increasingly important for fuels with low saturated vapor pressures because the fuel concentration of the mixture in the driven section (the concentration in the actual experiment) can be lower than that prepared manometrically in the mixing tank [39]. To ensure accuracy, the absorption cross section at T_1 was measured in two ways: using a $3.39\text{ }\mu\text{m}$ He-Ne laser and a Fourier Transform Infrared Spectrometer (FTIR), as shown in Figure 2. The experimental procedures of these two methods can be found in [39] and [40], respectively. Good agreement is found between both kinds of measurements. In addition, no pressure dependence of this absorption cross section was observed in these measurements. The uncertainty and scatter of these measurements can be attributed to the very low saturation vapor pressure of decalin even at $100\text{ }^\circ\text{C}$. Furthermore, since $3.39\text{ }\mu\text{m}$ He-Ne laser was employed in the pyrolysis experiments to monitor the presence of fuel behind incident and reflected shocks, absorption cross section at higher temperatures, i.e., T_2 and T_5 , can also be derived [41], as shown in Figure 3. The uncertainties of this absorption cross section at T_1 , T_2 , and T_5 , are 3%, 5%, and 10%, respectively. A second-order least-squares polynomial fit for all cross section points over the temperature range of $372 - 1600\text{ K}$ was used to reconcile the dataset to a simple expression.

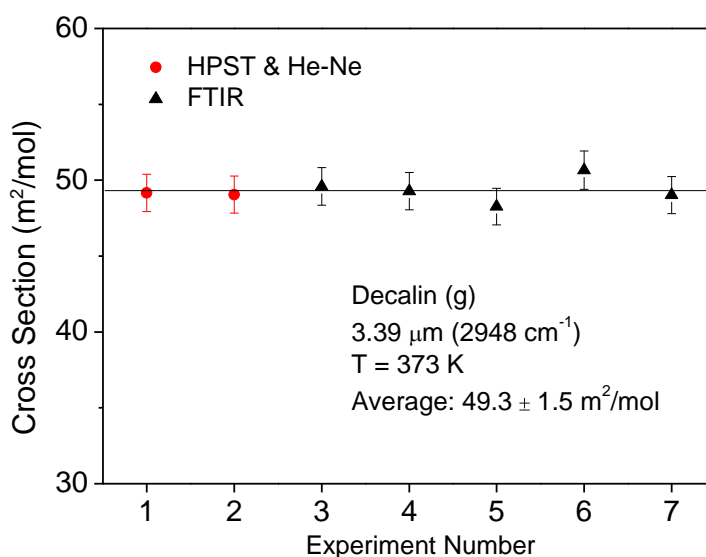


Figure 2. Measurements of absorption cross section of decalin using $3.39\text{ }\mu\text{m}$ He-Ne laser and FTIR

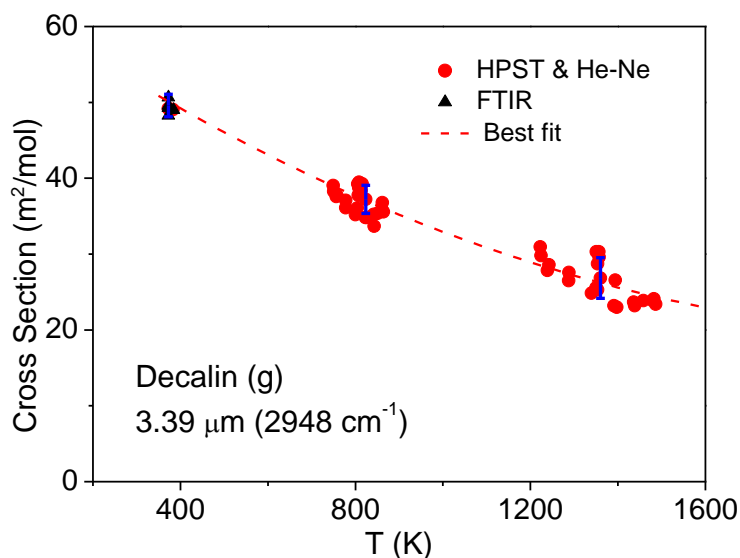


Figure 3. Temperature-dependent absorption cross section of decalin at 3.39 μm . Representative error bars are shown.

Ignition Delay Time Measurements

Figure 4 and 5 show representative ignition delay time measurements at high and low temperatures, respectively, and corresponding simulations using the semi-detailed chemical kinetic mechanism for decalin oxidation published by Dagaut *et al.* [18] using the conventional constant-volume (V), constant-energy (U) assumption. All simulations were performed with the OpenSMOKE code [42, 43]. Figure 4 shows representative pressure traces for both a non-reactive (pure N_2) case and reactive (decalin/ O_2/N_2) case and the OH^* emission record. In the current study, ignition delay time is defined as the time interval between the arrival of reflected shock at the measurement location and the onset of ignition determined by extrapolating the maximum slope of either pressure or OH^* record back to the baseline. As seen in Figure 4, the pressure trace and OH^* record exhibit consistent ignition delay times within $\pm 1\%$. In addition, the pressure trace from simulation of this experiment is plotted for comparison. Both measured and simulated pressure traces exhibit rapid and smooth exponential rises upon ignition, although slight pre-ignition pressure increase is evident in the simulation compared to the pressure trace in the non-reactive case. This comparison indicates that the constant U, V assumption is valid for simulating current higher-temperature (1200 – 920 K) experiments.

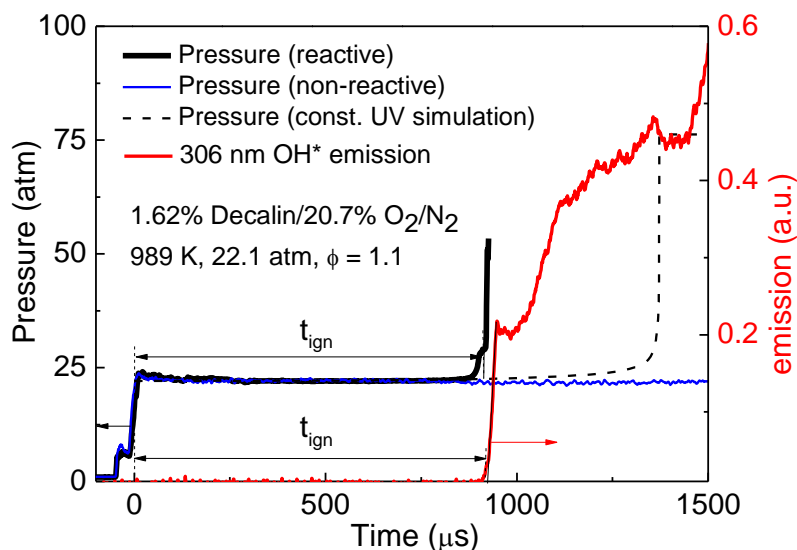


Figure 4. Example ignition delay time measurement at high temperature. The reaction mechanism used for simulating this measurement was published in [18].

Representative pressure traces for lower temperatures are presented in Figure 5. The pressure trace in the non-reactive experiment confirms that no reflected-pressure gradient (dP_5/dt) is evident in the long-test-time ignition experiments. However, significant pre-ignition pressure rises are clearly evident in the reactive experiments. These rises manifest themselves as either a ramp till the instant of ignition (830 K case) or a step before the final ignition event (802 K case). It is important to report these pressure traces associated with pronounced pre-ignition heat release when simulating shock tube experiments containing non-dilute mixtures, as the traditional constant U , V assumption might not be valid in the presence of pre-ignition pressure increases [44]. The goodness of this assumption can be evaluated by comparing the measured and simulated pressure profiles. Fortunately, simulations show very good agreement with the experiments, both qualitatively and quantitatively. Not only do the simulated pressure traces reproduce the behavior observed in the experiments (ramp or step), but also the predicted ignition delay times are very close to the measured ones based on the definition of ignition delay time mentioned above. Such agreement implies that the pre-ignition pressure rises shown in current measurements result from pre-ignition chemistry and justifies the constant U , V assumption. Nonetheless, to circumvent the controversy associated with the pre-ignition pressure rises, the innovative constrained-reaction-volume strategy [44, 45] will be employed in future work to revisit the autoignition of decalin/air mixtures, but at near-constant-pressure conditions.

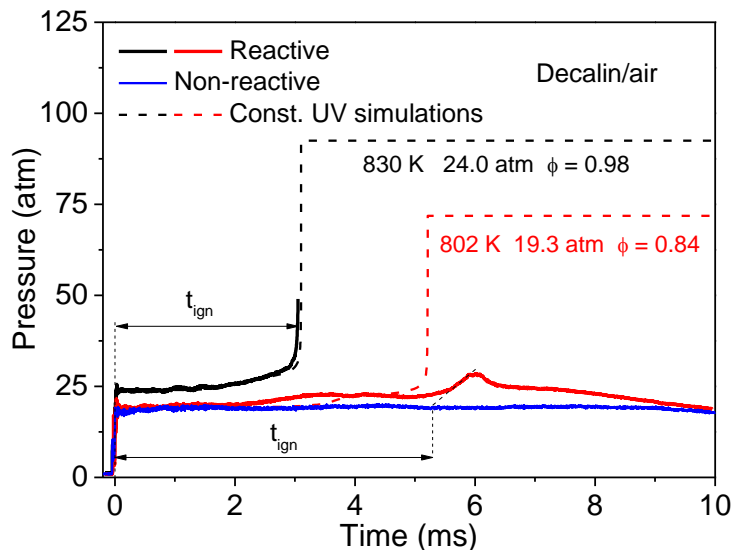


Figure 5. Example ignition delay time measurements at low temperature. The reaction mechanism used for simulating this measurement was published in [18].

All ignition delay data are classified into high-temperature (1200 – 920 K) and low-temperature (920 - 770 K) regimes and summarized in Table 4 (only those determined from pressure traces are reported). The uncertainties in the reflected shock temperature and pressure and initial decalin concentration are estimated to be 0.7%, 1.5%, and 5%, respectively, so the uncertainty of the current ignition delay time data is estimated to be 15% by the theory of propagation of uncertainty. An ignition delay time correlation will be derived based on only high-temperature data and used to scale the data in the high-temperature regime. The low-temperature data will be scaled by a temperature-dependent correlation derived from simulations to be discussed later.

High-temperature Ignition

Figure 6 shows ignition delay data of stoichiometric decalin/air mixture at various pressures from two sources of experiments. RPI refers to data measured by Oehlschlaeger *et al.* [32] and SU stands for data in the current study. Both sources of data are scaled to nominal pressures and equivalence ratios using individually reported correlations. The pressure-scaling dimensions are in excellent agreement, i.e., $t_{\text{ign}} \sim P^{-0.78}$, while the global activation energy from RPI's data (124 kJ/mol) is slightly higher than that from the current study (110 kJ/mol). There is some evidence in the 12 atm data at low temperatures that the Stanford ignition delay times are slightly shorter than those from RPI.

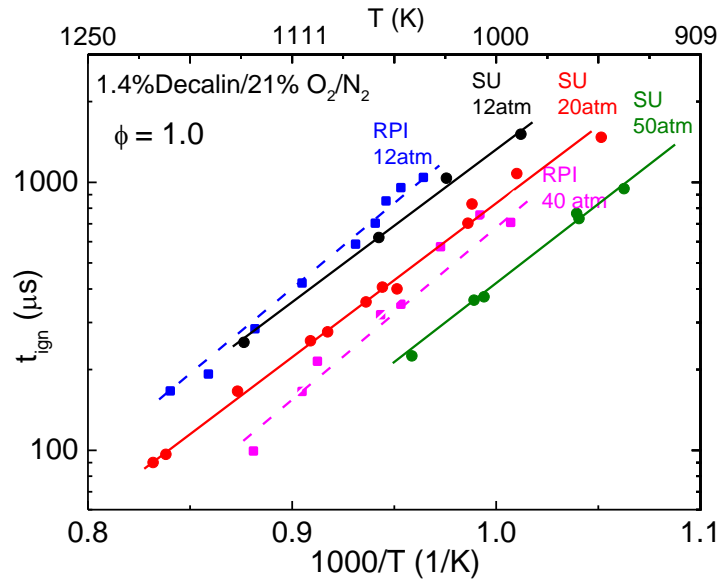


Figure 6. Comparison of ignition delay data of stoichiometric decalin/air mixture at various pressures from RPI [32] and SU (current studies). Solid lines are best fit to data points.

Figure 7 and 8 present variation of ignition delay time of decalin in air with equivalence ratio. As is evident in the two sources of data, the equivalence ratio dependence is negative over the pressure range of 12 to 50 atm. However, the equivalence ratio scaling based on RPI's data is $t_{\text{ign}} \sim \phi^{-0.81}$, while the current data support $t_{\text{ign}} \sim \phi^{-0.64}$. Given the negative dependence, if fuel loss were to occur, the actual equivalence ratio of the mixture in the ignition event would be lower than expected, and hence the ignition delay time would be longer. This might partially explain why current data appear shorter than those of RPI at the same condition. Specifically, due to the low saturated vapor pressure of decalin, it is plausible that the fuel concentration in the shock tube might be lower than that prepared manometrically in the mixing tank. In other words, a portion of the fuel may be lost somewhere along the "fuel line", either by condensation or adsorption. Since the initial fuel concentration was not monitored in RPI's studies, it is unsure whether they had such fuel-loss problem. In our current studies with this fuel, typical fractional fuel loss (i.e., the difference between the manometrically determined fuel concentration in the mixing tank and the in-situ fuel concentration in the shock tube measured using laser absorption) was ~10 - 20%. Similar losses may be expected in other shock tube facilities.

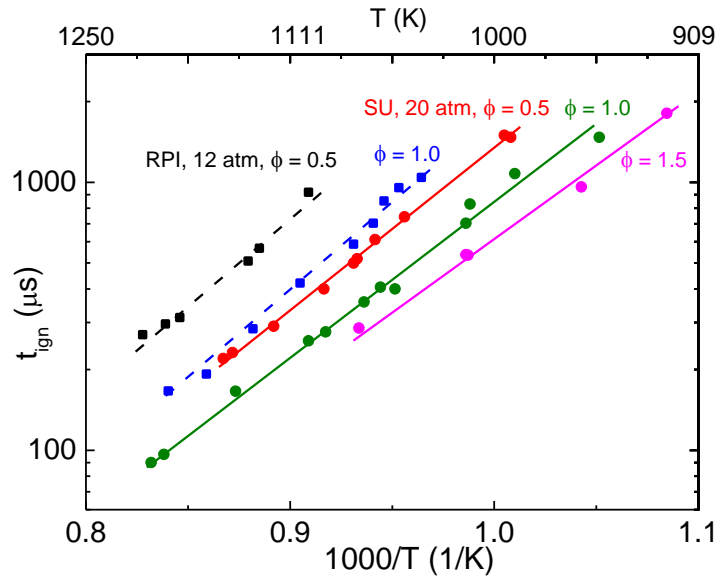


Figure 7. Comparison of ignition delay data of decalin/air mixture at various equivalence ratios from RPI [32] at 12 atm and SU (current studies) at 20 atm. Solid lines are best fits to data points.

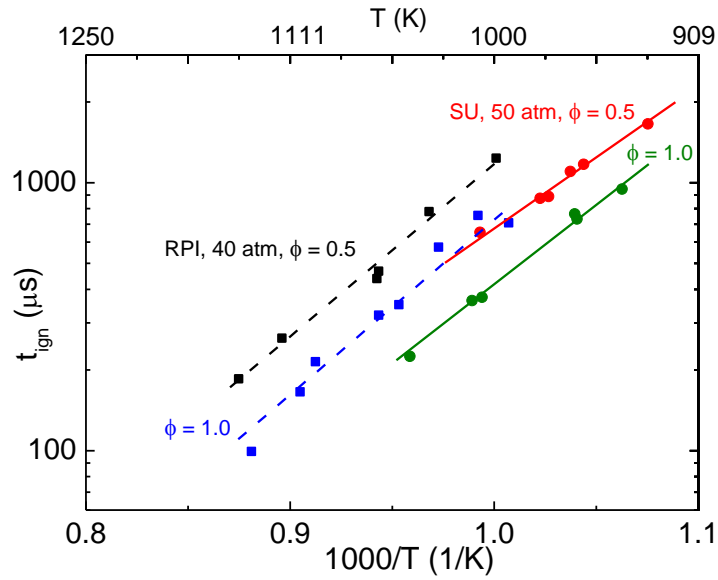


Figure 8. Comparison of ignition delay data of decalin/air mixture at various equivalence ratios from RPI [32] at 40 atm and SU (current studies) at 50 atm. Solid lines are best fits to data points.

Our measured ignition delay times at these high temperatures can be correlated through least-squares regression as

$$t_{\text{ign}} (\text{s}) = 1.52 \times 10^{-8} P^{-0.78} \phi^{-0.64} \exp(110 \text{ kJ/mol/RT})$$

where t_{ign} is the ignition delay time in seconds, T the temperature in Kelvin, and P the pressure in atm. This correlation is valid over the current experimental coverage of temperature, pressure and equivalence ratio parameter space for decalin in air, as delineated in Figure 6, 7 and 8.

Figure 9 and 10 compare current ignition delay times at high temperatures with kinetic modeling using the aforementioned mechanism [18] (Ranzi modeling for short). The Ranzi modeling generally overpredicts the ignition delay time of decalin at high temperatures by at most a factor of 2. In addition, while these mechanistic predictions yield a similar global activation energy (107 kJ/mol) to the measured value (110 kJ/mol), they show slightly stronger dependence on pressure ($t_{\text{ign}} \sim P^{-0.94}$) and weaker dependence on equivalence ratio ($t_{\text{ign}} \sim \phi^{-0.42}$) compared to current findings ($t_{\text{ign}} \sim P^{-0.78} \phi^{-0.64}$). Due to the propagation of low-temperature chemistry into high-temperature regimes at elevated pressures [46], it is possible to achieve better agreement between experiments and modeling in Figure 9 and 10, as will be discussed in a later section.

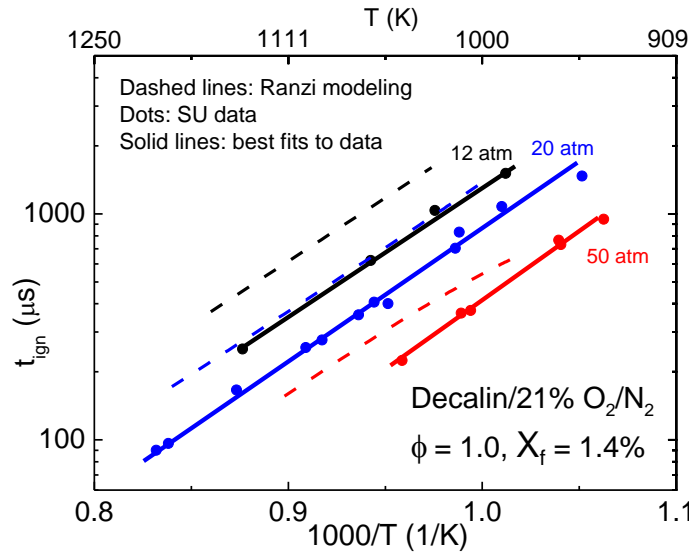


Figure 9. Comparison of measured and originally predicted ignition delay data of stoichiometric decalin/air mixture at 12, 20, and 50 atm over 1200 – 920 K. Mechanism predictions, or Ranzi modeling, were calculated using the reaction mechanism[18] and constant U , V assumption.

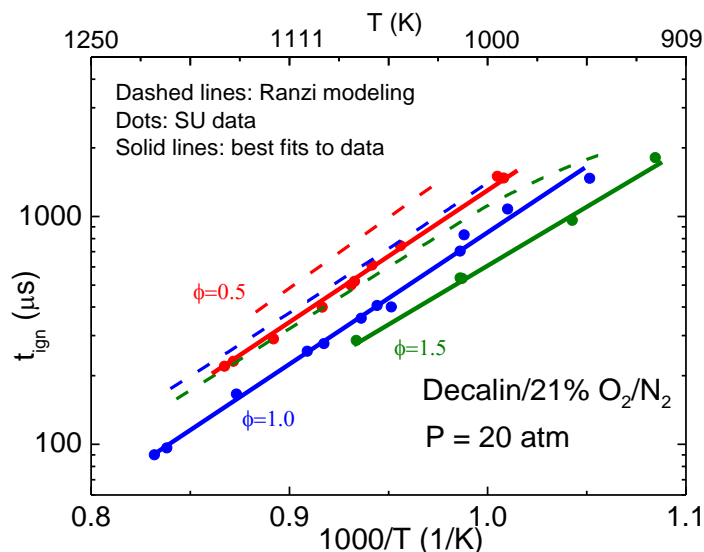


Figure 10. Comparison of measured and originally predicted ignition delay data of decalin/air mixture at $\phi = 0.5, 1.0$, and 2.0 , 20 atm over $1200 - 920\text{ K}$. Mechanism predictions, or Ranzi modeling, were calculated using the reaction mechanism [18] and constant U, V assumption.

Low-temperature Ignition

Figure 11 exhibits the negative-temperature-coefficient (NTC) behavior of decalin and its dependences on pressure and equivalence ratio. This NTC behavior is a well-acknowledged but incompletely characterized aspect of straight-chain alkanes [15, 17], branched-chain alkanes [12, 13], and some jet fuels [14, 16]. Similar NTC behavior for decalin oxidation is also noted by Agosta [34] in terms of carbon monoxide production. As shown in Figure 11, the widths of the NTC regime at three different conditions are quite close and relatively narrow. In addition, the start of the NTC regime at $\phi = 1.0$ and 50 atm occurs at higher temperature (around 940 K) compared to that at $\phi = 1.0$ and 20 atm (around 880 K), while the starting point at $\phi = 0.5$ and 1.0 , 20 atm are nearly the same. This pressure-induced shift is a typical aspect of NTC behavior and has been related to the equilibria of the addition reactions of oxygen to the alkyl (R) and hydroperoxy-alkyl (QOOH) radicals [47]. Furthermore, the influence of pressure and equivalence ratio on the ignition delay time of decalin/air mixture is most pronounced in the NTC regime, but cannot be quantitatively described by simple power law correlations as discovered at higher temperatures. The pressure and equivalence ratio dependences of the NTC regime for decalin autoignition are qualitatively in good agreement with those of *n*-heptane [48] and *n*-decane [49].

Kinetic model predictions using decalin oxidation mechanism [18] and the constant U, V assumption are also presented in Figure 11. Comparisons between measurements and modeling illustrate that Ranzi modeling captures many of the experimental trends. First, the overall

agreement between data and modeling is surprisingly good, with better agreement at lower temperatures for data at all three conditions. Second, the Ranzi-predicted pressure and equivalence ratio dependences also appear to be strongest in the NTC regime. These predicted dependences are employed to scale the experimental data at 920 – 770 K by the expression $t_{\text{ign}} \sim P^m \phi^n$ where m and n are functions of temperature, as shown in Figure 12. Nonetheless, some deviations in the experiments and modeling still exist. For example, the observed global activation energy in the NTC regime at $\phi = 1.0$ and 50 atm appears to be slightly negative, while the predicted one is positive. Although these differences are relatively small, improvement to modeling predictions is still possible but will require examination of the reactions responsible for both high- and low-temperature autoignition.

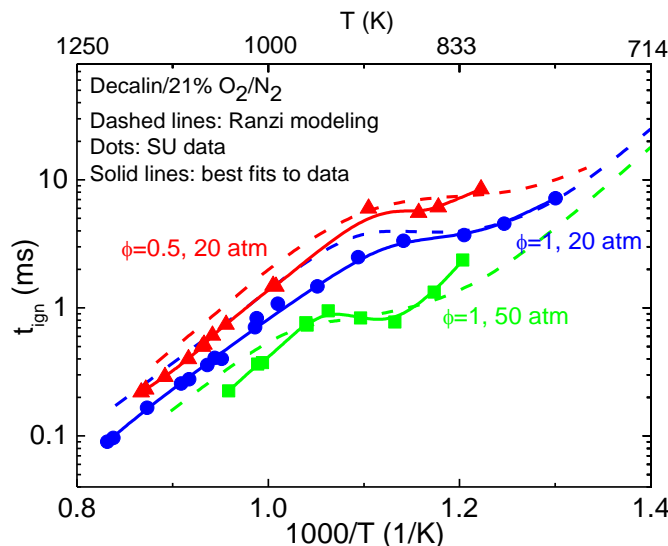


Figure 11. Comparison of measured and originally predicted ignition delay data of decalin/air mixture over 1200 – 770 K at three conditions: $\phi = 0.5$, 20 atm; $\phi = 1.0$, 20 atm; $\phi = 1.0$, 50 atm. Mechanism predictions, or Ranzi modeling, were calculated using the reaction mechanism [18] and constant U, V assumption. NTC behavior is evident at around 940 – 800 K.

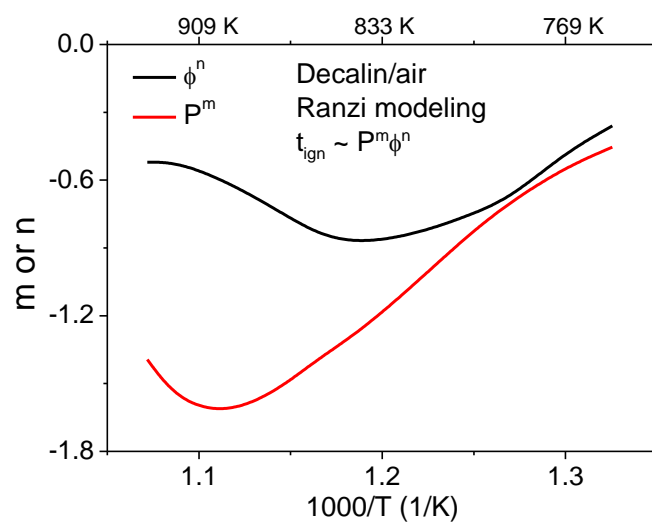


Figure 12. Temperature-dependent pressure and equivalence ratio scaling dimensions for ignition delay times at 920 – 770 K obtained from Ranzi modeling.

Table 4. Measured ignition delay times for decalin/air mixtures

P (atm)	ϕ	T (K)	t_{ign} (μs)
~20 atm, $\phi \sim 1.0$			
16.6	0.93	1202	109
18.8	0.93	1193	106
20.5	1.06	1145	157
18.9	0.91	1100	284
19.9	1.10	1090	261
19.2	0.95	1068	381
20.5	1.01	1059	396
19.3	0.90	1051	440
26.8	1.02	1014	553
23.3	0.90	1012	788
22.1	1.14	990	917
24.1	1.00	951	1271
19.5	0.96	914	2644
20.2	1.00	876	3291
24.0	0.98	830	3049
19.3	0.84	802	5341
15.5	0.87	769	8746
~20 atm, $\phi \sim 0.5$			
18.5	0.52	1153	228
19.3	0.51	1147	235

20.5	0.42	1121	318
20.6	0.47	1091	406
21.2	0.42	1074	533
19.4	0.41	1072	603
20.3	0.50	1062	604
21.9	0.49	1046	701
20.8	0.46	995	1531
20.0	0.46	992	1553
25.5	0.45	905	4324
19.9	0.46	864	5964
22.0	0.43	849	6114
16.7	0.49	818	10380
~20 atm, $\phi \sim 1.5$			
19.5	1.47	1071	295
27.5	1.41	1014	435
26.5	1.60	1013	412
24.5	1.42	959	849
24.7	1.33	922	1657
~50 atm, $\phi \sim 1.0$			
46.0	0.86	1043	264
50.4	0.81	1011	413
46.4	0.84	1006	443
47.9	0.83	962	891
50.1	0.86	961	804
50.6	0.87	941	1024
48.9	0.92	912	903
56.6	1.00	883	638
37.8	0.98	852	1984
48.3	0.69	831	3411
~50 atm, $\phi \sim 0.5$			
49.4	0.47	1007	685
48.4	0.51	978	885
51.2	0.48	974	895
48.8	0.53	964	1081
50.8	0.51	958	1143
49.8	0.50	930	1662
~12 atm, $\phi \sim 1.0$			
11.7	0.94	1141	268
12.8	1.00	1061	591
12.8	0.96	1025	1011
13.1	0.90	988	1509

Pyrolysis Experiments

Fast fuel cracking at early times allows decoupling of the fuel decomposition chemistry from the oxidation kinetics of the cracked products [50]; thus, it is feasible to focus in separate experiments on the chemistry of decalin pyrolysis. Pyrolysis experiments were carried out using a mixture of decalin/argon at 18.2 – 20.2 atm over a temperature range of 1197 – 1511 K within test times of ~2 ms. Before presenting the experimental results, it is useful to discuss the major products of decalin pyrolysis at these experimental conditions. Figure 13 shows an example kinetic modeling of decalin pyrolysis at a representative shock tube condition using the same reaction mechanism and gasdynamic assumption as in the autoignition cases. It reveals that the expected primary products are ethylene, benzene, propene, toluene, and 1,3-butadiene (the order is contingent on the specific experimental conditions). Also note that one intermediate species, ODECAL, using the notation of Ranzi which represents a group of cyclo-alkene species, indicates the lumping nature of the reaction scheme. Additionally, besides ethylene, it is not surprising to have benzene and toluene in the list of most prevalently formed products. In fact, the decalin pyrolysis system has received much attention because it is a significant feedstock hydrocarbon processed by the petroleum industry to produce other hydrocarbons, especially more aromatics than from pyrolysis of alkanes or mono-cyclic five- and/or six -membered cyclo-alkanes [8]. This list of primary products is confirmed by the flow reactor studies by Zeppieri *et al.* [27] and the *ab initio* study by Chae *et al.* [37] at similar conditions.

In the current study, the 3.39 μm diagnostic provides an overall check of the performance of the model for decalin pyrolysis, and the 10.6 μm diagnostic is conducive to a better understanding of products distribution, at least partially through ethylene mole fraction time-histories. The initial decalin concentrations utilized in the 3.39 μm and 10.6 μm experiments were around 2260 ppm and 3540 ppm, respectively.

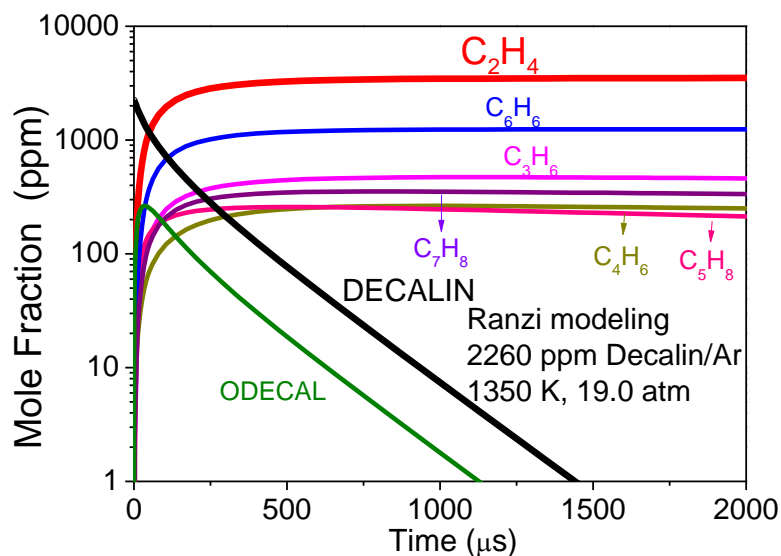


Figure 13. Example kinetic modeling of decalin pyrolysis at a representative shock tube condition using the reaction mechanism in [18] and constant U, V assumption.

3.39 μm Diagnostic

Figure 14 shows time-histories of 3.39 μm absorbance from five decalin pyrolysis experiments. Time zero is defined as the moment of arrival of the reflected shock at the measurement location. The indicated temperatures refer to the calculated values immediately behind the reflected shock. Although these absorbance time-histories generally exhibit exponential-decay-like behaviors, caution must be exercised that they represent the total absorbance from all hydrocarbons involved in the process of decalin pyrolysis, much more than those depicted in Figure 13. Therefore, it is not easy to extract information with respect to the behavior of the parent fuel, i.e., decalin. Instead of correcting the measured absorbance by either a simple one-step-reaction method [41] or a detailed kinetic mechanism method [51], we propose a simple approach to utilizing these measurements to evaluate the decalin pyrolysis kinetics. With a knowledge of absorption cross section database [40, 51-55] of hydrocarbons at high temperatures and pressures at a particular wavelength, such as those shown in Figure 3 for decalin at 3.39 μm , we can convert the predicted time-histories of species mole fraction to those of absorbance and compare the sum of these predicted absorbances with the measured ones. A summary of the database used in current studies is shown in Table 5. Since this approach requires a good prediction of the products distribution, the 10.6 μm diagnostic was employed to help impose some constraints on the decalin pyrolysis sub-mechanism.

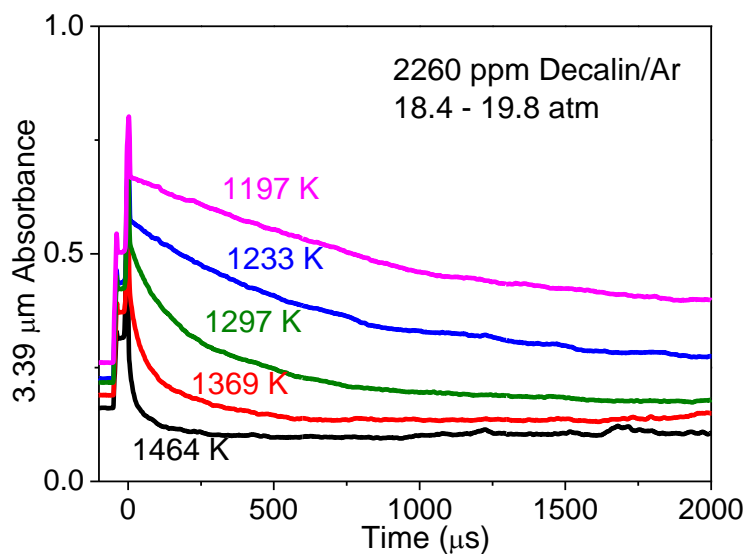


Figure 14. Absorbance time-histories at 3.39 μm during pyrolysis of 2260 ppm decalin/Ar at 1197 – 1464 K and 18.4 – 19.8 atm.

Table 5. Absorption cross sections at 3.39 and 10.675 μm of major hydrocarbons in the decalin pyrolysis system at 1197 – 1511 K and 18.2 – 20.2 atm

Species	Absorption Cross Section (m^2/mol)		References
	3.39 μm	10.675 μm	
DECALIN	$63.56087 - 0.03938 \cdot T + 8.75042 \cdot 10^{-6} \cdot T^2$	0.0236	Figure 3; [55] ^a
ODECAL	$41.1 + 0.0641 \cdot T - 9.41 \cdot 10^{-5} \cdot T^2 + 2.96 \cdot 10^{-8} \cdot T^3$	4	[53] ^b ; [53] ^c
C_2H_4	$0.5471 + 8.11437 \cdot 10^{-4} \cdot T$	4	[51]; [53]
C_6H_6	0.022	0.00418	[55]; [55]
C_3H_6	$6.29943 - 0.00168 \cdot T$	$4.88821 - 0.00185 \cdot T$	[51]; [53]
C_7H_8	$6.39337 - 0.00368 \cdot T$	0.36	[52]; [52]
C_4H_6	0.662	3.85	[55]; [55]
C_5H_8	4.78	0.558	[55]; [55]
CH_4	10	0	[54], [40]; [55]

a. taken as cyclohexane,

b. taken as methylcyclohexane

c. taken as ethylene

10.6 μm Diagnostic

The two-color differential absorbance method developed by MacDonald *et al.* [53] was employed to extract the time-history of ethylene mole fraction. This method requires separate experiments, usually first at 10.532 μm and then 10.675 μm , such that the interference absorption can be cancelled out. To have a sense of carbon conversion from decalin to ethylene, the ethylene mole fraction is normalized by the initial mole fraction of decalin to give rise to the ethylene yield. The uncertainty of current ethylene measurements comes from several sources including the original absorbance signals, reflected-shock temperature and pressure, and absorption cross sections of ethylene at two colors, with the first one being dominant due to relatively larger beam steering noise of the CO_2 laser beam. The combined uncertainty of the experimental ethylene yield is estimated to be 20 - 30%.

Figure 15 presents measured and predicted ethylene yield traces for four decalin pyrolysis experiments. We find that the data and modeling are in good agreement only in terms of shape but not magnitude. Specifically, the Ranzi modeling overpredicts both the early time rise and long-time plateau of the ethylene yield. This might imply that although the ethylene formation pathways are reasonably conceived, the corresponding rate parameters need refinement.

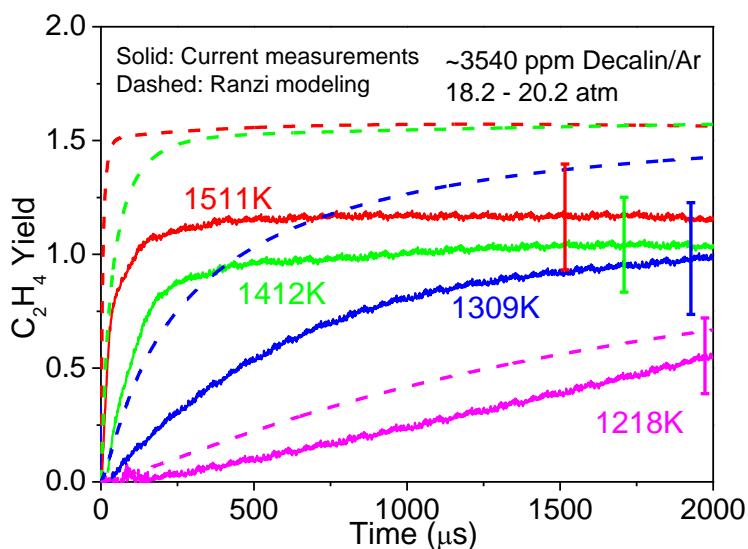


Figure 15. Comparison of measured and originally predicted ethylene yield time-histories during pyrolysis of ~3540 ppm decalin/Ar at 1218 – 1511 K and 18.2 – 20.2 atm. Mechanism predictions, or Ranzi modeling, were calculated using the reaction mechanism [18] and constant U, V assumption.

Comparison of the long-time plateau of ethylene yield, or peak ethylene yield, is helpful to assess the ability of decalin to produce ethylene. Figure 16 shows the observed and predicted peak

ethylene yields as a function of temperature. The observed values at 1218 K and 1309 K are obtained through exponential fit to the corresponding ethylene yield for the first 2 ms. The Ranzi modeling generally overpredicts the peak ethylene yield at these temperatures by around 50%. In addition, current measurements indicate that ethylene accounts for only 20 – 25% of the total carbon in the parent decalin molecule, which means that the yields of some interfering species, most probably other small alkenes (propene and 1,3-butadiene) or aromatics (benzene and toluene), are comparable to, or even higher than that of ethylene. Since these interfering species make significant contributions to the absorbance measured at 10.675 μm [53], adjustment of the decalin pyrolysis sub-mechanism should enable us to recover both the experimental ethylene yield profiles and the measured absorbance at 10.675 μm .

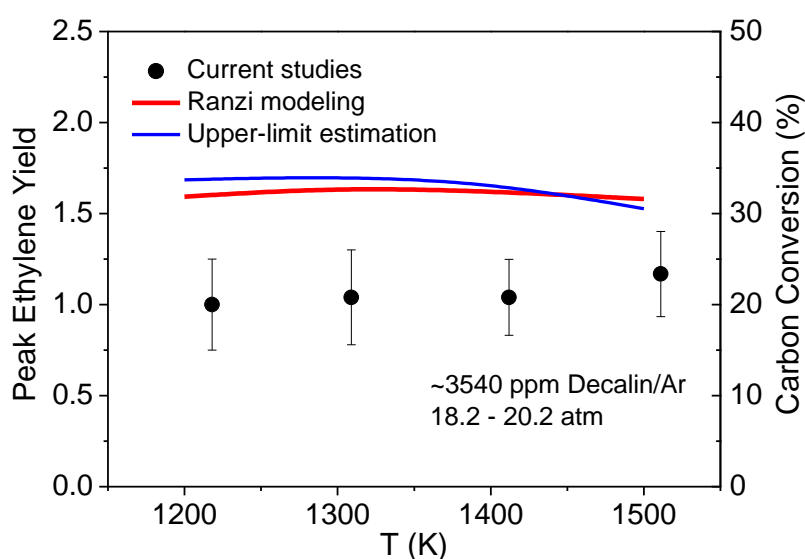


Figure 16. Comparison of measured, predicted and estimated peak ethylene yield during pyrolysis of ~3540 ppm decalin/Ar at 1218 – 1511 K and 18.2 – 20.2 atm. Mechanism predictions, or Ranzi modeling, were calculated using the reaction mechanism [18] and constant U, V assumption. Upper-limit estimation were derived based on analysis of the reaction pathways in Figure 17 (see text).

Adjustment of Decalin Reaction Mechanism

The goal of current measurements reported above is to validate and refine the decalin reaction mechanism. Since the Ranzi decalin model uses a lumped reaction/species approach, it might not be possible to make direct and specific kinetic adjustment based on a detailed analysis of individual pathways, species sensitivities, and reaction fluxes, etc.. Nonetheless, some preliminary suggestions can still be made within this framework of lumping reaction scheme, as will be discussed below.

Pyrolysis Kinetics

Before exploring possible improvement to the mechanism, it is necessary to check with other decalin pyrolysis mechanisms to confirm the overprediction aspect of Ranzi modeling. To the best of our knowledge, there exist two other mechanisms that describe the pyrolysis of decalin at relatively high temperatures (above 1000 K), i.e., the computational kinetic mechanism developed based on and validated against the flow reactor studies by Zeppieri [8] and the *ab initio* study of thermal decomposition of decalin [37], mentioned previously. Unfortunately, we have found that the former does not yield reasonable results at the current shock tube experimental conditions. This is not surprising as parameters important in an intermediate-temperature flow reactor experiment might not be the same as those in a high-temperature shock tube simulation [56]. In addition, the reaction scheme and thermochemical data assembled in [37] are not entirely available, so a direct use of this model cannot be made. Nonetheless, an analysis of the reaction scheme released in [37] inspires us to estimate the upper-limit of ethylene formation at current experimental conditions. Specifically, consider the initiation kinetics of decalin pyrolysis shown by pathways below (see Figure 17). Pathway C-C refers to the breaking of the bridgehead bond of decalin molecule, and pathways 1-1, 10-1, and 12-1 represent the hydrogen-abstraction reactions at three types of carbon sites in the decalin molecule and subsequent reactions leading to the formation of ethylene, benzene, etc.. If we only take into account pathways 1-1 and 12-1, the upper-limit of ethylene formation can be deduced. Although pathway C-C can also give birth to ethylene [37], it has been experimentally studied [25-27] and mechanistically argued [8] that the bridgehead bond homolysis route is a minor route of decalin decay. This route is not included in the decalin sub-mechanism published in [18], either. Therefore, pathway C-C is neglected in current endeavor of upper-limit estimation. Results of this estimation are also shown in Figure 16. Clearly, the estimated upper-limits of peak ethylene yield are nearly identical with those obtained from Ranzi modeling (within 6%). This justifies the necessity of adjusting the decalin pyrolysis sub-mechanism released in [18].

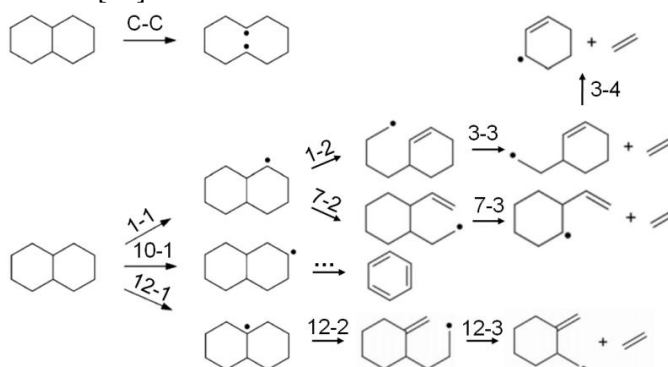


Figure 17 Initial decomposition pathways of decalin adapted from [37] (using the same reaction labels). Only pathways 1-1 and 12-1 were included in the estimation of upper-limit of peak ethylene yield.

To seek guidance, A-factor sensitivity analysis for ethylene was conducted, as shown in Figure 18.

Generally, ethylene formation is most sensitive to several reactions that compete with each other. At very early times ($\sim 100 \mu\text{s}$), it is very sensitive to the isomerization reaction of decalin to ODECAL, a group of cyclo-alkene species as mentioned before, while at long time, its fate is mostly determined by the two competing decomposition reactions of ODECAL, i.e., reactions “pyr 1” and “pyr 2” with rate constants $k_{\text{pyr 1}}$ and $k_{\text{pyr 2}}$, respectively. Although $k_{\text{pyr 1}}$ and $k_{\text{pyr 2}}$ have been adjusted to explain the large formation of benzene and toluene [18], the actual branching ratios and reaction rate constants of these initial individual channels and the subsequent reactions that lead from these intermediates to stable final products are still somewhat a matter of conjecture. Hence, it is still possible to make improvement, at least to reproduce the experimental ethylene yield reported here.

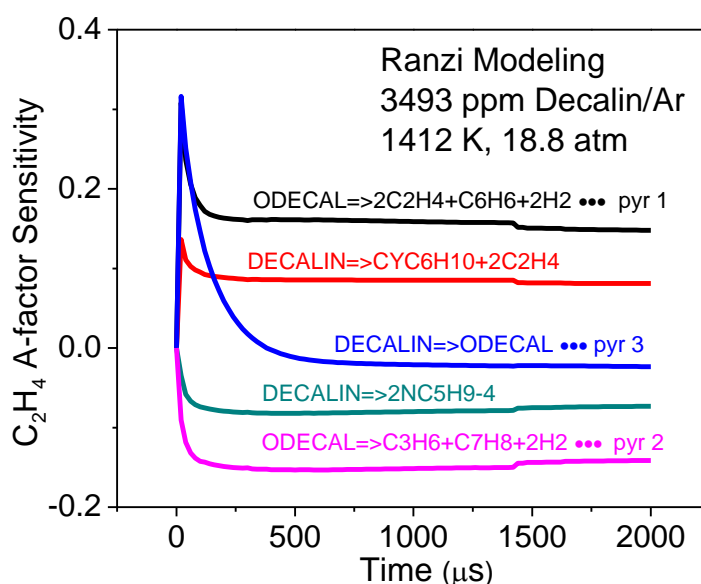


Figure 18. A-factor sensitivity analysis for ethylene during pyrolysis of 3493 ppm decalin in Ar at 1412 K and 18.8 atm.

As discussed earlier, adjustment of $k_{\text{pyr 1}}$ and $k_{\text{pyr 2}}$ should make the modeling match both the ethylene yield and $10.675 \mu\text{m}$ absorbance. Two options are available: the first one is to multiply $k_{\text{pyr 1}}$ and $k_{\text{pyr 2}}$ by the same factor maintaining the branching ratio $k_{\text{pyr 1}}/(k_{\text{pyr 1}} + k_{\text{pyr 2}})$, while the second one is to increase the branching ratio holding the sum $k_{\text{pyr 1}} + k_{\text{pyr 2}}$ constant. The second option is chosen here, as current ethylene measurements are independent of the overall decomposition rate of ODECAL. After changing the branching ratio $k_{\text{pyr 1}}/(k_{\text{pyr 1}} + k_{\text{pyr 2}})$ from 76.9% to 35.0%, significant improvement of agreement is achieved between experimental results and modeling. This improvement is evident not only in terms of ethylene yield time-histories, but also of peak ethylene yields, as shown in Figure 19 and Figure 20, respectively, within the uncertainty limits of current measurements. Nonetheless, Figure 19 shows that the modified mechanism predictions still overpredict the early time rise of ethylene, which might be due to deficiency in the untouched reaction “pyr 3”, $\text{DECALIN} \rightarrow \text{ODECAL}$.

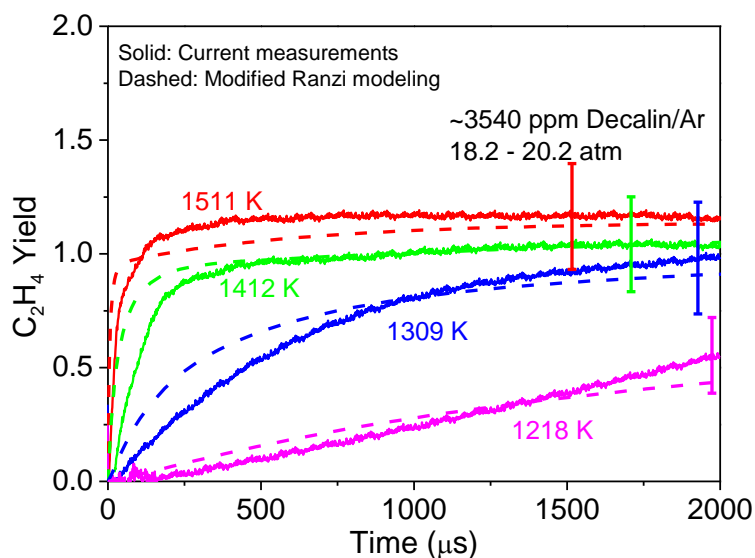


Figure 19. Comparison of measured and newly predicted ethylene yield time-histories during pyrolysis of ~3540 ppm decalin/Ar at 1218 – 1511 K and 18.2 – 20.2 atm. Modified Ranzi modeling was made using the reaction mechanism [18] with modified rate constants for reactions “pyr 1” and “pyr 2” in Figure 18 and constant U, V assumption.

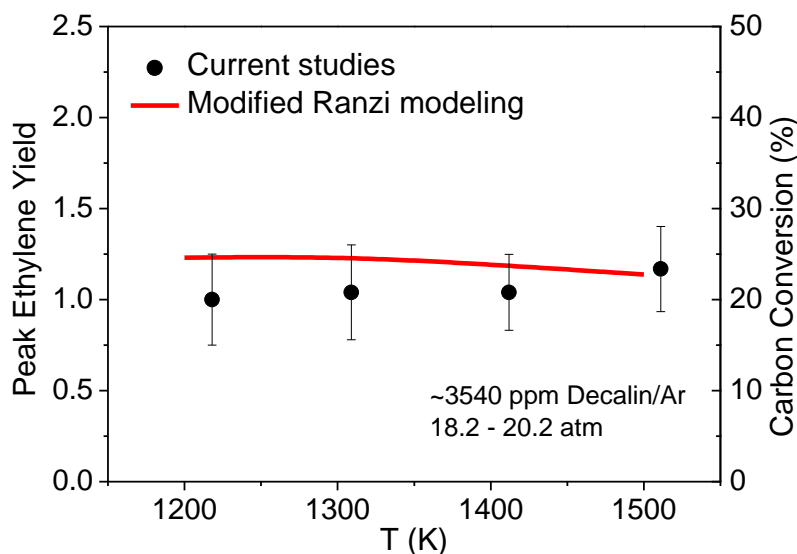


Figure 20. Comparison of measured and predicted peak ethylene yield during pyrolysis of ~3540 ppm decalin/Ar at 1218 – 1511 K and 18.2 – 20.2 atm. Modified Ranzi modeling was made using the reaction mechanism [18] with modified rate constants for reactions “pyr 1” and “pyr 2” in Figure 18 and constant U, V assumption.

Additionally, a comparison of peak ethylene yields of different classes of alkanes [53] is shown in Figure 21. Clearly, the peak ethylene yields of n-dodecane (straight-chain alkane) are typically much higher than those of decalin and methylcyclohexane (cyclo-alkanes) by around a factor of four, and the latter two species have nearly the same peak ethylene yields, while those of iso-cetane (branched-chain alkane) are almost negligible. Such information is quite useful for formulation of chemical kinetic surrogates for practical fuels containing a large fraction of cyclo-alkanes [57].

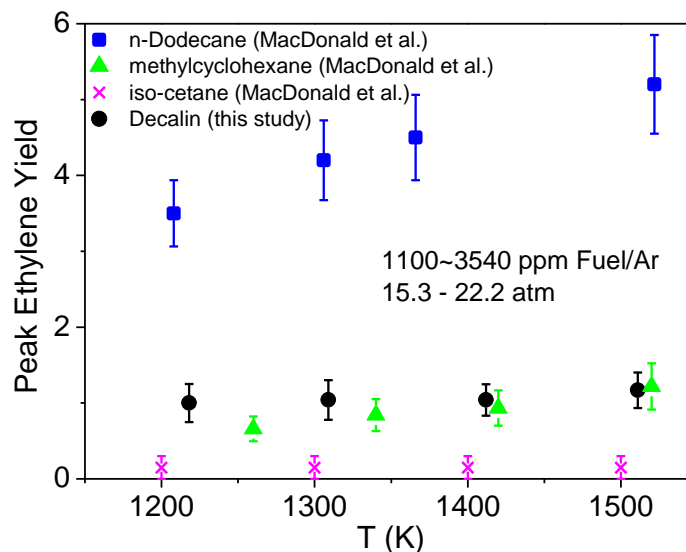


Figure 21. Comparison of peak ethylene yields of different classes of alkanes: n-dodecane [53], methylcyclohexane [53], iso-cetane [53], and decalin (this study).

Besides ethylene yield, the modified modeling is validated against the measured absorbance at $10.675\ \mu\text{m}$ in four decalin pyrolysis experiments, as shown in Figure 22. Fortunately, the agreement is generally satisfactory, within 20% for the three lower temperature cases. At the highest temperature case, although the calculated absorbance overpredicts the long-time behavior, it still captures the peak of the measured absorbance. It is also noted that the primary interfering species to $10.6\ \mu\text{m}$ diagnostic for decalin are propene and 1, 3-butadiene, which holds the promise of applying more infrared diagnostics under development in our laboratory to measure these interfering species for a pyrolysis system like that of decalin.

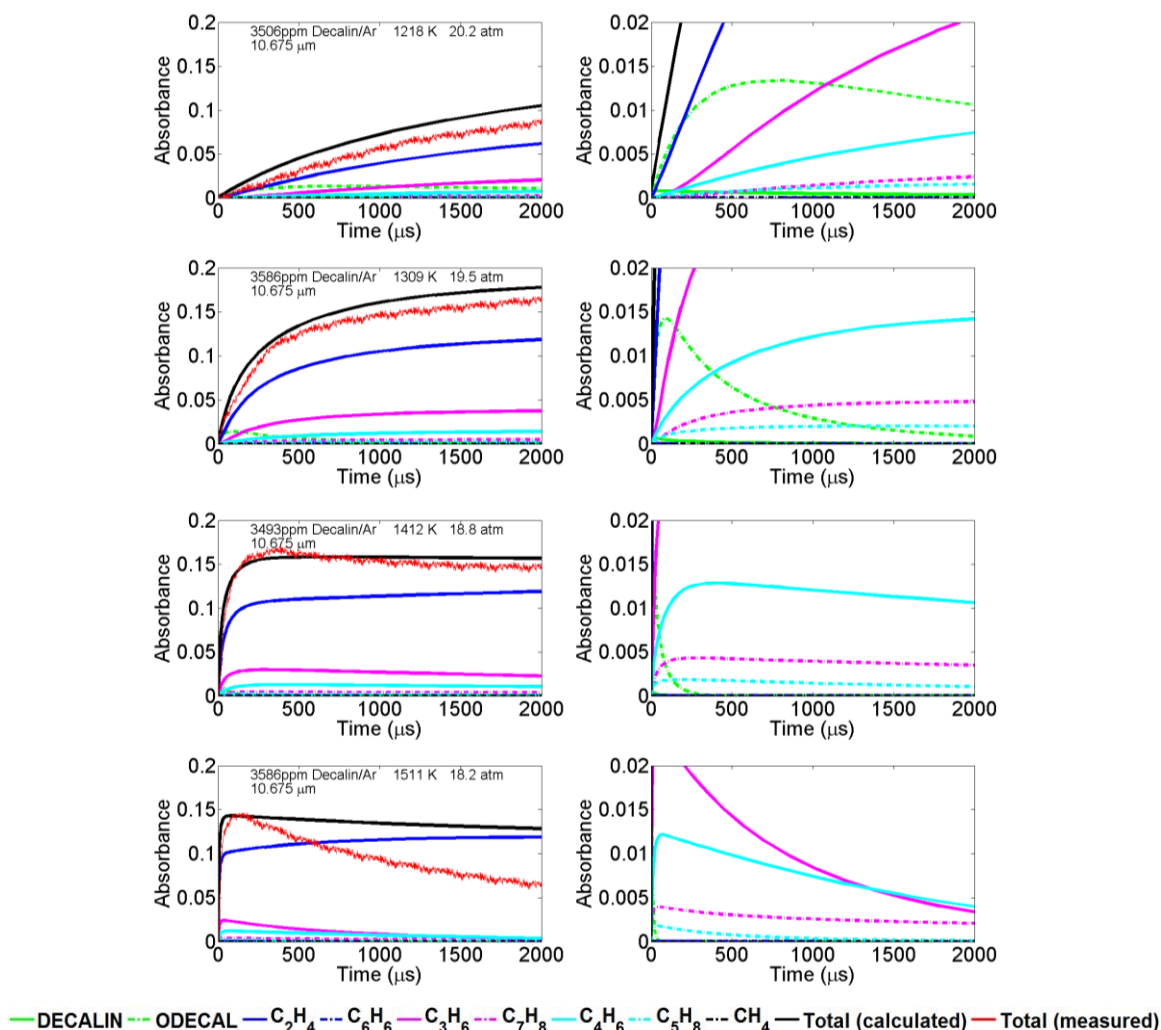


Figure 22. Comparison of calculated (black) and measured (red) absorbances at 10.675 μm during pyrolysis of ~ 3540 ppm decalin/Ar at 1218 – 1511 K and 18.2 – 20.2 atm. Calculations were made using the reaction mechanism [18] with modified rate constants for reactions “pyr 1” and “pyr 2” in Figure 18 and constant U, V assumption. Figures at right show zoomed-in view of those at left.

Similar validation work can be performed with regard to the measured absorbance at 3.39 μm shown in Figure 14. As mentioned before, the vibrational mode of stretch of C-H bond in any hydrocarbon is strongly resonant with the 3.39 μm laser light, so more species should be considered in the validation at 3.39 μm , as shown in Table 5. Comparison of calculated and observed absorbances at 3.39 μm is shown in Figure 23. The overall agreement is satisfactory (within 25%), given the limited set of species involved in the calculations and the fidelity of absorption cross section of ODECAL at high temperatures and pressures. It is learned that the primary contributor other than decalin to the 3.39 μm absorbance at the early 500 μs is ODECAL, while those at intermediate-to-long times are propene and ethylene. The contribution of methane to the total calculated absorbance increases with increasing temperature, while those from the

remaining species considered are usually less than 0.01. Such validation, in a global sense, tests the overall goodness of the modified decalin pyrolysis sub-mechanism. Further refinement could be made with the help of a diagnostic sensitive only to decalin as well as diagnostics for additional decomposition products.

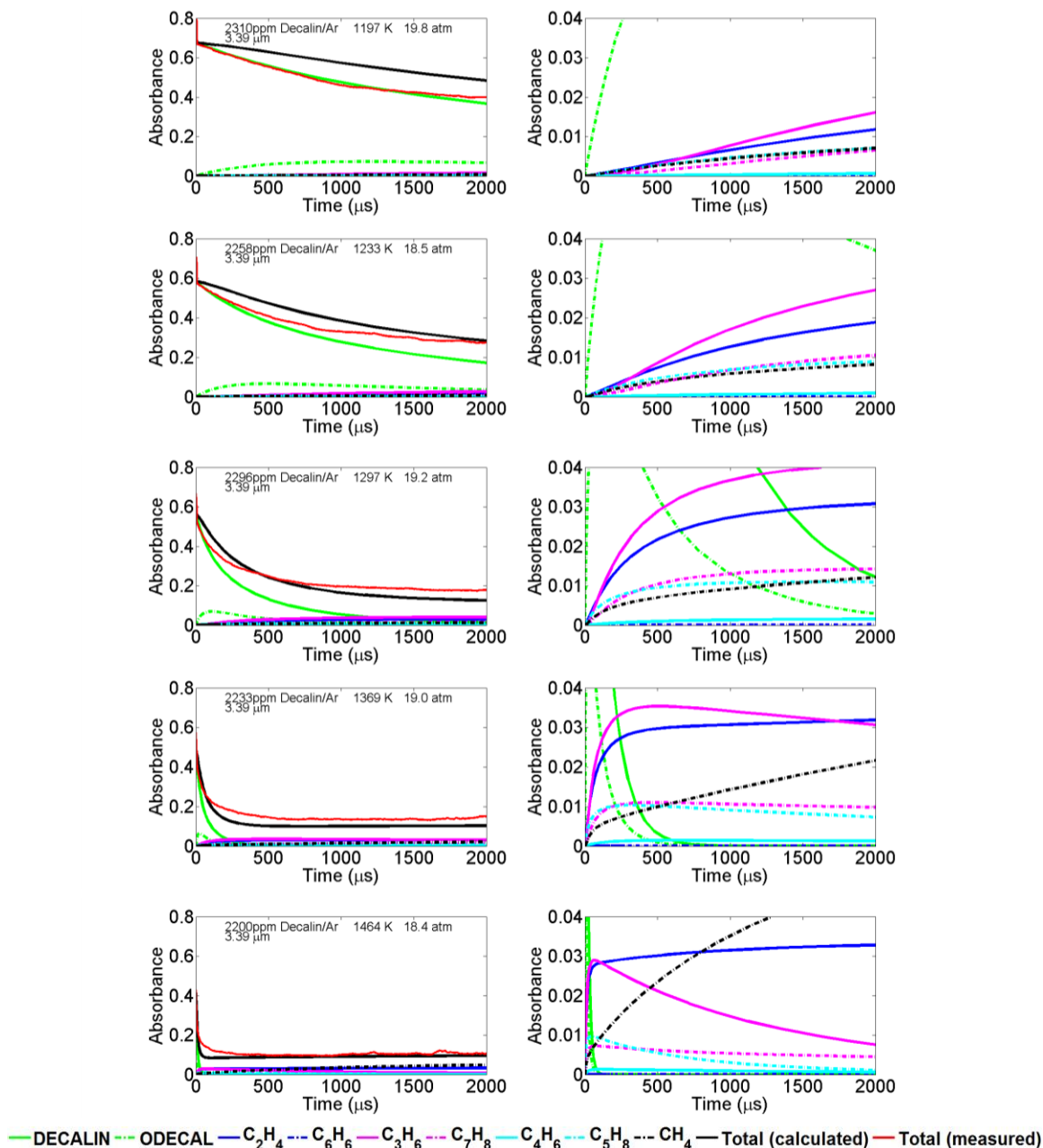


Figure 23. Comparison of calculated (black) and measured (red) absorbances at 3.39 μm during pyrolysis of ~2260 ppm decalin/Ar at 1197 – 1464 K and 18.4 – 19.8 atm. Calculations were made using the reaction mechanism [18] with modified rate constants for reactions “pyr 1” and “pyr 2” in Figure 18 and constant U, V assumption. Figures at right show zoomed-in view of those at left.

Oxidation Kinetics

Figure 24 shows a brute-force sensitivity analysis of ignition delay time of decalin in air at 20 atm (top) and 50 atm (bottom), $\phi = 1.0$. Sensitivities of ten reactions at 1250, 1000, and 833 K are examined. At the highest temperature at 20 atm, reaction “oxi 1” plays the predominant role in the oxidation of decalin, as expected, while reactions “oxi 3” and “oxi 4” come second and third. At the lowest temperature at 20 atm, reactions “oxi 6” and “oxi 7” have dramatic influence on the ignition delay time. These reactions are typical examples of low-temperature autoignition chemistry [58], representing classes of $R + O_2 \rightarrow RO_2$ and $QOOH + O_2 \rightarrow OOQOOH$, respectively. Abstraction by hydroperoxy radical (HO_2), hydroxyl radical (OH), and oxygen (O_2) from the decalin molecule (reactions “oxi 3”, “oxi 2”, “oxi 4”, and “oxi 5”) also affects the final ignition delay time at 20 atm, in the decreasing order, and reactions “oxi 2” and “oxi 5” appear to be significant only at the lowest temperature at 20 atm. The three most influential reactions in the decalin pyrolysis system, i.e., reactions “pyr 1”, “pyr 2”, and “pyr 3”, have negligible impact on the ignition delay time at all three temperatures at 20 atm, which further justifies the decoupling of adjustments to the pyrolysis kinetics from those of the oxidation kinetics. Sensitivity of ignition delay time of decalin at 50 atm exhibits similar patterns as those at 20 atm, except the increasing importance of reactions “oxi 6” and “oxi 7” at 1000 K, which confirms the shift of NTC regime to higher temperature with increasing pressure observed in Figure 11.

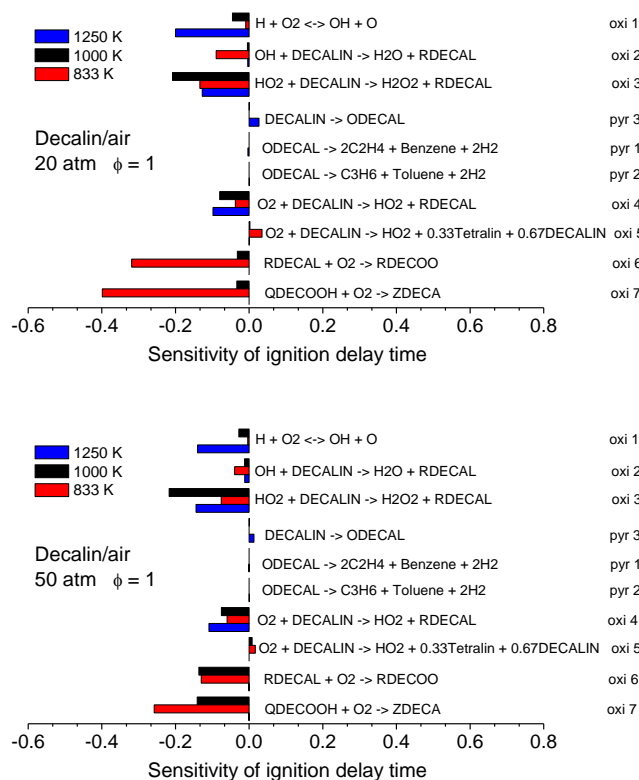


Figure 24. Brute-force sensitivity analysis of ignition delay time of decalin in air at 20 atm (TOP) and 50

atm (BOTTOM), $\phi = 1.0$.

As shown in Figure 11, while it generally satisfactorily reproduces the ignition delay time of decalin in air at 50 atm, the original Ranzi modeling generally overpredicts the ignition delay time of decalin in air at above 900 K and 20 atm. Among the reactions shown in Figure 24, besides reaction “oxi 1”, both reactions “oxi 3” and “oxi 4” exhibit relatively larger sensitivities at above 900 K. One possible way of improving the performance of the original decalin oxidation sub-mechanism at higher temperatures is to multiply the rate constant of reaction “oxi 4” by a factor of two, as an example. Figure 25 presents the results of this modification. Clearly, improved kinetic modeling is achieved for current data at 20 atm. In addition, generally good agreement is also found between previous measurements by Oehlschlaeger *et al.* [32] and the updated mechanism predictions using this kinetic modification, as shown in Figure 26. More theoretical and experimental studies are required to further refine the Ranzi decalin sub-mechanism.

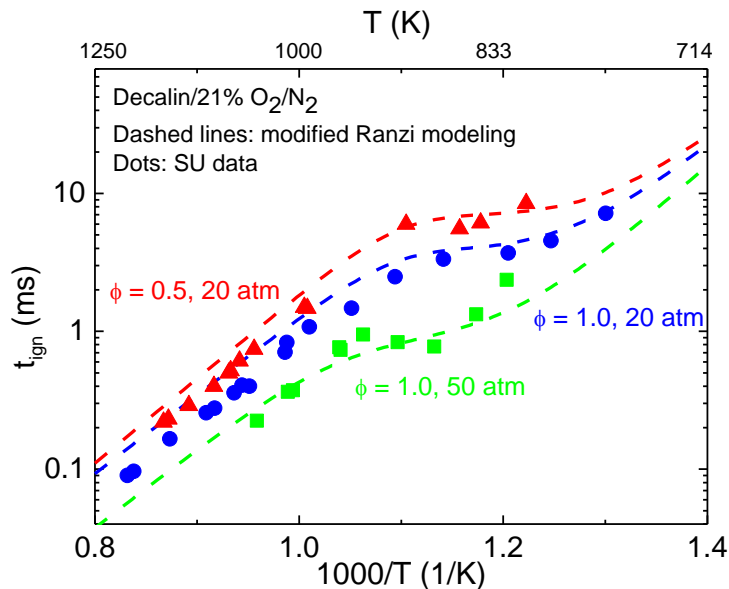


Figure 25. Comparison of currently measured and newly predicted ignition delay data of decalin/air mixture over 1200 – 770 K at three conditions: $\phi = 0.5$, 20 atm; $\phi = 1.0$, 20 atm; $\phi = 1.0$, 50 atm. Modified Ranzi modeling was made using the reaction mechanism [18] with modified rate constant for reaction “oxi 4” in Figure 24 and constant U, V assumption.

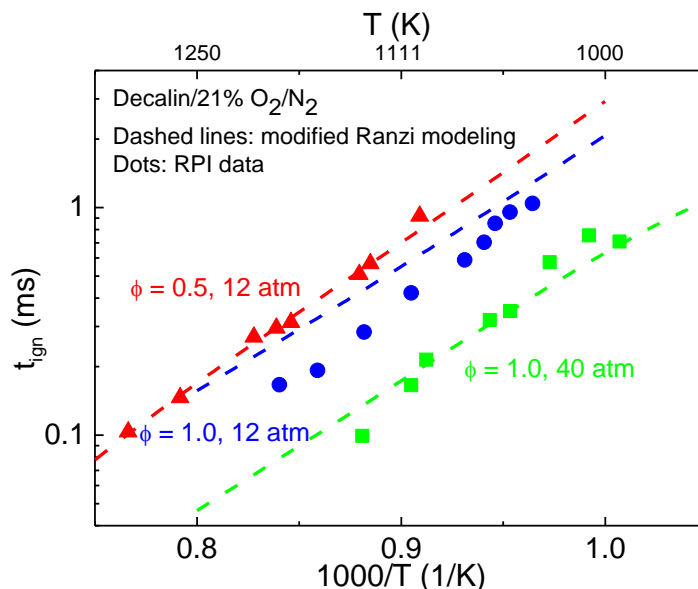


Figure 26. Comparison of previously measured (Oehlschlaeger *et al.* [32]) and newly predicted ignition delay data of decalin/air mixture over 1305 – 993 K at three conditions: $\phi = 0.5$, 12 atm; $\phi = 1.0$, 12 atm; $\phi = 1.0$, 40 atm. Modified Ranzi modeling was made using the reaction mechanism [18] with modified rate constant for reaction “oxi 4” in Figure 24 and constant U, V assumption.

Conclusions

Ignition delay time measurements and 3.39 and 10.6 μm diagnostics were performed during the oxidation and pyrolysis of decalin, respectively, over a wide range of temperatures, pressures and equivalence ratios. The measured ignition delay data are characterized by relatively low scatter and strong variation with pressures and equivalence ratios. For temperatures below 920 K, current ignition delay measurements provide clear evidence of pre-ignition heat release and NTC roll-off behavior. While comparisons of previous and current measurements yield the same pressure dependence but different equivalence ratio dependence, the chemical kinetic predictions of decalin/air ignition delay time are generally in fairly good agreement with current data. More accurate rate parameters of some key reactions in the decalin oxidation system, such as the attack of oxygen to decalin, are required to improve kinetic predictions.

The 10.6 μm diagnostic provides unique and critical target data, i.e., ethylene concentration time-histories, for improvement of the decalin pyrolysis system. Adjustment of the branching ratio of ODECAL to produce ethylene yields better agreement between experiment and modeling. The modified decalin pyrolysis sub-mechanism is also validated against the experimental 3.39 and 10.675 μm absorbance traces. Besides current preliminary modifications for both pyrolysis and oxidation kinetics of decalin, we believe that the adjustment of decalin reaction mechanism requires further

theoretical and experimental work.

Acknowledgement

This work was supported by the Air Force Office of Scientific Research through AFOSR Grant No. FA9550-08-1-0040, under the AFRL Integrated Product Team, with Dr. Julian Tishkoff as contract monitor and by the Army Research Office through ARO Grant No. W911NF-10-1-0125 with Dr. Ralph Anthenien as contract monitor.

References

1. T. Edwards, *Journal of Propulsion and Power* 19 (6) (2003) 1089-1107 10.2514/2.6946.
2. A. M. Knepp; G. Meloni; L. E. Jusinski; C. A. Taatjes; C. Cavallotti; S. J. Klippenstein, *Phys Chem Chem Phys* 9 (31) (2007) 4315-4331
3. M. E. Law; P. R. Westmoreland; T. A. Cool; J. Wang; N. Hansen; C. A. Taatjes; T. Kasper, *Proceedings of the Combustion Institute* 31 (2007) 565-573
4. E. J. Silke; W. J. Pitz; C. K. Westbrook; M. Ribaucour, *J Phys Chem A* 111 (19) (2007) 3761-3775
5. H. Z. R. Zhang; L. K. Huynh; N. Kungwan; Z. W. Yang; S. W. Zhang, *J Phys Chem A* 111 (19) (2007) 4102-4115
6. H. Huang, in: 2002; Vol. AIAA 2002-3871.
7. H. Lander; A. C. Nixon, *Journal of Aircraft* 8 (4) (1971) 200-207 10.2514/3.44255.
8. S. P. Zeppieri. *High Temperature Experimental and Computational Studies of the Pyrolysis and Oxidation of Endothermic Fuels*. Princeton University, Princeton, New Jersey, 1999.
9. A. Violi; S. Yan; E. G. Eddings; F. Sarofim; S. Granata; T. Faravelli; E. Ranzi, *Combust Sci Technol* 174 (11-2) (2002) 399-417 Doi 10.1080/00102200290021740.
10. W. J. Pitz; C. J. Mueller, *Prog Energ Combust* 37 (3) (2011) 330-350 <http://dx.doi.org/10.1016/j.pecs.2010.06.004>.
11. S. Granata; T. Faravelli; E. Ranzi, *Combust Flame* 132 (3) (2003) 533-544 [http://dx.doi.org/10.1016/S0010-2180\(02\)00465-0](http://dx.doi.org/10.1016/S0010-2180(02)00465-0).
12. K. Fieweger; R. Blumenthal; G. Adomeit, *Combust Flame* 109 (4) (1997) 599-619
13. S. M. Sarathy; C. K. Westbrook; M. Mehl; W. J. Pitz; C. Togbe; P. Dagaut; H. Wang; M. A. Oehlschlaeger; U. Niemann; K. Seshadri; P. S. Veloo; C. Ji; F. N. Egolfopoulos; T. Lu, *Combust Flame* 158 (12) (2011) 2338-2357
14. S. S. Vasu; D. E. Davidson; R. K. Hanson, *Combust Flame* 152 (1-2) (2008) 125-143
15. S. S. Vasu; D. F. Davidson; Z. Hong; V. Vasudevan; R. K. Hanson, *Proceedings of the Combustion Institute* 32 (2009) 173-180
16. H. W. Wang; M. A. Oehlschlaeger, *Fuel* 98 (2012) 249-258
17. C. K. Westbrook; W. J. Pitz; O. Herbinet; H. J. Curran; E. J. Silke, *Combust Flame* 156 (1) (2009) 181-199
18. P. Dagaut; A. Ristori; A. Frassoldati; T. Faravelli; G. Dayma; E. Ranzi, *Proceedings of the*

Combustion Institute 34 (2013) 289-296

19. P. Bredael; D. Rietvelde, *Fuel* 58 (3) (1979) 215-218
20. H. N. Woebecke; A. Korosi; P. S. Virk, *Abstr Pap Am Chem S* 175 (Mar) (1978) 27-27
21. M. Bajus; J. Baxa, *Collect Czech Chem C* 47 (7) (1982) 1838-1847
22. W. Hillebrand; W. Hodek; G. Kolling, *Fuel* 63 (6) (1984) 756-761
23. G. Zimmermann; F. D. Kopinke; R. Rehm, *J Anal Appl Pyrol* 7 (3) (1985) 195-205
24. F. Billaud; P. Chaverot; E. Freund, *J Anal Appl Pyrol* 11 (1987) 39-53
25. B. Ondruschka; G. Zimmermann; M. Remmler; M. Sedlackova; J. Pola, *J Anal Appl Pyrol* 18 (1) (1990) 19-32 Doi 10.1016/0165-2370(90)85002-5.
26. B. Ondruschka; G. Zimmermann; U. Ziegler, *J Anal Appl Pyrol* 18 (1) (1990) 33-39 Doi 10.1016/0165-2370(90)85003-6.
27. S. Zeppieri; K. Brezinsky; I. Glassman, in: *Eastern State Section of the Combustion Institute 1997 Technical Meeting*, 1997.
28. J. A. Yu; S. Eser, *Ind Eng Chem Res* 37 (12) (1998) 4601-4608
29. J. Stewart; K. Brezinsky; I. Glassman, *Combust Sci Technol* 136 (1-6) (1998) 373-390 Doi 10.1080/00102209808924178.
30. P. Zámotný; Z. Bělohav; L. Starkbaumová; J. Patera, *J Anal Appl Pyrol* 87 (2) (2010) 207-216 <http://dx.doi.org/10.1016/j.jaap.2009.12.006>.
31. A. C. Nixon; G. H. Ackerman; L. E. Faith; R. D. Hawthorn; H. T. Henderson; A. W. Ritchie; L. B. Ryland, in: *U.S. Air Force*: 1967.
32. M. A. Oehlschlaeger; H. P. S. Shen; A. Frassoldati; S. Pierucci; E. Ranzi, *Energ Fuel* 23 (2009) 1464-1472
33. J. S. Heyne; A. L. Boehman; S. Kirby, *Energ Fuel* 23 (2009) 5879-5885
34. A. Agosta. Development of a Chemical Surrogate for JP-8 Aviation Fuel Using a Pressurized Flow Reactor. Drexel University, 2002.
35. R. H. Natelson; M. S. Kurman; D. L. Miller; N. P. Cernansky, in: *46th AIAA Aerospace Sciences Meeting and Exhibit*, Reno, Nevada, 2008; Vol. AIAA 2008-970.
36. Y. Yang; A. L. Boehman, *Combust Flame* 157 (3) (2010) 495-505
37. K. Chae; A. Violi, *J Org Chem* 72 (9) (2007) 3179-3185 Doi 10.1021/Jo062324x.
38. E. L. Petersen; R. K. Hanson, *Shock Waves* 10 (6) (2001) 405-420
39. Z. K. Hong; K. Y. Lam; D. F. Davidson; R. K. Hanson, *Combust Flame* 158 (8) (2011) 1456-1468
40. A. E. Klingbeil; J. B. Jeffries; R. K. Hanson, *Meas Sci Technol* 17 (7) (2006) 1950-1957
41. M. E. MacDonald; D. F. Davidson; R. K. Hanson, *Journal of Propulsion and Power* 27 (5) (2011) 981-989
42. A. Cuoci; A. Frassoldati; T. Faravelli; E. Ranzi, in: *XXXIV Meeting of the Italian Section of the Combustion Institute*, A. D'anna; C. K. Westbrook, (Eds.) Rome, Italy, 2011; pp 1 - 6.
43. A. Frassoldati <ftp://project.chem.polimi.it/ftpChemEngLeonardo/Stanford/> (Feb. 2013),
44. Y. Zhu; D. F. Davidson; R. k. Hanson, *Combust Flame* accepted (2013)
45. R. K. Hanson; G. A. Pang; S. Chakraborty; W. Ren; S. Wang; D. F. Davidson, *Combust Flame* (2013) <http://dx.doi.org/10.1016/j.combustflame.2013.03.026>.
46. R. X. Fernandes; J. Zador; L. E. Jusinski; J. A. Miller; C. A. Taatjes, *Phys Chem Chem Phys* 11 (9)

(2009) 1320-1327

47. H. J. Curran; P. Gaffuri; W. J. Pitz; C. K. Westbrook, *Combust Flame* 114 (1-2) (1998) 149-177
48. H. K. Ciezki; G. Adomeit, *Combust Flame* 93 (4) (1993) 421-433
49. U. Pfahl; K. Fieweger; G. Adomeit, *Symposium (International) on Combustion* 26 (1) (1996) 781-789
[http://dx.doi.org/10.1016/S0082-0784\(96\)80287-6](http://dx.doi.org/10.1016/S0082-0784(96)80287-6).
50. X. Q. You; F. N. Egolfopoulos; H. Wang, *Proceedings of the Combustion Institute* 32 (2009) 403-410 DOI 10.1016/j.proci.2008.06.041.
51. M. E. MacDonald. *Decomposition Kinetics of the Rocket Propellant RP-1 and Its Chemical Kinetic Surrogates*. Stanford University, Stanford, CA 94305 U.S.A., 2012.
52. A. E. Klingbeil; J. B. Jeffries; R. K. Hanson, *J Quant Spectrosc Ra* 107 (3) (2007) 407-420
53. M. E. MacDonald; W. Ren; Y. Y. Zhu; D. F. Davidson; R. K. Hanson, *Fuel* 103 (2013) 1060-1068
54. W. G. Mallard; W. C. Gardiner, *J Quant Spectrosc Ra* 20 (2) (1978) 135-149
55. S. W. Sharpe; T. J. Johnson; R. L. Sams; P. M. Chu; G. C. Rhoderick; P. A. Johnson, *Appl Spectrosc* 58 (12) (2004) 1452-1461
56. C. K. Westbrook; W. J. Pitz; H. J. Curran; M. Mehl, in: *Chemical Engineering Greetings to Prof. Eliseo Ranzi on Occasion of His 65th Birthday, AIDIC (Italian Association of Chemical Engineering) with the cultural partnership of Reed Business Information*, M. Dente, (Ed.) 2008.
57. M. E. MacDonald; D. F. Davidson; R. K. Hanson; W. J. Pitz; M. Mehl; C. K. Westbrook, *Fuel* 103 (2013) 1051-1059
58. J. Zador; C. A. Taatjes; R. X. Fernandes, *Prog Energ Combust* 37 (4) (2011) 371-421
59. C. J. Mueller; W. J. Cannella; T. J. Bruno; B. Bunting; H. D. Dettman; J. A. Franz; M. L. Huber; M. Natarajan; W. J. Pitz; M. A. Ratcliff; K. Wright, *Energ Fuel* 26 (6) (2012) 3284-3303 Doi 10.1021/Ef300303e.



Methane and ethylene time-history measurements in *n*-butane and *n*-heptane pyrolysis behind reflected shock waves

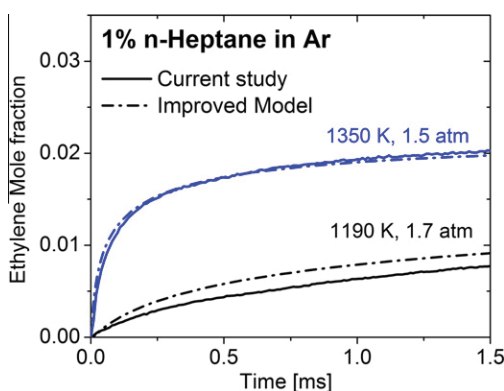
Sung Hyun Pyun, Wei Ren, David F. Davidson *, Ronald K. Hanson

Department of Mechanical Engineering, Stanford University, Stanford, CA 94305, USA

HIGHLIGHTS

- Shock tube/laser absorption study of *n*-butane and *n*-heptane pyrolysis.
- CH₄ and C₂H₄ time-histories acquired during high-temperature pyrolysis.
- Data provides basis for *n*-alkane mechanism revisions.

GRAPHICAL ABSTRACT



ARTICLE INFO

Article history:

Received 1 October 2012

Received in revised form 7 December 2012

Accepted 8 December 2012

Available online 25 December 2012

Keywords:

Shock tube
Laser absorption
Pyrolysis
n-Butane
n-Heptane

ABSTRACT

CH₄ and C₂H₄ concentration time-histories were measured behind reflected shock waves during the pyrolysis of two *n*-alkanes: *n*-butane and *n*-heptane. Experiments were conducted at temperatures of 1200–1600 K and at pressures near 1.5 atm, with fuel concentrations of 1% in Ar. A mid-IR scanned-wavelength laser absorption diagnostic with a difference frequency generation (DFG) laser near 3.43 μm was used to measure CH₄ concentration time-histories. C₂H₄ was measured using a fixed-wavelength absorption scheme at 10.532 μm with a CO₂ laser. The mechanism of Wang et al. with a constant volume gasdynamic model was used to calculate temperature and pressure profiles and the mole fraction time-histories of CH₄ and C₂H₄. The measured CH₄ and C₂H₄ time-histories in *n*-butane pyrolysis were compared to simulations based on the comprehensive *n*-alkane mechanism by Wang et al. and the detailed *n*-butane mechanism by Marinov et al. Based on these comparisons, the *n*-butane decomposition rates measured by Oehlschlaeger et al. were incorporated into the Wang et al. mechanism and two additional butane abstraction reaction rate constant adjustments were also made. The measured CH₄ and C₂H₄ time-histories during *n*-heptane pyrolysis were also compared to simulations based on the mechanisms by Wang et al. and Curran et al. The overall *n*-heptane decomposition rate measured by Davidson et al. was incorporated into the Wang et al. mechanism, and the two methyl abstraction reactions from *n*-heptane were adjusted, and the H-abstraction reaction rate from ethylene was updated. Using these modified mechanisms the agreement between simulation and experimental time-histories of CH₄ and C₂H₄ were both significantly improved for *n*-butane and *n*-heptane pyrolysis.

© 2012 Elsevier Ltd. All rights reserved.

* Corresponding author. Tel.: +1 650 725 2072.

E-mail address: dfd@stanford.edu (D.F. Davidson).

1. Introduction

Normal alkanes have been widely used as fuels and are major components of many commercial transportation fuels. In particular, over 90% of the normal alkanes in commercial gasoline fuels are represented by just the small normal alkanes with carbon numbers (C_N) of four to seven: *n*-butane (C_4), *n*-pentane (C_5), *n*-hexane (C_6) and *n*-heptane (C_7). *n*-Butane is also found as a component in LPG (liquefied petroleum gas) and gasoline. *n*-heptane is widely used as one component of a Primary Reference Fuel (PRF) for gasoline (the other component being iso-octane). It is also used as a diesel fuel surrogate to study diesel combustion chemistry because of the similarity of its cetane number to that of conventional diesel. The modeling of practical problems in diesel engines, such as auto-ignition can be simplified using *n*-heptane as the fuel surrogate [1].

Detailed *n*-butane and *n*-heptane oxidation mechanisms have been extensively developed by many groups [2–6]. The *n*-butane mechanism of Marinov et al. [5] was developed to model rich sooting *n*-butane flames and was validated for burner measurements of C_3H_4 , C_4H_2 , C_4H_4 , C_4H_6 , C_4H_8 , C_5H_6 , $C_6H_5CH_3$, and higher aromatics [1]. The detailed *n*-heptane mechanism of Curran et al. [6] was developed (and updated [7]) and validated by comparison with experiments in plug-flow and jet-stirred reactors, shock tubes and rapid compression machines over an initial pressure range from 3 to 50 atm, and temperatures from 650 to 1200 K. These experiments included measurements of CO, O_2 , CH_2O , CH_3 , CHO, C_2H_5CHO , C_7H_{14} , and $C_7H_{14}O$ [1]. The mechanism of Wang et al. [8], *JeffSurF* 2.0, is a detailed mechanism developed for the combustion of jet fuel surrogates. The model was validated against laminar flame speeds, ignition delay times, species profiles behind reflected shock waves, and jet-stirred and flow reactor data to describe the pyrolysis and oxidation kinetics of all *n*-alkanes up to *n*-dodecane and mono-alkylated cyclohexanes at high temperatures.

Recently, Oehlschlaeger et al. [9] measured the high temperature rate constants of the two *n*-butane decomposition reactions, (1) $n-C_4H_{10} \rightarrow n-C_3H_7 + CH_3$ and (2) $n-C_4H_{10} \rightarrow C_2H_5 + C_2H_5$, in a shock tube by monitoring CH_3 radicals in *n*-butane oxidation. The overall *n*-heptane decomposition rate combining three major decomposition pathways, (1) $n-C_7H_{16} \rightarrow p-C_4H_9 + n-C_3H_7$, (2) $n-C_7H_{16} \rightarrow C_5H_{11} + 1 + C_2H_5$ and (3) $n-C_7H_{16} \rightarrow C_6H_{13} + 1 + CH_3$, was measured by Davidson et al. [10] in a shock tube by monitoring CH_3 radicals in *n*-heptane oxidation. C_2H_4 time-histories were recently measured behind reflected shock waves in the pyrolysis of *n*-heptane by Pilla et al. [11]. However, the temperature and C_2H_4 absorption coefficient were assumed to be constant during pyrolysis in that study. An improved gasdynamic/kinetic model to account for changes in temperature due to the endothermic nature of the pyrolysis process has now been developed. A mid-IR scanned-wavelength laser absorption diagnostic for interference-free CH_4 detection was recently developed by Pyun et al. [12], however, information on CH_4 concentrations during *n*-alkane pyrolysis has not previously been available. In this study, to extend the kinetic database for *n*-butane and *n*-heptane, we measured CH_4 and C_2H_4 concentration time-histories behind reflected shock waves during the high-temperature pyrolysis of *n*-butane and *n*-heptane. The changes in temperature and pressure during fuel pyrolysis were calculated using a constant volume gasdynamic model and the recent chemical mechanism by Wang et al. [8]. The calculated pressure and temperature profile and the temperature-dependent absorption coefficients were used to infer CH_4 and C_2H_4 time-histories, allowing some refinements to the relevant detailed kinetic mechanisms.

2. Experimental setup

2.1. Shock tube facility

High temperatures were generated behind reflected shock waves in a 15.24 cm diameter shock tube. The reflected shock conditions were calculated based on incident shock speeds using a chemically frozen shock code (FROSH) and species thermodynamic data from Kee et al. [13]. Incident shock speeds were determined using shock arrival times measured using five piezo-electric pressure transducers (PZT), located over the last section of the driven section, and four interval counters (Fluke PM6666). Laser diagnostics and a Kistler piezo-electric pressure transducer (601B1) used to monitor pressure time-histories were located in the test section at 2 cm from the end wall. 1% fuel in argon mixtures was used for all experiments. Mixtures were prepared manometrically in a high-purity mixing assembly. Gas phase *n*-butane (99.9%) and the 99+% spectrophotometric grade *n*-heptane liquid were supplied by Sigma–Aldrich Co. (St. Louis, MO) and the research-grade Ar (99.999%) was supplied by Praxair Inc. (Danbury, CT).

2.2. Laser absorption measurements

2.2.1. DFG laser absorption of CH_4

A mid-IR scanned-wavelength laser absorption diagnostic for interference-free CH_4 detection reported by Pyun et al. [12] was used to measure CH_4 concentration time-histories. The scanned-wavelength diagnostic uses a difference frequency generation (DFG) laser and a differential absorption scheme that takes advantage of the spectral structure difference between CH_4 and other hydrocarbon products near 3.43 μm where the fundamental C–H stretching vibrational bands are located. This CH_4 diagnostic using a common mode rejection scheme offers 20 μs time resolution with a detection limit of ~ 200 ppm for a path length of 15.24 cm at 1500 K and 1.5 atm. Absolute calibration of this diagnostic using known concentrations of CH_4 in separate experiments enabled the determination of an overall concentration uncertainty; this was dominated by the influence of uncertainties in temperature described in the next section, and were typically less than $\pm 5\%$.

2.2.2. CO_2 laser absorption of C_2H_4

C_2H_4 was measured using a fixed-wavelength absorption scheme at 10.532 μm with a CO_2 laser. A single-wavelength scheme was feasible owing to the lack of interference absorption. The $P(14)$ line of the CO_2 laser at 10.532 μm line has been used previously to measure C_2H_4 concentrations [11,14] because it is coincident with the strong Q-branch of the ν_7 ethylene band. The C_2H_4 mole fraction in a given experiment is determined using Beer's law:

$$\frac{I}{I_0} = \exp \left(- \frac{P_{total} \chi_{C_2H_4} \sigma_{C_2H_4} L}{RT} \right)$$

where I/I_0 is the fractional transmission, L the path length, and $\sigma_{C_2H_4}$ is the C_2H_4 absorption cross-section at 10.532 μm . Since the values of $\sigma_{C_2H_4}$, L and total pressure, P_{tot} , were measured or known, the mole fraction of C_2H_4 could be inferred from the measurement of the fractional transmission, I/I_0 . The minimum detection limit for CO_2 laser diagnostics using a common mode rejection scheme is approximately 100 ppm C_2H_4 at 1500 K and 1.5 atm. Overall uncertainties in C_2H_4 concentrations were similar to, and controlled by the same physical processes as, CH_4 . Interference absorption at 10.532 μm was not significant because other species with absorption at this wavelength (e.g. propene, and butene) had substantially weaker absorption cross-sections and occurred as much lower concentrations.

3. Experimental results and discussion

3.1. Species concentration time-histories and gasdynamic models

As described in Section 2.2.2, species concentration time-histories were inferred from the raw absorbance signals using Beer's law, which describes the species concentration as a function of temperature, pressure and its absorption coefficient. The changes in temperature and pressure caused by chemical reactions associated with fuel pyrolysis slightly change the species absorption coefficients that are temperature dependent. To determine the appropriate temperature profile to use in the conversion of absorbance to mole fraction, two different gasdynamic models were used in the simulation: constant volume and constant pressure. The time-varying temperature, pressure and species absorption coefficient during fuel pyrolysis was discussed by Pyun et al. [12].

Figs. 1 and 2 show the calculated pressure and temperature changes during 1% *n*-butane pyrolysis using the two different chemical mechanisms by Wang et al. [8] and Marinov et al. [5] and both the constant volume and the constant pressure gasdynamic models. Fig. 1 also includes the measured pressure in the shock tube experiments. The Wang et al. [8] mechanism predicts 7.3% change between initial pressure and the pressure at 1 ms, and the Marinov et al. [5] mechanism predicts 7.5% pressure change, based on the constant volume gasdynamic model. Notably, the measured pressure trace falls more slowly than the models. The constant volume gasdynamic model with the mechanisms by Wang et al. [8] and Marinov et al. [5] predicts 9.2% and 9.3% temperature drop in 1 ms, respectively. Meanwhile, the constant pressure gasdynamic model with the mechanisms by Wang et al. [8] and Marinov et al. [5] predict temperature drops of 7.1% and 7.3%, respectively. As confirmed above, the calculated pressure and temperature profiles are more strongly dependent on the gasdynamic models than the chemical mechanisms for *n*-butane pyrolysis.

Figs. 3 and 4 show the calculated pressure and temperature changes during 1% *n*-heptane pyrolysis using the different chemical mechanisms by Wang et al. [8] and Curran et al. [7] with the constant volume and the constant pressure gasdynamic models. The Wang et al. [8] mechanism predicts 8.9% change between initial pressure and the pressure at 1 ms while the Curran et al. [7] mechanism predicts 9.8% pressure change based on the constant volume gasdynamic model. Note that the rapid fall in pressure suggested by the models is not captured by the measured pressure trace. The constant volume gasdynamic model with the mecha-

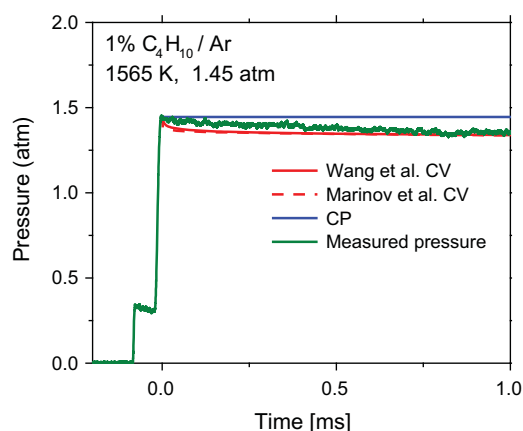


Fig. 1. Simulated pressure profiles with the mechanisms of Wang et al. [8] and Marinov et al. [5] with the constant volume and the constant pressure gasdynamic models. Initial conditions: 1% *n*-butane in argon, 1565 K, 1.45 atm.

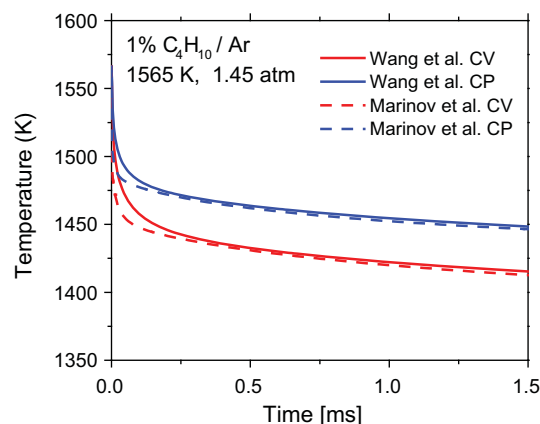


Fig. 2. Simulated temperature profiles with the mechanisms of Wang et al. [8] and Marinov et al. [5] with the constant volume and the constant pressure gasdynamic models. Initial conditions: 1% *n*-butane in argon, 1565 K, 1.45 atm.

nisms by Wang et al. [8] and Curran et al. [7] predicts 12.0% and 12.9% temperature drop at 1 ms, respectively. Similarly, the constant pressure gasdynamic model with the mechanisms by Wang et al. [8] and Curran et al. [7] predict temperature drops of 9.9% and 10.5%. The temperature and pressure drop of *n*-heptane pyrolysis is slightly higher than that of *n*-butane due to the higher energy absorbed during the endothermic decomposition reactions with the larger *n*-heptane molecule.

It is desirable to ensure that the species concentrations inferred from measured raw absorbance do not change significantly regardless of which chemical mechanisms and gasdynamic models are used to simulate temperature and pressure during *n*-butane and *n*-heptane pyrolysis. The highest temperature cases of *n*-butane (1565 K) and *n*-heptane (1597 K) pyrolysis experiments that show the largest difference between chemical mechanisms and gasdynamic models are analyzed in Tables 1 and 2.

For *n*-butane pyrolysis, Table 1 shows the measured mole fractions of CH₄ and C₂H₄ at 1 ms inferred using the T, P values from the mechanisms of Wang et al. [8] and Marinov et al. [5] with the constant volume and the constant pressure gasdynamic models. The differences between measured mole fractions derived using the mechanisms by Wang et al. [8] and Marinov et al. [5] with the identical gasdynamic model are negligible. However, the difference between measured mole fractions from the constant volume and constant pressure gasdynamic models is slightly lar-

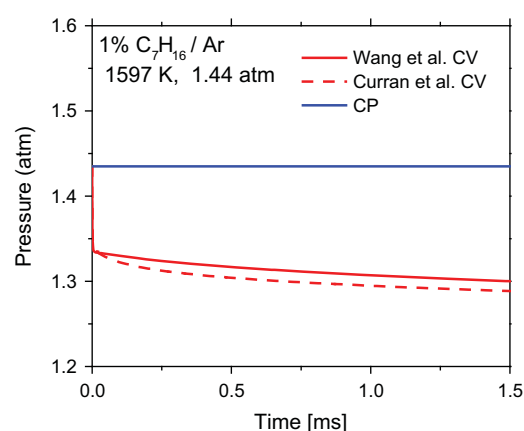


Fig. 3. Simulated pressure profiles with the mechanisms of Wang et al. [8] and Curran et al. [7] with the constant volume and the constant pressure gasdynamic models. Initial conditions: 1% *n*-heptane in argon, 1597 K, 1.44 atm.

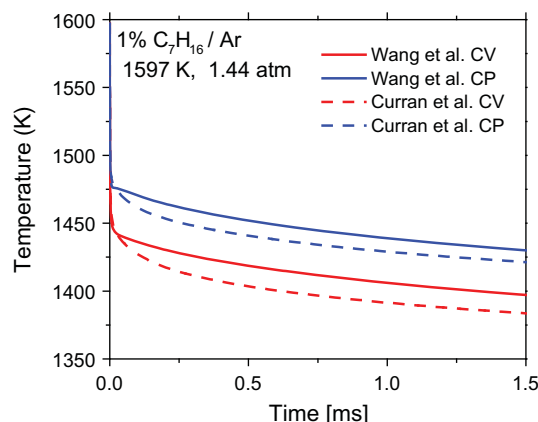


Fig. 4. Simulated temperature profiles with the mechanisms of Wang et al. [8] and Curran et al. [7] with the constant volume and the constant pressure gasdynamic models. Initial conditions: 1% *n*-heptane in argon, 1597 K, 1.44 atm.

ger, up to 2.7%, which is somewhat smaller than the detection limit of our laser diagnostics.

For *n*-heptane pyrolysis, Table 2 shows the measured mole fraction of CH₄ and C₂H₄ at 1 ms inferred using the *T*, *P* values from the mechanisms by Wang et al. [8] and Curran et al. [7] with the constant volume and the constant pressure gasdynamic models. The differences between measured mole fractions derived using the mechanisms by Wang et al. [8] and Curran et al. [7] are relatively higher, up to 5.4 % in the highest temperature case where the temperature and pressure change is maximized.

Even though the pressure and temperature changes during high concentration fuel pyrolysis are significant, up to 12% in the highest temperature cases, the convolution of these two effects (temperature and pressure change) and the temperature-dependent absorption coefficients made the inferred mole fractions almost indistinguishable for four different combinations of the chemical mechanisms and the gasdynamic models. A shock tube is neither a perfect constant volume nor a perfect constant pressure system, but it has been widely assumed to be a constant volume system, and our long-time pressure data seem to be closer to the constant volume prediction. The Wang et al. [8] mechanism and with the constant volume gasdynamic model was selected for use in calculating temperature and pressure profiles and to infer mole fractions of CH₄ and C₂H₄ during *n*-butane and *n*-heptane pyrolysis in this study. This choice is supported by the excellent agreement between the Wang et al. model and recent multi-species time-history measurements acquired by Davidson et al. [15] in the heptane oxidation system.

3.2. Sensitivity analysis and updated chemical mechanisms

3.2.1. *n*-butane pyrolysis

The CH₄ and C₂H₄ concentration time-histories were measured in mixtures of 1% *n*-butane in argon at temperatures from 1254 to 1565 K and pressures from 1.45 to 1.64 atm. Sensitivity analysis in

Figs. 5 and 6 show that CH₄ and C₂H₄ concentration are sensitive to many different reactions, labeled here: (1)–(7) (reactions (1)–(3) were not modified in the Wang et al. [8] mechanism, while the reactions (4)–(7) were updated or adjusted to fit measured CH₄ and C₂H₄ time-histories as will be described in this section). Rxn. (1) (CH₄ + H → CH₃ + H₂) was reviewed extensively over the temperature ranges from 350 K to 2500 K by Baulch et al. [16], combining 10 sets of measurements and five sets of reviews and evaluations. This evaluated rate *k*₁ by Baulch et al. [16] is within 7% error of the one used in the Wang et al. [8] mechanism between 1200 K and 1600 K. The C₂H₆ decomposition reaction (Rxn. (2): C₂H₆ → CH₃ + CH₃) is relatively well established by Oehlschlaeger et al. [17] and Kiefer et al. [18]. Both CH₄ and C₂H₄ concentration time-histories are sensitive to Reaction (3), the H-abstraction from *n*-butane (Rxn. (3): *n*C₄H₁₀ + H → *p*C₄H₉ + H₂). However, the adjustment of this rate *k*₃ was not necessary to fit measured CH₄ and C₂H₄ time-histories.

The major decomposition reactions, Rxns. (4) and (5), are important initiation steps in the *n*-butane chemical mechanisms. These two *n*-butane decomposition rates, *k*₄ (Rxn. (4): *n*C₄H₁₀ → *n*C₃H₇ + CH₃) and *k*₅ (Rxn. (5): *n*C₄H₁₀ → C₂H₅ + C₂H₅) were recently measured by Oehlschlaeger et al. [9]. RRKM model were fit from 1320 to 1600 K to describe the measured decomposition rates with the following parameters: *k*_{∞,4}(*T*) = 4.28 × 10¹⁴exp(−35180/*RT*) s^{−1}, *k*_{0,4}(*T*) = 5.34 × 10¹⁷exp(−21620/*RT*) cm³ mol^{−1} s^{−1} and *F*_{cent,4}(*T*) = 0.28 × exp(−*T*/1500 K) for Rxn. (4), *k*_{∞,5}(*T*) = 4.28 × 10¹⁴exp(−35180/*RT*) s^{−1}, *k*_{0,5}(*T*) = 5.34 × 10¹⁷exp(−21620/*RT*) cm³ mol^{−1} s^{−1} and *F*_{cent,5}(*T*) = 0.28 × exp(−*T*/1500 K) for Rxn. (5) [9].

In an effort to generate an improved reaction mechanism for *n*-butane pyrolysis, the *n*-butane decomposition rate values from Oehlschlaeger et al. [9] were used in the Wang et al. [8] mechanism. In addition to these measured *n*-butane decomposition rates, two other reactions with large sensitivities were adjusted to improve agreement between the simulations and the measured CH₄ and C₂H₄ time-histories. The two additional H-abstraction reactions (Rxns. (6) and (7): CH₃ + and H + *n*-butane) were modified. Improved fits to the measurements were achieved by: increasing *k*₆ (Rxn. (6): *n*C₄H₁₀ + CH₃ → *s*C₄H₉ + CH₄) by a factor of 2 and decreasing *k*₇ (Rxn. (7): *n*C₄H₁₀ + H → *s*C₄H₉ + H₂) by a factor of 2, within the estimated uncertainty of these reaction rate values. Increasing *k*₆ by a factor of 2 improved the predicted CH₄ plateau level by 6–25%, while decreasing *k*₇ by a factor of 2 improved the predicted C₂H₄ plateau level by 10–17%. The two *n*-butane decomposition rates measured by Oehlschlaeger et al. [9] and two adjusted rates (i.e., *k*₄, *k*₅, *k*₆ and *k*₇) were incorporated into the original Wang et al. [8] mechanism to form the modified Wang et al. [8] mechanism for *n*-butane. All reactions that were modified in the Wang et al. [8] mechanism are shown in Table 3.

3.2.2. *n*-Heptane pyrolysis

The CH₄ and C₂H₄ concentration time-histories were measured in mixtures of 1% *n*-heptane in argon at temperatures from 1190 to 1597 K and pressures from 1.44 to 1.69 atm. Sensitivity analysis in Figs. 7–9 show that CH₄ and C₂H₄ concentrations are sensitive to many different reactions including Rxns. (1) and (2) described in

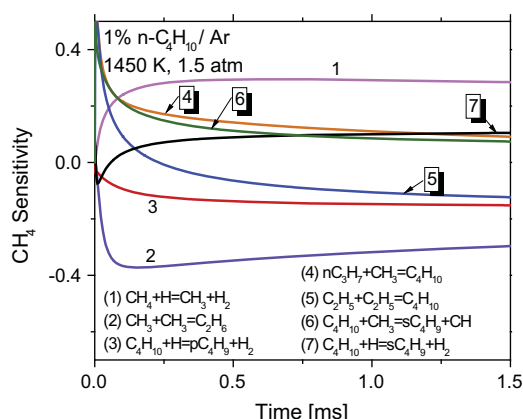
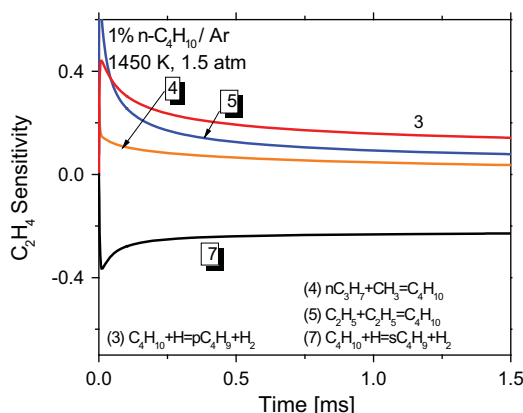
Table 1

Measured mole fraction of CH₄ and C₂H₄ in the pyrolysis of 1% *n*-butane in argon at 1 ms derived using different chemical mechanisms and gasdynamic models.

1% <i>n</i> -Butane in Ar, 1565 K, 1.44 atm	Wang et al.		Marinov et al.	
	CV model	CP model	CV model	CP model
Measured CH ₄ mole fraction at 1 ms	0.00298	0.00302	0.00297	0.00301
Relative difference to Wang et al. CV model		1.3%	−0.3%	1.0%
Measured C ₂ H ₄ mole fraction at 1 ms	0.0122	0.0120	0.0122	0.0119
Relative difference to Wang et al. CV model		−2.4%	−0.2%	−2.7%

Table 2Measured mole fraction of CH₄ and C₂H₄ in the pyrolysis of 1% *n*-heptane in argon at 1 ms derived using different chemical mechanisms and gasdynamic models.

1% <i>n</i> -Heptane in Ar, 1597 K, 1.44 atm	Wang et al.		Marinov et al.	
	CV model	CP model	CV model	CP model
Measured CH ₄ mole fraction at 1 ms	0.00299	0.00298	0.0029	0.0029
Relative difference to Wang et al. CV model		−0.3%	−3.0%	−3.0%
Measured C ₂ H ₄ mole fraction at 1 ms	0.0122	0.0120	0.0122	0.0119
Relative difference to Wang et al. CV model		−3.9%	−1.5%	−5.4%

**Fig. 5.** CH₄ sensitivity for *n*-butane pyrolysis using the Wang et al. [8] mechanism. Only the seven reactions with the largest sensitivities are shown; of these, only the four reactions in highlighted boxes, Rxn. (4–7), were varied in this study. Initial conditions: 1% *n*-butane in argon, 1450 K, 1.5 atm.**Fig. 6.** CH₄ sensitivity for *n*-butane pyrolysis using the Wang et al. [8] mechanism. Only the four reactions with the largest sensitivities are shown. Initial conditions: 1% *n*-butane in argon, 1450 K, 1.5 atm.

the previous section and six other reactions related to *n*-heptane decomposition (reactions (1), (2) were not modified in the Wang et al. [8] mechanism, while the rates for reactions (8)–(13) were updated or adjusted to fit measured CH₄ and C₂H₄ time-histories as will be described in this section).

The three major decomposition pathways of *n*-heptane pyrolysis reactions are (8), (9) and (10): Rxn (8): $n\text{C}_7\text{H}_{16} \rightarrow p\text{C}_4\text{H}_9 + n\text{C}_3\text{H}_7$, Rxn. (9): $n\text{C}_7\text{H}_{16} \rightarrow \text{C}_5\text{H}_{11} + \text{C}_2\text{H}_5$ and Rxn. (10): $n\text{C}_7\text{H}_{16} \rightarrow \text{C}_6\text{H}_{13} + \text{CH}_3$. The overall *n*-heptane decomposition rate constants ($k_{\text{tot}} = k_8 + k_9 + k_{10}$) were recently measured by Davidson et al. [10] near 1.8 atm. Their expression for the overall decomposition rate is $k_{\text{tot}} = 9.00 \times 10^{14} \exp(-67300/RT) \text{ s}^{-1}$ [10]. Each *n*-heptane decomposition reaction was then specified using the *n*-heptane branching ratio estimated by Babushok and Tsang [19] at

0.1 MPa. In addition to the measured *n*-heptane decomposition rates, two other reactions with large sensitivities were adjusted to improve the simulations to the measured CH₄ and C₂H₄ time-histories. As will be described below, improved fits to the measurements were achieved by decreasing k_{11} (Rxn. (11): $n\text{C}_7\text{H}_{16} + \text{CH}_3 \rightarrow \text{C}_7\text{H}_{15} + 3 + \text{CH}_4$) and k_{12} (Rxn. (12): $n\text{C}_7\text{H}_{16} + \text{CH}_3 \rightarrow \text{C}_7\text{H}_{15} + 2 + \text{CH}_4$), both by a factor of 2. These changes are within the expected uncertainties for these reaction rate constants. Increasing both of k_{11} and k_{12} by a factor of 2 resulted in the reduction of the predicted CH₄ plateau level by 14–43%. However, this modification did not make notable changes of the predicted C₂H₄ time-histories. Finally, the rate constant of Rxn. (13) ($\text{C}_2\text{H}_4 + \text{H} \rightarrow \text{C}_2\text{H}_3 + \text{H}_2$) was updated with the estimated value by Baulch et al. [16], combining seven sets of measurements and two sets of reviews and evaluations to fit especially the high-temperature C₂H₄ time-history at 1597 K. The C₂H₄ sensitivity analysis at this temperature is shown in Fig. 9. The review value of k_{13} proposed in Baulch et al. is approximately twice the value found in the Wang et al. Recent optimizations of the C₂ Foundation Fuels mechanism by the CEFR (Combustion Energy Frontier Research Center) support this higher value (H. Wang, private communication.)

The measured *n*-heptane decomposition rates, modeled *n*-heptane branching ratio and three adjusted rates (k_8 – k_{13}) were incorporated into the original Wang et al. [8] mechanism to form the modified mechanism of Wang et al. [8] for *n*-heptane. All reactions that were modified in the Wang et al. [8] mechanism are shown in Table 4.

3.3. Measured methane and ethylene time-histories

3.3.1. *n*-Butane pyrolysis

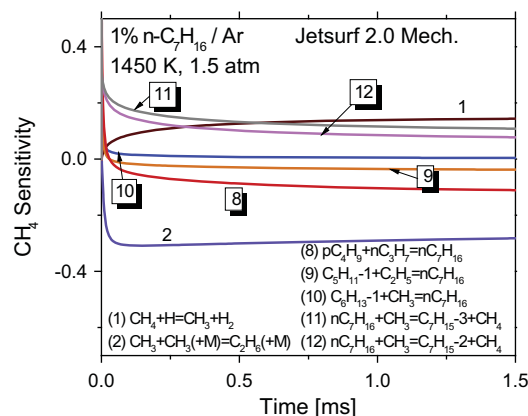
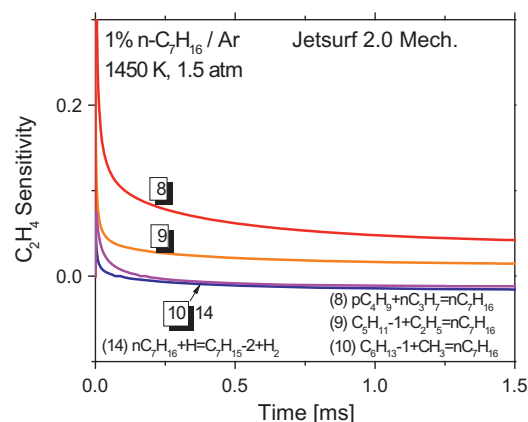
Fig. 10 shows the measured CH₄ time-histories during 1% *n*-butane pyrolysis at lower temperatures of 1254 and 1375 K and Supplementary Fig. S1 shows the CH₄ time-histories at higher temperatures of 1482 K and 1565 K. The mechanism of Wang et al. [8] performs significantly better than that of Marinov et al. [5] for predicting CH₄ time-histories in the two high-temperature cases. The modeled CH₄ concentration from the Wang et al. [8] mechanism is higher than the measured concentration by 5% and 7% at 1 ms for 1482 K and 1565 K, respectively, while the Marinov et al. [5] mechanism is higher by 24% and 28%.

At the lowest temperature, the simulated CH₄ time-histories from the mechanisms by Wang et al. [8] and Marinov et al. [5] are almost indistinguishable. The Marinov et al. [5] performs better than the Wang et al. [8] only at 1375 K. The modified mechanism of Wang et al. [8] for *n*-butane significantly improved the simulated CH₄ time-histories, fitting the data very well in all cases ranging from 1254 K to 1565 K. The modeled CH₄ concentrations from the modified Wang et al. [8] mechanism for *n*-butane are within 2%, 8%, 1% and 7% of the measured concentration at 1 ms, and within our detection uncertainties in each case from 1254 K to 1565 K.

The measured C₂H₄ time-histories during 1% *n*-butane pyrolysis at the same temperatures as CH₄ are shown in Fig. 11 and Supplementary Fig. S2. In all cases, the Marinov et al. [5] mechanism showed faster C₂H₄ production rate than the Wang et al. [8] mech-

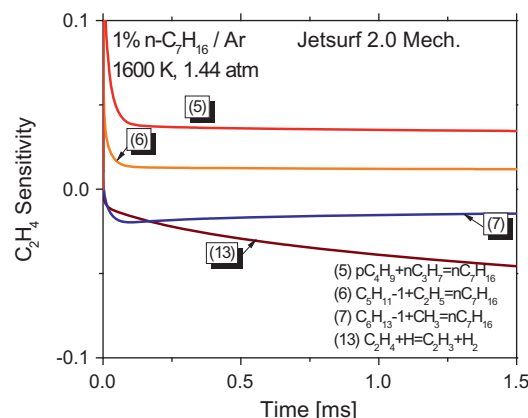
Table 3All reactions that were modified in the Wang et al. [9] mechanism to form the modified mechanism of Wang et al. [9] for *n*-butane.

No.	Reaction	Modifications to the modified Wang et al. mechanism for <i>n</i> -butane
4	$n\text{C}_4\text{H}_{10} \rightarrow n\text{C}_3\text{H}_7 + \text{CH}_3$	Modified with the measured rate by Oehlschlaeger et al. [9] Increased by a factor of 2 Decreased by a factor of 2
5	$n\text{C}_4\text{H}_{10} \rightarrow \text{C}_2\text{H}_5 + \text{C}_2\text{H}_5$	
6	$n\text{C}_4\text{H}_{10} + \text{CH}_3 \rightarrow \text{sC}_4\text{H}_9 + \text{CH}_4$	
7	$n\text{C}_4\text{H}_{10} + \text{H} \rightarrow \text{sC}_4\text{H}_9 + \text{H}_2$	

**Fig. 7.** CH₄ sensitivity for *n*-heptane pyrolysis using the Wang et al. [8] mechanism. Only the seven reactions with the largest sensitivities are shown; of these, only the five reactions in highlighted boxes, Rxn. (8)–(12), were varied in this study. Initial conditions: 1% *n*-heptane in argon, 1450 K, 1.5 atm.**Fig. 8.** C₂H₄ sensitivity for *n*-heptane pyrolysis using the Wang et al. [8] mechanism. Only the four reactions with the largest sensitivities are shown. Initial conditions: 1% *n*-heptane in argon, 1450 K, 1.5 atm.

anism. The mechanism of Marinov et al. [5] performs better than Wang et al. [8] for simulating C₂H₄ time-histories in the two low temperature cases. The modeled C₂H₄ concentration from the Marinov et al. [5] mechanism is lower than the measured concentration at 1 ms by 24% and 12% for 1254 K and 1375 K, respectively, while the Wang et al. [8] mechanism is lower by 45% and 30%. At higher temperatures, the modeled C₂H₄ plateau-levels from both mechanisms are not much different from each other. The modeled C₂H₄ concentrations using the Marinov et al. [5] mechanism are lower than the measured concentration by 12% at 1 ms for both 1482 K and 1565 K, and the Wang et al. [8] simulation is lower by 16% and 17%.

Finally, the modified mechanism of Wang et al. [8] for *n*-butane significantly improved the simulated C₂H₄ time-histories, fitting the data very well in all cases ranging from 1254 K to 1565 K.

**Fig. 9.** C₂H₄ sensitivity for *n*-heptane pyrolysis using the Wang et al. [8] mechanism. Only the four reactions with the largest sensitivities are shown. Initial conditions: 1% *n*-heptane in argon, 1600 K, 1.44 atm.

The modeled C₂H₄ concentrations from the modified mechanism for *n*-butane at 1 ms are different from the measured data by only 1%, 7%, 1% and 1.5%.

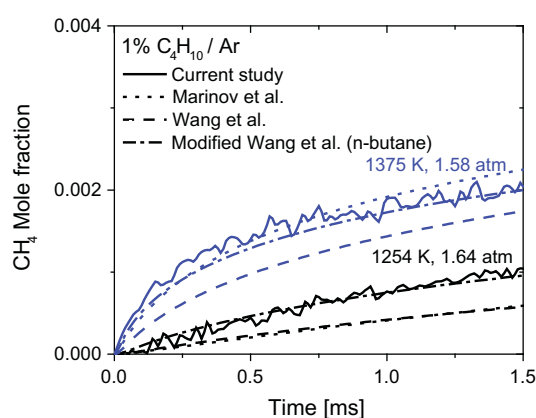
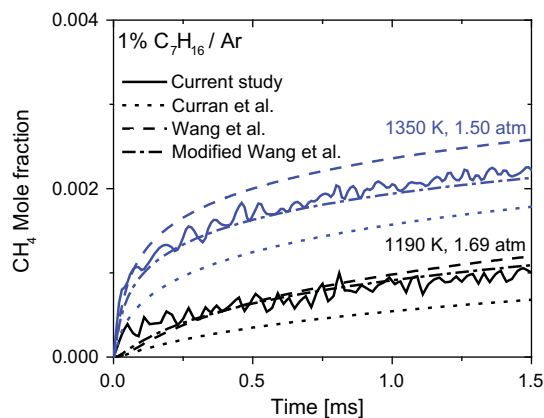
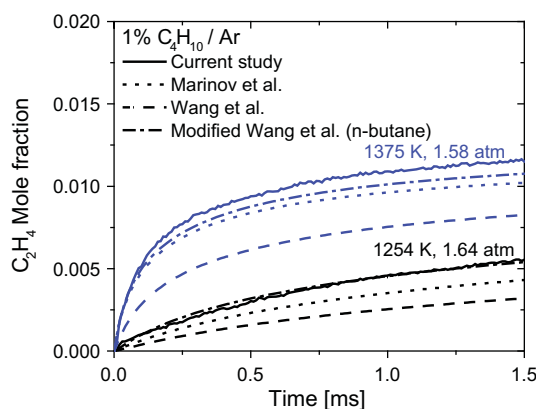
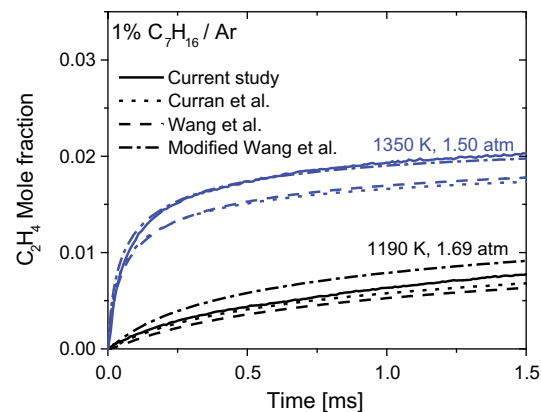
Several uncertainties contribute to the uncertainty in the determination of CH₄ and C₂H₄ time histories. The uncertainties in scanned laser intensity noise and absorption coefficients were found to be the major sources of uncertainty for CH₄ time-histories, and the uncertainties in absorption coefficients have the largest effect for C₂H₄ time-histories. Other contributions to uncertainties in the CH₄ and C₂H₄ time histories are temperature ($\pm 1\%$) and pressure ($\pm 0.5\%$). Error analyses yielded uncertainty estimates of 8.5% for CH₄ and 5% for C₂H₄ time histories at 1.5 ms for 1565 K.

3.3.2. *n*-Heptane pyrolysis

Fig. 12 shows the measured CH₄ time-histories during 1% *n*-heptane pyrolysis at lower temperatures of 1190 and 1350 K and Supplementary Fig. S3 shows the CH₄ time-histories at higher temperatures of 1450 K and 1597 K. The mechanism of Wang et al. [8] performs better than that of Curran et al. [7] for predicting CH₄ time-histories in all cases except for the 1450 K case. The modeled CH₄ concentration from the Wang et al. [8] mechanism is higher than the measured concentration by 8%, 16%, 19% and 27% at 1 ms for four different temperatures, in the order of the lowest to the highest, while the Curran et al. [7] mechanism is lower by 40% and 23% and higher by 2% and 55%. The modified mechanism of Wang et al. [8] for *n*-heptane significantly improved the predicted CH₄ time-histories at all temperatures, fitting the measured ones very well in three cases ranging from 1190 K to 1450 K. The modeled CH₄ concentrations from the modified mechanism by Wang et al. [8] for *n*-heptane at 1 ms are within 5%, 0% and 1% of the measured concentrations, comparable with our detection uncertainty in each case from 1190 K to 1450 K. As described for *n*-butane pyrolysis experiments, similar error analyses yielded uncertainty estimates of 8.5% for CH₄ and 5% for C₂H₄ time histories at 1.5 ms for 1597 K.

Table 4All reactions that were modified in the Wang et al. [8] mechanism to form the modified mechanism of Wang et al. [8] for *n*-heptane.

No.	Reaction	Modifications to the modified Wang et al. mechanism for <i>n</i> -heptane
8	$n\text{C}_7\text{H}_{16} \rightarrow \text{pC}_4\text{H}_9 + \text{nC}_3\text{H}_7$	Modified with the measured rate by Davidson et al. [10] and the modeled branching ratio by Babushok et al. [19]
9	$n\text{C}_7\text{H}_{16} \rightarrow \text{C}_5\text{H}_{11} + \text{C}_2\text{H}_5$	
10	$n\text{C}_7\text{H}_{16} \rightarrow \text{C}_6\text{H}_{13} + \text{CH}_3$	Decreased by factor of 2
11	$n\text{C}_7\text{H}_{16} + \text{CH}_3 \rightarrow \text{C}_7\text{H}_{15} + \text{CH}_4$	
12	$n\text{C}_7\text{H}_{16} + \text{CH}_3 \rightarrow \text{C}_7\text{H}_{15} + \text{CH}_4$	
13	$\text{C}_2\text{H}_4 + \text{H} \rightarrow \text{C}_2\text{H}_3 + \text{H}_2$	Modified with the estimated rate by Baulch et al. [16]

**Fig. 10.** Comparison of measured CH_4 time-histories at two low temperatures with the mechanisms by Wang et al. [8], Marinov et al. [5] and the modified Wang et al. [8] for *n*-butane. Initial conditions: 1% *n*-butane in argon, 1254 K, 1.64 atm and 1375 K, 1.58 atm.**Fig. 12.** Comparison of measured CH_4 time-histories at two low temperatures with the mechanisms by Wang et al. [8], Curran et al. [7] and the modified Wang et al. [8] for *n*-heptane. Initial conditions: 1% *n*-heptane in argon, 1190 K, 1.69 atm and 1350 K, 1.50 atm.**Fig. 11.** Comparison of measured C_2H_4 time-histories at two low temperatures with the mechanisms by Wang et al. [8], Marinov et al. [5] and the modified Wang et al. [8] for *n*-butane. Initial conditions: 1% *n*-butane in argon, 1254 K, 1.64 atm and 1375 K, 1.58 atm.**Fig. 13.** Comparison of measured C_2H_4 time-histories at two low temperatures with the mechanisms by Wang et al. [8], Curran et al. [7] and the modified Wang et al. [8] for *n*-heptane. Initial conditions: 1% *n*-heptane in argon, 1190 K, 1.69 atm and 1350 K, 1.50 atm.

The measured C_2H_4 time-histories during 1% *n*-heptane pyrolysis at the same temperatures as CH_4 are shown in Fig. 13 and Supplementary Fig. S4. The mechanism of Wang et al. [8] performs better than that of Curran et al. [7] for predicting C_2H_4 time-histories in the two high-temperature cases. The modeled C_2H_4 concentrations by the Wang et al. [8] mechanism at 1 ms are within 3% of the measured concentrations for 1450 K and 1597 K, while the Curran et al. [7] mechanism is lower by 10% and 9%. However, the mechanisms of Wang et al. [8] and Curran et al. [7] perform similarly for C_2H_4 concentration in the two low temperature cases of 1190 K and 1350 K. The modified Wang et al. mechanism for *n*-heptane significantly improved the fit of the predicted C_2H_4

time-histories in all cases except for the lowest temperature of 1190 K. The modeled C_2H_4 concentrations from the modified Wang et al. mechanism for *n*-heptane at 1 ms are different from the measured ones by 25%, 2%, 0% and 0%, in each case from 1190 K to 1597 K.

4. Conclusions

The high-temperature pyrolysis of *n*-butane and *n*-heptane was studied behind reflected shock waves by measuring time-histories of CH_4 and C_2H_4 in mixtures of 1% fuel in argon at temperature of 1200–1600 K and a pressure near 1.5 atm. It was shown that the

species mole fractions inferred from measured raw absorbance data were not a strong function of the chemical mechanisms and gasdynamic models used to simulate temperature and pressure during *n*-butane and *n*-heptane pyrolysis. The Wang et al. [8] mechanism with a constant volume gasdynamic model was used to calculate temperature and pressure profiles and to infer mole fractions of CH₄ and C₂H₄. The measured species time-histories were compared with the several decomposition mechanisms for both *n*-butane and *n*-heptane: Marinov et al. [5] for *n*-butane, Curran et al. [7] for *n*-heptane, and Wang et al. [8] commonly for *n*-butane and *n*-heptane.

For *n*-butane, the two measured *n*-butane decomposition rates by Oehlschlaeger et al. [9] were incorporated into the mechanism of Wang et al. [8]. Two additional rates were also adjusted for CH₃-abstraction and H-abstraction from *n*-butane to form a modified Wang et al. mechanism for *n*-butane. For *n*-heptane, the overall *n*-heptane decomposition rate measured by Davidson et al. [10] was incorporated into the Wang et al. mechanism and the two CH₃-abstraction reactions from *n*-heptanes were also adjusted and the H-abstraction reaction from ethylene was finally updated to form the modified mechanism of Wang et al. for *n*-heptane. Those mechanistic changes are listed in the Tables 3 and 4. The modified mechanisms of Wang et al. for *n*-butane and *n*-heptane agree with the measured time-histories of CH₄ and C₂H₄ reasonably well for both *n*-butane and *n*-heptane pyrolysis.

Acknowledgements

The diagnostic development aspects of this work were supported by the Air Force of Scientific Research (AFOSR) with Dr. Julian M. Tishkoff as contract monitor. The chemical kinetics and

gasdynamic modeling work was supported by the Army Research Office (ARO) with Dr. Ralph Anthenien Jr. as technical monitor.

Appendix A. Supplementary material

Supplementary data associated with this article can be found, in the online version, at <http://dx.doi.org/10.1016/j.fuel.2012.12.034>.

References

- [1] Davidson DF, Herbon JT, Horning DC, Hanson RK. Int J Chem Kinet 2001;33:775.
- [2] Warth V, Stef N, Glaude PA, Battin-Leclerc F, Scacchi G, Come GM. Combust Flame 1998;114:81.
- [3] Held TJ, Marchese AJ, Dryer FL. Combust Sci Technol 1997;123:107.
- [4] Lindstedt RP, Maurice LQ. Combust Sci Technol 1995;107:317.
- [5] Marinov NM, Pitz WJ, Westbrook CK, Vincitore AM, Castaldi MJ, Senkan SM. Combust Flame 1998;114:192.
- [6] Curran HJ, Gaffuri P, Pitz WJ, Westbrook CK. Combust Flame 1998;114:149.
- [7] Mehl M, Pitz WJ, Westbrook CK, Curran HJ. Proc Combust Inst 2011;33:193.
- [8] Wang H, Dames E, Sirjean B, Sheen DA, Tangko R, Violi A. JetSurF version 2.0 September 19, 2010. <<http://melchior.usc.edu/JetSurF/JetSurF2.0>>
- [9] Oehlschlaeger MA, Davidson DF, Hanson RK. Phys Chem A 2004;108:4247.
- [10] Davidson DF, Oehlschlaeger MA, Hanson RK. Proc Combust Inst 2007;31:321.
- [11] Pilla GL, Davidson DF, Hanson RK. Proc Combust Inst 2011;33:333.
- [12] Pyun SH, Cho J, Davidson DF, Hanson RK. Meas Sci Technol 2011;22:025303.
- [13] Kee RJ, Rupley FM, Miller JA. Report No. SAND-87-8215B. CA (USA): Sandia National Lab, Livermore.
- [14] Ren W, Davidson DF, Hanson RK. Int J Chem Kinet 2011. <http://dx.doi.org/10.1002/kin.20599>.
- [15] Davidson DF, Hong Z, Pilla GL, Farooq A, Cook RD, Hanson RK. Combust Flame 2010;157:1899–905.
- [16] Baulch DL, Bowman CT, Cobos CJ, Cox RA, Just Th, Kerr JA, et al. J Phys Chem Ref Data 2005;34:757.
- [17] Oehlschlaeger MA, Davidson DF, Hanson RK. Proc Combust Inst 2005;30:1119.
- [18] Kiefer JH, Santhanam S, Srinivasan NK, Tranter RS, Klippenstein SJ, Oehlschlaeger MA. Proc Combust 2005;30:1129.
- [19] Babushok VI, Tsang W. J Prop Power 2004;20:403.

IR Laser Absorption Diagnostic for C₂H₄ in Shock Tube Kinetics Studies

WEI REN, DAVID F. DAVIDSON, RONALD K. HANSON

High Temperature Gasdynamics Laboratory, Department of Mechanical Engineering, Stanford University, Stanford, CA 94305

Received 13 April 2011; revised 11 July 2011; accepted 17 July 2011

DOI 10.1002/kin.20599

Published online 10 January 2012 in Wiley Online Library (wileyonlinelibrary.com).

ABSTRACT: An IR laser absorption diagnostic has been further developed for accurate and sensitive time-resolved measurements of ethylene in shock tube kinetic experiments. The diagnostic utilizes the P14 line of a tunable CO₂ gas laser at 10.532 μm (the (0 0 1) \rightarrow (1 0 0) vibrational band) and achieves improved signal-to-noise ratio by using IR photovoltaic detectors and accurate identification of the P14 line via an MIR wavemeter. Ethylene absorption cross sections were measured over 643–1959 K and 0.3–18.6 atm behind both incident and reflected shock waves, showing evident exponential decay with temperature. Very weak pressure dependence was observed over the pressure range of 1.2–18.6 atm. By measuring ethylene decomposition time histories at high-temperature conditions (1519–1895 K, 2.0–2.8 atm) behind reflected shocks, the rate coefficient of the dominant elementary reaction $\text{C}_2\text{H}_4 + \text{M} \rightarrow \text{C}_2\text{H}_2 + \text{H}_2 + \text{M}$ was determined to be $k_1 = (2.6 \pm 0.5) \times 10^{16} \exp(-34,130/T, \text{K}) \text{ cm}^3 \text{ mol}^{-1} \text{ s}^{-1}$ with low data scatter. Ethylene concentration time histories were also measured during the oxidation of 0.5% C₂H₄/O₂/Ar mixtures varying in equivalence ratio from 0.25 to 2. Initial reflected shock conditions ranged from 1267 to 1440 K and 2.95 to 3.45 atm. The measured time histories were compared to the modeled predictions of four ethylene oxidation mechanisms, showing excellent agreement with the Ranzi et al. mechanism (updated in 2011). This diagnostic scheme provides a promising tool for the study and validation of detailed hydrocarbon pyrolysis and oxidation mechanisms of fuel surrogates and realistic fuels. © 2012 Wiley Periodicals, Inc. *Int J Chem Kinet* 44: 423–432, 2012

INTRODUCTION

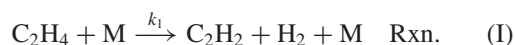
Ethylene is a stable intermediate species and dominant alkene formed by fuel fragmentation processes dur-

ing the oxidation and pyrolysis of large alkanes [1–3]. Formation of ethylene and its subsequent reactions to acetylenic derivatives are also involved in the formation and growth of polycyclic aromatic hydrocarbons, the most likely precursors to soot [4]. Finally, a better understanding of ethylene reactions may play an important role in developing and validating comprehensive mechanisms for the pyrolysis and oxidation of *n*-alkane fuel surrogates. It follows that analysis

Correspondence to: Wei Ren; e-mail: renwei@stanford.edu.
Supporting Information is available in the online issue at wileyonlinelibrary.com.
© 2012 Wiley Periodicals, Inc.

of a wide variety of hydrocarbon kinetic mechanisms would benefit from a sensitive and quantitative diagnostic for ethylene concentration time histories in shock tube experiments.

Very few reports about the direct measurement of ethylene in shock tube studies can be found in the literature. Roth and Just first employed an IR emission technique to directly monitor ethylene and acetylene and measured an overall rate of ethylene decomposition [5]. Zelson et al. developed a diagnostic scheme for ethylene by implementing a microwave discharge lamp near 174.4 nm [6]. Using this diagnostic, Zelson et al. measured the C₂H₄ decomposition rate in a shock tube. However, emission from the discharge lamp exhibited low-frequency fluctuations. Their data were also prone to uncertainties due to the wide monochromator slits employed, resulting in nonnegligible spectral width compared to the ethylene absorption profile. In addition, interference absorption by C₂H₂ needed to be calibrated in the UV region and subtracted from the absorption data. Very recently, Pilla et al. of our laboratory developed a sensitive ethylene detection scheme for shock tube experiments by using a cw CO₂ gas laser at 10.532 μ m [7]. In this wavelength region, ethylene is the main absorber for hydrocarbon intermediates formed during alkane pyrolysis, effectively diminishing the interference problems occurring with mid-IR laser diagnostics near 3.4 μ m [8]. Using the 10.5- μ m ethylene diagnostic, the ethylene cross sections at room temperature and elevated temperatures (600–1900 K) were measured, as was the rate constant k_1 of the dominant ethylene decomposition reaction at high temperatures:



However, large experimental scatter was found in the ethylene cross-section data and the rate coefficient determination, due particularly to the $1/f$ noise and low dynamic range of the dc-coupled photoconductive detectors used (see the Experimental section for further discussion). In addition, oscillations in the concentration time histories (low signal-to-noise ratio [SNR]) measured during the *n*-heptane pyrolysis caused difficulties in making comparisons with the modeled predictions.

The main goal of the present work was to further develop this ethylene diagnostic and to obtain accurate measurements of ethylene time histories at high temperatures for improved determination of the elementary reaction rate k_1 and the examination of several ethylene oxidation mechanisms. We will first describe the improvements to the IR ethylene laser-absorption

diagnostic. The light source we used was the same CO₂ laser as that in [7]. However, the new diagnostic system achieved improved SNR by applying IR photovoltaic detectors and better identification of the target CO₂ line via a mid-IR wavemeter. These improvements enable substantially reduced data scatter in the determinations of the ethylene absorption cross section and subsequently the decomposition rate. Ethylene cross sections were measured at temperatures between 643 and 1959 K behind both incident and reflected shock waves over a large pressure range from 0.3 to 18.6 atm (1 atm = 0.101 MPa) in two different shock tubes. In addition, the rate constant k_1 was determined over 1519–1895 K and 2.0–2.8 atm, showing good agreement with previous research. The ethylene diagnostic was then applied in shock tube studies of ethylene oxidation from 1221 to 1440 K and 2.95 to 3.45 atm with 0.5% C₂H₄/O₂/Ar mixtures varying in equivalence ratio from 0.25 to 2. We also provided comparisons of our measurements with the predictions of four currently available detailed kinetic mechanisms: Marinov et al. [9], Healy et al. [10], Wang et al. [11], and Ranzi et al. [12].

EXPERIMENTAL

Shock Tube Facilities

The high-temperature (>1000 K), low-pressure (1.3–3.6 atm) ethylene cross section and concentration time-history measurements were performed behind reflected shock waves in a 15.24-cm-diameter stainless-steel high-purity shock tube. The driven section has a length/diameter (L/D) ratio of 70 and is separated from the helium-filled driver section (with an L/D of 30) by a polycarbonate diaphragm. Incident shock speeds were extrapolated to the end wall by measuring the incident shock arrival times using five piezoelectric pressure transducers (PCB 134) spread over the last meter of the driven section. Temperatures and pressures behind the reflected shock waves were calculated using standard normal-shock relations and the measured incident shock speed, with an uncertainty of $\sim 1\%$ over the high-quality test time of 2 ms [13]. The laser diagnostic, along with a Kistler piezoelectric pressure transducer (601B1) for pressure measurements, was located in the test section at 2 cm from the end wall. Research grade high-purity gases (argon, oxygen, and helium; >99.999%) were supplied by Praxair, Inc. (San Ramon, CA), and used without further purification. The gas mixture of 1% C₂H₄/Ar was also from Praxair with uncertainty <1%. All the other test mixtures were manometrically prepared in a

turbo-pumped stainless-steel mixing tank (14 L) with a magnetically driven stirrer. Between experiments, the shock-tube-driven section and mixing manifold were turbopumped for half an hour down to $\sim 6 \times 10^{-6}$ Torr (760 Torr = 101,325 Pa) to remove residual impurities.

In contrast, all experiments at pressures higher than 15 atm were conducted in the Stanford stainless-steel, high-purity, high-pressure shock tube (HPST); see [14] for a complete description of this facility. The shock tube driver section is 3 m long with a 7.5-cm inner diameter, and the driven section is 5 m long with a 5-cm inner diameter; these sections were separated by a 1.25-mm-thick, cross-scribed aluminum diaphragm. Helium was used for the driver gas, providing approximately 2–3 ms of high-quality test time. All measurements were made at a test location 1 cm from the driven section end wall. Pressure time histories in the test section were monitored by a Kistler pressure transducer (603B1). The incident shock speeds were measured using six piezoelectric pressure transducers (PCB 113A), spaced over the last 2 m of the shock tube and extrapolated to the end wall. Incident and reflected shock conditions were determined using the same method as described above.

Ethylene Diagnostic

Ethylene was monitored in shock tube measurements using CO₂ laser absorption at 10.532 μm . Absorption is due to the strong Q-branch of the ν_7 ethylene band, which has a strong overlap with the P14 line of the CO₂ laser transitions associated with the (0 0 1) to (1 0 0) vibrational levels. We utilized a grating-tuned CO₂ gas laser (model Lasy-4G; Access Laser Co., Everett, WA) with 230 mW output. The CO₂ transition is primarily Doppler broadened with a full width at half maximum of less than 100 kHz (i.e., 3×10^{-6} cm⁻¹); the drift for this laser line is about 1–2 MHz. To obtain accurate cross-section measurements, the laser source needs to have a stable center wavelength and its spectral width should be much smaller than the width of the ethylene absorption feature. The CO₂ emission line was well identified by passing a portion of the laser output (through a beam splitter) into a mid-IR wavemeter (Bristol 721) and observed to be stable over hours. The HITRAN database indicates that the absorption features of ethylene near 10.5 μm have broadening coefficients on the order of ~ 0.1 cm⁻¹ atm⁻¹ [15]. Thus, the CO₂ laser emission at the P14 line can be considered monochromatic at the pressures in the present study.

Liquid-nitrogen-cooled photoconductive HgCdTe detectors (IR Associates MCT-12.5) with dc-coupled

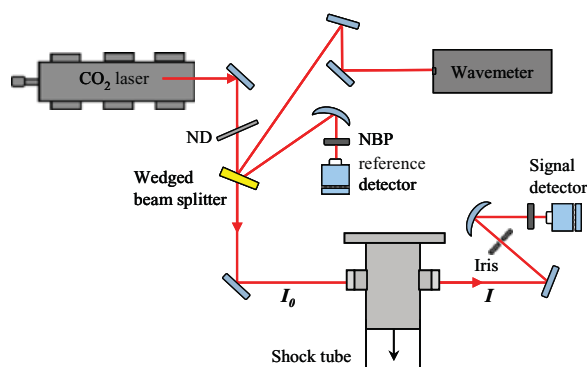


Figure 1 Schematic of ethylene detection using cw CO₂ laser near 10.5 μm in shock tube measurements; ND: neutral density filter; NBP: narrow bandpass filter.

preamplifiers were previously used for the laser-light detection at this wavelength [7]. However, excess noise (1/f noise) was observed in the detection, showing non-negligible drift with time in the detector background signal. This detector type also suffered from the problem of small linear dynamic range, leading to a constraint to maintain the detected signal intensity below 0.1 mW to prevent nonlinear response. These problems resulted in low SNR and large uncertainties in the absorption data. In the present work, new thermoelectric-cooled IR photovoltaic detectors (PVM-2TE-10.6; Vigo Systems) with large linear dynamic range were implemented. A detection noise of $\sim 1\%$ was reported in [7] by using common mode rejection (CMR). With this new detection system, however, we have found that the detection noise can be reduced to $< 0.3\%$ (typically over 2 ms, shock tube test time), even without CMR.

A schematic of the experimental setup is illustrated in Fig. 1. The light from the CO₂ laser is directed through a ZnSe wedge and is split into three beams: one transmitted beam for the absorption measurement and two reflected beams (from the two wedge surfaces with different wedged angles) into a reference detector and a mid-IR wavemeter, respectively. The reference detector was used to monitor the laser intensity variation. The transmitted beam was pitched through two opposing barium fluoride (BaF₂) windows mounted on the shock tube sidewall. Finally, a narrow band-pass 10.6 μm IR filter (half power bandwidth 100 nm) was used to filter out emission and unwanted light from the ambient before the laser beam was collected by the detector. The fractional transmission through the test gas in the shock tube is determined by Beer's law:

$$I/I_0 = \exp(-k_{\text{C}_2\text{H}_4}L) = \exp(-\alpha) \quad (1)$$

where I is the transmitted intensity, I_0 is the initial intensity, $k_{\text{C}_2\text{H}_4}$ is the spectral absorption coefficient of the absorbing medium (here ethylene), $L(\text{cm})$ is the path length of the sample, and α is known as the absorbance. It is convenient to rewrite this relation in terms of species absorption cross section, $\sigma(\text{m}^2/\text{mol})$:

$$I/I_0 = \exp(-\sigma n_{\text{C}_2\text{H}_4} L) \quad (2)$$

where $n_{\text{C}_2\text{H}_4}$ (mol/cm^3) is the ethylene number density.

Figure 2 depicts a representative nonreactive example of the pressure and the laser absorbance time histories measured in the 15.24-cm-diameter shock tube. The gas mixture was 1% ethylene in argon, and the ethylene was unreactive at the three temperatures (1170, 1210, and 1340 K) behind the reflected shock waves. The arrival of the reflected shock at the side-wall location (and therefore time zero) was determined from the step rise in pressure signals shown in the bottom graph of Fig. 2. Behind the reflected shock waves, highly uniform pressure profiles with a test time of 1 ms were observed, implying constant temperature profiles by assuming isentropic behavior of the gas at the test section. This has been confirmed previously using two distributed feedback diode lasers near $2.7 \mu\text{m}$ [16,17] for sensitive temperature measurement. According to the laser absorption signals illustrated in the top graph, strong absorbance was achieved at these high temperatures ($>1000 \text{ K}$) and the noise in the absorbance signal is mainly from the digital noise of the data acquisition system. Considering the minimum detectivity of ap-

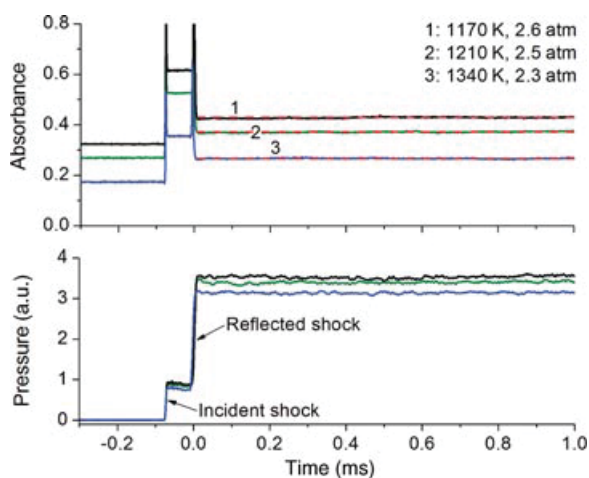


Figure 2 Pressure and laser absorbance time histories for a nonreactive test gas of 1% $\text{C}_2\text{H}_4/\text{Ar}$ in the Stanford 15.24-cm-diameter shock tube. Schlieren spikes caused by the density gradient across the shock waves. [Color figure can be viewed in the online issue, which is available at wileyonlinelibrary.com.]

proximately 0.1% absorbance using direct absorption spectroscopy in our shock tube experiments, this diagnostic tool is capable of detecting 100 ppm levels of ethylene for a path length of 15 cm at 1200 K, 3 atm.

ETHYLENE ABSORPTION CROSS SECTION

The ethylene absorption coefficient at $10.532 \mu\text{m}$ has been previously measured by Pilla et al. [7] using a Fourier transform (FTIR) spectrometer between 300 and 700 K and CO_2 laser absorption spectroscopy between 600 and 1950 K in a shock tube. However, large data scatter (root-mean-square (rms) deviation of 9%) was found in the cross section measured at 1167–1950 K, resulting in relatively large uncertainties in the ethylene concentration time-history data. Here, we have reinvestigated the temperature and pressure dependence of the absorption coefficient using the new diagnostic system.

Gas mixtures of 1%, 0.5%, and 0.25% $\text{C}_2\text{H}_4/\text{Ar}$ were filled into the driven section of the shock tube to the desired initial pressures (0.04–0.18 and 0.38–1.07 atm for the low-pressure shock tube and the HPST facilities, respectively). The ethylene cross sections at room temperature (297 K) were first determined from the initial absorbance before the arrival of shock waves and are plotted in Fig. 3. At pressures between 0.04 and 1.07 atm, the measured cross sections exhibited evident pressure dependence and were fitted with a logarithmic function:

$$\sigma(297\text{K}, P), \text{ m}^2/\text{mol} = 90.0 + 24.7 \times \ln(P), \quad \text{with } P = 0.04 - 1.07 \text{ atm} \quad (3)$$

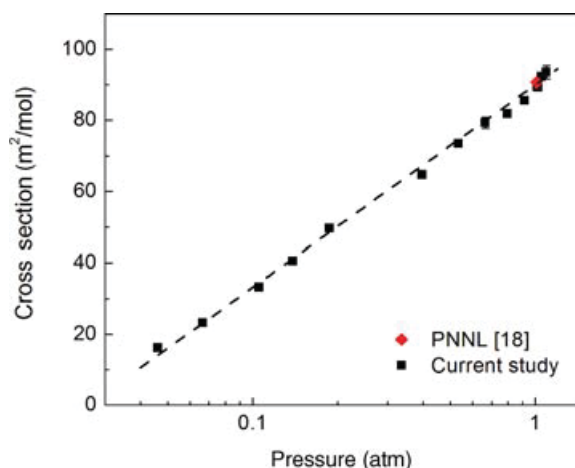


Figure 3 Room temperature (297 K) ethylene absorption cross section as a function of pressure; best fit using Eq. (3), with rms error of 3.8%.

Table I Comparison of Measured Ethylene Cross Section with Data in the Literature at 297 K, 1 atm

Reference	PNNL [18]	FTIR [7]	CO ₂ Laser [7]	Current Study
Cross section (m ² /mol)	90.68	92.25	91.80	90.06
Uncertainty (%)	2–4	— ^a	— ^a	2

^aUncertainty data not provided in [7].

Notice that the ethylene diagnostic is designed based on the overlap between the P14 CO₂ emission line and the absorption feature of the ν_7 ethylene fundamental band. The pressure dependence of the absorption cross section in this low-pressure range is due to the change in line shape of the transitions comprising the Q-branch absorption feature. Comparisons of the current measurements (297 K and 1 atm) with the data available in the literature are summarized in Table I. We measured the atmospheric ethylene cross section of (90.06 ± 1.6) m²/mol, showing excellent agreement with previous research and differing <1% from the value reported by Pacific Northwest National Laboratories (PNNL) [18]. The main factors contributing to uncertainty in our measurements are uncertainties in pressure and the baseline signal I_0 .

By filling helium into the driver section of the shock tube until the rupture of the polycarbonate (in the low-pressure shock tube) or aluminum (in the HPST) diaphragm, a shock wave was generated to compress and heat the test gas. The C₂H₄/Ar mixtures were first shock-heated to 643–1075 K and 0.3–5.5 atm by the incident shock waves and were then further heated and compressed to 1054–1959 K and 1.3–18.6 atm by the reflected shocks. The absorption coefficient

was determined by measuring the time-zero absorption of the mixture immediately behind shock waves. The measured high-temperature ethylene cross sections are plotted in Fig. 4 with estimated uncertainties. Evident pressure dependence was observed at lower pressures (0.3–1 atm); see incident shock data in Fig. 4. At pressures larger than 1 atm, however, the ethylene cross section was only weakly dependent on pressure across the full temperature range of 643–1959 K.

The absorption cross section can be modeled as a product of two independent functions for T and P :

$$\sigma(T, P) = \sigma(T) \cdot \chi(P) \quad (4)$$

Since ethylene $\sigma(T, P)$ at pressures larger than 1 atm is substantially sensitive to temperature, the $\sigma(T)$ factor can be first separated out from the measured ethylene cross sections within a finite pressure range. Figure 5 plots the measured ethylene cross section (1.8–5.5 atm) as a function of temperature between 643 and 1895 K. Best fits of experimental determinations of $\sigma(T)$ in this pressure range yield the following double exponential expression:

$$\sigma(T), \text{ m}^2/\text{mol} = a_0 + a_1 \times \exp(-T/b_1) + a_2 \times \exp(-T/b_2), \quad P = 1.8\text{--}5.5 \text{ atm} \quad (5)$$

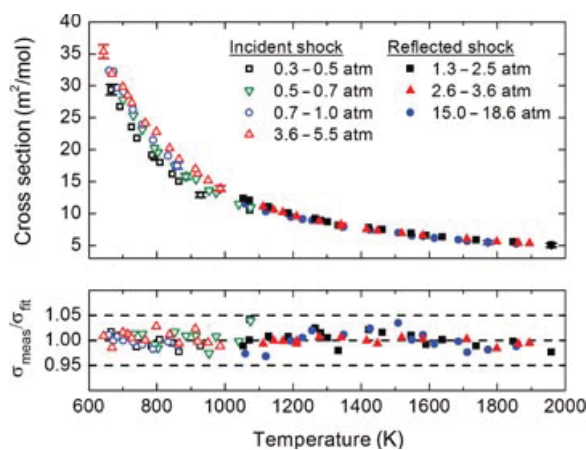


Figure 4 Ethylene cross sections ($\lambda = 10.532 \mu\text{m}$) over 643–1959 K and 0.3–18.6 atm. Upper panel: measured absorption cross section, σ_{meas} ; lower panel: comparisons of σ_{meas} with σ_{fit} calculated using Eq. (4). [Color figure can be viewed in the online issue, which is available at wileyonlinelibrary.com.]

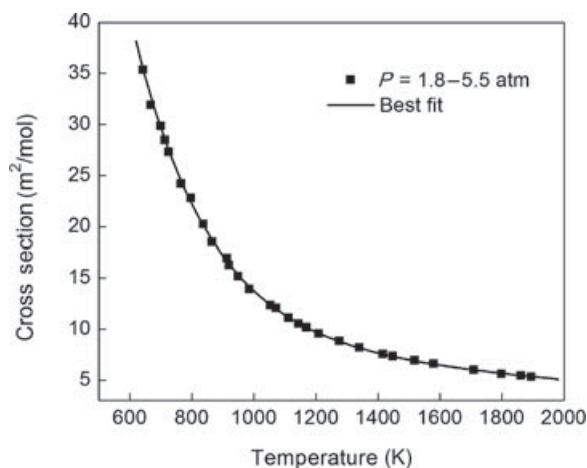


Figure 5 Pressure-independent ethylene cross section (1.8–5.5 atm) as a function of temperature; best fit using Eq. (5), with rms error of 0.9%.

where $a_0 = 4.8$, $a_1 = 383.7$, and $a_2 = 103.5$, in m^2/mol ; $b_1 = 183.0$ and $b_2 = 378.8$, in K. This expression agrees with the measured values with an rms deviation less than 1% (compared with 9% in [7]). By comparing the experimental data with the fitted $\sigma(T)$ function, the pressure-dependent factor $\chi(P)$ is then determined over the temperature range from 643 to 1959 K:

$$\chi(P) = \begin{cases} 0.68 + 0.47 \times P - 0.16 \times P^2, & P = 0.3\text{--}1.2 \text{ atm} \\ 0.82 + 0.2 \times P^{-0.1}, & P = 1.2\text{--}18.6 \text{ atm} \end{cases} \quad (6)$$

According to Eq. (4), $\sigma(T, P)$ is a direct product of $\sigma(T)$ and $\chi(P)$ and is found to have an rms deviation of 1.4% for the data across the full range of pressure (0.3–18.6 atm) and temperature (643–1959 K). Note that the pressure dependence of the cross section is seen to be much weaker than the temperature dependence. At a fixed pressure of 1.5 atm, $\sigma(T, P)$ decreased by 10% with 8% increase in temperature (from 1423 to 1547 K); however, at 1423 K, for a pressure change from 1.5–17 atm, $\sigma(T, P)$ changed by only 3.5%. Pilla et al. [7] did observe somewhat stronger pressure dependence for ethylene cross sections at temperatures above 1000 K and pressures between 1 and 4 atm, but this may have been a result of the large scatter in their data.

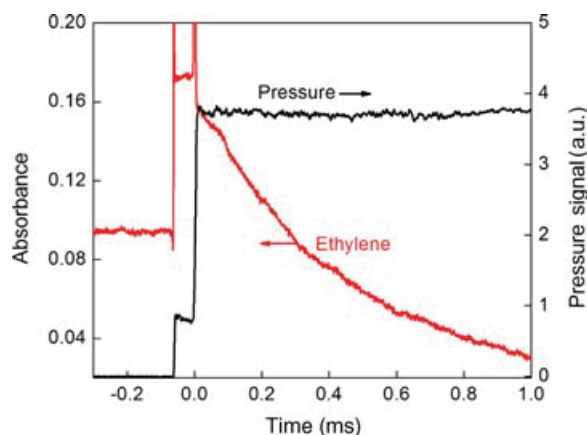


Figure 6 Measured ethylene absorbance and pressure profiles during ethylene decomposition. Reflected shock conditions: 1799 K, 2.7 atm, 1% $\text{C}_2\text{H}_4/\text{Ar}$.

HIGH-TEMPERATURE ETHYLENE PYROLYSIS

Ethylene is very stable at temperatures below 1400 K, which can be seen in Fig. 2 from the laser absorbance under constant temperature and pressure conditions. At temperatures high enough for the molecule to dissociate, the absorbance time history, which is directly proportional to the molecular number density, provides a sensitive measurement of the decomposition rate of the absorbing species. A representative laser absorbance time history (1% $\text{C}_2\text{H}_4/\text{Ar}$, 1799 K) during ethylene pyrolysis is presented in Fig. 6 along with the pressure trace measured at the same test location (2 cm from end wall). The pressure time history indicates uniform test conditions behind the reflected shock wave. However, the evident absorbance decay reflects the ethylene decomposition during this period. Since reaction (1) is the dominant channel for ethylene decomposition, the direct measurement of ethylene concentration can provide an experimental determination of the reaction rate constant k_1 at high temperatures.

To determine the rate constant k_1 , the measured ethylene concentration time histories were fitted using a detailed kinetic model by Marinov et al. [9]. Kinetic computations were performed using the CHEMKIN-PRO software code [19]. Fortunately, under the current experimental conditions, the ethylene concentrations allow fits that are quite insensitive to the choice of the other rate coefficients. In our analysis, only the rate coefficient of reaction (1) is updated in the mechanism for the purpose of fitting measured ethylene pyrolysis data. In addition, interfering absorption due to other hydrocarbon intermediates such as acetylene in the early decomposition is negligible [7].

An example of data trace and sensitivity plot is shown in Fig. 7. The sensitivity coefficient is the partial derivative of a species mole fraction with respect to the rate constant k of a reaction, normalized by the maximum species mole fraction and the parameter k . In this work, the ethylene sensitivity $S_{\text{C}_2\text{H}_4}$ is defined as follows:

$$S_{\text{C}_2\text{H}_4}(t) = (dX_{\text{C}_2\text{H}_4}/X_{\text{C}_2\text{H}_4}^{\max})/(dk_i/k_i) \quad (7)$$

where $X_{\text{C}_2\text{H}_4}$ is the local C_2H_4 mole fraction and k_i is the rate constant for reaction i . The sensitivity analysis shown in the bottom panel of Fig. 7 confirms that the ethylene decomposition is predominantly controlled by k_1 . By modifying only k_1 in the chemical kinetics model, we obtain excellent fits to the experimental C_2H_4 time histories. The best-fit k_1 for the example

case is determined to be $3.7 \times 10^8 \text{ cm}^3 \text{ mol}^{-1} \text{ s}^{-1}$ (compare to $4.4 \times 10^8 \text{ cm}^3 \text{ mol}^{-1} \text{ s}^{-1}$ in the Marinov et al. mechanism [9]) with an estimated fitting error of <5%. Notice that the rate coefficient was fitted only to the early-time (500–900 μs) behavior of the C₂H₄ trace; at later times, a complication arises from temperature variation due to nonideal effects in the shock tube.

The present values for k_1 are tabulated in Table II and illustrated in Fig. 8, on an Arrhenius plot along with the least-squares fit. Note that the experimental scatter is greatly reduced compared to Pilla's earlier

Table II Test Conditions and Rate Data of Reaction: C₂H₄ + Ar \rightarrow C₂H₂ + H₂ + Ar

T (K)	P (atm)	k_1 (cm ³ mol ⁻¹ s ⁻¹)
1519	2.85	5.5×10^6
1562	2.13	7.3×10^6
1581	2.80	1.1×10^7
1639	2.05	2.3×10^7
1710	2.71	5.4×10^7
1739	2.00	6.8×10^7
1799	2.72	1.6×10^8
1847	2.54	2.6×10^8
1862	2.62	3.0×10^8
1895	2.58	3.7×10^8

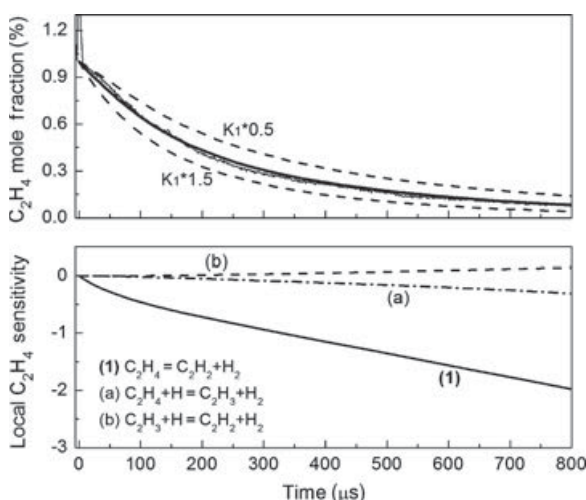


Figure 7 Example ethylene data, modeling, and sensitivity. Reflected shock conditions: 1% C₂H₄/Ar, $T = 1895 \text{ K}$, $P = 2.58 \text{ atm}$. Top graph: solid line: fitted to data using the Marinov et al. mechanism [9] and adjusting k_1 ; dashed lines: variation of $k_1 \pm 50\%$. Bottom graph: C₂H₄ sensitivity plot.

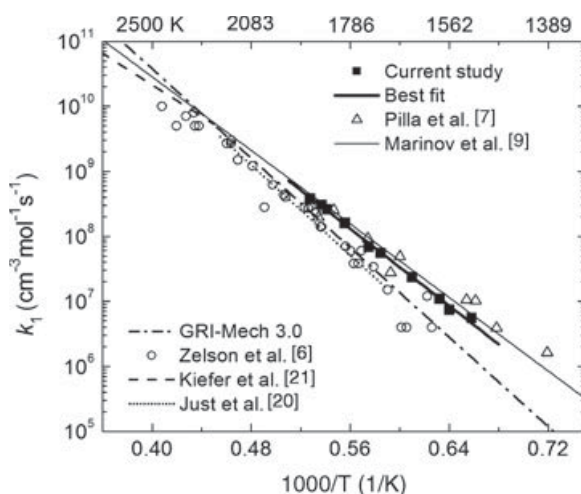


Figure 8 Comparison of measured k_1 (2.0–2.8 atm) with previous measurements and models.

measurements. A best-fit to the current data only yields a rate constant expression for k_1 valid over the range 1519–1895 K and 2.0–2.8 atm:

$$k_1 = 2.61 \times 10^{16} \exp(-34,130/T, \text{ K}) \text{ cm}^3 \text{ mol}^{-1} \text{ s}^{-1} \quad (8)$$

where the rms experimental scatter about the fit is <10%. There is no significant pressure dependence in this narrow pressure range, and the reaction is likely near the low-pressure limit. The primary contributions to uncertainties in the rate coefficients are: temperature (1%), fitting the data to computed profiles (5%), and C₂H₄ cross section (5%). These uncertainties give overall uncertainties in k_1 of 20%.

Figure 8 also compares the current study with previous measurements of k_1 . The early research by Just et al. inferred the rate constant of reaction (1) by measuring H-atoms in pyrolysis of 0.1–1.0% C₂H₄/Ar mixtures using atomic resonance absorption spectrophotometry [20]. Kiefer et al. used the laser schlieren technique for 3% C₂H₄ in krypton mixtures at much higher temperatures 2300–3200 K [21]. Zelson et al. measured the rate constant in 189–444 ppm C₂H₄/Ar mixtures over 1600–2300 K at 1.2 atm using UV lamp absorption for C₂H₄ [6]. Pilla et al. used the 10.5 μm diagnostic system for 1% C₂H₄/Ar mixtures at 1390–1870 K and 2.3–3.1 atm [7], which was quite close to our experimental conditions. The current experimental results fall between the previous measurements but with much reduced data scatter. Comparisons of the measured rate constant with those employed in the Marinov et al. mechanism [9] (validated in premixed *n*-butane and propane flames) and GRI-Mech 3.0 [22] (an optimized mechanism for natural gas combustion) are also made, as plotted in Fig. 8. Particularly good agreement between the rate constant in the Marinov

et al. mechanism [9] and the current experimental measurements is seen.

C₂H₄ TIME HISTORIES DURING ETHYLENE OXIDATION

Ethylene oxidation experiments were performed in the 15.24-cm-diameter shock tube at pressures near 3 atm. Figure 9 provides representative examples of C₂H₄ concentration time histories for stoichiometric oxidation over 1267–1440 K using 0.5% C₂H₄/1.5% O₂/Ar mixtures. The experimental time resolution is sufficient to observe a pronounced induction period (27–50 μ s over the current temperature range) prior to the onset of steady C₂H₄ removal. In addition, the time-history data indicate that a pseudoplateau level of ethylene remains at the end of the fuel oxidation; however, this is now known to be caused by H₂O absorption interference.

Near 10.5 μ m where ethylene is the primary absorber, there exists interfering absorbance from the oxidation products. Pilla et al. measured the absorption cross sections of H₂O, CO₂, and small hydrocarbons [7] and are here summarized in Fig. 10. Propene and water seem to be the two main interfering species, with absorption cross sections approximately 5 and 15 times weaker than ethylene. Figure 11 presents the calculated time histories (using the Ranzi et al. [12] mechanism) for several different classes of species such as reactants, combustion products, and stable intermediates, during the oxidation of ethylene at the same test conditions as the 1267 K case shown in Fig. 9. According to the predictions of the model, H₂O is the primary combustion product when C₂H₄ is completely consumed after 0.7 ms. Although CO₂ is also a main

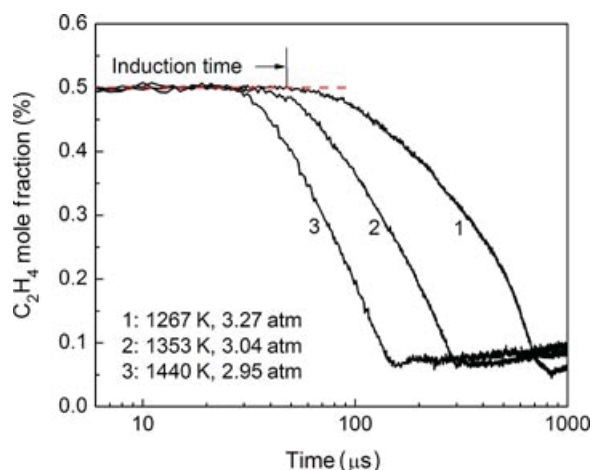


Figure 9 Stoichiometric ethylene oxidation profiles. Initial mixture: 0.5% C₂H₄, 1.5% O₂, and 98% Ar.

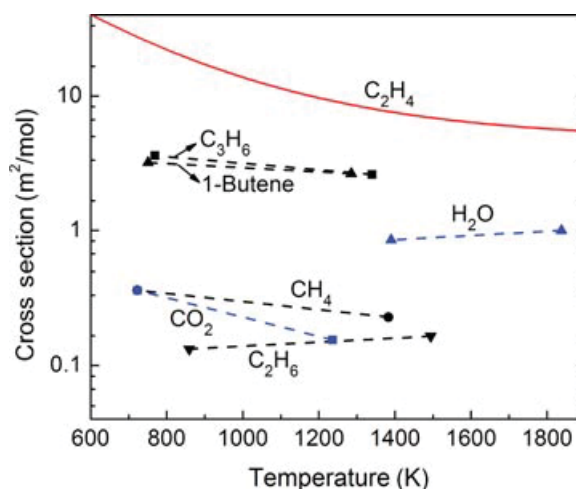


Figure 10 Absorption cross sections of interfering species during ethylene oxidation (2–3 atm) [7]; ethylene cross section from the current study.

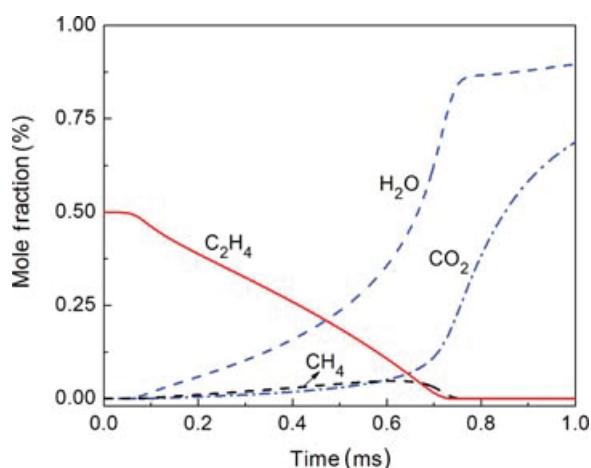


Figure 11 Calculated species time histories for C₂H₄/O₂/Ar mixture. Initial conditions: 1267 K, 3.27 atm; 0.5% C₂H₄, 1.5% O₂, and 98% Ar, $\phi = 1$. Simulations performed using the Ranzi et al. mechanism [12].

product, its interfering absorbance is negligible due to the much lower absorption cross section.

By subtracting the H₂O absorption interference based on the calculated H₂O concentration time history combined with the measured cross section, we are able to correct the C₂H₄ time history from the measured 10.532 μ m absorbance data. Figure 12 compares the measured time histories (corrected and uncorrected) with the predictions of four currently available models (Marinov et al. [9], Healy et al. [10], Wang et al. [11], and Ranzi et al. [12]). Comparisons between the corrected and uncorrected data reveal the fact that H₂O

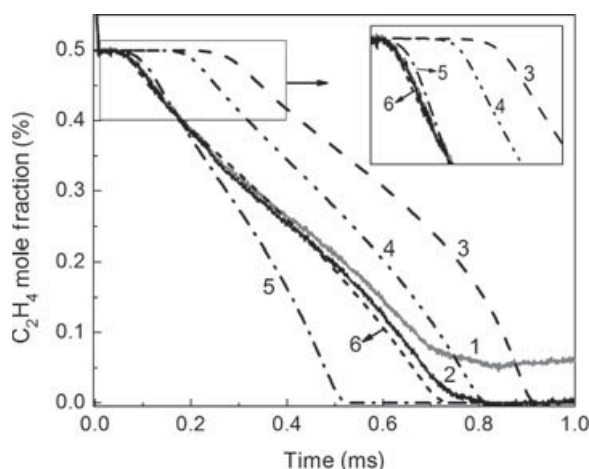


Figure 12 Measured (uncorrected and corrected) and simulated C₂H₄ concentration time histories during ethylene oxidation: 1, uncorrected measurement; 2, corrected measurement; 3, Healy et al. [10]; 4, Marinov et al. [9]; 5, Wang et al. [11]; and 6, Ranzi et al. [12]. Initial mixture: 0.5% C₂H₄/1.5% O₂/Ar, $\phi = 1$; reflected shock conditions: 1267 K, 3.27 atm.

interference only affects the later times of the ethylene profile, i.e., > 0.4 ms. It seems that the Marinov et al. [9] and Healy et al. [10] mechanisms track the ethylene decay rate closely, but they are substantially shifted in time. The JetSurF 2.0 model of Wang et al. [11] is close to the measurement at early times, but the ethylene removal rate at longer times is overestimated by this mechanism. Finally, the Ranzi et al. [12] mechanism almost duplicates the full range of ethylene time history, although, it overpredicts the C₂H₄ removal rate by $\sim 10\%$ after 0.5 ms. Similar observations are made for the fuel-lean case ($\phi = 0.5$) and the fuel-rich case ($\phi = 2$) shown in Fig. 13. Predictions from the Ranzi et al. [12] mechanism are consistently in very good agreement with the measurements, whereas the other three mechanisms fail to recover either the induction period or the ethylene removal rate.

In future work, the H₂O concentration during hydrocarbon oxidation could be measured directly and accurately using tunable diode laser absorption near 2.5 μm , a method which has been developed and widely applied in shock tube studies of H₂/O₂ combustion system in our laboratory [13,23,24]. Alternatively, a second CO₂ line (i.e., the P(28) transition at 10.675 μm), which is away from the peak ethylene absorption, could be selected to account for the H₂O interfering absorbance. The approach is similar to the multiwavelength strategy used in our laboratory for OH and CH₃ radical diagnostics in UV region [24–27].

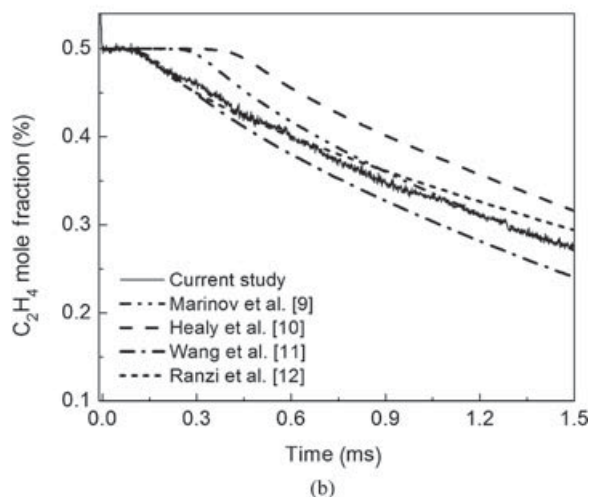
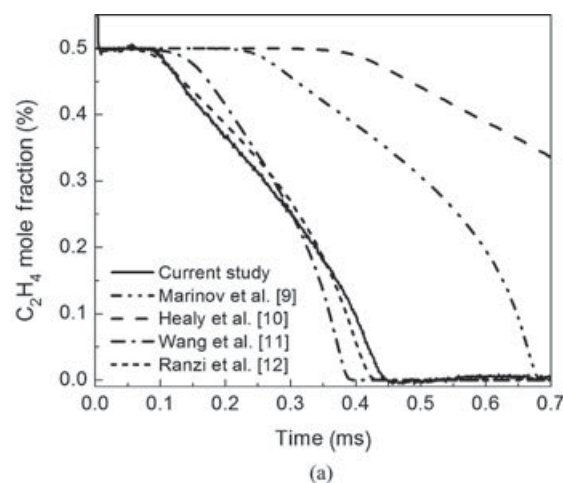


Figure 13 Measured (corrected) and simulated C₂H₄ concentration time histories during ethylene oxidation for (a) 0.5% C₂H₄/3% O₂/Ar, $\phi = 0.5$, 1221 K, 3.42 atm and (b) 0.5% C₂H₄/0.75% O₂/Ar, $\phi = 2$, 1244 K, 3.45 atm.

CONCLUSIONS

A quantitative absorption diagnostic has been further developed for measuring ethylene concentration time histories in shock tube experiments using CO₂ laser absorption spectroscopy at 10.532 μm . The absorption cross section of ethylene was carefully studied at 643–1959 K and 0.3–18.6 atm behind incident and reflected shock waves, and the data scatter was substantially reduced compared to previous measurements by Pilla et al. [7]. The relatively large absorption cross sections of ethylene at this wavelength enable 100 ppm detection at typical reflected shock conditions of 1200 K and 3 atm with a path length of 15 cm. A preferred reaction rate constant (k_1) for C₂H₄ + M \rightarrow C₂H₂ + H₂ + M was inferred from the ethylene pyrolysis experiment at reflected shock conditions ranging from

1519 to 1895 K and 2.0 to 2.8 atm. Our measurements show good agreement with previous research, and the updated rate constant provides the possibility to improve the prediction of ethylene removal rates in large alkane mechanisms.

Ethylene time histories were also measured behind reflected shock waves during the oxidation of 0.5% C₂H₄/O₂/Ar mixtures at temperatures from 1221 to 1440 K, varying in equivalence ratio from 0.25 to 2. Comparisons of the measured ethylene concentration time histories with the predictions of four currently available detailed kinetic mechanisms show excellent agreement with the Ranzi et al. [12] mechanism. Planned extensions of this diagnostic to studies of hydrocarbon fuel oxidation include the use of a diode laser diagnostic near 2.5 μ m to track H₂O production directly, or to utilize off-line measurements near 10.6 μ m to completely account for the interfering absorbance. Future shock tube experiments are planned to apply this extended diagnostic scheme to pyrolysis and oxidation of other fuels, including jet fuel and biodiesel fuel surrogates.

SUPPORTING INFORMATION

The ethylene concentration time histories for Figs. 12 and 13 are available in the Supporting Information file in the online issue at wileyonlinelibrary.com.

This work was supported by the Army Research Office with Dr. Ralph A. Anthenien as contract monitor and the Air Force Office of Scientific Research with Dr. Julian Tishkoff as technical monitor.

BIBLIOGRAPHY

- Westbrook, C. K.; Dryer, F. L.; Schug, K. P. *Symp Int Combust Proc* 1982, 19, 153–166.
- Curran, H. J.; Gaffuri, P.; Pitz, W. J.; Westbrook, C. K. *Combust Flame* 2002, 129, 253–280.
- Davidson, D. F.; Hong, Z.; Pilla, G. L.; Farooq, A.; Cook, R. D.; Hanson, R. K. *Proc Combust Inst* 2011, 33, 151–157.
- Wang, H.; Frenklach, M. *Combust Flame* 1997, 110, 173–221.
- Roth, P.; Just, Th. *Phys Chem* 1973, 77, 1114.
- Zelson, L. S.; Davidson, D. F.; Hanson, R. K. *J Quant Spectrosc Radiat Transfer* 1993, 52, 31–43.
- Pilla, G. L.; Davidson, D. F.; Hanson, R. K. *Proc Combust Inst* 2011, 33, 333–340.
- Klingbeil, A. E.; Jeffries, J. B.; Davidson, D. F.; Hanson, R. K. *Appl Phys B* 2008, 93, 627–638.
- Marinov, N. M.; Pitz, W. J.; Westbrook, C. K.; Vincitore, A. M.; Castaldi, M. J.; Senkan, S. M. *Combust Flame* 1998, 114, 192–213.
- Healy, D.; Donato, N. S.; Aul, C. J.; Petersen, E. L.; Zinner, C. M.; Bourque, G.; Curran, H. J. *Natural Gas III*; 2010. Accessed 16 August 2011 at <http://c3.nuigalway.ie/naturalgas3.html>.
- Wang, H.; Dames, E.; Sirjean, B.; Sheen, D. A.; Tangko, R.; Violi, A.; Lai, J. Y. W.; Egolfopoulos, F. N.; Davidson, D. F.; Hanson, R. K.; Bowman, C. T.; Law, C. K.; Tsang, W.; Cernansky, N. P.; Miller, D. L.; Lindstedt, R. P. *JetSurF version 2.0*; 2010. Accessed 16 August 2011 at <http://melchior.usc.edu/JetSurF/JetSurF2.0>.
- Ranzi, E.; Dente, M.; Goldaniga, A.; Bozzano, G.; Faravelli, T. *Kinetic Mechanism/C1–C3 mechanism version 1101*; 2011. Accessed 16 August 2011 at <http://creckmodeling.chem.polimi.it/kinetic.html>.
- Hong, Z.; Farooq, A.; Barbour, E. A.; Davidson, D. F.; Hanson, R. K. *J Phys Chem A* 2009, 113, 12919–12925.
- Petersen, E. L.; Hanson, R. K. *Shock Waves* 2001, 10, 405–420.
- Rothman, L. S.; Gordon, I. E.; Barbe, A.; Benner, D. C.; Bernath, P. F.; Birk, M.; Boudon, V.; Brown, L. R.; Campargue, A.; Champion, J.-P.; Chance, K.; Coudert, L. H.; Danaj, V.; Devi, V. M.; Fally, S.; Flaud, J.-M.; Gamache, R. R.; Goldman, A.; Jacquemart, D.; Kleiner, I.; Lacome, N.; Lafferty, W. J.; Mandin, J.-Y.; Massie, S. T.; Mikhailenko, S. N.; Miller, C. E.; Moazzen-Ahmadi, N.; Naumenko, O. V.; Nikitin, A. V.; Orphal, J.; Perevalov, V. I.; Perrin, A.; Predoi-Cross, A.; Rinsland, C. P.; Rotger, M.; Simeckova, M.; Smith, M. A. H.; Sung, K.; Tashkun, S. A.; Tennyson, J.; Toth, R. A.; Vandaele, A. C.; VanderAuwera, J. *J Quant Spectrosc Radiat Transfer* 2009, 110, 533–572.
- Farooq, A.; Jeffries, J. B.; Hanson, R. K. *Appl Phys B* 2009, 96, 161–173.
- Ren, W.; Jeffries, J. B.; Hanson, R. K. *Meas Sci Technol* 2010, 21, 105603.
- Sharpe, S. W.; Johnson, T. J.; Sams, R. L.; Chu, P. M.; Rhoderick, G. C.; Johnson, P. A. *Appl Spectrosc* 2004, 58, 452–461.
- Kee, R. J.; Ruply, F. M.; Miller, J. A. *CHEMKIN-PRO*; Reaction Design, Inc., San Diego, CA, 2010.
- Just, Th.; Roth, P.; Damm, R. *Proc Combust Inst* 1977, 16, 961–969.
- Kiefer, J. H.; Dapsalis, S. A.; Al-Alami, M. Z.; Budach, K. A. *Combust Flame* 1983, 51, 79–93.
- Smith, G. P.; Golden, D. M.; Frenklach, M.; Moriarty, N. W.; Eiteneer, B.; Goldenberg, M.; Bowman, C. T.; Hanson, R. K.; Song, S.; Gardiner, W. C., Jr.; Lissianski, V.; Qin, Z. *GRI-Mech Version 3.0*; 1999. Accessed 16 August 2011 at http://www.me.berkeley.edu/gri_mech/.
- Hong, Z.; Vasu, S. S.; Davidson, D. F.; Hanson, R. K. *J Phys Chem A* 2010, 114, 5520–5525.
- Hong, Z.; Davidson, D. F.; Barbour, E. A.; Hanson, R. K. *Proc Combust Inst* 2011, 33, 309–316.
- Cook, R. D.; Pyun, S. H.; Cho, J.; Davidson, D. F.; Hanson, R. K. *Combust Flame* 2011, 158, 790–795.
- Vasudevan, V.; Hanson, R. K.; Golden, D. M.; Bowman, C. T.; Davidson, D. F. *J Phys Chem* 2007, 111, 4062–4072.
- Davidson, D. F.; Oehlschlaeger, M. A.; Hanson, R. K. *Proc Combust Inst* 2007, 31, 321–328.

CO concentration and temperature sensor for combustion gases using quantum-cascade laser absorption near 4.7 μm

W. Ren · A. Farooq · D.F. Davidson · R.K. Hanson

Received: 29 February 2012 / Revised version: 23 March 2012 / Published online: 25 May 2012
© Springer-Verlag 2012

Abstract A sensor for sensitive in situ measurements of carbon monoxide and temperature in combustion gases has been developed using absorption transitions in the ($v' = 1 \leftarrow v'' = 0$) and ($v' = 2 \leftarrow v'' = 1$) fundamental bands of CO. Recent availability of mid-infrared quantum-cascade (QC) lasers provides convenient access to the CO fundamental band near 4.7 μm , having approximately 10^4 and 10^2 times stronger absorption line-strengths compared to the overtone bands near 1.55 μm and 2.3 μm used previously to sense CO in combustion gases. Spectroscopic parameters of the selected transitions were determined via laboratory measurements in a shock tube over the 1100–2000 K range and also at room temperature. A single-laser absorption sensor was developed for accurate CO measurements in shock-heated gases by scanning the line pair $v'' = 0$, R(12) and $v'' = 1$, R(21) at 2.5 kHz. To capture the rapidly varying CO time-histories in chemical reactions, two different QC lasers were then used to probe the line-center absorbance of transitions $v'' = 0$, P(20) and $v'' = 1$, R(21) with a bandwidth of 1 MHz using fixed-wavelength direct absorption. The sensor was applied in successful shock tube measurements of temperature and CO time-histories during the pyrolysis and oxidation of methyl formate, illustrating the capability of this sensor for chemical kinetic studies.

1 Introduction

Laser absorption spectroscopy techniques play a large and growing role in the measurement of flow-field parameters such as temperature, gas composition, velocity, and pressure [1–4]. These sensors are highly attractive for combustion and propulsion applications due to their nonintrusive nature, fast time response, and in situ measurement capability. Carbon monoxide (CO) is a particularly significant target for hydrocarbon-fueled systems, since it is a toxic pollutant from combustion devices and a primary product of incomplete combustion, and its concentration can be interpreted to indicate combustion efficiency.

The absorption spectra of CO, H₂O, and CO₂ in the near- to mid-infrared region at 1500 K are illustrated in Fig. 1, where the absorption line-strengths (from the HITRAN 2004 database [5]) are plotted as a function of wavelength from 1–6 μm . The fundamental band of CO holds the most promising candidate transitions owing to their much stronger line-strengths and relatively weaker interference from other combustion species. Work has been reported using transitions in three different vibrational bands of CO: the second overtone band ($\Delta v = 3$) near 1.55 μm [6–8], the first overtone band ($\Delta v = 2$) near 2.3 μm [9–12], and the fundamental band ($\Delta v = 1$) near 4.6 μm [13–19]. The absorption strength of the fundamental band is approximately 10^4 and 10^2 times stronger compared to the overtone bands near 1.55 μm and 2.3 μm , respectively, making it promising for sensitive detection with relatively low CO concentration and/or short path length.

Early studies of CO detection in the fundamental band were carried out by Hanson et al. [13, 14] using lead-salt tunable diode laser (TDL) absorption. However, this sensor has limited practical applications, as the laser source is multimode and requires cryogenic cooling. Barron-Jimenez et

W. Ren (✉) · D.F. Davidson · R.K. Hanson
High Temperature Gasdynamics Laboratory, Department
of Mechanical Engineering, Stanford University, Stanford,
CA 94305, USA
e-mail: renwei@stanford.edu
Fax: +1-650-7231748

A. Farooq
Clean Combustion Research Center, King Abdullah University
of Science and Technology, Thuwal 23955, Saudi Arabia

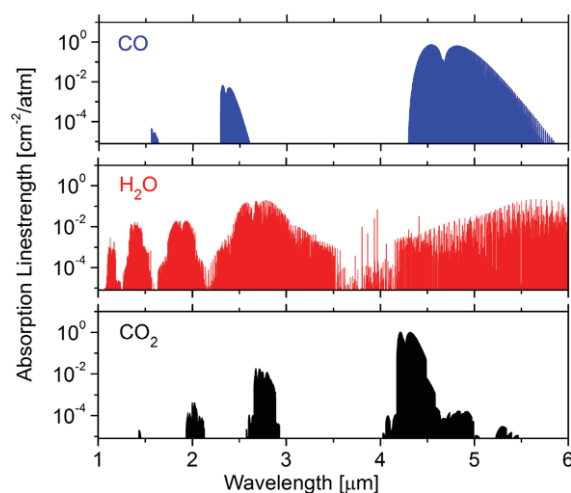


Fig. 1 Absorption line-strengths of CO, H₂O, and CO₂ at 1500 K (from HITRAN 2004 database [5])

al. [17] demonstrated a CO sensor in the 4.4–4.8 μm spectral region using difference-frequency mixing of radiation from a near-IR external-cavity diode laser (ECDL) and a compact Nd:YAG laser in a periodically poled lithium niobate (PPLN) crystal. CO concentration measurements were performed in a room-temperature gas cell, a well-stirred reactor, and a near-adiabatic hydrogen/air CO₂-doped flame by probing the fundamental band CO transitions R(23), R(11), and P(19). Although these demonstrations of the diode-laser-based CO sensor were successful, the weak mid-IR power ($<1 \mu\text{W}$) significantly limited the sensitivity and signal-to-noise ratio of this sensor. Developments in quantum-cascade (QC) laser technology, resulting in room-temperature, relatively high power (mW), narrow line-width, and single-mode QC lasers, have led to broad applications of these sources in high-resolution spectroscopy and high-sensitivity detection of trace gases [20–22]. Kosterev et al. [18] reported the application of a pulsed, distributed-feedback quantum-cascade laser (DFB-QCL) for CO sensing in ambient air by probing the R(3) transition at 2158.30 cm^{-1} . A noise-equivalent detection limit of 12 parts per billion was demonstrated experimentally with a 102 cm path length at a 10 kHz pulsed-laser repetition rate. Compared to lasers employing pulsed operation, the continuous-wave (cw) lasers generally offer relatively simpler operation and narrower laser line-widths. In work related to the current paper, a cw QC laser was used recently to detect CO absorption in the fundamental band and measure temperature in shock-heated nonreactive gases between 950 and 3500 K near 1 atm by Vanderover and Oehlschlaeger [19]. Temperature measurements were made via a two-line ratio technique using the line pairs R(9) and R(17), and R(10) and R(18), by tuning the laser wavelength across the absorption features at 1–2 kHz. This laser scan rate limits the time response of the

sensor for time-resolved measurements in many combustion applications and in shock tube experiments.

In this paper, we discuss the extension of cw DFB-QCL-based mid-IR absorption of CO for in situ detection in combustion gases and specifically in shock tube flows. Sensors for temperature and CO concentration measurements using scanned-wavelength direct absorption (DA) with a single room-temperature QC laser and using fixed-wavelength DA with dual QC lasers are both developed to provide fast and flexible diagnostics for different applications. We first examine the fundamental band of CO (4.3–5.8 μm) to find candidate CO transitions suitable for high-temperature ($>1000 \text{ K}$) in situ detection that are isolated from interference of other primary combustion products such as H₂O and CO₂. Two different cw QC lasers are used to access transitions R(12), R(21), R(13) and R(22) in the R-branch of the vibrational band near 4.6 μm , and P(20) and P(14) in the P-branch near 4.8 μm , respectively. For gas-temperature sensing based on the ratio of two-line absorption, the well-separated lower-state internal energies among these transitions provide high temperature sensitivity. Fundamental spectroscopic parameters are verified (line-strength, included in the HITRAN database [5]) and measured (Ar-broadening coefficient) for the selected lines using a shock tube. The accuracy of both the scanned- and fixed-wavelength CO temperature sensors is then validated in shock-heated nonreactive CO–H₂–Ar mixtures. Measurements of temperature and CO concentration are subsequently carried out in the pyrolysis and oxidation of methyl formate to demonstrate the applications of this CO sensor in shock tube chemical kinetic studies. These quantitative validation measurements confirm the potential of mid-IR QC-laser-based sensing of CO concentration and temperature in combustion environments.

2 Fundamental spectroscopy

The fundamental theory of direct absorption spectroscopy is reproduced here only briefly to define our notation, since the theory is well understood and has been detailed in the literature [23]. When spectrally narrow radiation at frequency ν passes through a uniform gas medium of length L [cm], the transmitted intensity I_t is related to the incident intensity I_0 by the Beer–Lambert law:

$$\left(\frac{I_t}{I_0}\right)_\nu = \exp(-SPx_i\phi_\nu L), \quad (1)$$

where S [$\text{cm}^{-2} \text{ atm}^{-1}$] is the line-strength of the specific transition, P [atm] the total pressure, x_i the mole fraction of the absorbing species i , and ϕ_ν [cm] the line-shape function. The dimensionless product $\alpha_\nu = SPx_i\phi_\nu L$ is defined as absorbance, with $k_\nu = SPx_i\phi_\nu$ the absorption coefficient. Since the line-shape function ϕ_ν is normalized to have unit

area across the line, the integrated absorbance can be expressed as

$$A_i = \int \alpha_v dv = S_i(T) P x_i L. \quad (2)$$

The Voigt line-shape function ϕ_v combines both temperature and collisional broadening. The collision-broadened full-width at half maximum (FWHM) of the absorbing species i is

$$\Delta v_c \text{ cm}^{-1} = P \sum_j x_j 2\gamma_{ji}, \quad (3)$$

where x_j is the mole fraction of the collisional partner j , and $2\gamma_{ji}$ [$\text{cm}^{-1} \text{ atm}^{-1}$] is the broadening coefficient of j with i . From an experimental point of view, it is of practical interest to have a simple model of the variation of the FWHM with temperature, typified by the following commonly-used expression [24]:

$$2\gamma(T) = 2\gamma(T_0) \left(\frac{T_0}{T} \right)^n, \quad (4)$$

where T_0 is the reference temperature (usually 296 K) and n is the temperature coefficient. The line-strength S [$\text{cm}^{-2} \text{ atm}^{-1}$] has a temperature dependence:

$$S(T) = S(T_0) \frac{Q(T_0)}{Q(T)} \left(\frac{T_0}{T} \right) \exp \left[-\frac{hcE''}{k} \left(\frac{1}{T} - \frac{1}{T_0} \right) \right] \times \left[1 - \exp \left(\frac{-hc\nu_0}{kT} \right) \right] \left[1 - \exp \left(\frac{-hc\nu_0}{kT_0} \right) \right]^{-1}, \quad (5)$$

where $Q(T)$ is the partition function, E'' [cm^{-1}] is the lower-state energy, ν_0 [cm^{-1}] is the line-center frequency, and h , c , k are Planck's constant, speed of light, and Boltzmann's constant, respectively.

The absorption measurement of temperature is commonly based on a two-line technique [15]. Temperature is inferred from the ratio of the integrated absorbance under the absorption feature or the line-center absorbance of two molecular transitions of the same species.

3 Line selection

Absorption spectra of CO fundamental band between 4.3 and 5.8 μm were computed based on the HITRAN database [5] for typical shock tube combustion flows (1000–2000 K, 1 atm, 0.1 % CO/1 % H_2O /1 % CO_2) to find suitable CO transitions. A systematic line-selection procedure was used to find lines with sufficient absorption strength, isolation from interfering absorption, temperature sensitivity, and the availability of the commercial laser sources [25].

Two cw, room-temperature, DFB-QC lasers were subsequently acquired from Alpes Lasers SA to access the R-branch near 4.6 μm and the P-branch near 4.8 μm of the

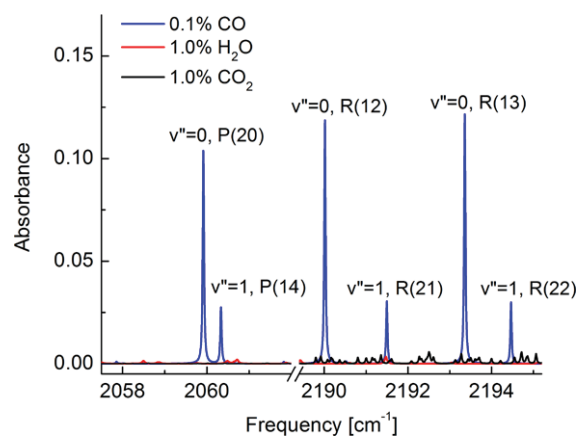


Fig. 2 Calculated spectra of 0.1 % CO, 1 % H_2O , and 1 % CO_2 in air under shock tube combustion conditions: $T = 1500$ K, $P = 1$ atm, $L = 10$ cm

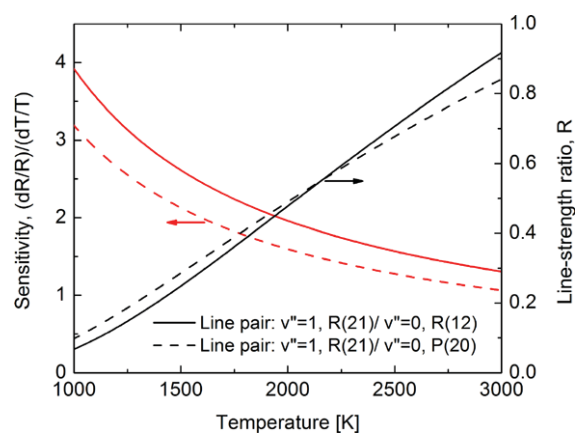
fundamental band of CO, respectively. For the laser frequency ranges of 2048.6 to 2061.3 cm^{-1} and 2185.8 to 2200.3 cm^{-1} , three sets of closely spaced line pairs were selected for single-laser, scanned-wavelength temperature sensing: line pair A ($v'' = 0$, R(12) and $v'' = 1$, R(21) near 2190 cm^{-1}), line pair B ($v'' = 0$, R(13) and $v'' = 1$, R(22) near 2194 cm^{-1}), and line pair C ($v'' = 0$, P(20) and $v'' = 1$, P(14) near 2060 cm^{-1}). Their spectroscopic parameters (for line pairs A, B, and C) from the HITRAN database [5] are summarized in Table 1. A spectral simulation of 0.1 % CO in air ($T = 1500$ K, $P = 1$ atm, $L = 10$ cm) for these three line pairs is illustrated in Fig. 2, along with the interfering absorption of 1 % H_2O and CO_2 . It should be noticed that the interference from H_2O and CO_2 is mostly negligible at these wavelengths.

These three line pairs, each with CO transitions from two different vibrational levels, have a spectral separation of 0.4–1.5 cm^{-1} , within the typical 2 cm^{-1} rapid-tuning range of the commercial QC lasers. A representative analysis of the line-strength ratio and temperature sensitivity for the line pair A is plotted as solid lines in Fig. 3. Typically, the line-strength ratio should not be too far from unity. The sensitivity, defined here as the unit change in line-strength ratio for a unit change in temperature should at least be 1 for sensitive temperature measurements. These two curves suggest this line pair can be used for accurate temperature sensing at elevated temperatures, e.g., between 1000 and 3000 K.

Two-line thermometry, achieved by scanning two neighboring transitions with a single laser, enables a relatively simpler system with lower cost. However, the tuning rate of the QC lasers limited the sensor bandwidth to several kHz. High-temperature chemical kinetic studies in a shock tube, where chemical reactions happen within milliseconds, require a faster sensor, with 100 kHz bandwidth or greater. Thus, a dual-laser, fixed-wavelength method was pursued to provide highly time-resolved measurements. We selected

Table 1 Candidate CO lines for the measurements of temperature and CO concentration based on the HITRAN 2004 database [5]

Line pair	Transition (v'', J'')	Frequency (cm^{-1})	Wavelength (nm)	Separation (cm^{-1})	$S@296\text{ K}$ ($\text{cm}^{-2}\text{ atm}^{-1}$)	E'' (cm^{-1})
A	0, R(12)	2190.02	4566.17	1.48	7.13	299.77
	1, R(21)	2191.50	4563.08		4.32×10^{-5}	3022.09
B	0, R(13)	2193.36	4559.22	1.10	6.04	349.70
	1, R(22)	2194.46	4556.93		3.02×10^{-5}	3105.65
C	0, P(20)	2059.91	4854.58	0.42	8.76×10^{-1}	806.38
	1, P(14)	2060.33	4853.59		2.64×10^{-4}	2543.06

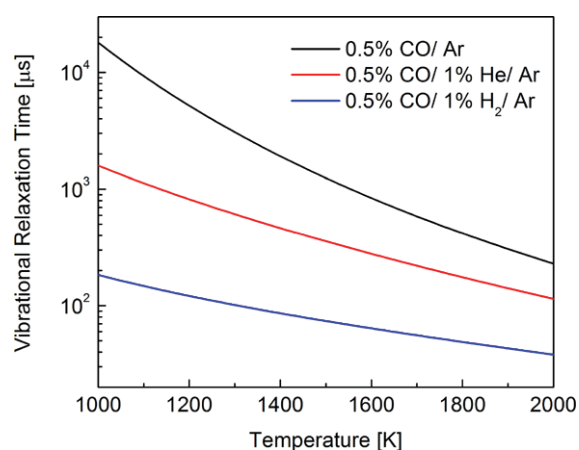
**Fig. 3** Temperature sensitivities (*left-hand axis*) and line-strength ratios (*right-hand axis*) for two representative line pairs. *Solid line*: line pair A ($v'' = 1$, R(21) and $v'' = 0$, R(12)) for single-laser scanned-wavelength temperature sensing; *dashed line*: the $v'' = 1$, R(21) and $v'' = 0$, P(20) lines for dual-laser fixed-wavelength temperature sensing (selected from the six individual lines listed in Table 1)

the $v'' = 0$, P(20) and $v'' = 1$, R(21) lines from the six individual lines listed in Table 1 as the optimum line pair for temperature measurement using two different QC lasers. The corresponding line-strength ratio and temperature sensitivity for this line pair are shown as dashed lines in Fig. 3.

4 Spectroscopic measurement and verification

The fundamental spectroscopic parameters such as line-strength, self- and air-broadening coefficients of CO can be found in the HITRAN database [5]. However, argon instead of air is usually used as the bath gas in shock tube kinetic studies. Accordingly, there is need to investigate the Ar-broadening coefficient of each line and its temperature dependence. Moreover, the validation of CO line-strength at high temperature is essential for the accurate measurements as the measured absorbance is compared with the simulation to infer gas mole fraction and temperature.

All spectroscopic measurements were performed in a 15.2 cm diameter stainless-steel high-purity shock tube. The incident shock wave propagates through the tube, raising

**Fig. 4** Calculated vibrational relaxation time ($P = 1.5\text{ atm}$) for CO–Ar, CO–He–Ar, and CO–H₂–Ar mixtures (calculations from [27])

the temperature and pressure of the test gas from (T_1, P_1) to (T_2, P_2) . When the shock wave reaches the end-wall of the tube, it is reflected and further elevates the temperature and pressure of the test gas to (T_5, P_5) . The gas temperature and pressure immediately behind the shock wave can be calculated accurately using standard normal-shock relations and the measured incident shock speed, with an uncertainty of $\sim 1\%$ in temperature over the high-quality test time of 2 ms. Further details about the shock tube can be found in [26]. Research grade gases (argon, helium, and hydrogen $>99.999\%$; 0.5 % CO/Ar mixture with uncertainty $<0.1\%$) were supplied by Praxair Inc. Due to the significant time for CO to vibrationally relax behind the reflected shock wave, a small portion of H₂ (1 %) is added to the 0.5 % CO/Ar mixture to accelerate the vibrational relaxation; see Fig. 4 for the evaluation. The test mixtures were manometrically prepared in a turbo-pumped stainless-steel mixing tank (14 L) with a magnetically driven stirrer.

A schematic of the experimental setup is demonstrated in Fig. 5. The room-temperature operated QC laser (Alpes Lasers) used for these measurements was thermoelectrically-cooled and housed with collimation optics in a sealed laser housing (Alpes HHL-L module). In addition, a laboratory water-cooled heat sink was installed to the laser housing to achieve more stable laser performance. The laser wave-

length is tuned by varying the injection current and base temperature, which are controlled by a combination of commercial temperature and injection current controllers (Alpes Lasers TCU 200 and ILX Lightwave LDX-3232). The laser wavelength is rapidly tuned (1–10 kHz scan rate) over the desired absorption feature with a linear ramp of current from a function generator. A ZnSe beam splitter was used to split the collimated laser beam (20–40 mW) into two arms to be received by a pair of matched TE-cooled IR photovoltaic detectors (Vigo Systems, 1 MHz bandwidth); one beam passes through the test gas of 15.2 cm path length in the shock tube, while the other propagates through a 7.6 cm long solid germanium etalon in the ambient air. The etalon with a free

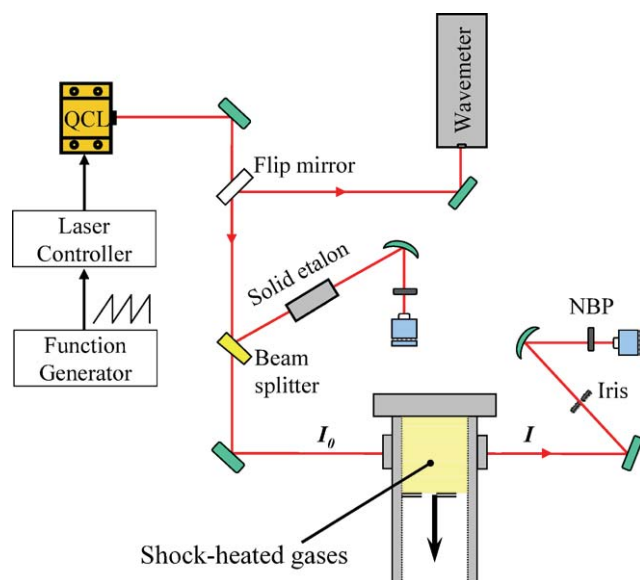


Fig. 5 Experimental setup for the measurement of spectroscopic parameters of CO transitions in a shock tube

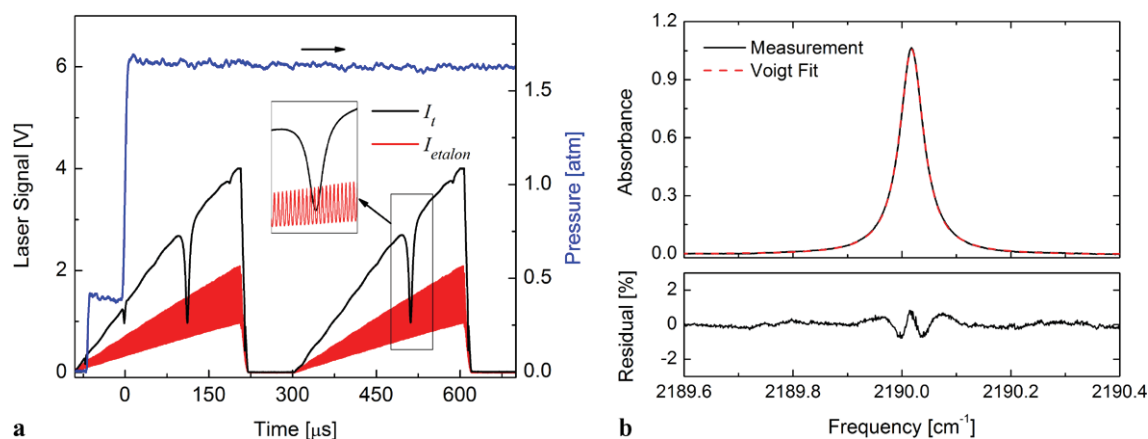


Fig. 6 Illustration of (a) the measured raw-data traces (pressure, transmission through the shock tube and the etalon) of the R(12) transition at 2190.02 cm^{-1} , taken at 2.5 kHz with 0.496 % CO/1 % H_2 /Ar mixtures behind the reflected shock (vibrationally equilibrated reflected

spectral range (FSR) of 0.016 cm^{-1} enables the conversion of scan time to relative wavelength. A narrow-bandpass IR filter (half power bandwidth 50 nm) was used to filter out emission and unwanted ambient light. Before each shock tube experiment, the laser wavelength was tuned to the desired transition by monitoring the absolute wavelength using a free-space mid-IR wavemeter (Bristol 621).

The laser wavelength was typically tuned over a range of $\sim 1 \text{ cm}^{-1}$ at a frequency of 2.5 kHz, while the detector signal was sampled at 10 MHz to fully capture the absorption feature. The data acquisition system was triggered by the pressure transducer located at 2 cm from the shock tube end-wall to record pressure and transmission signal (I_t) of the laser during the shock heating. In the present experiments with large fractional absorption and no significant noise problems, only one single scan of I_t behind the reflected shock was analyzed to infer spectroscopic parameters.

The raw data traces of a typical experiment for high-temperature line-strength and Ar-broadening measurements of CO are plotted in Fig. 6(a). The laser intensity and wavelength were scanned over the R(12) transition at 2190.02 cm^{-1} and recorded behind the reflected shock at 1450 K and 1.63 atm (vibrational equilibrium) with a mixture of 0.496 % CO/1 % H_2 /Ar. Prior to each experiment, the shock tube is evacuated by a turbomolecular pump and the baseline reference intensity (I_0) recorded. The spectral absorbance is then determined by the Beer–Lambert law and plotted as a function of wavenumber calibrated using the etalon trace, as demonstrated in Fig. 6(b). The measurement was overlaid with a best-fit Voigt profile in the same figure. The peak-normalized residual values are less than 0.8 % over the entire absorption feature, indicating that the Voigt profile adequately models the absorption line-shape.

The line-strength at a selected temperature can be inferred using Eq. (2) by calculating the integrated absorbance

shock conditions: 1450 K, 1.63 atm); (b) the reduced line-shape of the R(12) transition (solid line, top panel), its best-fit Voigt profile (dashed line, top panel), and the residual (bottom panel)

of the target line from the best-fit Voigt values. Figure 7 illustrates the measured line-strengths of four representative transitions at 1100–2000 K behind reflected shock waves. The calculated values using Eq. (5) with the line-strength $S(296\text{ K})$ and the lower-state energy E'' from the HITRAN database [5] are also plotted for comparison, illustrating excellent agreement ($1 - \sigma$ deviation between 1.4 % and 1.8 %) with our measurements.

Similarly, the collisional full-width at half maximum (FWHM) was inferred from the Voigt fit of the absorption profile as shown in Fig. 6(b). The collisional width is dominantly affected by the Ar-broadening as CO (0.5 %) and H_2 (1 %) are both significantly diluted in argon. Thus, at a given temperature, the Ar-broadening coefficient is inferred directly from the measured collisional width with self- and H_2 - broadening neglected. Figure 8 plots the measured Ar-broadening coefficients ($2\gamma_{\text{CO-Ar}}$) as a function of temperature for CO transitions $v'' = 0$, R(12) and R(13) and $v'' = 1$, R(21). A two-parameter best fit to the experimental data

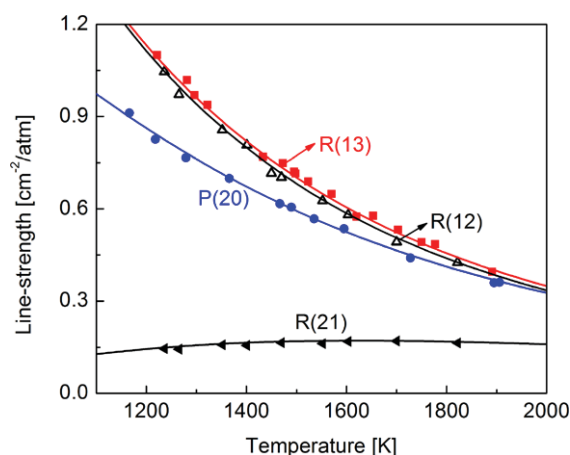


Fig. 7 Comparison of the measured line-strengths for the CO transitions at high temperatures with the HITRAN database [5]

following Eq. (4) gives $2\gamma_{\text{CO-Ar}}$ (296 K) and its temperature coefficient n , as illustrated in Fig. 8 and summarized in Table 2. Note that the errors quoted in the table for the experimental results correspond only to the standard deviations derived by linear least-squared fits of $\log(2\gamma_{\text{CO-Ar}})$ versus $\log(296/T)$. Experimental results of the line $v'' = 1$, R(22) at 2194.46 cm^{-1} are not included in Table 2, since this line was found to be blended with a neighboring transition $v'' = 2$, R(32) at 2194.44 cm^{-1} especially at higher temperatures, leading to larger uncertainties in the measurement.

In addition, the room-temperature (296 K) line-strengths and Ar-broadening coefficients of the ground state transitions ($v'' = 0$) can be directly determined by examining a frequency scan prior to the passage of the incident

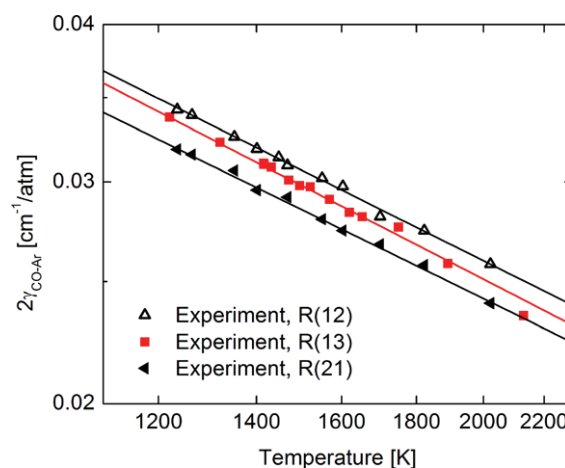


Fig. 8 Ar-broadening coefficient $2\gamma_{\text{CO-Ar}}$ measurements for the CO transitions: R(12), R(13) and R(21). The two-parameter best fit to the high-temperature data, extrapolated to 296 K, gives $2\gamma_{\text{CO-Ar}}$ (296 K) = $0.079 \pm 0.007\text{ cm}^{-1}/\text{atm}$ and $n = 0.581 \pm 0.012$ for transition R(12), $2\gamma_{\text{CO-Ar}}$ (296 K) = $0.079 \pm 0.009\text{ cm}^{-1}/\text{atm}$ and $n = 0.600 \pm 0.016$ for transition R(13), and $2\gamma_{\text{CO-Ar}}$ (296 K) = $0.072 \pm 0.007\text{ cm}^{-1}/\text{atm}$ and $n = 0.571 \pm 0.012$ for transition R(21), respectively

Table 2 Line-strength and broadening parameters for the CO transitions. Uncertainties of measurements are given in the parentheses; the extrapolation of $2\gamma_{\text{CO-Ar}}$ to 296 K following Eq. (4) is based on the experimental data over the temperature range of 1100–2000 K

Transition (v'', J'')	S @ 296 K ($\text{cm}^{-2}\text{ atm}^{-1}$)		$2\gamma_{\text{CO-Ar}}$ (296 K) ($\text{cm}^{-1}/\text{atm}$)				n
	HITRAN	Measured	Bouanich [28]	Varghese [29]	Measured@ 296 K	Fit to 1100–2000 K data	
0, R(12)	7.13 (2–3 %)	7.16 (2.3 %)	0.088	0.096	0.088 (3.0 %)	0.079 ± 0.007	0.581 ± 0.012
1, R(21)	4.32×10^{-5} (2–3 %)	–	–	–	–	0.072 ± 0.007	0.571 ± 0.012
0, R(13)	6.04 (2–3 %)	5.95 (2.3 %)	0.087	0.084	0.085 (2.9 %)	0.079 ± 0.009	0.600 ± 0.016
0, P(20)	0.876 (2–3 %)	0.872 (2.5 %)	0.079	0.083	0.079 (3.3 %)	0.083 ± 0.011	0.639 ± 0.024
1, P(14)	2.64×10^{-4} (2–3 %)	–	–	–	–	0.074 ± 0.018	0.560 ± 0.045

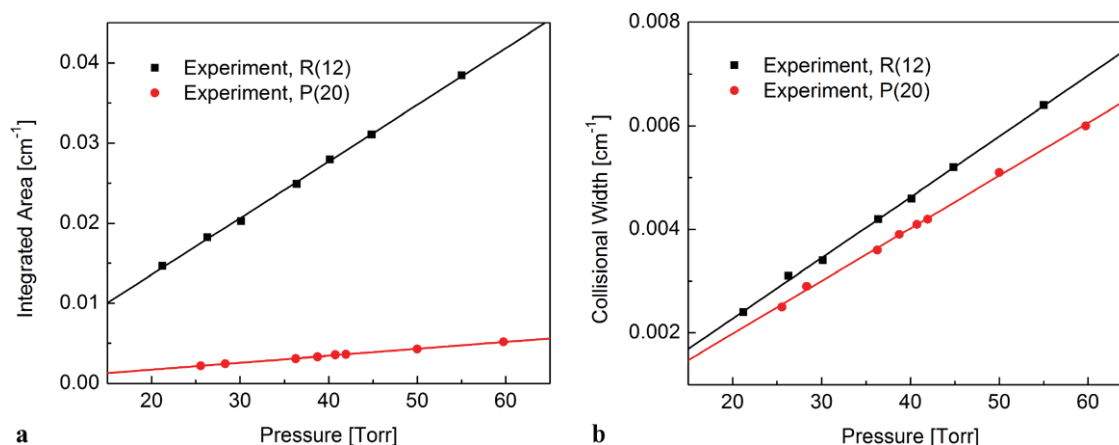


Fig. 9 Room-temperature (296 K) spectroscopic parameter measurements for (a) line-strength using the measured integrated absorbance versus P_1 (20–60 Torr), and (b) Ar-broadening coefficient using the measured collisional FWHM versus P_1

shock. Figure 9 illustrates the variation of the measured integrated absorbance and FWHM with pressure at 296 K for the representative transitions $v'' = 0$, R(12) and $v'' = 0$, P(20). Following Eq. (2) and Eq. (3), the line-strength and Ar-broadening coefficient at 296 K are inferred from the slope of the linear fit to the data as shown in Fig. 9(a) and (b), respectively. These experimental results are also summarized in Table 2. The measured line-strength at 296 K shows excellent agreement with the HITRAN database [5] (within 1.5 %), and the measured Ar-broadening coefficient is also in quite good agreement with the previous room-temperature studies by Bouanich and Haeusler [28], and Varghese and Hanson [29], respectively.

We also compared the $2\gamma_{\text{CO-Ar}}$ (296 K) obtained from the direct measurements at room temperature with the extrapolated values (assuming constant n) from the shock tube measurements over the 1100–2000 K range. It should be noted that a 3–10 % difference of $2\gamma_{\text{CO-Ar}}$ (296 K) can be found between these two methods. This may be explained by the fact that the temperature coefficient n in Eq. (4) itself is a weak function of temperature over the range from 296 K to 2000 K. Since the Ar-broadening coefficient as a function of temperature on a log-log plot is well-fit by a straight line as illustrated in Fig. 8, n can be treated as a constant over this specific temperature range of 1100–2000 K and utilized in the sensor development for shock tube and combustion applications.

5 Sensor validation in shock tube experiments

CO concentration and temperature sensors using both scanned-wavelength and fixed-wavelength direct absorption strategies are first validated in nonreactive shock-heated gases before being used in combustion kinetics applications.

The bandwidth of the fixed-wavelength CO sensor is typically 1 MHz (limited by the detector bandwidth), compared to 2.5 kHz for the scanned-wavelength scheme, which is limited by the scan rate of the laser injection current.

5.1 Scanned-wavelength temperature and CO sensor using a single QC laser

Single-laser sensing has the advantages of simplifying the sensor system and reducing cost. Transitions $v'' = 1$, R(21) and $v'' = 0$, R(12) with relatively large difference in E'' are close enough to be covered by a single scan of the QC laser. Temperature can be inferred by comparing the measured peak absorbance ratio with the simulation. The simulated peak absorbance ratio for this line pair is plotted in Fig. 10 as a function of temperature. Notice that the pressure effect is also investigated to show that the uncertainty due to pressure variation is negligible in the pressure range of 1–2 atm. At 1500 K, for example, the temperature uncertainty is ~ 6 K (0.4 %) with a pressure change from 1 to 2 atm.

The experimental setup for the single-laser sensor validation in a shock tube is the same as that shown in Fig. 5. The test gas mixture is known to be 0.49 % CO/ 2 % H_2 /Ar; similarly, hydrogen is added to accelerate vibrational relaxation. Figure 11 illustrates a representative laser absorption measurement of temperature behind the reflected shock at 1526 K and 1.57 atm (vibrationally relaxed). The laser intensity and wavelength were tuned across these two absorption profiles of interest at 2.5 kHz, as shown in the top panel of Fig. 11, along with the corresponding absorbance profile shown in the bottom panel. Assuming ideal shock conditions, the gas properties were reasonably regarded to be unchanged within each scan of 0.4 ms. During the test time of 2.5 ms, the sensor produced six data points of temperature as illustrated in the bottom panel of Fig. 11, which was in good agreement (1527–1529 K in the first 1 ms, less than

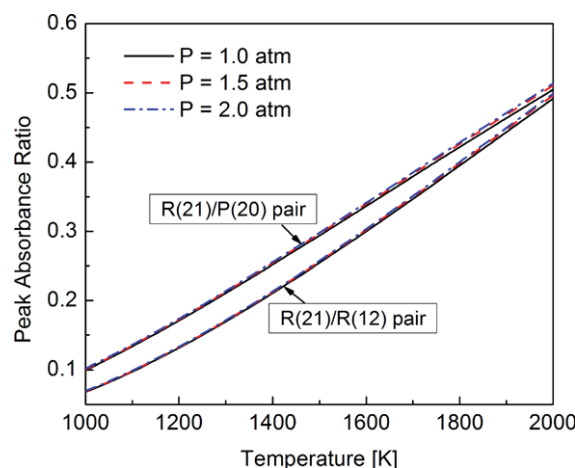


Fig. 10 Simulated peak absorbance ratio for the line pair R(21)/R(12) and R(21)/P(20) using the spectroscopic parameters listed in Table 2

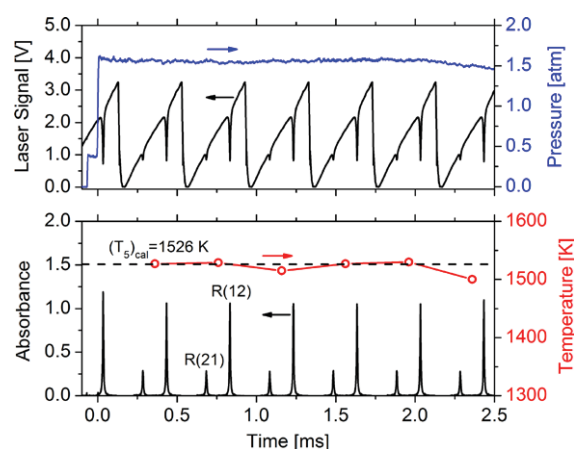


Fig. 11 Sample traces of laser transmission and pressure (top panel), as well as absorbance and temperature (bottom panel) measured in non-reactive test gases (0.49 % CO/ 2 % H₂/ Ar, vibrationally equilibrated reflected shock conditions: 1526 K, 1.57 atm). A single QCL was used to scan over the line pair R(21) and R(12) at 2.5 kHz

0.2 % difference) with the known value calculated using normal shock equations. Notice that the measured temperature drops significantly by ~ 30 K at 2.4 ms, possibly due to a weak interaction of the reflected shock wave with the contact surface (driven and driver gas).

With the temperature measured, the CO mole fraction is then inferred from either line of these two transitions. The CO mole fraction is measured to be $(0.491 \pm 0.003)\%$ using line R(12), again showing good agreement with the known CO concentration of 0.49 %. Moreover, at 2.4 ms when the nonideal shock condition happens, the CO mole fraction is still accurately measured to be 0.489 %.

Experiments were repeated under different shock conditions to measure gas temperature and CO concentration, and the results for a single scan are compared with the known values and plotted in Fig. 12 (solid squares). Good agreement can be seen between measurements and the known val-

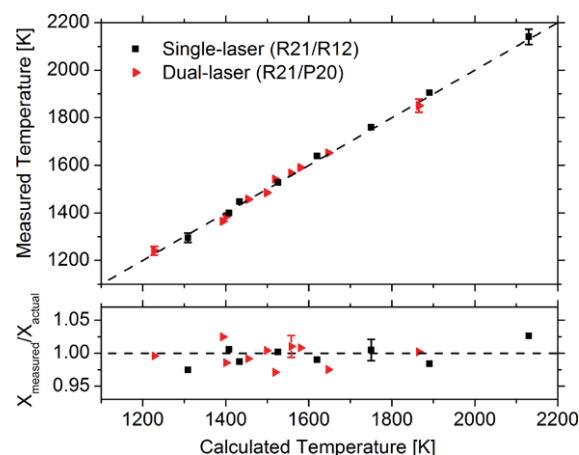


Fig. 12 Shock tube validation measurements for the single-laser scanned-wavelength (measured for a single scan behind the reflected shock, *solid squares*) and the dual-laser fixed-wavelength (averaged over the first 0.3–1 ms after the shock, *solid triangles*) direct absorption CO sensors (0.49 % CO/ 2 % H₂/ Ar, 1.3–1.7 atm)

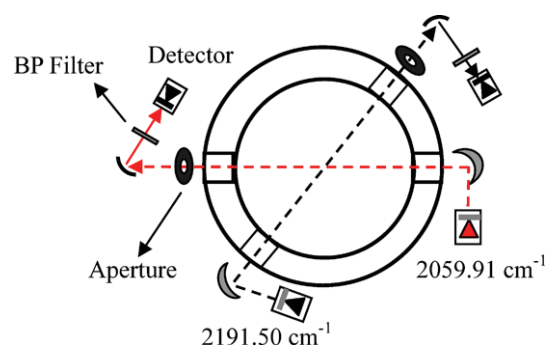


Fig. 13 Experimental setup for the fixed-wavelength two-line temperature and CO concentration measurements in a shock tube

ues for both the temperature ($1 - \sigma$ deviation 0.8 %) and CO concentration ($1 - \sigma$ deviation 1.6 %).

5.2 Fixed-wavelength temperature and CO sensor using two QC lasers

The sensor bandwidth of scanned-wavelength direct absorption is limited to several kHz, making it impossible to capture the rapid change of gas properties in chemical reactions. Here a fixed-wavelength CO concentration and temperature sensor with a bandwidth of ~ 1 MHz is developed for shock tube experiments using a dual-laser fixed-wavelength diagnostic strategy.

Figure 13 is a schematic of the experimental setup. The light from each laser is collimated and transmitted through a different pair of windows on the shock tube sidewall. The laser wavelengths are fixed at the line-centers of the two selected transitions $v'' = 1$, R(21) at 2191.50 cm^{-1} and $v'' = 0$, P(20) at 2059.91 cm^{-1} , respectively. This optical configuration utilizes the fact that the gas properties across the shock tube are uniform.

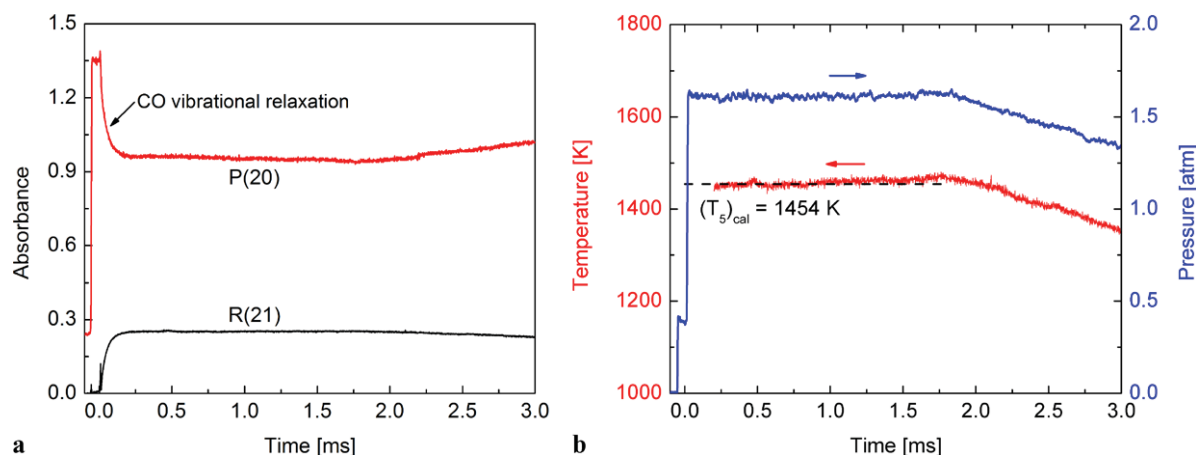


Fig. 14 Fixed-wavelength temperature measurements using two QC lasers with 0.49 % CO/2 % H₂/Ar: (a) measured absorbance traces for the two lasers; (b) measured temperature and pressure. Vibrationally equilibrated reflected shock conditions: $P_5 = 1454 \text{ K}$, $T_5 = 1.62 \text{ atm}$

Figure 14(a) demonstrates a sample time-history of the laser absorbance recorded behind a reflected shock at 1454 K and 1.62 atm with 0.49 % CO/2 % H₂/Ar mixture. The laser absorption reaches the plateau level as the CO is fully relaxed at $\sim 0.2 \text{ ms}$. Note that the sensor essentially measures the vibrational temperature, and hence the absorbance in the $v'' = 1$, R(21) line increases with time, after the shock, from zero to its plateau value. Conversely, the $v'' = 0$, P(20) absorbance decreases from its elevated initial value to its plateau value as vibrational relaxation takes place. Measured time-histories of pressure and temperature are plotted in Fig. 14(b). The average measured temperature over the time interval 0.2–1.5 ms is 1456 K with a standard deviation of 6 K (0.4 %), showing excellent agreement with the calculated value of 1454 K. Note that the sensor is capable of capturing the slight rise of temperature at later times from about 0.9–1.8, which results from the nonideal shock tube effects of boundary layer growth and incident-shock attenuation. CO mole fraction can be computed using the measured pressure, temperature, and transmission signal of either laser.

The experimental results are summarized and plotted in Fig. 12 (solid triangles). The measured and calculated temperatures are in good agreement (within 1.1 %) over the tested temperature range of 1200–1900 K, and the measured mole fraction agrees with the known values within 1.7 %. These results confirm the sensor accuracy for temperature and CO concentration measurements at combustion temperatures. It is noteworthy that this sensor has the potential to measure both translational/rotational temperatures and vibrational temperatures, when these temperatures differ, by employing line pairs with the same v'' value or with different v'' values, respectively.

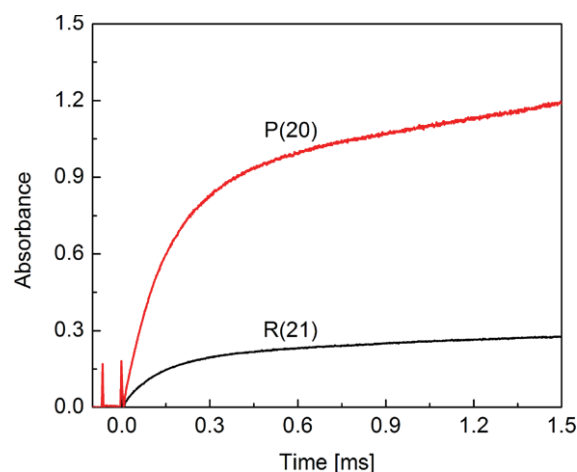


Fig. 15 Absorbance time-histories of R(21) and P(20) during the pyrolysis of methyl formate. Initial reflected shock conditions: $T_5 = 1364 \text{ K}$, $P_5 = 1.63 \text{ atm}$, 0.5 % MF/Ar

6 Temperature and CO concentration measurements in combustion gases

Shock tubes are used to study gas phase combustion reactions by measuring ignition delay times and by monitoring species time-histories over a wide range of temperatures and pressures [4]. Accurate, time-resolved measurements of combustion species in shock tube are therefore critical with laser absorption the most commonly employed method [4, 30]. Here, the fixed-wavelength CO sensor validated in Sect. 5.2 is demonstrated in a kinetic study of the high-temperature pyrolysis and oxidation of methyl formate (MF), a simple biodiesel surrogate.

The shock tube/laser diagnostic experimental setup is shown in Fig. 13. Typical absorbance time-histories for both lasers are plotted in Fig. 15 for a test mixture of 0.5 % MF/Ar shock-heated to 1364 K, 1.63 atm. The absorbance

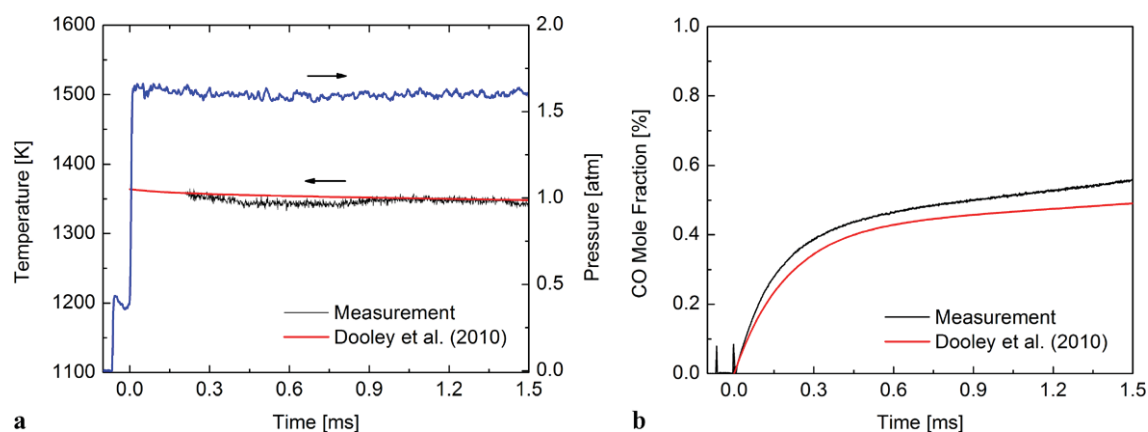


Fig. 16 Temperature and CO concentration measured during a shock with initial mixture of 0.5 % MF/Ar; simulations using the Dooley et al. [31] mechanism are shown for comparison. Initial reflected shock conditions: $T_5 = 1364$ K, $P_5 = 1.63$ atm

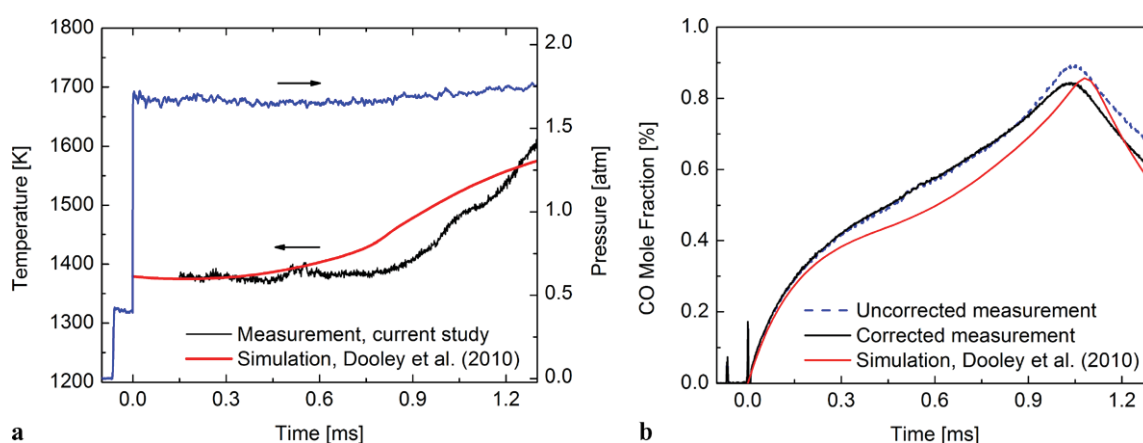


Fig. 17 Temperature and CO concentration measurements during MF oxidation for a mixture of 0.494 % MF, 0.988 % O_2 ($\phi = 1$) and Ar; simulations using the Dooley et al. [31] mechanism are shown for com-

parison. Initial temperature and pressure behind the reflected shock are $T_5 = 1379$ K, $P_5 = 1.67$ atm

profile for each laser directly represents the CO formation during the high-temperature pyrolysis of methyl formate. Temperature is inferred from the measured absorbance ratio, showing the slight decrease (15 K) that occurs during the decomposition of methyl formate. Our measurement is compared with the chemical kinetic simulation using the Dooley et al. [31] mechanism, performed in a commercial software package CHEMKIN-PRO [32], as illustrated in Fig. 16(a).

CO concentration time-history is then inferred from either absorption trace; here, the R(21) transition is used. Figure 16(b) compares the sensor measurement with the simulation using the Dooley et al. [31] mechanism. The model underpredicts the rate of CO formation by about 10 % during MF pyrolysis, revealing the need for minor modifications to the kinetic model.

Similar measurements were performed for high-temperature MF oxidation in the shock tube. The measured temperature and CO mole fraction are plotted in Fig. 17 for a shock with 0.494 % MF and 0.988 % O_2 ($\phi = 1$) in Ar as the ini-

tial mixture. The measured temperature time-history shown in Fig. 17(a) reveals that the gas temperature remains almost constant before the ignition happens at ~ 1 ms, and then rises significantly by 150 K at 1.2 ms. However, the simulation using the Dooley et al. [31] mechanism significantly overpredicts the temperature rise during the MF oxidation. Since the temperature rises significantly (~ 150 K after ignition) during the MF oxidation, it is critical to take into account these temperature and pressure changes in specifying the absorption coefficient when inferring the CO mole fraction. Figure 17(b) illustrates a comparison of the uncorrected CO concentration (assumes unchanged temperature and pressure) with the corrected values using the measured temperature and pressure data. A modest discrepancy (5.3 % difference) is seen after 1 ms when ignition starts in the reaction system. Our measurement is also compared with the model prediction using the Dooley et al. [31] mechanism. The simulation shows good agreement with our measurement at early times (< 0.2 ms) and accurately predicts the

peak value of CO (8420 ppm in experiment, compared to 8560 ppm in simulation) before starting to decline at 1 ms. Quantitative data sets such as these should greatly aid the validation of existing kinetic mechanisms and the development of more accurate chemical kinetic models.

7 Summary

QC-laser-based absorption measurements of temperature and CO concentration in high-temperature shock-heated gases were reported using the fundamental band of CO near $4.7\ \mu\text{m}$. The selected transitions, $v'' = 0$, R(12), R(13), P(20) and $v'' = 1$, R(21), R(22), P(14) were successfully accessed by two different QC lasers. The spectroscopic parameters including line-strengths and broadening coefficients $2\gamma_{\text{CO-Ar}}$ were determined at room-temperature (296 K) and high temperatures (1100–2000 K) and compared with literature values. A scanned-wavelength direct absorption CO sensor using a single QC laser was first validated for accurate measurements of temperature and CO concentration in a shock tube. The sensor measured temperature at a scan rate of 2.5 kHz by comparing the measured peak absorbance ratio of the line pair R(21) and R(12) with spectral simulations, showing very good agreement (within 0.8 %) with the calculated temperatures at 1300–2200 K. A fixed-wavelength CO temperature sensor based on transitions R(21) and P(20), accessed by two different lasers centered at $2194.46\ \text{cm}^{-1}$ and $2059.91\ \text{cm}^{-1}$, was then developed to provide in situ detection with faster time response. Sensor validation was first demonstrated in a shock tube by measuring temperatures (1200–1900 K) and CO concentrations of CO/H₂/Ar mixtures with 1 MHz bandwidth. The sensor was then applied to the shock tube study of the pyrolysis and oxidation of methyl formate by measuring CO concentration and temperature time-histories to illustrate its capability in chemical kinetic studies. The increased absorption strength in this wavelength region provides opportunities for more sensitive and accurate combustion measurements with shorter optical path length and lower CO concentration than was possible using overtone band absorption. Future shock tube experiments are planned to apply this CO sensor, combined with other species-specific laser diagnostics, to chemical kinetic studies of oxygenates such as esters, ketones, and alcohols.

Acknowledgements This work was supported by the Combustion Energy Frontier Research Center funded by the US Department of Energy, Office of Science, Office of Basic Energy Sciences under Award Number DE-SC0001198, the Army Research Office (ARO) with Dr. Ralph Anthenien as contract monitor, and the Air Force Office of Scientific Research (AFOSR) with Dr. Julian Tishkoff as technical monitor. The authors thank Dr. Jay Jeffries for his help on the selection and specification of the lasers and acquisition of the needed support electronics.

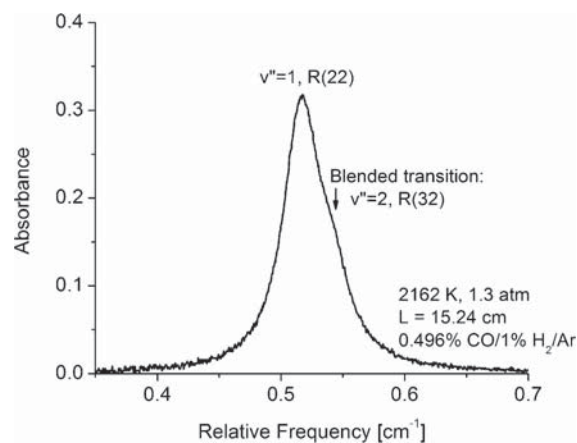


Fig. 18 Absorption data of $v'' = 1$, R(22) taken at 2.5 kHz with 0.496 % CO/1 % H₂/Ar. Vibrationally equilibrated reflected shock conditions: 2162 K, 1.3 atm. A blended transition ($v'' = 2$, R(32), $0.024\ \text{cm}^{-1}$ away) is observed

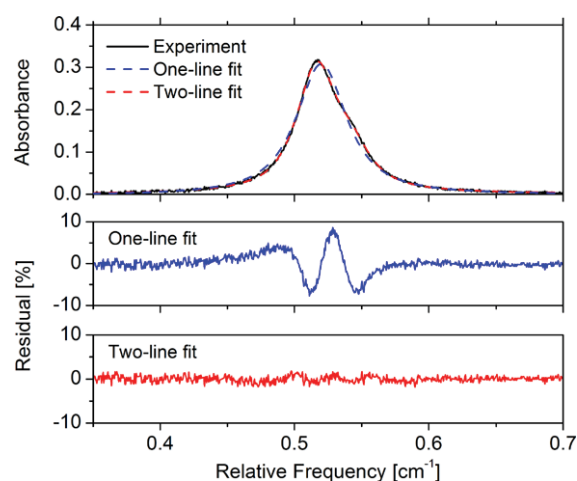


Fig. 19 One-line and two-line best-fit Voigt profiles for the absorption data in Fig. 18. The residual of the fits are shown in the lower panels

Appendix

High-resolution absorption spectroscopy of the CO transition $v'' = 1$, R(22) at $2194.46\ \text{cm}^{-1}$ has been recorded in high temperature shock tube experiments (0.496 % CO/1 % H₂/Ar, hydrogen is added to accelerate CO vibrational relaxation). A representative line-shape for the R(22) transition at 2162 K, 1.3 atm is illustrated in Fig. 18. It is found that R(22) is blended with a weak, nearby transition $v'' = 2$, R(32) centered at $2194.44\ \text{cm}^{-1}$. Our observation is also proved by fitting the absorption data using the Voigt profile as shown in Fig. 19. The one-line Voigt fit gives a peak-normalized residual of 10 %, compared to 1.8 % using the two-line Voigt fit. This unknown transition is probably coming from an isotope of CO in the mixture.

References

1. M.G. Allen, *Meas. Sci. Technol.* **9**, 545 (1998)
2. H. Teichert, T. Fernholz, V. Ebert, *Appl. Opt.* **42**, 2043 (2003)
3. K. Kohse-Höinghaus, R.S. Barlow, M. Aldén, J. Wolfrum, *Proc. Combust. Inst.* **30**, 89 (2005)
4. R.K. Hanson, *Proc. Combust. Inst.* **33**, 1 (2011)
5. HITRAN, <http://www.cfa.harvard.edu/hitrان/>
6. D.T. Cassidy, L.J. Bonnell, *Appl. Opt.* **27**, 2688 (1988)
7. R.M. Mihalcea, D.S. Baer, R.K. Hanson, *Meas. Sci. Technol.* **9**, 327 (1998)
8. B.L. Upschulte, D.M. Sonnenfroh, M.G. Allen, *Appl. Opt.* **38**, 1506 (1999)
9. M.E. Webber, J. Wang, S.T. Sanders, D.S. Baer, R.K. Hanson, *Proc. Combust. Inst.* **28**, 407 (2000)
10. J. Wang, M. Maiorov, D.S. Baer, D.Z. Garbuzov, J.C. Connolly, R.K. Hanson, *Appl. Opt.* **39**, 5579 (2000)
11. V. Ebert, H. Teichert, P. Strauch, T. Kolb, H. Seifert, J. Wolfrum, *Proc. Combust. Inst.* **30**, 1611 (2005)
12. X. Chao, J.B. Jeffries, R.K. Hanson, *Meas. Sci. Technol.* **20**, 115201 (2009)
13. R.K. Hanson, P.A. Kuntz, C.H. Kruger, *Appl. Opt.* **16**, 2045 (1977)
14. R.K. Hanson, P.K. Falcone, *Appl. Opt.* **17**, 2477 (1978)
15. M. Schoenung, R.K. Hanson, *Combust. Sci. Technol.* **24**, 227 (1981)
16. J.H. Miller, S. Elreedy, B. Ahvazi, F. Woldu, P. Hassanzadeh, *Appl. Opt.* **32**, 6082 (1993)
17. R. Barron-Jimenez, J.A. Caton, T.N. Anderson, R.P. Lucht, T. Walther, S. Roy, M.S. Brown, J.R. Gord, *Appl. Phys. B* **85**, 185 (2006)
18. A.A. Kosterev, F.K. Tittel, R. Köhler, C. Gmachl, F. Capasso, D.L. Sivco, A.Y. Cho, S. Wehe, M.G. Allen, *Appl. Opt.* **41**, 1169 (2002)
19. J. Vanderover, M.A. Oehlschlaeger, *Appl. Phys. B* **99**, 353 (2010)
20. F. Capasso, R. Paiella, R. Martini, R. Colombelli, C. Gmachl, T.L. Myers, M.S. Taubman, R.M. Williams, C.G. Bethea, K. Unterrainer, H.Y. Hwang, D.L. Sivco, A.Y. Cho, A.M. Sergent, H.C. Liu, E.A. Whittaker, *IEEE J. Quantum Elect.* **38**, 511 (2002)
21. A. Kosterev, G. Wysocki, Y. Bakhirkin, S. So, R. Lewicki, M. Fraser, F. Tittel, R.F. Curl, *Appl. Phys. B* **90**, 165 (2008)
22. R.F. Curl, F. Capasso, C. Gmachl, A.A. Kosterev, B. McManus, R. Lewicki, M. Pusharsky, G. Wysocki, F.K. Tittel, *Chem. Phys. Lett.* **487**, 1 (2010)
23. V. Nagali, S.I. Chou, D.S. Baer, R.K. Hanson, J. Segall, *Appl. Opt.* **35**, 4026 (1996)
24. G. Birnbaum, in *Adv. Chem. Phys.*, ed. by J.O. Hirschfelder. Intermolecular forces, vol. 12 (Interscience, New York, 1967)
25. X. Zhou, J.B. Jeffries, R.K. Hanson, *Appl. Phys. B* **81**, 711 (2005)
26. W. Ren, D.F. Davidson, R.K. Hanson, *Int. J. Chem. Kinet.* doi:10.1002/kin.20599 (2012)
27. R.C. Millikan, D.R. White, *J. Chem. Phys.* **39**, 3209 (1963)
28. J.-P. Bouanich, C. Haeusler, *J. Quant. Spectrosc. Radiat. Transfer* **12**, 695 (1972)
29. P.L. Varghese, R.K. Hanson, *J. Quant. Spectrosc. Radiat. Transfer* **24**, 479 (1980)
30. D.F. Davidson, Z. Hong, G.L. Pilla, A. Farooq, R.D. Cook, R.K. Hanson, *Proc. Combust. Inst.* **33**, 151 (2011)
31. S. Dooley, M.P. Burke, M. Chaos, Y. Stein, F.L. Dryer, V.P. Zhukov, O. Finch, J.M. Simmie, H.J. Curran, *Int. J. Chem. Kinet.* **42**, 527 (2010)
32. R.J. Kee, F.M. Ruply, J.A. Miller, *Chemkin Collection* (Reaction Design, Inc., San Diego, 2010)



Constrained reaction volume approach for studying chemical kinetics behind reflected shock waves



Ronald K. Hanson, Genny A. Pang, Sreyashi Chakraborty, Wei Ren, Shengkai Wang, David Frank Davidson*

High Temperature Gasdynamics Laboratory, Mechanical Engineering Department, Stanford University, Stanford, CA, USA

ARTICLE INFO

Article history:

Received 29 January 2013

Received in revised form 22 March 2013

Accepted 23 March 2013

Available online 27 April 2013

Keywords:

Constrained reaction volume

Shock tube

Gasdynamic models

Hydrogen/oxygen

Ethylene/oxygen

ABSTRACT

We report a constrained-reaction-volume strategy for conducting kinetics experiments behind reflected shock waves, achieved in the present work by staged filling in a shock tube. Using hydrogen–oxygen ignition experiments as an example, we demonstrate that this strategy eliminates the possibility of non-localized (remote) ignition in shock tubes. Furthermore, we show that this same strategy can also effectively eliminate or minimize pressure changes due to combustion heat release, thereby enabling quantitative modeling of the kinetics throughout the combustion event using a simple assumption of specified pressure and enthalpy. We measure temperature and OH radical time-histories during ethylene–oxygen combustion behind reflected shock waves in a constrained reaction volume and verify that the results can be accurately modeled using a detailed mechanism and a specified pressure and enthalpy constraint.

© 2013 The Combustion Institute. Published by Elsevier Inc. All rights reserved.

1. Introduction

Ignition delay time experiments behind reflected shock waves in a shock tube provide a valuable type of data for validating and refining detailed kinetic mechanisms for combustion. A significant advantage of these experiments at short reaction times (i.e. high temperatures) is that the reactive mixture adjacent to the endwall can be adequately modeled neglecting heat loss and assuming constant volume (V) and internal energy (U) up to the time of ignition. However, at long test times (greater than 1–2 ms, typically required to measure ignition delay times at temperatures less than ~ 1000 K), several complications can occur in reflected-shock ignition studies. In previous studies [1,2], we found that at long test times, the reaction zone deviates from constant U , V behavior due to non-ideal facility effects including incident shock attenuation and boundary layer growth, which lead to discrepancies between measured ignition delay times and values predicted using the common constant U , V assumption. Such discrepancies can be addressed using improved gasdynamic modeling in the ignition delay time simulations [1] or by experimentally removing the induced pressure-change effects [2]. Another issue we have discovered in experiments with long ignition delay times is the occurrence of a remote ignition phenomenon where the initial ignition event first occurs away from the shock tube endwall,

resulting in pressure waves that can modify the reaction progress in the observation region (typically located immediately adjacent to the endwall.) This phenomenon complicates and leads to uncertainties in simulating the measured ignition delay time. In addition to the issues mentioned above regarding non-constant-volume behavior in ignition delay time studies, pressure change due to chemistry in the reaction volume, for either exothermic or endothermic reactions, also causes the reflected shock environment to deviate from constant-volume behavior in studies at any temperature. This effect too begs the question as to how to accurately model reactive reflected-shock experiments.

The motivation for our current work is twofold: we desire to remove remote ignition as a complicating factor in reflected-shock ignition studies, and we seek to demonstrate a strategy for conducting reflected shock experiments at near-constant pressure, so that quantitative modeling throughout the combustion event can be done using a simple constant-pressure constraint. In this paper, we present a staged-filling strategy to constrain the reaction volume so that nearly constant pressure behavior is achieved. We first present non-reactive studies using this staged-filling strategy to quantify the test-gas concentration near the endwall of the shock tube. We then present measured hydrogen–oxygen ignition delay times in constrained-reaction-volume (CRV) experiments to show that this strategy is successful at eliminating the occurrence of remote ignition in shock tube experiments. We also show that this same staged-filling strategy effectively mitigates ignition-induced pressure changes in the reaction environment. This result establishes the possibility of accurately modeling the shock tube

* Corresponding author.

E-mail address: dfd@stanford.edu (D.F. Davidson).

ignition experiments based on a simple thermodynamic–gasdynamic model of constant pressure (P) and enthalpy (H), or specified P and H in the case that modest pressure changes are present, e.g. due to non-ideal facility effects or chemistry-induced pressure change. Finally, we present the results of ethylene–oxygen combustion studies in CRV experiments and verify that these data can be accurately modeled using a constant (or specified) P and H constraint.

2. Experimental apparatus and method

2.1. Shock tube facility

An ultra-high-purity kinetics shock tube at Stanford was used for all the current experiments. This stainless-steel shock tube has an 8.54-m-long driven section and a 3.35-m-long driver section; both have an inner diameter of 14.13 cm and are separated by a polycarbonate diaphragm of thickness 0.25 or 0.50 mm, depending on the desired experimental pressure. Five axially-spaced PCB pressure transducers (113A26 transducer, 483B08 amplifier), at locations 2 cm, 38.8 cm, 69.3 cm, 99.7 cm and 130.2 cm away from the endwall of the driven section, were used to measure pressure during the ignition experiments. A thin layer of RTV was placed on all pressure transducers to eliminate thermal shock effects and provide more accurate pressure measurements. These pressure transducers were connected to four Philips counter timers (model PM6666) to determine the incident shock velocity at the end wall, from which the initial temperature and pressure behind the reflected shock wave were calculated to an accuracy of better than $\pm 1\%$ using 1-D shock relations assuming vibrational equilibrium behind both the incident and reflected shock waves. Additional details of this experimental facility have been described by Oehlschlaeger et al. [3]. Tailored driver gas mixtures of 20–40% nitrogen in helium were used as the driver gas to achieve reflected shock test times of greater than 6 ms. The composition of the driver gas was varied for each experiment based on the reflected-shock temperature, where the relationship was determined based on the work of Hong et al. [4].

2.2. Diagnostics

In addition to pressure, OH emission was measured 2 cm from the driven-section endwall using an in-house-modified UV-enhanced Thorlabs PDA55 photodiode detector. A vertical slit and lens optical setup was used to constrain the spatial (and temporal) resolution of the emission measurement, and a Schott Glass UG5 filter was used to ensure collection only of emission near 306 nm. For the ethylene–oxygen combustion experiments, measurements of ethylene mole fraction, OH mole fraction, and temperature were all conducted at the same (2 cm) location. These time-resolved ethylene measurements allowed quantitative monitoring of fuel concentration throughout passage of the incident and reflected shock waves, leading to well-known post-reflected shock reaction mixtures. Ethylene mole fraction measurements were also conducted at additional axial locations as part of the effort to characterize mixing of the reactive and non-reactive gases at their interface. All measured signals were sampled at a rate of 1 MHz via an National Instruments LabVIEW data acquisition system.

The *in situ* species mole fraction measurements were achieved using fixed-wavelength, continuous wave (cw) narrow-linewidth laser absorption diagnostics and applying the Beer–Lambert relationship. Ethylene mole fraction was measured via CO_2 laser absorption at $10.532\ \mu\text{m}$ using a grating-tuned CO_2 gas laser (model Lasy-4G, Access Laser Co., Everett, WA). Thermoelectric-cooled IR photovoltaic detectors (PVM-2TE-10.6, Vigo Systems) with large

linear dynamic range were used for measurements of transmitted laser intensities. The ethylene absorption cross-sections from Ren et al. [5] was used. OH mole fraction was measured using a ring-dye laser (Spectra-Physics model 380) tuned to the center of the $R_1(5)$ line of the $\text{OH } A^2\Sigma^+ - X^2\Pi$ (0,0) band at $306.6871\ \text{nm}$ ($32606.52\ \text{cm}^{-1}$). The absorption coefficient of OH was taken from Herbon et al. [6]. This reference also provides additional details of the OH mole fraction measurement system used for the current work.

Trace amounts of CO_2 were seeded into the test mixtures for the experiments where temperature measurements were desired, and the two-line CO_2 laser absorption temperature measurement technique of Farooq et al. [7] was applied. Temperature measurement was achieved using two DFB lasers, each of power 2 mW, where their wavelengths were varied using commercial controllers (ILX Lightwave LDT-5910B and LDX-3620) that adjust the temperature and injection current inputs. The DFB lasers were tuned such that each one was centered on one of the $R(28)$ and $P(70)$ CO_2 transitions probed, with line center wavelengths of $2752.48\ \text{nm}$ ($3633.08\ \text{cm}^{-1}$) and $2743.06\ \text{nm}$ ($3645.56\ \text{cm}^{-1}$), respectively. A free-space mid-IR wavelength meter (Bristol 621) was used to confirm the correct wavelength of the DFB lasers. Liquid-nitrogen-cooled InSb detectors (IR Associates IS-2.0, 1 MHz bandwidth) were used to record the transmitted laser intensities, and the temperature was determined from the relative absorption of the two measured CO_2 transitions [7].

2.3. Test mixtures

A stoichiometric mixture of 4% H_2 , 2% O_2 , balance Ar, prepared by Praxair (from ultra-high-purity gases, and with an accuracy of 2% for each component), was used for the hydrogen–oxygen ignition studies. For the ethylene–oxygen ignition studies, test mixtures of 0.5% C_2H_4 , 5% O_2 , 2% CO_2 , balance Ar were prepared manometrically using an in-house mixing facility containing a mixing manifold and a 12-l stainless steel mixing tank with an internal magnetically driven stirrer. These test gas components were high-purity gases obtained from Praxair.

2.4. Experimental procedure for staged-filling strategy

Before we present the procedure for achieving a constrained reaction volume, the conventional operation procedure for ignition experiments behind reflected shock waves in this facility will be summarized. In a typical ignition experiment, the driven section of the shock tube is filled with the test gas mixture until a desired pressure P_1 is achieved. The driver section is filled with the driver gas until the diaphragm spontaneously ruptures through contact with a cross-shaped cutting blade located on the driven-section side of the diaphragm. We refer to the pressure behind the incident shock wave, formed due to the diaphragm rupture, as P_2 , and the pressure near the endwall following shock reflection as P_5 . In this conventional operation, the reaction volume (compressed volume of the combustible test gas) extends a length typically 1–3 m from the driven section endwall if completely compressed by the reflected shock wave.

The goal of the staged-filling strategy is to minimize the extent of the reaction volume. Because measurements are taken at a location 2 cm from the driven section endwall, a reaction volume that extends beyond 2 cm from the driven section endwall is desired, but not excessively further. The procedure for achieving this constrained reaction volume using a staged-filling strategy is as follows. First, the driven section is filled with the reactive test gas mixture (dilute in argon) to a pressure P_1^a . Immediately after this, argon is slowly introduced into the driven section at an axial location 40 cm from the diaphragm until the driven section reaches a total pressure of P_1 . This two-step process compresses

the test gas to a reduced reaction volume at the driven-section endwall with a nominal length

$$L_1 = (8.54 \text{ m} - 0.40 \text{ m})(P_1^a)/(P_1)$$

that extends from the driven section endwall, assuming no mixing at the interface of the argon and the test gas. We experimented with several different flow rates for the argon filling and determined an optimum fill time, for our apparatus, of 5–6 min that minimized mixing at the interface of the argon and the test gas. The shock tube is fired quickly after filling with argon to minimize further growth of this mixing zone. After compression by the reflected shock, the heated reaction volume will extend a length of

$$L_5 = (L_1)(T_5 P_1)/(P_5 T_1)$$

from the driven-section endwall, again assuming no mixing at the interface between the non-reactive and reactive gases. The temperatures T_1 and T_5 correspond to the regions of P_1 and P_5 , respectively. Figure 1 illustrates the different length scales in this staged-filling technique. For reflected shock wave experiments near 980 K and 3.5 atm for the current $\text{H}_2/\text{O}_2/\text{Ar}$ mixtures, the ratio of L_5/L_1 is approximately 4.5. P_1 values for these experiments are near 180 torr.

3. Non-reactive experiments to characterize the staged-filling strategy

3.1. Non-reactive pressure and temperature traces

A facility-induced gradual pressure rise (termed dP_5/dt in recent literature) typically occurs during reflected-shock experiments due to incident shock boundary layers and attenuation, and this should

be characterized and accounted for in any low-temperature ignition time experiments with test times greater than approximately 2 ms [1], or removed through use of driver inserts [8]. Through reflected-shock experiments of non-reactive mixtures using the current experimental setup and driver gas selection, we found that a nearly steady, facility-induced dP_5/dt of approximately 1.7%/ms was present in our unmodified shock tube. (More precisely, we typically observed an initial period of about 0.5 ms of near-constant pressure, followed by a gradual rise, but we can approximate the overall behavior with a single dP_5/dt value.) Nearly identical pressure changes were observed at all axial locations where pressure was measured. Because this gradual pressure rise can lead to significant changes in pressure over a time span of several milliseconds, the gasdynamic effect of a finite dP_5/dt was accounted for in all kinetic modeling presented in this paper. This was achieved by applying the specified-pressure (P) and enthalpy (H) constraint in the CHEMKIN-Pro suite of programs by Reaction Design.

A corresponding temperature rise of dT_5/dt also arises due to the facility-induced dP_5/dt . (For argon, with $\gamma = 5/3$, the fractional change in T_5 is approximately 40% of the fractional change in P_5 , assuming an isentropic process.) This temperature rise in shock tube experiments has been confirmed by Farooq et al. [9], where measurements of the CO_2 absorbance ratio at two wavelengths were used to accurately determine gas temperature changes in the presence of gradual pressure rises behind reflected shock waves.

3.2. Mixing characterization in the constrained reaction volume

The expressions for L_1 and L_5 presented above apply for an ideal system with no dilution of the test gas (i.e. no mixing at the

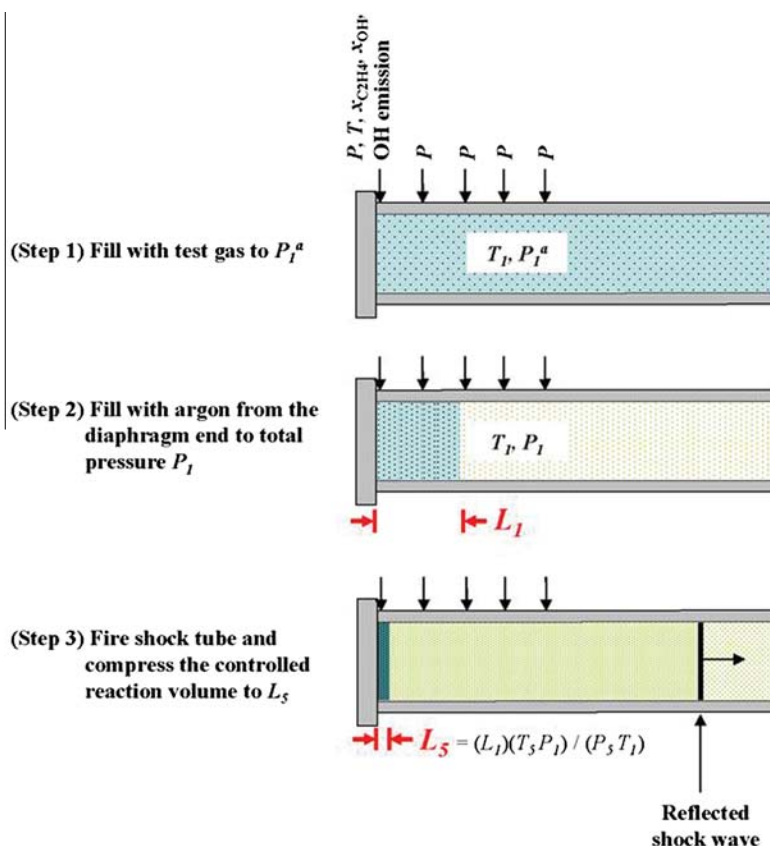


Fig. 1. Schematic of the test-gas volumes during each step in the staged-filling strategy. Shown is the ideal test-gas volume with L_5 such that the constrained reaction volume extends just past the measurement location. The locations of the sidewall pressure sensors P are also indicated.

interface of the non-reactive and reactive gases). However, in an actual experiment, there will be some amount of dilution of the test gas due to diffusion and turbulent mixing from the introduction of argon. Factors influencing the amount of dilution include the flow rate of argon fill, the specific design of the filling system, and the time between the completion of filling and firing of the shock, among other possibilities. To characterize the mixing and possible dilution of the test mixture in the constrained reaction volume, we conducted extensive tests with variable filling rates for the second filling stage. We used laser absorption at $10.532\ \mu\text{m}$ at multiple axial locations to measure ethylene mole fraction in non-reactive experiments with a mixture containing 0.5% C_2H_4 , with an uncertainty of $\pm 5\%$. These experiments confirmed the nominal value of L_1 expected as a function of P_1^a/P_1 and led to the experimentally-determined optimal flow rate (minimizing the test gas dilution) for the argon-filling step equivalent to a total shock tube filling time of 5–6 min. Even with this optimal flow rate, a small amount of test gas dilution is inevitable using the staged-filling procedure if a very small constrained reaction volume is desired. While the dilution is non-ideal, as long as the amount of dilution is known for a specific value of L_5 behind the reflected shock wave, kinetics experiments can be simulated correctly (i.e., with the actual reactant mixtures in the stagnant observation volume through direct measurements of fuel concentration). In this section, we present the results of experiments that characterize the amount of dilution for a constrained reaction volume with length $L_5 = 6\ \text{cm}$.

We used the same $10.532\ \mu\text{m}$ laser absorption technique to characterize the dilution of the test gas at the 2 cm measurement location. Figure 2 presents the measured ethylene mole fraction (time averaged over a few milliseconds): (a) at room temperature (Region 1) and (b) behind the reflected shock wave (Region 5). Also shown is the comparison with the results from an experiment employing conventional shock tube filling. The temperature- and pressure-dependent ethylene absorption cross-sections from Ren et al. [5] were used to determine the ethylene mole fraction from the measured fractional transmission at $10.532\ \mu\text{m}$ in each gas region (i.e., L_1 , L_2 and L_5). From Fig. 2, we can see that the measured ethylene mole fraction in the shock tube when conventional filling is employed is in excellent agreement with the manometrically-prepared predicted value. However, we can also conclude that the staged-filling strategy used to achieve a constrained reaction volume with length $L_5 = 6\ \text{cm}$ leads to a dilution loss of 20% in ethylene in Region 1 and a 24% loss in ethylene in Region 5. Further study is needed to determine whether these losses might be

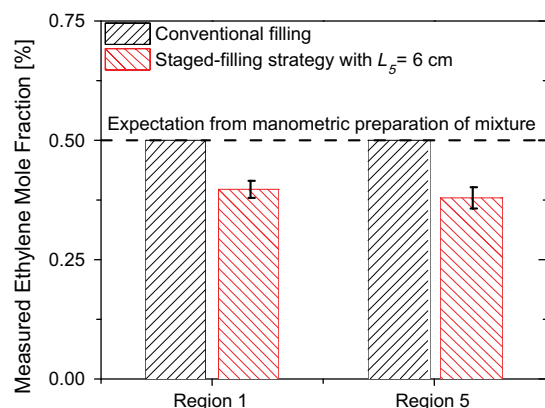


Fig. 2. Measurements of ethylene mole fraction in a 0.5% $\text{C}_2\text{H}_4/\text{Ar}$ mixture at $x = 2\ \text{cm}$ for room temperature (Region 1) and behind the reflected shock wave (Region 5) in a conventional filling experiment and a staged-filling experiment with a constrained reaction volume of nominally $L_5 = 6\ \text{cm}$ in extent. Variations in the staged-fill strategy measurements shown as $\pm 5\%$.

reduced through design modifications of the filling system and its operation. However, repetition of these measurements for several experiments performed using the same argon filling rate for the staged-filling strategy and the same constrained reaction volume with length $L_5 = 6\ \text{cm}$ confirmed a consistent loss in fuel concentration, and therefore we will assume in the remainder of this paper that every ignition experiment with a constrained reaction volume with $L_5 = 6\ \text{cm}$ has a concentration loss of 24% (of all non-argon components) relative to the manometrically-prepared value. Similar measurements were made with other small values of L_5 , e.g. $L_5 = 4\ \text{cm}$, to characterize dilution and ensure that the proper reactive mixture was specified in reactive gas simulations.

Using a similar experimental procedure, we determined that for no dilution to occur (i.e. when the fuel composition in the constrained reaction volume is measured to be identical to the manometrically-prepared fuel composition) a constrained reaction volume greater than or equal to $L_5 \approx 15\ \text{cm}$ was sufficient, for the representative experimental conditions of this work. This larger value of L_5 implies a relatively broad mixing layer at the interface between the argon and the test gas as a result of the staged filling. Alternative techniques for achieving the constrained reaction volume that could minimize the length of this mixing layer are thus of interest. One of our current efforts in this direction is to incorporate a sliding valve near the driven section endwall to separate the test gas mixture and the argon used for filling the remainder of the driven section. We should note that valves have been used previously for mixture isolation in single-pulse shock tubes, though to our knowledge these have been in smaller diameter tubes (enabling the use of commercial ball valves) and with much larger values of L_5 ; see for example Rajukumar et al. [10]. (We learned in the preparation of this paper of related earlier work by Brown and Thomas [11] that used a buffer gas section separated from the test gas mixture by a slide valve in a small diameter shock tube to stabilize the incident shock and to reduce spurious ignition).

4. Hydrogen–oxygen ignition in a constrained reaction volume

4.1. Defining remote ignition

In this section, we present the results of ignition studies of a stoichiometric 4% H_2 , 2% O_2 , balance Ar reactive mixture at a nominal pressure $P_5 = 3.5\ \text{atm}$. We will first present evidence of the remote (i.e., outside the reaction volume near the endwall) ignition phenomenon that occurs during low-temperature shock tube ignition of this hydrogen–oxygen mixture when conventional operation of the shock tube is employed. Figure 3 presents the measured pressure time-histories at each of the five axial locations where pressure transducers are located on the shock tube. This is for an experiment with initial post-shock conditions (at the endwall) of $T_5 = 979\ \text{K}$, and $P_5 = 3.44\ \text{atm}$, with $dP_5/dt = 1.7\%/ms$. The time zero is defined such that it represents the time of the passing of the reflected shock wave at the 2 cm pressure transducer (measurement location A as indicated in Fig. 3). The first steep rise in pressure in each trace in Fig. 3 is caused by the passing of the reflected shock wave, and the second steep rise in pressure in each trace indicates the onset of ignition. From Fig. 3, it is obvious that the ignition event occurs first at the 38.8 cm axial location and before ignition is observed at the 2 cm axial location. This is the phenomenon that we refer to as “remote” or non-localized ignition. We have found in our shock tube facility that the remote ignition phenomenon occurs and is repeatable for hydrogen–oxygen mixtures at temperatures low enough that ignition delay times are longer than about 2 ms. This phenomenon does not occur at (higher) temperatures having short ignition delay times. For the current $\text{H}_2/\text{O}_2/\text{Ar}$ mixture (and pressure P_5), the temperature at which

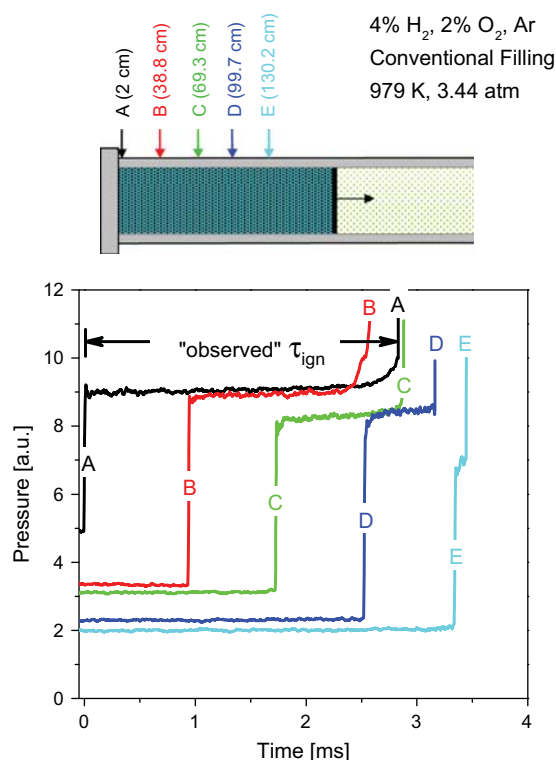


Fig. 3. Pressure traces at five measurement locations for a stoichiometric hydrogen–oxygen mixture with conventional shock tube operation. The pressure traces are staggered vertically for differentiability. The first rise in pressure indicates the passing of the reflected shock wave at each measurement location and the second rise in pressure is the ignition at each measurement location. The “observed” experimental ignition delay time at the measurement location A is also indicated. Note that non-localized ignition originates at measurement location B.

remote ignition begins to occur is near 990 K, where the ignition delay time is approximately 3 ms. The location of remote ignition is found to vary with T_5 and has been observed at locations up to 1 m from the end wall.

4.2. Eliminating remote ignition

The remote ignition phenomenon leads to potential complications in accurately determining (and simulating) the ignition delay time, which is traditionally defined as the time interval between the heating of the combustible mixture and the spontaneous onset of

ignition in a homogeneous (uniform) volume at constant conditions (e.g., U and V). For most experimental conditions, the ignition event originates at the driven section endwall (the location where the test gases are first heated to T_5). Therefore, measurement of the ignition delay time at the endwall or a nearby measurement location (e.g. 1 or 2 cm from the driven section endwall) is typically sufficient. In the case of remote ignition, however, the ignition delay time at the primary measurement location may be modified and differ from that associated with a homogeneous volume of gas at P_5 and T_5 . The exact mechanism leading to the remote ignition phenomenon is generally unknown and varies with reactive mixtures and conditions, and certainly varies between shock tube facilities. Several possible explanations of remote ignition include increased post-reflected-shock temperatures away from the driven section endwall due to incident shock attenuation, deflagration-to-detonation transitions, and the formation of hot spots along the shock tube walls due to shock wave-boundary layer interactions. We defer the detailed study of the cause of the remote ignition phenomenon for another paper. Here, we note only the existence of this phenomenon and that it is repeatable in our facility, and we present a method for eliminating its existence such that ignition delay time experiments can be interpreted without complication.

To eliminate the occurrence of remote ignition, we apply the staged-filling strategy to achieve a constrained reaction volume such that there is no reactive mixture to ignite remotely (away from the endwall region). In Fig. 4, we show measured pressure traces at each axial location for constrained reaction volumes with $L_5 = 22$ cm (where we are confident that no dilution occurs) and $L_5 = 11$ cm (where minimal dilution of the hydrogen–oxygen mixture by argon occurs). From these figures, we can see that in a constrained reaction volume of $L_5 = 22$ cm, heat release due to reaction (leading to a minor pressure rise) begins away from the endwall at the 38.8 cm axial location, through a sharp rise in the internal pressure occurs first at the measurement location 2 cm from the driven section endwall. By reducing the size of the constrained reaction volume to $L_5 = 11$ cm, we can completely eliminate the appearance of any initial remote pressure rise due to reaction occurring, and the chemical reaction is clearly seen to occur initially at the axial location 2 cm from the endwall before occurring in any of the other measurement locations in the shock tube. Thus in experiments without remote ignition, the measured ignition delay time at an axial location 2 cm from the endwall more closely represents the actual time required for spontaneous ignition at constant reaction conditions (typically taken as constant U and V). Hence, we recommend that in ignition delay time measurements at low temperatures, the presence of remote ignition should be monitored, and if the phenomenon is present, efforts should be made to eliminate

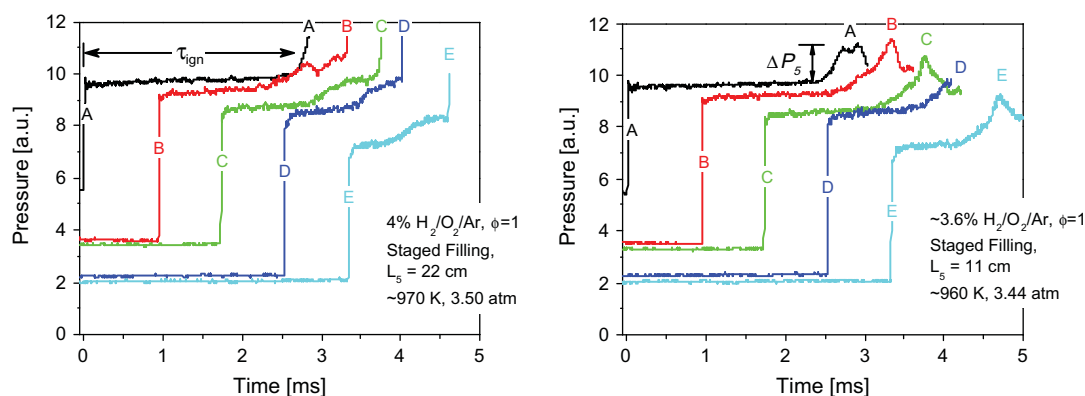


Fig. 4. Pressure traces for hydrogen–oxygen mixture with the staged-filling strategy to achieve a constrained reaction volume of different lengths with negligible dilution of the test mixture. Measurement locations are the same as in Fig. 3. (LEFT) $L_5 = 22$ cm and (RIGHT) $L_5 = 11$ cm.

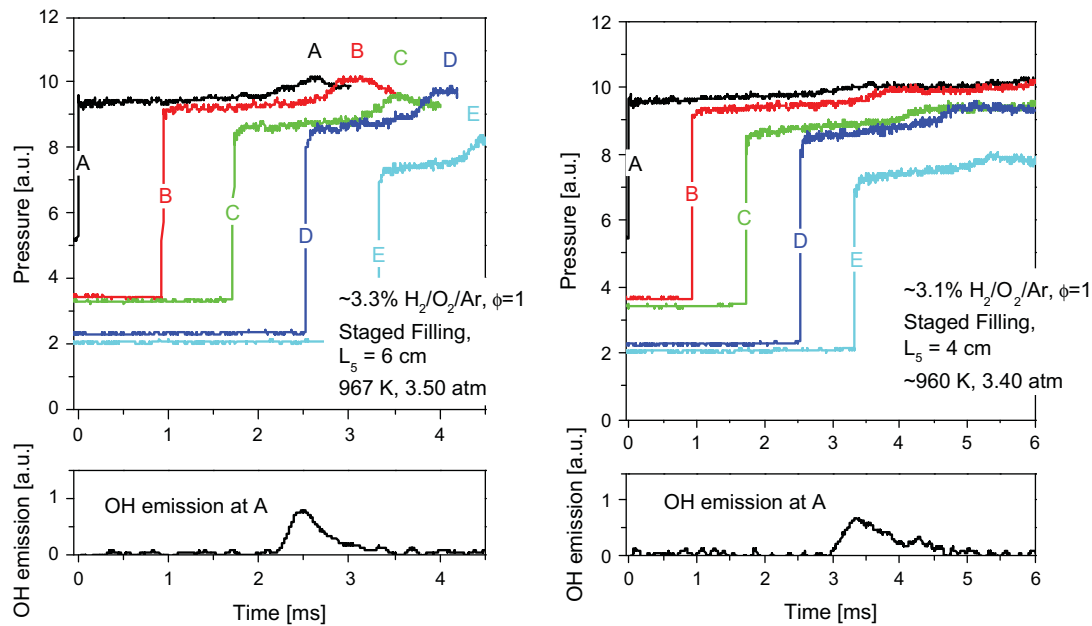


Fig. 5. Pressure traces for hydrogen–oxygen mixture with the staged-filling strategy and a constrained reaction volume of different lengths. Some dilution of the nominal test mixture is present, but this was quantified by laser absorption measurements of the mixture composition at measurement location A. Measurement locations are the same as in Fig. 3. (LEFT) $L_5 = 6$ cm and (RIGHT) $L_5 = 4$ cm. The measured OH emission is also shown for both cases. Note that the dP_5/dt at A is approximately 1.7%/ms for both values of L_5 , as expected.

it or to model the measured ignition delay accounting for this phenomenon.

4.3. Minimizing pressure perturbations caused by ignition

In addition to the elimination of remote ignition, we introduce here another advantage of performing ignition experiments in a constrained reaction volume, namely the minimization or elimination of the post-ignition pressure change. From Fig. 4, we can observe that the post-ignition pressure rise in the experiment with the smaller constrained reaction volume is smaller and less pronounced than in the experiment with a larger constrained reaction volume (and also that of an experiment with conventional filling, as seen in Fig. 3). The abrupt post-ignition pressure rise caused by heat release in ignition delay time experiments with conventional shock tube filling seriously complicates the quantitative modeling of combustion past the initial ignition event. This is due to the fact that this pressure rise cannot be correctly accounted for when simple constant U and V constraints are used in the kinetic modeling, since shock reflection in a reactive mixture is not a constant volume process (except in the limit of a highly diluted mixture). In Fig. 5, it is evident that the effect of the ignition heat release on the post-ignition pressure rise is reduced when experiments are performed in smaller constrained reaction volumes (lengths $L_5 = 6$ cm and $L_5 = 4$ cm are shown). In such cases, OH emission is measured to mark the onset of ignition. For $L_5 = 4$ cm, the pressure trace is nearly linear, rising only to follow the facility-induced dP_5/dt measured in the non-reactive experiments, and thus can be assumed to be conveniently modeled using a specified P and H constraint that applies both during and following ignition (constant P and H could be applied when facility-induced dP_5/dt is negligible). Although some dilution of the initial reactive mixture occurs for the experiments in Fig. 5, the actual composition of the reactive mixture was quantified with laser absorption measurements at the 2 cm measurement location before and immediately after reflected shock passage. Since there is relatively little change in density due to reaction in the volume observed, the

gas can be assumed to be stationary and therefore modeled as a homogeneous system at specified P and H for direct comparisons with species and temperature measurements.

Next, we characterize the effect of the constrained reaction volume size on the reduction of post-ignition pressure rise (which we define as $\Delta P_5/P_5$, where ΔP_5 is the change in pressure during ignition, see Fig. 4, and P_5 is the initial post-reflected-shock pressure) in Fig. 6 for a set of experiments at nominally 960 K.

We also have characterized the effect of the constrained reaction volume size on the “observed” experimental ignition delay time for each experiment, defined as the interval between time zero, indicated by the passing of the reflected shock at 2 cm measured by the pressure transducer, and the initial rise in the pressure and OH emission traces at this location. With conventional shock tube filling (and even with the staged-filling strategy with

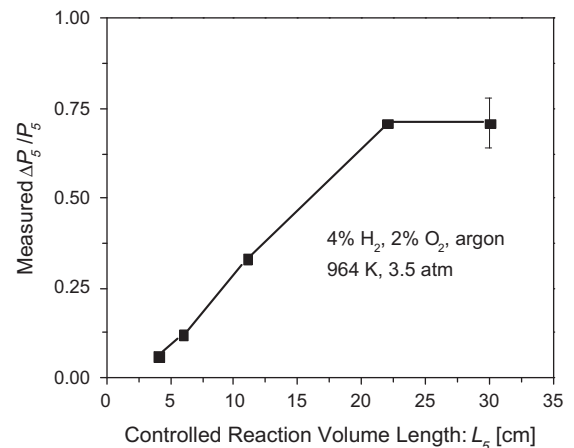


Fig. 6. Variation of normalized post-ignition pressure rise $\Delta P_5/P_5$ as a function of lengths of the constrained reaction volume L_5 for a set of experiments at nominally 965 K. Small changes in dilution at small L_5 as a result of the current staged-filling strategy make only a small contribution to the reduction in $\Delta P_5/P_5$.

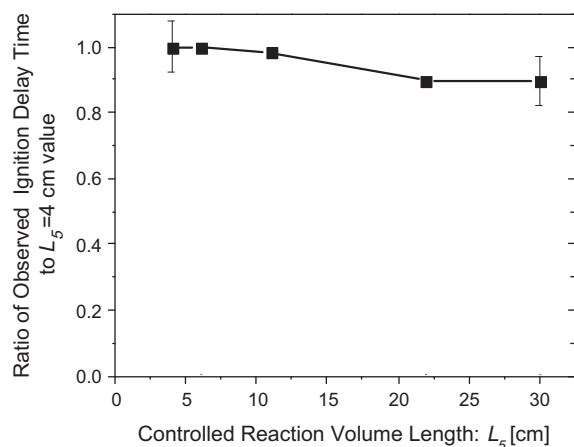


Fig. 7. Ratio of observed ignition delay time to measured value at $L_5 = 4$ cm as a function of constrained reaction volume L_5 for a set of experiments at nominally 4% $H_2/O_2/Ar$, $\phi = 1$ and 965 ± 10 K in the Stanford shock tube.

a large constrained reaction volume), local ignition occurs first at some remote location away from the endwall and the 2 cm measurement location. Therefore, the “observed” experimental ignition delay time may not accurately reflect the delay time corresponding to homogenous ignition at the initial post-shock values of T_5 and P_5 for the 2 cm location. Figure 7 presents a plot of the ratio of the observed experimental ignition delay time to the value measured for $L_5 = 4$ cm as a function of the constrained reaction volume size (specified by L_5) for a set of experiments at a nominal temperature of 965 K. Because the temperatures in each experiment vary by a few Kelvin, the times shown in Fig. 7 are scaled to 965 K using a scaling correlation based on the experimental measurements of ignition delay time. We can see that the observed experimental ignition delay time decreases slightly as the constrained reaction volume size increases. The maximum observed experimental ignition delay time in the dataset is about 10% longer than those of the conventional filling experiment or with a large constrained reaction volume. Note that the magnitude of these remote-ignition effects will vary with reaction conditions and between different shock tube facilities.

4.4. Implications for previous work

The occurrence of remote ignition raises concerns regarding the validity of previous hydrogen–oxygen ignition delay time studies

at low temperatures, including our own work [1] where the ignition delay times were measured only at an axial location 2 cm from the endwall for experimental conditions similar to the current work. If remote ignition first occurs further from the endwall than the 2 cm measurement location, then the measured ignition delay time may be reduced. In our previous work, we were careful not to include data that suffered from these remote ignition phenomena. In this study, we repeated several representative ignition delay time experiments with the staged-filling strategy and a constrained reaction volume with $L_5 \approx 22$ cm (no expected dilution in the test mixture). In confirmation of our earlier study, we found that the ignition delay times measured in the current work show no significant discrepancies from the previously reported data, beyond the reproducibility and uncertainty limits of both studies. Nonetheless, remote ignition remains a potential source of concern and uncertainty in experiments using conventional filling, when the ignition delay times are long. We emphasize that these issues are of growing concern at increasing delay times, and are likely to vary between different facilities of different design and with different incident shock attenuation rates.

5. Ethylene–oxygen ignition in a constrained reaction volume

5.1. Ethylene–oxygen ignition experiment results

Constrained-reaction-volume experiments were carried out in ethylene–oxygen–argon mixtures (seeded with CO_2 for temperature measurements), and the results show that the constrained reaction volume yields a similar reduction in post-ignition pressure rise as with the hydrogen–oxygen experiments. Pressure was measured at all axial locations of the shock tube where there are pressure transducers, and OH mole fraction and temperature were measured at an axial location 2 cm from the driven section endwall. We see in Fig. 8 that for an experiment with conventional shock tube filling, there is a significant pressure rise of approximately 30% that occurs during ignition. Using the staged-filling strategy to achieve a constrained reaction volume of $L_5 = 6$ cm effectively eliminates the post-ignition pressure rise. Both reactive experiments in Fig. 8 are for initial reflected-shock conditions of 1135 K and 2.3 atm. Note the close similarity between the pressure traces for non-reactive and staged-filled experiments.

The pressure time-history behavior in the ethylene–oxygen ignition experiments support the conclusions drawn from the hydrogen–oxygen data about eliminating the post-ignition pressure rise. We can gain further information about the CRV

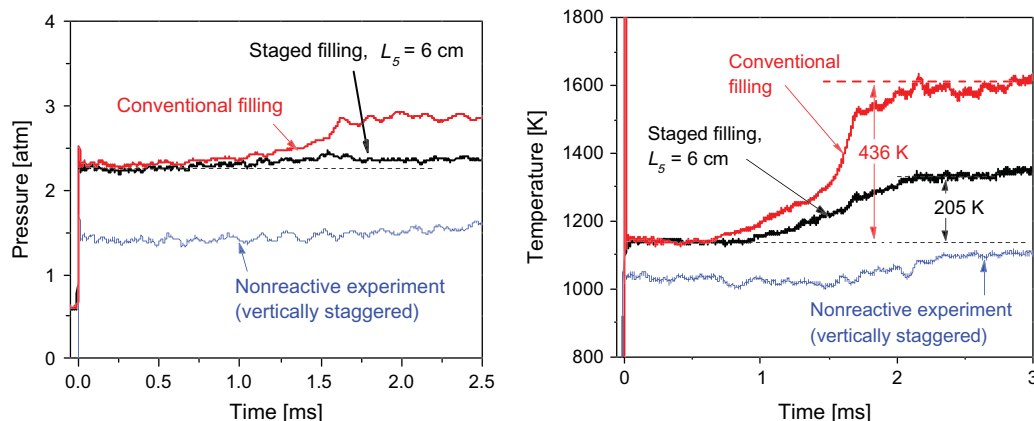


Fig. 8. Measured pressure (LEFT) and temperature (RIGHT) time-histories for ethylene–oxygen ignition experiment with conventional shock tube filling, staged-filling strategy with a constrained reaction volume of $L_5 = 6$ cm, and non-reactive trace. Reflected shock conditions: $T_5 = 1135$ K, $P_5 = 2.30$ atm. All measurements made at the axial location 2 cm from the driven section endwall. Test gas mixtures: conventional fill, 0.5% C_2H_4 , 5% O_2 , 2% CO_2 balance Ar; staged fill, 0.38% C_2H_4 , 3.8% O_2 , 1.5% CO_2 balance Ar.

experiments from an examination of the temperature time-history measurements in the ethylene–oxygen experiments shown in Fig. 8. In the experiment with conventional shock tube filling, an abrupt increase in temperature is observed at a time corresponding to the abrupt increase in pressure. This temperature change is caused by heat release due to ignition combined with compression due to pressure change. Unfortunately, there is no accepted way to simulate or model this process as it is not a homogeneous reactor with a simple gasdynamic constraint, e.g. constant U , V . Therefore, modeling the temperature time-history is typically done only prior to the ignition event. However, for the experiment with a constrained reaction volume of $L_5 = 6$ cm, there is no added pressure change during ignition. Therefore, the measured temperature time-history for the constrained reaction volume of $L_5 = 6$ cm represents the temperature change due to chemical reaction in a near-constant-pressure environment (including the pressure change evident in the non-reactive experiments). The temperature rise of 205 K due to ignition in the constrained reaction volume experiment (with negligible pressure change at ignition) is considerably lower than the temperature rise of 436 K due to ignition in the conventional filling experiment (with a pressure change during ignition). The important distinction is that the CRV process can be modeled directly, as a specified P , H process, while no such gasdynamic specification is available for the conventional-fill experiments (except in the limit of high dilution of reactants).

OH mole fraction time-histories were also measured for the ethylene–oxygen ignition experiments where the OH mole fraction was calculated from the measured fractional transmission near 306 nm using a time-varying absorption cross-section, determined using the measured pressure and temperature time-histories in accordance with the pressure- and temperature-dependent OH absorption cross-section from Herbon et al. [6]. The results are presented and discussed in the following section.

5.2. Validation of specified P and H modeling for constrained-reaction-volume experiments

We have demonstrated that CRV ignition experiments have minimal pressure change for constrained reaction volumes small enough that the total heat release due to combustion in the reactive volume is not sufficient to perturb the pressure throughout Region 5. The success of this strategy rests in part on the fact that reflected shocks do not produce a true constant volume system, since the reflected shock speed can adjust itself in response to

changing pressure. It follows that the CRV strategy will work best when L_5 is a small fraction of the reflected-shock region, when the reactant mixture is dilute, and when the shock tube diameter is large. From these observations, we expect that the kinetics of the combustion reaction can be successfully modeled throughout the entire ignition event using a specified P and H constraint. The sample experimental case of ethylene–oxygen ignition in a constrained reaction volume experiment of $L_5 = 6$ cm at 1135 K and 2.3 atm (the same case shown in Fig. 8) is used to test this hypothesis. The CHEMKIN-Pro suite of programs by Reaction Design was employed for the simulations, and the specified P and H constraint was applied where the time-varying P is specified to have a gradual pressure rise of 1.7%/ms (the measured dP_5/dt). We use two detailed kinetic mechanisms for comparison to the experimental data: the GRI-Mech 3.0 [12] and JetSurF 2.0 [13] mechanisms.

Figure 9 presents the simulated temperature time-histories from the two mechanisms in comparison with an experimental data trace. The temperature simulation from the GRI-Mech 3.0 [12] mechanism shows reasonable agreement with the final temperature measured after ignition. This agreement is expected because the post-ignition temperature is primarily a function of thermochemistry parameters which are expected to be well-known. However, the prediction by the GRI-Mech 3.0 mechanism of the rate at which the temperature changes to reach the final post-ignition temperature does not agree well with the current measurement. This is not alarming, because the GRI-Mech 3.0 mechanism was optimized only for methane combustion. Therefore, we turn our attention to the JetSurF 2.0 [13] mechanism, developed for jet fuel components. From Fig. 9, we can see that the temperature time-history simulated with the JetSurF 2.0 mechanism under specified P and H constraints is in excellent agreement with the measurement, further supporting the hypothesis that the specified P and H assumption is an accurate assumption for CRV experiments where there is negligible pressure change during ignition.

The simulated OH mole fraction from the GRI-Mech 3.0 [12] and JetSurF 2.0 [13] mechanisms are compared to the measured results in Fig. 10. The GRI-Mech 3.0 mechanism is seen to effectively predict the ignition delay time (marked by the long steep rise of OH mole fraction), but does not accurately recover the detailed slope of the OH mole fraction time-history. In comparison, the JetSurF 2.0 mechanism overpredicts the ignition delay time by approximately 5%, but does capture the subtle features of the measured

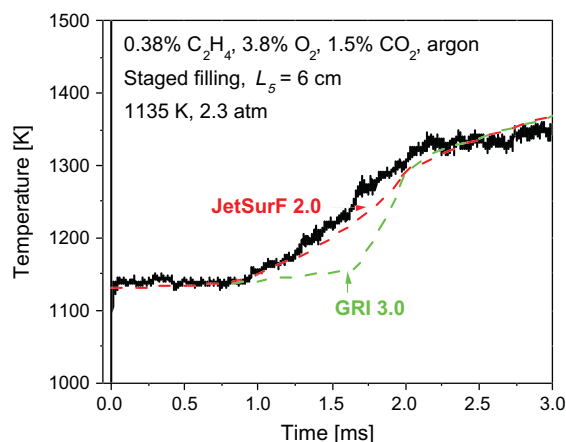


Fig. 9. Comparison of simulated temperature time-histories (dashed lines) from the GRI-Mech 3.0 [12] and JetSurF 2.0 [13] mechanisms with the measured data (solid line) for a constrained-volume-reaction experiment with $L_5 = 6$ cm (and no pressure change at ignition).

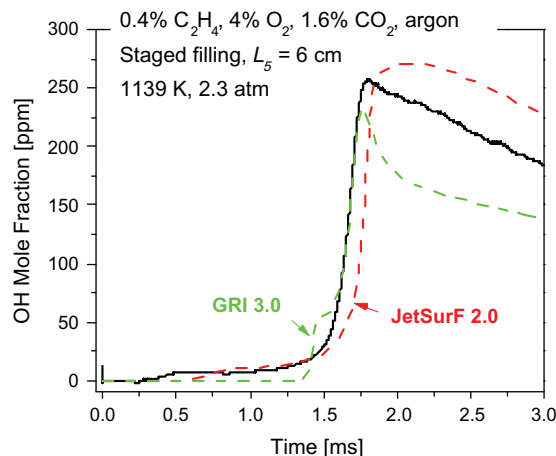


Fig. 10. Comparison of simulated OH mole fraction time-histories (dashed lines) from the GRI-Mech 3.0 [12] and JetSurF 2.0 [13] mechanisms with the measured data (solid line) for a CRV experiment with $L_5 = 6$ cm (and no incremental pressure change at ignition).

trace better than the GRI-Mech 3.0 mechanism, such as the initial formation of OH (near 600 μ s) and the steady rate of decay after the peak OH mole fraction (after 2 ms). We anticipate that current research on detailed kinetics modeling and pathway hypotheses should benefit substantially from the availability of such high-accuracy species time-histories to distinguish the subtle differences in the proposed pathways of current detailed mechanisms. Hence we believe that the CRV concept, coupled with specified P , H time-histories, will prove to be an important new approach for advancing combustion chemistry.

6. Concluding remarks

Ignition delay time experiments were carried out in a high-purity stainless-steel kinetics shock tube for hydrogen–oxygen–argon and ethylene–oxygen–argon mixtures using a staged-filling strategy to constrain the reaction volume in the shock tube to a region near the endwall. We demonstrated that CRV ignition experiments such as these can successfully remove the occurrence of remote, non-localized ignition phenomena in ignition experiments. Furthermore, we showed that for a small constrained reaction volume size, pressure changes due to heat release during ignition could be effectively mitigated, and the experiment proceeds as if in a near-constant-pressure reactor. This type of experiment is advantageous because it allows quantitative modeling of the experiment through the entire combustion event, unlike conventional shock tube experiments where the constant volume assumption fails if there is significant pressure change due to heat release. We illustrated that in a CRV ignition experiment with negligible pressure change at ignition, using a specified pressure (P) and enthalpy (H) constraint in kinetic modeling enabled accurate modeling of the measured temperature time-histories before, during, and after the ignition event. In CRV ignition experiments where there is negligible pressure change due to non-ideal facility effects (such as if driver section inserts [4] were used), it is likely a constant P and H

constraint would be sufficient. We found that neither of the GRI-Mech 3.0 [12] or JetSurF 2.0 [13] mechanisms was capable of accurately predicting all aspects of the measured OH mole fraction time-history with C_2H_4/O_2 mixtures, likely due to deficiencies in the mechanisms. We anticipate that this new CRV approach will lead to expanded use of reflected-shock species time-history data in evaluating and refining detailed kinetic mechanisms. Lastly, we note that the CRV approach advocated here also applies to studies of endothermic reaction processes.

Acknowledgments

The authors acknowledge Tamour Javed from KAUST for his assistance in the operation of the shock tube. This work was supported by the Army Research Office, with Dr. Ralph Anthenien as Contract Monitor.

References

- [1] G.A. Pang, D.F. Davidson, R.K. Hanson, *Proc. Combust. Inst.* 32 (1) (2009) 181–188.
- [2] K.-Y. Lam, Z. Hong, D.F. Davidson, R.K. Hanson, *Proc. Combust. Inst.* 33 (1) (2011) 251–258.
- [3] M.A. Oehlschlaeger, D.F. Davidson, R.K. Hanson, *J. Phys. Chem. A* 108 (2004) 4247–4253.
- [4] Z. Hong, D.F. Davidson, R.K. Hanson, *Shock Waves* 19 (2011) 331–336.
- [5] W. Ren, D.F. Davidson, R.K. Hanson, *Int. J. Chem. Kinet.* 44 (2011) 423–432.
- [6] J.T. Herbon, R.K. Hanson, D.M. Golden, C.T. Bowman, *Proc. Combust. Inst.* 29 (2002) 1201–1208.
- [7] A. Farooq, J.B. Jeffries, R.K. Hanson, *Appl. Phys. B* 90 (2008) 619–628.
- [8] Z. Hong, G.A. Pang, S.S. Vasu, D.F. Davidson, R.K. Hanson, *Shock Waves* 19 (2009) 113–123.
- [9] A. Farooq, J.B. Jeffries, R.K. Hanson, *Appl. Phys. B* 96 (2009) 161–173.
- [10] B. Rajakumar, K.P.J. Reddy, E. Arunan, *J. Phys. Chem. A* 106 (2002) 8366–8373.
- [11] C.J. Brown, G.O. Thomas, *Combust. Flame* 117 (1999) 861–870.
- [12] G.P. Smith, et al. <http://www.me.berkeley.edu/gri_mech/>, 1999 (accessed 12.12).
- [13] H. Wang, et al. <<http://melchior.usc.edu/JetSurF/JetSurF2.0>>, 2010 (accessed 12.12).



Contents lists available at SciVerse ScienceDirect

Combustion and Flame

journal homepage: www.elsevier.com/locate/combustflame

1-Butanol ignition delay times at low temperatures: An application of the constrained-reaction-volume strategy

Yangye Zhu, David Frank Davidson^{*}, Ronald K. Hanson

High Temperature Gasdynamics Laboratory, Department of Mechanical Engineering, Stanford University, Stanford, CA 94305, United States

ARTICLE INFO

Article history:
Available online xxxx

Keywords:
Shock tube
Ignition delay
Pre-ignition
1-Butanol
Constant pressure

ABSTRACT

Ignition delay times behind reflected shock waves are strongly sensitive to variations in temperature and pressure, yet most current models of reaction kinetics do not properly account for the variations that are often present in shock tube experiments. Particularly at low reaction temperatures with relatively long ignition delay times, substantial increases in pressure and temperature can occur behind the reflected shock even before the main ignition event, and these changes in thermodynamic conditions of the ignition process have proved difficult to interpret and model. To obviate such pressure increases, we applied a new driven-gas loading method that constrains the volume of reactive gases, thereby producing near-constant-pressure test conditions for reflected shock measurements. Using both conventional operation and this new constrained-reaction-volume (CRV) method, we have collected ignition delay times for 1-butanol/O₂/N₂ mixtures over temperatures between 716 and 1121 K and nominal pressures of 20 and 40 atm for equivalence ratios of 0.5, 1.0, and 2.0. The equivalence ratio dependence of 1-butanol ignition delay time was found to be negative when the oxygen concentration was fixed, but positive when the fuel concentration was held constant. Ignition delay times with strong pre-ignition pressure increases in conventional-filling experiments were found to be significantly shorter than those where these pressure increases were mitigated using the CRV strategy. The near-constant-pressure ignition delay times provide a new database for low-temperature 1-butanol mechanism development independent of non-idealities caused by either shock attenuation or pre-ignition perturbations. Comparisons of these near-constant-pressure measurements with predictions using several reaction mechanisms available in the literature were performed. To our knowledge this work is first of its kind that systematically provides accurate near-constant-enthalpy and -pressure target data for chemical kinetic modeling of undiluted fuel/air mixtures at engine relevant conditions.

© 2013 The Combustion Institute. Published by Elsevier Inc. All rights reserved.

1. Introduction

Recently, there has been strong interest in the combustion of 1-butanol and other butanol isomers due to their potential as biofuel candidates for next-generation green transportation fuels [1,2]. Butanol ignition data at high pressures and low temperatures are particularly needed due to their relevance to practical engine combustion environments and significance in the validation of detailed chemical reaction mechanisms at these conditions. Many experimental studies of the oxidation of one of the isomers, 1-butanol, have been performed by researchers using various facilities and techniques [3–11]. However, there still appears to be a lack of consensus among the ignition delay time measurements found in these studies (see Fig. 1), especially at low temperatures. In addition, while the pressure dependence of ignition delay time of 1-butanol/air mixture has been studied extensively to yield a

consistent result [3,6,11], few investigations exist for the equivalence ratio or oxygen concentration dependence except that reported in [6].

Computational studies of 1-butanol ignition are also abundant. Although detailed chemical kinetic reaction mechanisms for 1-butanol and the other isomers have been proliferating rapidly in recent years [11–15], Fig. 1 shows that there are significant discrepancies between the different mechanism predictions, particularly at relatively low temperatures ($T < 1000$ K). While it is true that some of these mechanisms were not optimized for low temperature chemistry, these discrepancies still imply that more high-quality data at low temperatures are of critical importance for improvement of these mechanisms.

This wide variation in model prediction thus motivates further measurements of high-pressure and low-temperature 1-butanol ignition delay times. In some of the previous 1-butanol oxidation studies behind reflected shocks, the mixtures utilized were highly diluted in argon and thus the energy release during reaction was small [4,5,7]. However, in many other cases, undiluted

^{*} Corresponding author.
E-mail address: dfd@stanford.edu (D.F. Davidson).

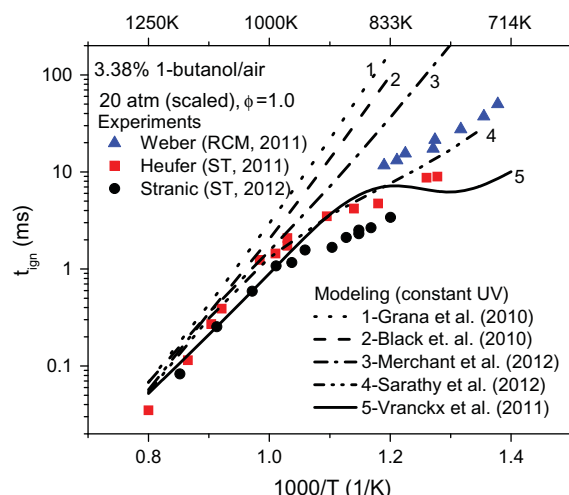


Fig. 1. Previous ignition delay time measurements for 1-butanol oxidation in air at $\phi = 1.0$. The constant-energy (U), constant-volume (V) model calculations utilize five recent mechanisms [11–15].

high-concentration mixtures (fuel/air) at elevated pressures and low temperatures were employed and these data were found to exhibit pre-ignition pressure ramps and/or steps prior to the primary ignition event [5,16–25]. The reasons for these rises are difficult to confirm as both real fuel chemistry inside the measurement volume and non-localized ignition outside of the reaction volume can contribute to the pressure increases observed inside the measurement volume [5]. Similar phenomena were also observed in rapid compression machines (RCM) [26–28] and research engines [29]. Such dramatic pressure effects are different from the normal, though undesired, gradual pressure increase (dP_5/dt) observed behind reflected shocks in dilute mixtures [30], and these effects may be temperature-dependent [11,31], pressure-dependent [11,31], and even fuel-dependent [32]. Generally these effects cannot be simply reproduced by a detailed kinetic mechanism under constant-energy (U), constant-volume (V) constraints. These complications are further motivation to seek strategies for interpreting data exhibiting pre-ignition pressure change, as well as to establish new techniques for generating databases without these thermodynamic complications.

In the current study, we measured ignition delay times of 1-butanol/ O_2/N_2 behind reflected shock waves at various temperatures, pressures and equivalence ratios, using two methods. First, data were collected using a conventional shock-tube test-gas-loading method. These data were simulated with both a constant-volume model and a specified-pressure model incorporating the measured pressure profiles into the chemical kinetic model calculations. The measurements were then repeated employing a new shock-tube test-gas-loading method, called constrained reaction volume (CRV) [33], that limits the volume of reacting gases and creates near-constant-pressure test conditions. These CRV measurements can be compared to mechanism predictions with a simple and appropriate gasdynamic model using constant or specified pressure (P) and enthalpy (H), thereby avoiding the complications and errors associated with constant U , V or constant P , H modeling of conventional (full shock tube filling) reflected shock experiments.

2. Experimental methods

2.1. High-pressure shock tube

All ignition delay time experiments were performed using the Stanford high-purity, high-pressure shock tube (HPST). The driver

section is 3 m long with a 7.5-cm internal diameter. The stainless steel driven section has a length of 5 m and an internal diameter of 5 cm and was heated to 91 °C to prevent condensation of the test gas mixture. A tailored gas mixture (40% N_2/He) was used as the driver gas for experiments to achieve test times up to 10 ms. Driver inserts were implemented in all shock tube experiments to eliminate the non-ideal pressure rise typically seen in the reflected shock region at long test times [30,34]. Five axially-spaced PCB pressure transducers (PCB 113A), at locations 1.1 cm, 31.6 cm, 69.7 cm, 92.5 cm and 123.0 cm away from the endwall of the driven section, were employed to record pressure during the ignition experiments and connected to four Philips time-interval counters (model PM6666) for measurement of the incident shock speed. The initial reflected shock temperature and pressure were calculated from the incident shock speed at the endwall, using one-dimensional shock-jump relations and assuming vibrational equilibrium and frozen chemistry, with uncertainties in initial post-shock temperature and pressure of less than $\pm 1.5\%$. The driven section was evacuated to an ultimate pressure of less than 10^{-5} torr, with a combined leak and outgassing rate of less than 10^{-4} torr/min before each shock. Liquid fuel was introduced by direct injection using a gas-tight syringe (model 1010 TLL SYR) into a 12.8-liter stainless-steel mixing tank maintained at 120 °C. Oxygen and nitrogen were from Praxair (research grade) and Sigma Aldrich anhydrous 1-butanol (99.8%) was used as the fuel source without further preparation. A test gas mixture of 1-butanol/ O_2/N_2 was prepared manometrically and stirred using a magnetically-driven vane assembly for at least 30 min prior to the experiments. Further details on the shock tube facility can be found in [35].

2.2. Shock tube diagnostics

Three diagnostics were used during the experiments: laser absorption at 3.39 μm , OH^* emission near 306 nm and sidewall pressure (see Fig. 2). Initial fuel concentration was measured by laser absorption using a 3.39 μm Spectra-Physics He–Ne laser. Liquid-nitrogen-cooled IR photovoltaic InSb detectors (Infrared Associates, IS-2.0) with a large linear dynamic range were used for measurements of incident and transmitted laser intensities. Ignition was indicated by emission near 306 nm from the $A^2\Sigma^+ - X^2\Pi(0,0)$ band of excited OH radical (OH^*) that was detected using a modified UV-enhanced PDA36A Si detector and Schott UG5 filter (not shown) with an optical arrangement that provided a temporal resolution of better than 10 μs . A flip mirror placed between shock tube windows and PDA36A detector was used to switch between laser absorption measurements in Regions 1, 2, and 5 and detection of OH^* chemiluminescence. Pressure time-history in the test section was monitored using a Kistler pressure transducer (603B1) coated with a thin 0.5 mm layer of RTV silicone, which provided an alternative definition of ignition delay time. The measurement location of all diagnostics was 1.1 cm from the endwall.

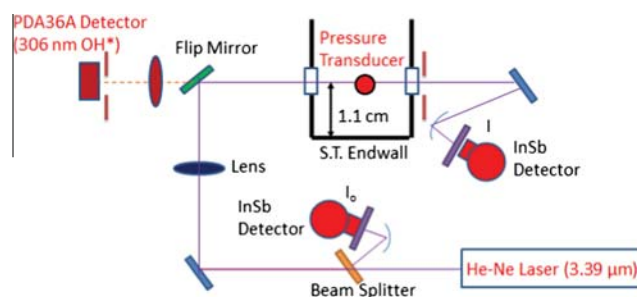


Fig. 2. Schematic of experimental set-up for ignition delay time measurements.

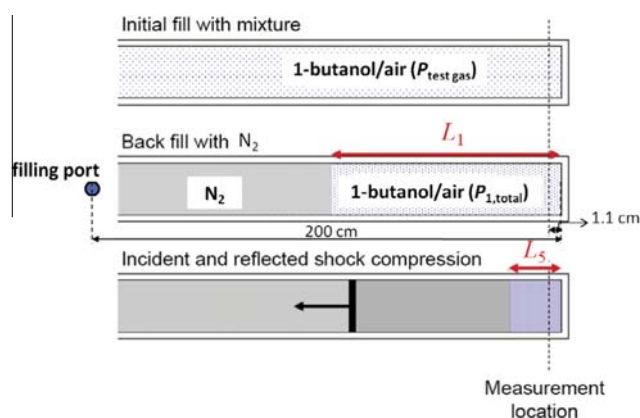


Fig. 3. Idealized schematic of the gas mixtures during the staged-filling process.

2.3. Constrained-reaction-volume strategy

The implementation and characterization of the constrained-reaction-volume approach in our low-pressure shock tube are detailed in [33]. Here, we apply this strategy in our high-pressure shock tube to achieve a near-constant-pressure autoignition environment, seeking to avoid ambiguity in data analysis that pre-ignition pressure increases entail. Before we present the final pressure time-histories, both the conventional operation and staged-filling procedures will be summarized.

2.3.1. Experimental procedure

In a conventional shock wave ignition-time-delay experiment, the entire driven section of the shock tube is filled with the test gas. However, in a constrained-reaction-volume experiment using staged-filling, only a small portion of the driven section is filled with test gas. Figure 3 shows the filling stages that the gas mixtures progress through. In the first filling stage, the test mixture (similar to the non-reactive gas except for the presence of fuel and oxidizer) is filled into the shock tube to an initial pressure ($P_{\text{test gas}}$) lower than the desired ultimate driven-section pressure ($P_{1, \text{total}}$). Then, in the second stage, a non-reactive gas (in this study, N_2 or a N_2/CO_2 mixture) is filled into the driven section from a port about 200 cm away from the endwall, compressing the reactive gas from the initial-stage fill to a small “slug” near the endwall. To minimize mixing between the non-reactive and reactive mixtures, the second-stage filling is done slowly such that the filling takes place over 2–3 min. The nominal length of the reactive “slug” at the test section before shock (L_1) can be calculated according to

$$L_1 = (200 \text{ cm})P_{\text{test gas}}/P_{1, \text{total}} \quad (1)$$

The most important variable in designing a staged-filling experiment is the length of the reactive “slug” at the test section behind the reflected shock (L_5) [33]. This can be calculated according to Eq. (2), where ρ_1 and ρ_5 refer to the gas densities in Regions 1 (initial static test gas) and 5 (post-reflected-shock), respectively. Empirically, we have found that the smaller the value of L_5 , the more closely a constant-pressure condition can be achieved, though more dilution of the test gas can occur, due to diffusive mixing between the initial-stage test gas mixture and the second-stage N_2 . In the current studies, the optimal L_5 was found to be around 4–5 cm.

$$L_5 = (\rho_1/\rho_5)L_1 \quad (2)$$

To ensure the accuracy and reproducibility of current CRV data, different staged-filling strategies were tested including changing the location of staged-filling port (filling at 5 m from the endwall)

and using different staged-filling gas mixtures (staged-filling with N_2/CO_2 blends). Experiments performed with the N_2/CO_2 blend staged-filling gas mixtures did exhibit lower incident shock attenuation rates, but produced no statistically significant change in the measured ignition delay times.

2.3.2. Mixing characterization

To establish the actual reactive gas mixtures present in the experiment, a 3.39 μm He–Ne laser was used to make quantitative measurements of the fuel concentration throughout the staged-filling process. An example fuel concentration monitoring experiment is shown in Fig. 4. Right after the first filling stage, the 1-butanol concentration was measured to be in good agreement (within $\pm 10\%$) with the test gas mixture concentration prepared manometrically in the mixing tank. The $\sim 10\%$ loss of fuel from 0.68% to 0.62% is attributed to wall effects in the mixing tank and shock tube. During the second filling stage, the fuel concentration oscillates somewhat owing to varying pressure. The fuel concentration decreases near the end of the second filling stage, but became relatively constant 30 s after the end of this filling stage. These experiments demonstrate that the staged-filling process has the potential to dilute the test gas mixture, so it is important to measure the fuel concentration soon after the end of the second filling stage. Additionally, it is necessary to fire the shock tube soon after the second filling stage to minimize further dilution through mixing. Figure 5 presents the shock-based absorbances in Regions 1, 2 and 5 (only first 800 μs) obtained right after this monitoring experiment. The 1-butanol concentration in Region 5 (R5) was found to be approximately 10% less than that measured in Region 1 (R1) for our nominal values of $L_5 \sim 4\text{--}5$ cm, owing to the shock-induced displacement of the mixture boundary. Such variation of post-shock fuel concentration is also reported in [33]. Direct fuel concentration measurements in R5 were not usually feasible in the ignition experiments because of the prohibitively high absorbances (3–4), but measurements in R2, just prior to reflected shock arrival, served to confirm this 10% reduction. Several representative fuel concentration monitoring experiments of this kind were conducted to confirm these trends of fuel concentration drop for varying manometrically measured fuel concentrations. To account for this drop in fuel concentration, test gas mixtures with higher fuel concentration than ultimately desired were made manometrically, in order to perform ignition delay experiments at the desired fuel concentration.

3. Results and discussion

3.1. Conventional-filling experiments

1-butanol ignition delay times were measured at reflected-shock initial temperatures between 716 and 1121 K and nominal pressures of 20 and 40 atm at $\phi = 0.5, 1.0$ and 2.0 using the conventional-filling protocol. The ignition delay time is defined as the time interval between the arrival of the reflected shock at the observation station and the onset of ignition determined by extrapolating the maximum slope of either pressure or OH^* record back in time to the baseline. Ignition delay time values obtained from the pressure and emission traces were consistent within $\pm 1\%$.

Table 1 provides a full listing of current test conditions and ignition delay times; selected pressure traces and ignition delay time plots are given in Figs. 6–9. Ignition delay time data presented in the figures have small experiment-to-experiment pressure variations and have been scaled to a common pressure using $t_{\text{ign}} \sim P^{-1}$, which was experimentally validated and commonly adopted by previous researchers [3,6,11]. The overall uncertainty in ignition

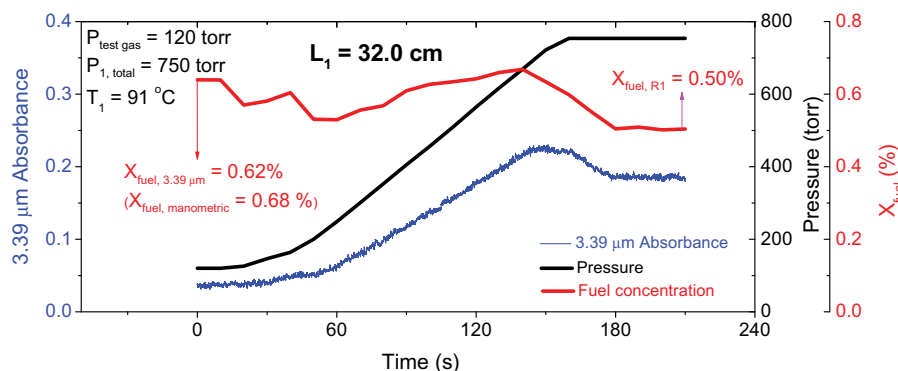


Fig. 4. Example monitoring of the pressure in the driven section, the 3.39 μm He–Ne absorbance and the derived 1-butanol concentration in the test gas during the staged-filling process, for staged filling with $L_1 = 32$ cm. $X_{\text{fuel,manometric}}$, $X_{\text{fuel,3.39}\mu\text{m}}$ and $X_{\text{fuel,R1}}$ stand for the fuel concentration prepared manometrically in the mixing tank, the one measured *in situ* in the shock tube at the end of first filling stage, and the one at the end of second filling stage, respectively.

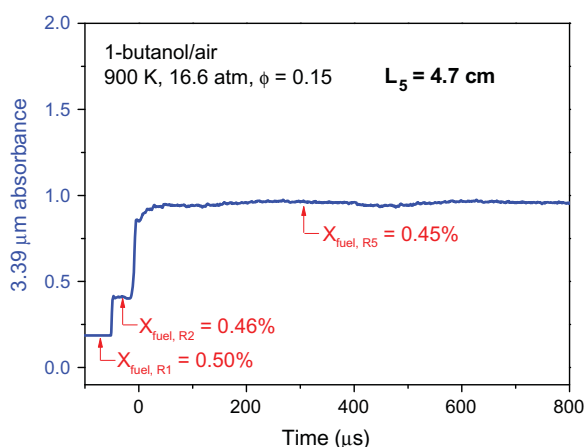


Fig. 5. Example monitoring of the 3.39 μm He–Ne laser absorbances and the derived 1-butanol concentrations in Regions 1, 2, and 5 ($X_{\text{fuel,R1}}$, $X_{\text{fuel,R2}}$, and $X_{\text{fuel,R5}}$) after the staged-filling process for a very lean ($\phi = 0.15$) reflected shock wave experiment (shown in Fig. 4). The slow rise immediately behind the reflected shock is associated with the reflected-shock bifurcation at the sidewall.

delay time measurements is approximately $\pm 20\%$, with the primary contribution from the uncertainty in reflected shock temperatures.

Figure 6 presents representative pressure profiles obtained from 1-butanol ignition experiments with conventional filling at high, intermediate and low temperatures, showing the influence of initial post-shock temperature on the pressure profiles and ignition delay. At the highest temperature shown (1014 K), the pressure trace is flat until a smooth and rapid exponential rise to ignition, which is usually classified as “strong” or “sharp” ignition [18–20,36–38]. At the lowest temperature (792 K), interestingly, the flat pressure time-history lasts for only approximately 2 ms and then slowly increases to ignition without any evidence of pressure rocketing or ringing, a form usually called “mild” ignition [18–20,36–38]. However, at the intermediate temperatures, the strong pressure rise prior to the final ignition event exhibits multiple ramps and/or humps, which can be regarded as a mild-to-strong transition ignition mode [24,39]. These pre-ignition pressure rises are temperature dependent with lower-temperature experiments showing higher pre-ignition pressure rises; this is consistent with the findings of Vranckx et al. [11] and Lee et al. [31]. In addition, such pre-ignition effects are pressure dependent with higher-pressure experiments showing less pre-ignition pressure rise, as shown in Fig. 7 and also reported previously [11,31]. The reasons for the “pre-ignition” pressure rise are discussed in later sections.

The measured ignition delay times in conventional-filling experiments with $\phi = 1.0$ at 20 and 40 atm are plotted in Figs. 8 and 9 and compared with shock tube data from previous studies [3,5]. Non-linear Arrhenius behavior for all sets of data is observed. As shown in Fig. 8, the current 20 atm data are in very good agreement with the previous results of Stranic et al. [5] using the same Stanford facility. However, although current data agree well with the results of Heufer et al. [3] at temperatures above 1100 K, the present data are approximately 40% lower than those of Heufer et al. [3] at temperatures below 1100 K. By contrast, and surprisingly, the present data at 40 atm are in good agreement with those measured by Heufer et al. [3] over the full temperature range studied. The reasons for such apparent inconsistency are difficult to trace, since all three sources of data collected at low temperatures were subject to pre-ignition pressure rises [3,5] and the impact of these rises might vary between different shock tube facilities [5]. In addition, the data by Heufer et al. [3] are affected by non-reactive facility-dependent pressure gradients (dP_5/dt) of, on average, 4.5%/ms and 3.6%/ms at 20 and 40 atm, respectively, while driver inserts were employed in both the Stranic et al. work [5] and the current study to eliminate such gradients prior to ignition. Thus, it is difficult to draw clear and useful kinetic conclusions from current comparisons, other than to emphasize the role of facility-dependent effects that are not yet fully accounted for in modeling these experiments.

For the ultimate goal of validation and refinement of a 1-butanol reaction mechanism, such comparisons among different sources of data naturally raise the question as to how to accurately model conventional-filling experiments, particularly at low temperatures where substantial pre-ignition pressure rises can exist. At the same time, there is a wish by experimentalists to advance experimental strategies that enable more quantitative ignition delay time measurements and modeling independent of uncertain thermodynamic–gasdynamic models.

3.2. Interpretation of conventional-filling ignition data

Figure 10 shows a comparison of $\phi = 1.0$ data in conventional-filling experiments and the corresponding simulation results using five different mechanisms with the CHEMKIN-PRO software suite [40] and the conventional constant-volume (V), constant-energy (U) constraints. The measured ignition delay times at intermediate temperatures (876–809 K) are significantly shorter than all the mechanism predictions. The reasons for such discrepancies are various, but ambiguous. It could be that the mechanisms are not well tuned and optimized, or that the thermodynamic–gasdynamic constant U , V model used, is not appropriate, or both. Thus, the

adjustment of reaction rate parameters to tune or refine these chemical kinetic mechanisms to fit global kinetic targets such as ignition delay time is questionable and unconvincing, a point previously stated by Lee et al. [31]. To resolve these disparities, we need to examine the pressure–time profiles during the ignition experiments and investigate the implications of gasdynamic models on simulating ignition delay times [31,41,42].

In previous studies [17–19,31–33,36], pressure traces recorded from transducers mounted at several locations on the driven section were utilized to unravel evidence of a remote (i.e., outside the reaction volume near the endwall) ignition phenomenon that occurred with long ignition delay times. A similar analysis was conducted here. Figure 11 presents the measured pressure time-histories at each of the five axial locations along the driven section as well as a duplicate pressure measurement at the 1.1 cm location recorded using a Kistler pressure transducer. We can see that the Kistler, PCB 5 and PCB 4 all exhibit features of pre-ignition pressure rises. Specifically, such rise appears to first take place at the Kistler location and then propagates to PCB 5 and PCB 4. Since the Kistler transducer is located at the observation point for the ignition delay time measurements, this observation favors the point of view that ignition in this case starts near endwall. This shock-induced inhomogeneous ignition process is characterized by a deflagration-to-detonation transition (DDT) of the fuel/air mixture where a moderate ramp is followed by a steep rise. Significant increases in pressure due to the development of this detonation are observed subsequently in the recordings of PCB 3, PCB 2 and PCB 1. In this specific experiment, then, the pre-ignition pressure change is likely not due to a distant or remote ignition, but could be due to local inhomogeneities in the reaction volume behind the reflected shock, or merely a result of pre-ignition chemistry.

The causes of such inhomogeneities, however, are difficult to ascertain. Fieweger et al. [19] point out that these might manifest themselves as non-uniformities in temperature, radical concentrations, or particles in the reflected shock region. Dryer and Chaos [43] discuss the potential relevance of inhomogeneous mixing and catalytic processes as perturbing factors. In an earlier study in our same shock tube facility, Petersen and Hanson [35] specifically discuss the causes of inhomogeneities by facility-dependent effects such as shock-boundary layer interaction. In another shock tube facility, Shen et al. [44] found that the presence of contaminants in the reactants or on experimental surfaces (soot deposits) in their facilities contributed to the occurrence of pre-ignition ramp behavior; however, this explanation was disproved by Vasu et al. [24] for the Stanford facility used in current work. More recently, Heufer et al. [32] adds that inhomogeneous ignition may also be strongly influenced by fuel chemistry. We reserve further investigation of the real causes of pre-ignition pressure-rise behavior for future work. A more important current task is to accurately model these pre-ignition-affected experiments.

In a preliminary effort to study this problem, two thermodynamic–gasdynamic models are discussed here. The first one is the traditional constant U , V model. The validity of such a model can be checked by comparing measured and simulated pressure profiles [45], as shown in Fig. 12. The simulations in this study were performed using the reaction mechanism of Sarathy et al. [15]. Interestingly, a pre-ignition pressure ramp is evident in both the measurement and simulation. However, a closer examination reveals that the measured ramp is composed of a slow exponential rise (ramp 1) followed by a fast increase (ramp 2) to the time of ignition. The simulation, however, can only reproduce ramp 1, but not ramp 2, which supports the thesis that constant U , V is not suitable for the simulation of such experimental data. The second thermodynamic–gasdynamic model is to use a specified pressure profile and solve the energy equation. This method has been used previously by others including Aul et al. [41]. In this model,

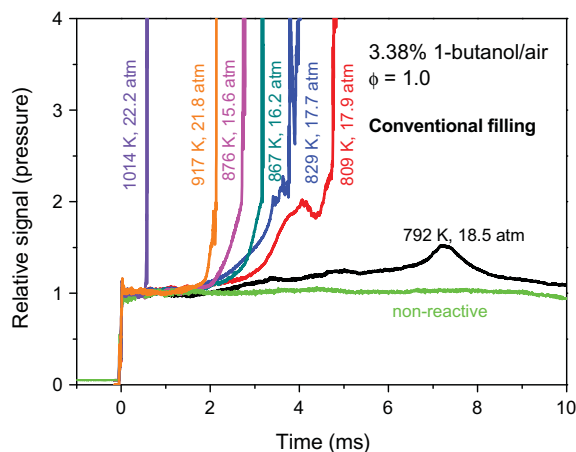
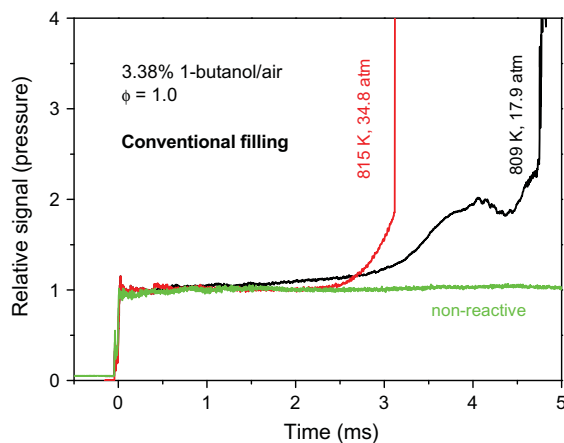
Table 1Ignition delay times of 1-butanol/ O_2/N_2 .

T_5 (K)	P_5 (atm)	t_{ign} (μ s)
3.38% 1-Butanol/20.3% O_2/N_2 , $\phi = 1.0$; conventional-filling		
1121	21.7	140
1047	16.3	514
1042	21.2	379
1014	22.2	572
982	22.4	851
939	21.5	1489
917	21.8	2134
876	15.6	2740
867	16.2	3144
831	16.4	3844
829	17.7	3722
812	22.6	4044
809	17.9	4747
792	18.5	6212
776	23.9	8183
3.38% 1-Butanol/20.3% O_2/N_2 , $\phi = 1.0$; CRV, $L_5 \sim 4$ cm		
1043	16.2	504
1012	22.8	672
959	23.0	1551
913	22.8	2847
882	17.5	5272
869	17.4	5702
858	17.2	7026
850	17.3	8000
848	18.1	8038
841	19.1	8204
839	19.0	9901
820	19.0	11,594
1.72% 1-Butanol/20.6% O_2/N_2 , $\phi = 0.5$; conventional-filling		
1093	19.8	418
1025	20.7	1103
966	21.3	2079
1.72% 1-Butanol/20.6% O_2/N_2 , $\phi = 0.5$; CRV, $L_5 \sim 4$ cm		
922	17.4	4238
908	17.1	4954
902	17.1	4756
883	17.3	6889
882	21.5	5414
880	21.4	5844
874	22.4	6619
856	17.5	9267
6.54% 1-Butanol/19.6% O_2/N_2 , $\phi = 2.0$; conventional-filling		
931	15.1	1505
902	20.3	1809
875	21.1	2373
802	17.3	5440
778	18.1	6196
749	18.6	9704
6.54% 1-Butanol/19.6% O_2/N_2 , $\phi = 2.0$; CRV, $L_5 \sim 4$ cm		
847	22.4	3405
830	24.0	5521
827	17.9	6693
806	23.8	7679
800	17.5	9083
3.38% 1-Butanol/40.6% O_2/N_2 , $\phi = 0.5$; conventional-filling		
976	23.1	424
933	23.2	677
3.38% 1-Butanol/40.6% O_2/N_2 , $\phi = 0.5$; CRV, $L_5 \sim 4$ cm		
879	17.3	2086
874	17.6	2609
851	17.5	3769
833	16.4	3890
822	19.0	4960
800	19.9	6259
777	19.6	10,230
3.38% 1-Butanol/10.2% O_2/N_2 , $\phi = 2.0$; conventional-filling		
1063	21.3	566
1040	21.8	633
1007	22.2	970
982	23.1	1485

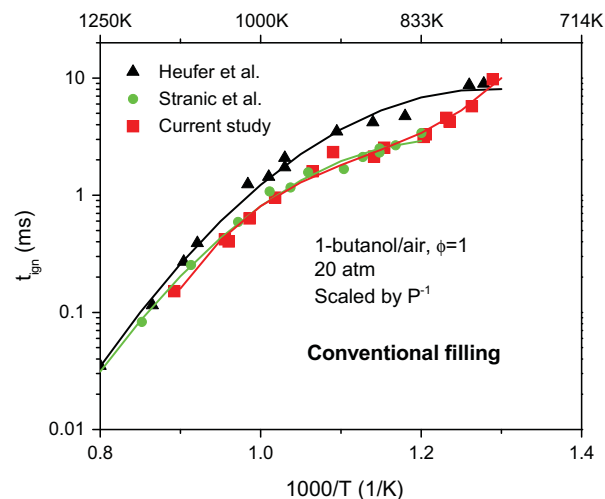
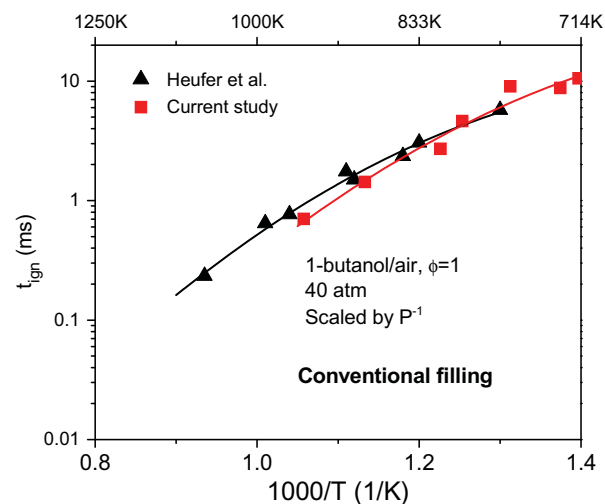
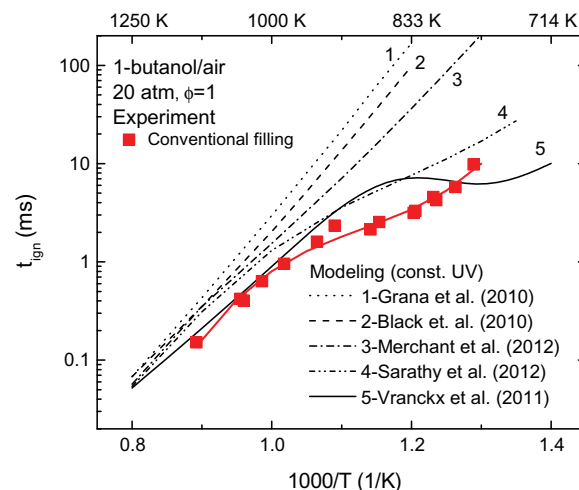
(continued on next page)

Table 1 (continued)

T_5 (K)	P_5 (atm)	t_{ign} (μs)
3.38% 1-Butanol/10.2% O_2/N_2 , $\phi = 2.0$; CRV, $L_5 \sim 4$ cm		
990	14.7	2171
980	16.8	2066
905	16.5	4728
890	16.5	5382
884	17.3	5810
862	17.4	7925
855	17.0	11,048
851	18.4	9168
829	18.3	12,278
3.38% 1-Butanol/20.3% O_2/N_2 , $\phi = 1.0$; conventional-filling		
945	34.1	825
883	34.3	1670
815	34.8	3113
798	38.3	4841
762	41.6	8704
728	41.0	8571
716	45.0	9385

**Fig. 6.** Normalized temperature-dependent pressure profiles for ignition delay time measurements of 1-butanol in air at $\phi = 1.0$ and near 20 atm with conventional filling.**Fig. 7.** Normalized pressure-dependent pressure profiles for ignition delay time measurements of 1-butanol in air at $\phi = 1.0$ with conventional-filling.

the measured reflected-shock pressure profile up to the instant of ignition is input directly into a zero-dimensional homogeneous batch reactor model to constrain the pressure; this then fixes the

**Fig. 8.** Comparison of current ignition delay times of 1-butanol in air with previous results at $\phi = 1.0$ and 20 atm with conventional filling.**Fig. 9.** Comparison of current ignition delay times of 1-butanol in air with previous results at $\phi = 1.0$ and 40 atm with conventional filling.**Fig. 10.** Comparison of current conventional-filling ignition delay times of 1-butanol in air at $\phi = 1.0$ and 20 atm with modeling results using five recent mechanisms [11–15].

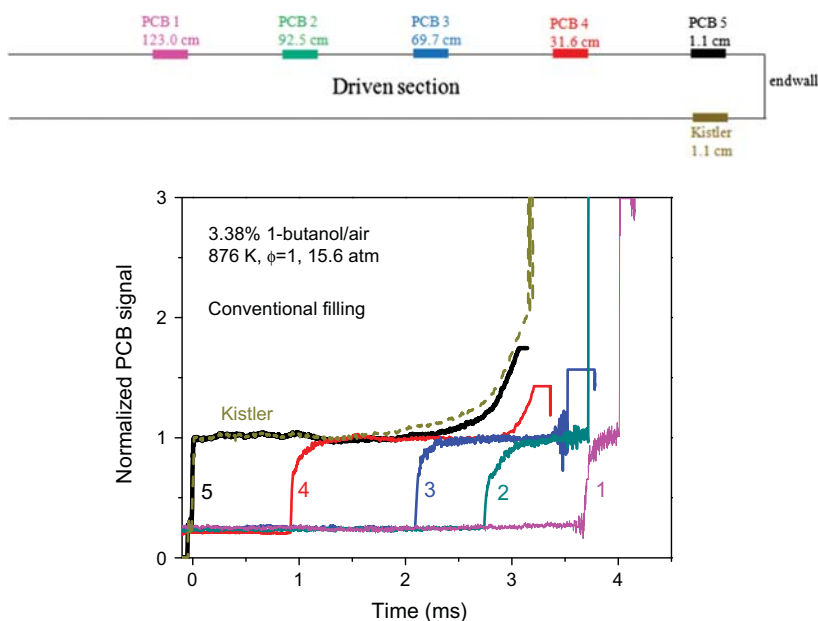


Fig. 11. Normalized pressure traces at five measurement locations for a 1-butanol/air mixture at $\phi = 1.0$ with conventional shock tube operation.

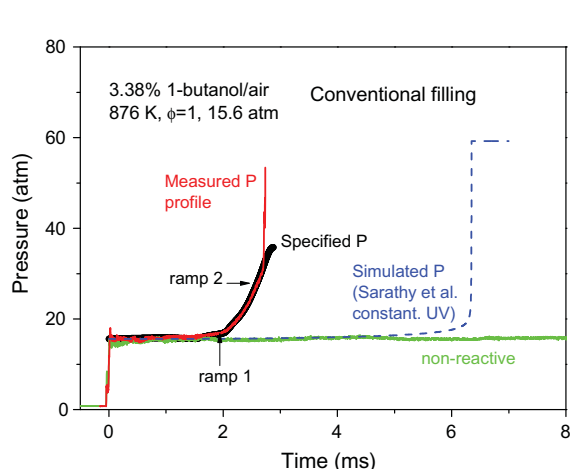


Fig. 12. Measured, specified, and simulated pressure profiles for an example ignition delay time measurement with conventional-filling. The simulated pressure profile was from calculations using the reaction mechanism of Sarathy et al. [15] and a constant U, V assumption.

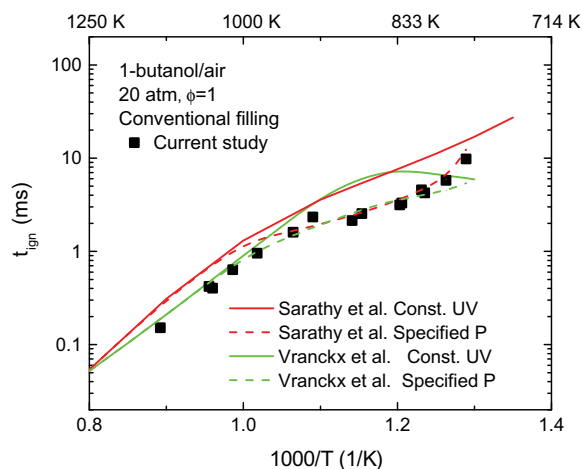


Fig. 13. Comparison of current conventional-filling ignition delay data with two model predictions using both constant U, V assumption and the specified-pressure method.

time-history of the enthalpy for an adiabatic system. We will refer to this as the “specified-pressure method”. An example specified-pressure profile is shown in Fig. 12. In these simulations, we directly used our pressure data together with the specified P option in CHEMKIN-PRO to solve for the OH mole-fraction time-history and hence ignition delay time. The same procedure was repeated for the other data affected by pre-ignition pressure change. We are aware that some researchers do not follow this procedure. For example, Chaos and Dryer [39] and Lee et al. [31] make use of pressure time-history data to generate time-varying volume and temperature profiles, respectively, based on an isentropic assumption, and used these profiles in predicting ignition delay times for comparison with data. However, this approach still communicates the pre-ignition pressure-rise information to the modeling.

Figure 13 presents a comparison of the current conventional-filling data with two mechanism predictions using two kinds of

gasdynamic models, i.e., constant U, V and specified-pressure models, respectively. At higher temperatures, as shown in Fig. 6 at 1014 K, there is no evidence of pre-ignition ramps, so the traditional constant U, V model is a good approximation of the actual test gas state. However, at lower temperatures where pre-ignition pressure change is observed, significant improvement of modeling results can be achieved by using the specified-pressure method. This is true for the three mechanism predictions investigated here [11,14,15]. Nonetheless, a caveat must be offered that such agreement is artificial in that the specified-pressure method tends to “force” ignition near the measured induction time. This may explain why the three mechanisms yielding significantly different values for constant U, V collapse to near-identical predictions when incorporating the specified-pressure time-histories. Thus, a satisfactory interpretation of shock tube experiments containing pre-ignition pressure increases is still lacking and more theoretical and computational work is needed to predict the trends of pressure change shown in Fig. 6.

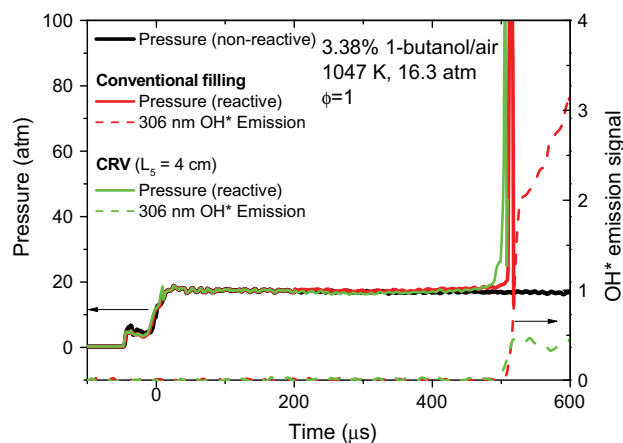


Fig. 14. Comparison of conventional-filling and CRV ignition delay data at 1047 K, ~ 20 atm, $\phi = 1.0$.

3.3. Constrained-reaction-volume experiments

As mentioned above, in order to obviate misinterpretation of ignition delay data, we applied a newly developed and validated driven-gas loading strategy, a constrained-reaction-volume (CRV) strategy [33], to the 1-butanol ignition measurements. Results of the experiments using this strategy at both high and low temperatures are presented below.

Figure 14 shows two sample measurements for the higher temperature case of 1047 K with both the conventional-filling and CRV approach. The ignition delay times in both experiments are very similar, as expected, particularly for our observation station so close to the endwall (1.1 cm). Additionally, no clear evidence of pre-ignition energy release is observed at this temperature. This is understandable, as in the strong ignition regime discussed earlier, a fairly sharp, uniform combustion wave starts at the endwall and then propagates into the test gas. This strong ignition mode has been seen in many optical visualization studies in shock tubes [19,32,36,46]. It also should be noted that prior to ignition, as indicated by the steepest rise of the pressure, the pressure is fairly constant, which implies that using a constant-pressure constraint is a valid gasdynamic model for the simulation of these experiments up to ignition.

However, at lower temperatures, for data affected by pre-ignition energy release, measurements using the CRV strategy exhibit a dramatic difference, as shown in Fig. 15. The pressure in the CRV experiment is reasonably constant, except a small bump

from 3 to 7 ms that is likely due to imperfect tailoring of the driver gas. In the CRV experiment, the energy release during chemical induction dissipates to the neighboring non-reactive gas (N_2 in this case) instead of creating a pre-ignition pressure ramp. This dissipation also explains the absence of any detonation-like pressure ringing. In the CRV experiments, the onset of ignition is marked by a rise in OH^* emission. Not only is the ignition delay time in the CRV experiment now longer than that in the conventional-filling one, but the peak of the emission trace is lower. Such phenomena are expected in the CRV experiment as the pressure change (and concomitant temperature change) during the chemical induction process is far less than that observed in the conventional-filling one. More importantly, an examination of the pressure traces at various axial locations (see Fig. 11) confirms that remote ignition did not occur. Thus, with the absence of either pre-ignition pressure change or remote ignition, the CRV approach enables the unambiguous and reliable quantitative modeling of ignition delay time using specified P , H gasdynamic constraints. Pressure histories even closer to constant P could be achieved with lower fuel concentrations and/or smaller L_5 .

More examples of CRV experiments at different temperatures and oxygen concentrations are shown in Fig. 16. For the same reasons mentioned above, the OH^* emission peaks decrease with decreasing temperature. Note the very high temperature sensitivity of the OH^* histories. In future work, we anticipate using laser absorption to measure OH and temperature, providing important new target data for quantitative comparisons with detailed kinetics simulations based on the specified P , H gasdynamic model.

Figure 17 shows a comparison of data from both conventional-filling and CRV experiments at $\phi = 1.0$ and 20 atm. At temperatures above ~ 1000 K, both types of experiments yield consistent data, while at temperatures below ~ 1000 K, the data in conventional-filling experiments become increasingly shorter than those in CRV experiments. Similar phenomena are also observed for data at $\phi = 0.5$ and 2.0 (not shown here, but included in Table 1). This comparative study is, to the best of our knowledge, the first of its type.

3.4. Interpretation of CRV ignition data

The use of the CRV strategy has allowed acquisition of an improved ignition delay time dataset with a well-defined, near-constant-pressure gasdynamic state. A clear and useful comparison of data and modeling is now possible. Figure 18 shows a comparison of CRV data at $\phi = 1.0$ and corresponding modeling results using three recent mechanisms and a constant P , H gasdynamic assumption. The Merchant et al. mechanism [14] overpredicts

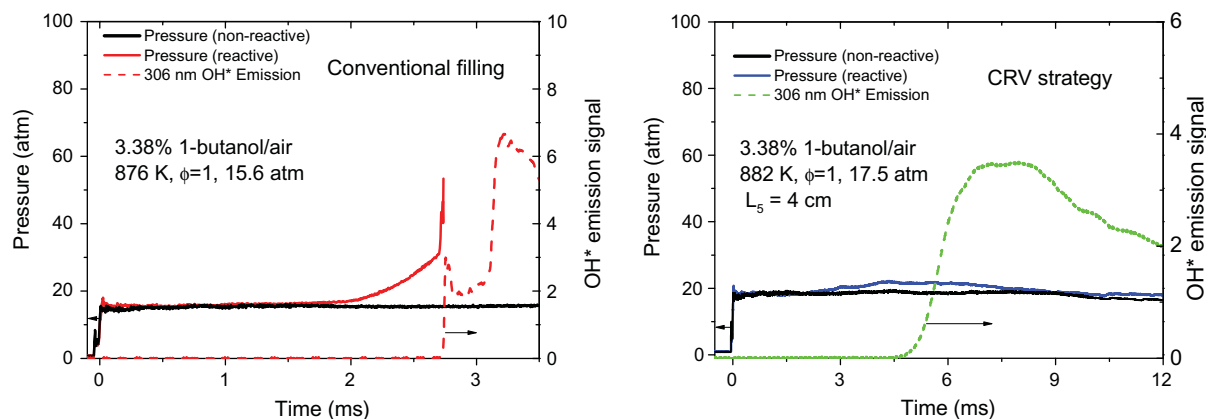


Fig. 15. Comparison of conventional-filling (left) and CRV (right) ignition delay data at ~ 880 K, ~ 20 atm, $\phi = 1.0$.

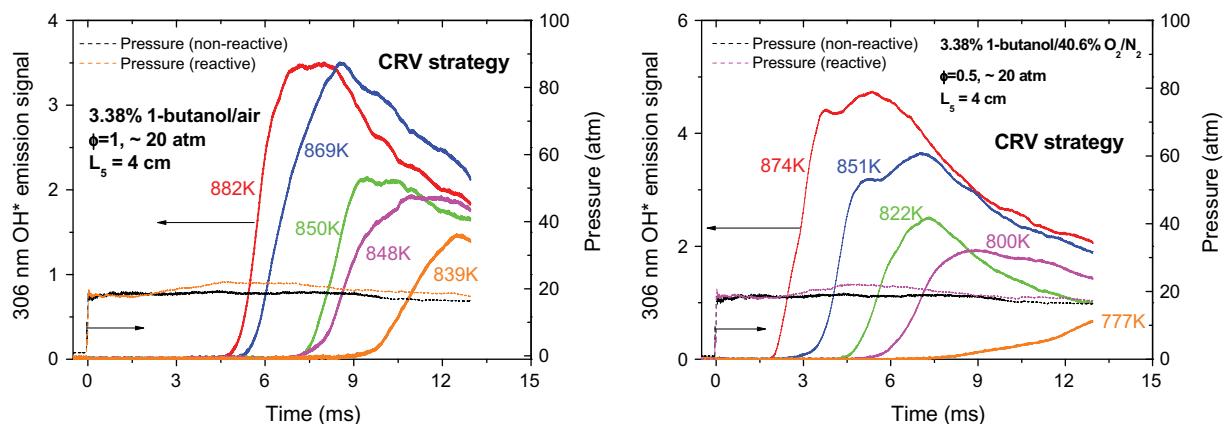


Fig. 16. Example CRV measurements of ignition delay time at low temperatures for 3.38% 1-butanol/20.3% O₂/N₂ (left) and 3.38% 1-butanol/40.6% O₂/N₂ (right). Shown here are representative pressure traces in the reactive case at 839 K (left) and 800 K (right).

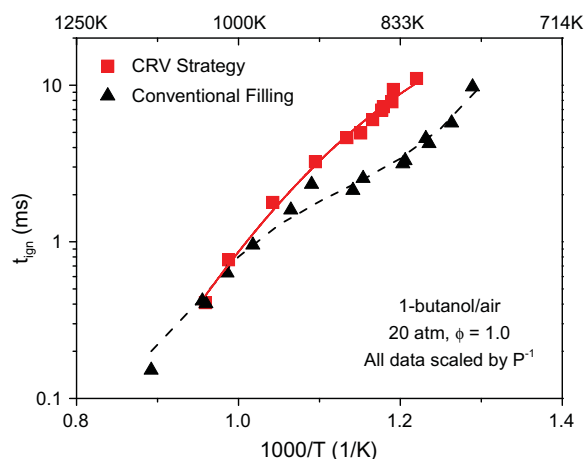


Fig. 17. Comparison of conventional-filling and CRV ignition delay times of 1-butanol in air at $\phi = 1.0$ and 20 atm.

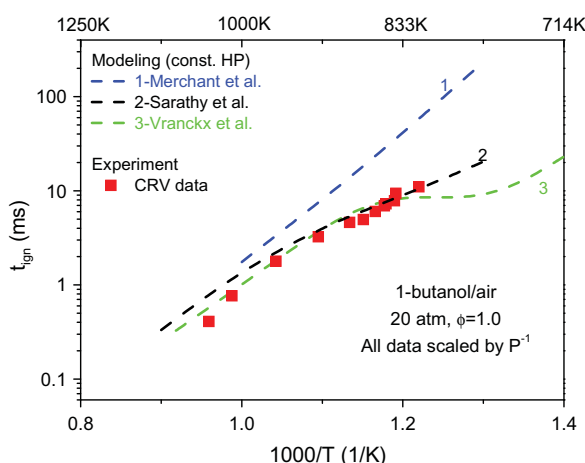


Fig. 18. Comparison of current CRV data at $\phi = 1.0$, 20 atm with model predictions at constant H , P .

the ignition delay time of 1-butanol at low temperatures by a factor of 4–5. The Sarathy et al. [15] mechanism shows excellent agreement with all CRV data. The Vranckx et al. [11] mechanism also shows excellent agreement with all CRV data, except at the lowest temperatures where the mechanism predictions show evidence of an NTC behavior at 820–770 K. This might be due to the

addition of a simplified butyl peroxy chemistry, which was mainly based on ethanol kinetics, in an effort to fit their 1-butanol ignition delay data at $\phi = 1.0$ and 80 atm [11]. However, pre-ignition pressure rises are still evident in that study [11], so it remains uncertain whether those rises are due to genuine fuel chemistry or not. In contrast, Sarathy et al. [15] state that low-temperature reactivity is suppressed in their model due to a choice of a reaction rate parameter for the reaction $1\text{-hydroxybutyl} + \text{O}_2 = n\text{C}_3\text{H}_7\text{CHO} + \text{HO}_2$ that allows it to compete with the low-temperature chain-branching reactions. Due to the test time limit of the current experiments, we have not yet conducted CRV experiments at temperatures below 820 K. However, extension of our test times is planned that should provide valuable information to confirm or contradict the existence of NTC behavior at temperatures below 820 K.

To avoid the complication introduced by pre-ignition pressure perturbations, the CRV strategy was applied in the investigation of equivalence ratio and oxygen concentration dependence of 1-butanol ignition delay time at low temperatures. Figures 19 and 20 present comparisons of current CRV data at 20 atm and Sarathy et al. mechanism predictions at different equivalence ratios/oxygen concentrations. As shown in Fig. 19, the overall agreement between the trends of the data and modeling is reasonable; there is general agreement in terms of the magnitude of ignition delay data and the shape of the general temperature-dependent trend. The experimental variation with equivalence ratio at fixed oxygen concentration, however, is smaller than in the simulation. Agreement is good for the rich mixtures in the case of fixed fuel concentration

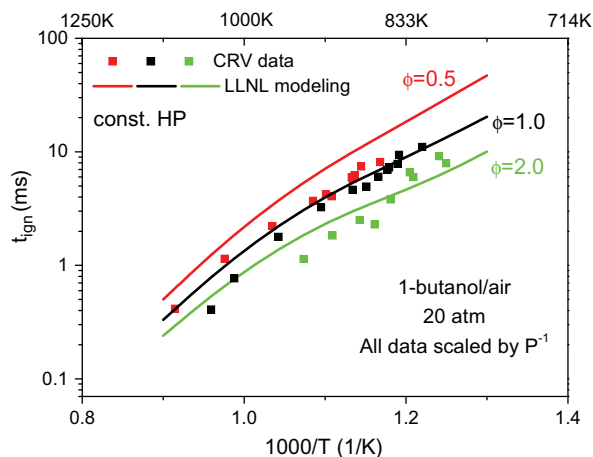


Fig. 19. Comparison of current CRV data and Sarathy et al. [15] mechanism predictions at $\phi = 0.5, 1.0, 2.0$, 20 atm with oxygen concentration held fixed ($\sim 20\%$).

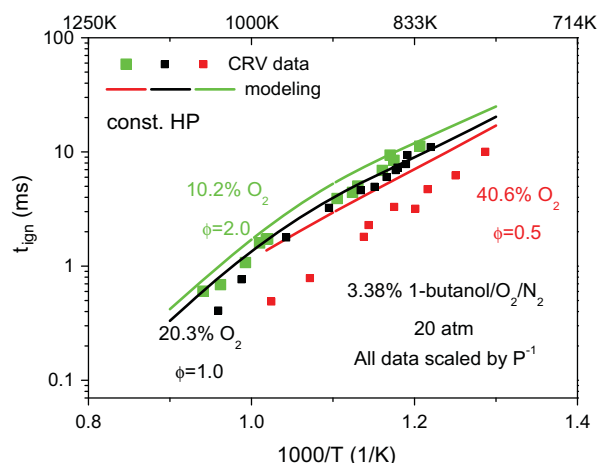


Fig. 20. Comparison of current CRV data and Sarathy et al. [15] mechanism predictions at $\phi = 0.5, 1.0, 2.0$, 20 atm with fuel concentration held fixed (3.38%).

(3.38%) and the 10.2% and 20.3% oxygen concentrations, as shown in Fig. 20. However, the simulations fail to predict the strong oxygen concentration dependence between 20.3% and 40.6% O_2 . Modeling results using two other mechanisms [14,15] (not shown) also fail to predict this strong oxygen concentration dependence. Lastly, these equivalence ratio/oxygen concentration dependences appear to be qualitatively in good agreement with those found by Weber et al. [6].

4. Conclusions

Ignition delay time measurements were carried out at elevated pressures and low temperatures for 1-butanol/ O_2/N_2 mixtures at various equivalence ratios/oxygen concentrations using both conventional-filling and staged-filling strategies. Conventional-filling experiments with pre-ignition pressure perturbations were inherently difficult to interpret and it is uncertain which gasdynamic model is the most appropriate to use in simulations. To resolve this problem, we applied the CRV concept and showed that this new strategy enables the generation of a wide range of ignition delay data that can be modeled effectively using a constant or specified P, H gasdynamic assumption. Using this CRV strategy, more confident comparisons of data with simulations from existing 1-butanol detailed reaction mechanisms are now possible. The current 1-butanol ignition delay time data does not show NTC behavior at the conditions of this study, in agreement with several of the models tested. We expect that besides the advantage of offering accurate constant P, H target data at low temperatures for modeling, the CRV concept will enable a quantitative experiment throughout the entire oxidation process, via species and temperature time-history measurements, thereby providing more extensively meaningful datasets in evaluating and refining detailed kinetic mechanisms.

Acknowledgments

The authors would like to thank Isabelle L.R. Bec from RWTH Aachen for her assistance in the operation of the shock tube. This material is based upon work supported as part of the Combustion Energy Frontier Research Center (CEFR) funded by the US Department of Energy, Office of Basic Energy Sciences under Award Number DE-SC0001198. The ongoing development of the CRV methodology is funded by the Army Research Office, with Dr. Ralph Anthenien as contract monitor.

References

- [1] S. Atsumi, T. Hanai, J.C. Liao, *Nature* 451 (7174) (2008) 86–U13, <http://dx.doi.org/10.1038/Nature06450>.
- [2] K. Kohse-Hoinghaus, P. Osswald, T.A. Cool, T. Kasper, N. Hansen, F. Qi, C.K. Westbrook, P.R. Westmoreland, *Angew. Chem., Int. Ed.* 49 (21) (2010) 3572–3597, <http://dx.doi.org/10.1002/anie.200905335>.
- [3] K.A. Heufer, R.X. Fernandes, H. Olivier, J. Beckmann, O. Rohl, N. Peters, *Proc. Combust. Inst.* 33 (2011) 359–366.
- [4] J.T. Moss, A.M. Berkowitz, M.A. Oehlschlaeger, J. Biet, V. Warth, P.A. Glaude, F. Battin-Leclerc, *J. Phys. Chem. A* 112 (43) (2008) 10843–10855.
- [5] I. Stranic, D.P. Chase, J.T. Harmon, S. Yang, D.F. Davidson, R.K. Hanson, *Combust. Flame* 159 (2) (2012) 516–527.
- [6] B.W. Weber, K. Kumar, Y. Zhang, C.J. Sung, *Combust. Flame* 158 (5) (2011) 809–819.
- [7] J.X. Zhang, L.J. Wei, X.J. Man, X. Jiang, Y.J. Zhang, E.J. Hu, Z.H. Huang, *Energy Fuels* 26 (6) (2012) 3368–3380.
- [8] J.H. Cai, L.D. Zhang, F. Zhang, Z.D. Wang, Z.J. Cheng, W.H. Yuan, F. Qi, *Energy Fuels* 26 (9) (2012) 5550–5568.
- [9] A. Frassoldati, R. Grana, T. Faravelli, E. Ranzi, P. Osswald, K. Kohse-Hoinghaus, *Combust. Flame* 159 (7) (2012) 2295–2311.
- [10] P. Dagaut, S.M. Sarathy, M.J. Thomson, *Proc. Combust. Inst.* 32 (2009) 229–237.
- [11] S. Vranckx, K.A. Heufer, C. Lee, H. Olivier, L. Schill, W.A. Kopp, K. Leonhard, C.A. Taatjes, R.X. Fernandes, *Combust. Flame* 158 (8) (2011) 1444–1455.
- [12] G. Black, H.J. Curran, S. Pichon, J.M. Simmie, V. Zhukov, *Combust. Flame* 157 (2) (2010) 363–373.
- [13] R. Grana, A. Frassoldati, T. Faravelli, U. Niemann, E. Ranzi, R. Seiser, R. Cattolica, K. Seshadri, *Combust. Flame* 157 (11) (2010) 2137–2154.
- [14] S.S. Merchant, E.F. Zanoelo, R.L. Speth, M.R. Harper, K.M. Van Geem, W.H. Green, *Combust. Flame* (2013), <http://dx.doi.org/10.1016/j.combustflame.2013.04.023>.
- [15] S.M. Sarathy, S. Vranckx, K. Yasunaga, M. Mehl, P. Oßwald, W.K. Metcalfe, C.K. Westbrook, W.J. Pitz, K. Kohse-Hoinghaus, R.X. Fernandes, H.J. Curran, *Combust. Flame* 159 (6) (2012) 2028–2055, <http://dx.doi.org/10.1016/j.combustflame.2011.12.017>.
- [16] D.F. Davidson, B.M. Gauthier, R.K. Hanson, *Proc. Combust. Inst.* 30 (2005) 1175–1182.
- [17] G.A. Pang, D.F. Davidson, R.K. Hanson, *Proc. Combust. Inst.* 32 (2009) 181–188.
- [18] H.K. Ciezki, G. Adomeit, *Combust. Flame* 93 (4) (1993) 421–433.
- [19] K. Fieweger, R. Blumenthal, G. Adomeit, *Combust. Flame* 109 (4) (1997) 599–619.
- [20] U. Pfahl, K. Fieweger, G. Adomeit, *Symp. Int. Combust.* 26 (1) (1996) 781–789, [http://dx.doi.org/10.1016/S0082-0784\(96\)80287-6](http://dx.doi.org/10.1016/S0082-0784(96)80287-6).
- [21] E.L. Petersen, D.M. Kalitan, A.B. Barrett, S.C. Reehal, J.D. Mertens, D.J. Beerer, R.L. Hack, V.G. McDonell, *Combust. Flame* 149 (1–2) (2007) 244–247.
- [22] J. Herzler, L. Jerig, P. Roth, *Combust. Sci. Technol.* 176 (10) (2004) 1627–1637.
- [23] P. Cadman, G.O. Thomas, P. Butler, *Phys. Chem. Phys.* 2 (23) (2000) 5411–5419.
- [24] S.S. Vasu, D.F. Davidson, R.K. Hanson, *J. Propul. Power* 26 (4) (2010) 776–783.
- [25] S.S. Vasu, D.F. Davidson, Z. Hong, V. Vasudevan, R.K. Hanson, *Proc. Combust. Inst.* 32 (2009) 173–180.
- [26] A. Roubaud, R. Minetti, L.R. Sochet, *Combust. Flame* 121 (3) (2000) 535–541.
- [27] S. Tanaka, F. Ayala, J.C. Keck, *Combust. Flame* 133 (4) (2003) 467–481.
- [28] J.F. Griffiths, W. Nimmo, *Combust. Flame* 60 (2) (1985) 215–218, [http://dx.doi.org/10.1016/0010-2180\(85\)90009-4](http://dx.doi.org/10.1016/0010-2180(85)90009-4).
- [29] G. Konig, C.G.W. Sheppard, *SAE Paper No.* 902135 (1990) 820–839.
- [30] K.Y. Lam, Z. Hong, D.F. Davidson, R.K. Hanson, *Proc. Combust. Inst.* 33 (2011) 251–258.
- [31] C. Lee, S. Vranckx, K.A. Heufer, S.V. Khomik, Y. Uygun, H. Olivier, R.X. Fernandes, *Z. Phys. Chem.* 226 (1) (2012) 1–27.
- [32] K.A. Heufer, H. Olivier, S.P. Medvedev, S.V. Khomik, in: *ICDERS*, vol. 163, Irvine, USA, 2011.
- [33] R.K. Hanson, G.A. Pang, S. Chakraborty, W. Ren, S. Wang, D.F. Davidson, *Combust. Flame* (2013), <http://dx.doi.org/10.1016/j.combustflame.2013.03.026>.
- [34] Z.K. Hong, G.A. Pang, S.S. Vasu, D.F. Davidson, R.K. Hanson, *Shock Waves* 19 (2) (2009) 113–123, <http://dx.doi.org/10.1007/s00193-009-0205-y>.
- [35] E.L. Petersen, R.K. Hanson, *Shock Waves* 10 (6) (2001) 405–420.
- [36] R. Blumenthal, K. Fieweger, K.H. Komp, G. Adomeit, *Combust. Sci. Technol.* 113 (1996) 137–166.
- [37] A.K. Oppenheim, *Philos. Trans. R. Soc. London, A* 315 (1534) (1985) 471–508.
- [38] C.J. Brown, G.O. Thomas, *Combust. Flame* 117 (4) (1999) 861–870.
- [39] M. Chaos, F.L. Dryer, *Int. J. Chem. Kinet.* 42 (3) (2010) 143–150.
- [40] CHEMKIN-PRO, in: *CHEMKIN-PRO* (Ed.), Reaction Design, Inc., San Diego, CA, 2010, vol. Release 15101.
- [41] C.J. Aul, E.L. Petersen, H.J. Curran, M. Fikri, C. Schulz, in: *ICDERS*, vol. 110, Irvine, USA, 2011.
- [42] F.L. Dryer, Marcos Chaos, *Int. J. Chem. Kinet.* 42 (2010) 143–150, <http://dx.doi.org/10.1002/kin.20471>.
- [43] F.L. Dryer, M. Chaos, *Combust. Flame* 152 (1–2) (2008) 293–299.
- [44] H.P.S. Shen, J. Vanderover, M.A. Oehlschlaeger, *Proc. Combust. Inst.* 32 (2009) 165–172.
- [45] D.F. Davidson, R.K. Hanson, *Int. J. Chem. Kinet.* 36 (9) (2004) 510–523.
- [46] Y.J. Zhang, Z.H. Huang, J.H. Wang, S.L. Xu, *Chin. Sci. Bull.* 56 (1) (2011) 85–93.

Multi-species time-history measurements during *n*-hexadecane oxidation behind reflected shock waves

D.R. Haylett, D.F. Davidson^{*}, R.D. Cook, Z. Hong, W. Ren,
S.H. Pyun, R.K. Hanson

Mechanical Engineering Department, Stanford University, Stanford, CA 94305, United States

Available online 20 September 2012

Abstract

Species concentration time-histories were measured during oxidation for the large, normal-alkane, diesel-surrogate component *n*-hexadecane. Measurements were performed behind reflected shock waves in an aerosol shock tube, which allowed for high fuel loading without pre-test heating and possible decomposition and oxidation. Experiments were conducted using near-stoichiometric mixtures of *n*-hexadecane and 4% oxygen in argon at temperatures of 1165–1352 K and pressures near 2 atm. Concentration time-histories were recorded for five species: C₂H₄, CH₄, OH, CO₂, and H₂O. Methane was monitored using DFG laser absorption near 3.4 μm; OH was monitored using UV laser absorption at 306.5 nm; C₂H₄ was monitored using a CO₂ gas laser at 10.5 μm; and CO₂ and H₂O were monitored using tunable DFB diode laser absorption at 2.7 and 2.5 μm, respectively. These time-histories provide critically needed kinetic targets to test and refine large reaction mechanisms. Comparisons were made with the predictions of two diesel-surrogate reaction mechanisms (Westbrook et al. [1]; Ranzi et al. [9]) that include *n*-hexadecane, and areas of needed improvement in the mechanisms were identified. Comparisons of the intermediate product yields of ethylene for *n*-hexadecane with those found for other smaller *n*-alkanes, show that an *n*-hexadecane mechanism derived from a simple hierarchical extrapolation from a smaller *n*-alkane mechanism does not properly simulate the experimental measurements.

© 2012 The Combustion Institute. Published by Elsevier Inc. All rights reserved.

Keywords: *n*-Hexadecane oxidation; Laser absorption; Species time-histories; Shock tube; *n*-Alkane mechanisms

1. Introduction

Current mechanism development strategies for large *n*-alkanes rely on a hierarchical approach that bases the requisite chemistry for larger *n*-alkanes on the sub-mechanisms developed for smaller *n*-alkanes. Using this methodology, several mechanisms that cover *n*-hexadecane oxidation have been developed; a review of recent

large *n*-alkane model development can be found in Westbrook et al. [1].

However, because of the low vapor pressure of the larger *n*-alkanes (e.g., *n*-dodecane and *n*-hexadecane), gas-phase experiments with these fuels are considerably more complicated to perform, and little data are available to validate this hierarchical assumption. One of the objectives of the shock tube research program at Stanford University is to provide data to fill this need.

Simulations of reflected shock wave experiments for a series of *n*-alkanes (*n*-heptane to

^{*} Corresponding author.

E-mail address: dfd@stanford.edu (D.F. Davidson).

n-hexadecane) using as an example one of the hierarchical models, the Westbrook et al. mechanism [1] (referred to in this paper as the LLNL C16 mechanism), predict that ignition delay times should be nearly identical for the entire series of *n*-alkanes. An experimental test of this prediction using ignition delay times is shown in Fig. 1. For *n*-heptane and *n*-dodecane at high pressures (20 atm) shown in Fig. 2, the simulated ignition delay times are similar (within ~20%), while the experimental values are significantly different (~2× and greater). In particular, at the temperatures of this comparison (below 1250 K), the ignition delay times of the simulations are always longer than the experiment, and significantly longer for the larger *n*-dodecane. Similar trends in the variation with carbon number are seen in the work of Shen et al. [4] who performed ignition delay time measurements for C7 to C14 alkanes. Those measurements, however, show smaller variations with carbon chain length than Vasu et al.

Though the LLNL C16 model does not accurately capture the low-temperature, high-pressure behavior for these two *n*-alkanes, it does fare better for *n*-hexadecane at higher temperatures and low pressures (2 atm) as shown in Fig. 2. Here the approximate similarity of model and experiment is evident; the activation energies differ only by 6%, and the ignition delay times by 60%. Considering that very few kinetic target data existed when the LLNL mechanism was developed, this is a very good first effort. Of note is the difference in the simulation behavior with pressure; the simulations at low pressures (Fig. 2) under-predict the ignition delay times, while at high pressures, (Fig. 1) the simulations over-predict the data. This variation may be linked to the sub-mechanism for ethylene oxidation, a key *n*-hexadecane decomposition

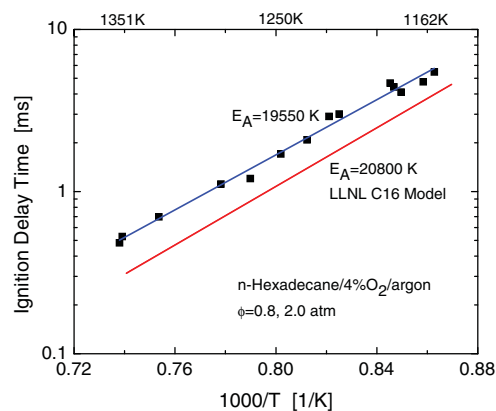


Fig. 2. Simulation and experiment: *n*-hexadecane/4% O₂/Argon ignition delay times for 2 atm, $\phi = 0.8$. *n*-Hexadecane measurements from Haylett et al. [3].

species, which does not capture the pressure dependence of ethylene ignition delay times at high pressures and work is continuing at LLNL and NUI/Galway to update and refine this aspect of the mechanism. (W.J. Pitz, private communication).

The LLNL C16 mechanism also predicts that the species time histories of large *n*-alkanes should be very similar. Figure 3 shows a comparison of the major species time-histories during *n*-dodecane and *n*-hexadecane oxidation. Time scales and plateau values of key species are predicted to be nearly identical for similar temperatures, stoichiometries and fuel carbon loading.

With a model as large as the LLNL C16 mechanism (2115 species, 8157 reactions), which data should an experimentalist acquire to provide kinetic targets for the improvement of the mechanism? Because ignition delay time measurements

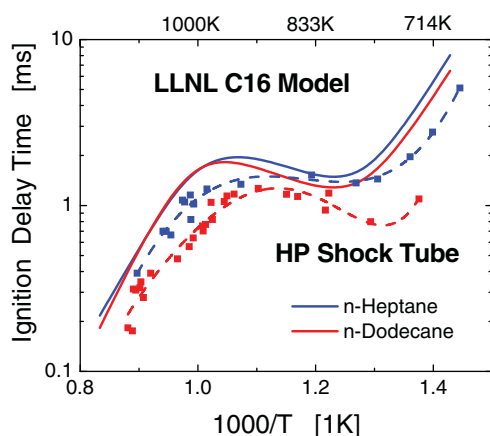


Fig. 1. Simulation and experiment: *n*-alkane/air ignition delay times for 20 atm, $\phi = 1$. *n*-Dodecane measurements from Vasu et al. [2] and *n*-heptane measurements from Vasu et al. [10].

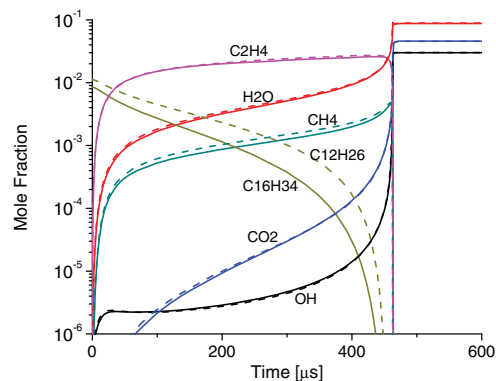


Fig. 3. Simulations of *n*-dodecane (dashes) and *n*-hexadecane (solid) oxidation using the LLNL C16 mechanism. Initial conditions: fuel/21% O₂/Argon, $\phi = 1$, 1250 K (C₁₆H₃₄), 1258 K (C₁₂H₂₆), 2 atm, constant volume constraint.

are a global test of the model and provide only a limited constraint on the details of the mechanism (many different mechanisms can reproduce ignition delay times with similar fidelity), information about the individual species behavior is needed. Such speciation data, in the form of species concentration time-history measurements, can be obtained in simple systems such as near-constant-volume shock tube experiments. The aerosol shock tube used in conjunction with laser absorption diagnostics, in particular, is well-suited to provide this type of data for low-vapor-pressure fuels.

Laser-absorption measurements in shock tubes can be used to provide kinetic targets in three different types of experiments: ignition delay times, species concentration time-histories, and direct measurements of elementary reaction rates. While there continues to be increasing experimental coverage of ignition delay times for different fuels and conditions, there is still only a limited amount of species concentration time-history and elementary reaction rate data available. These species and rate data are critically important to efforts aimed at testing and validating large reaction mechanisms and refining their component sub-mechanisms.

In our laboratory, we have developed sensitive, species-specific, and quantitative UV and visible laser absorption diagnostics for an array of important combustion species including OH, CH₃, CH, NH₂, and NO [5]. Recently, we have extended the wavelength range of our suite of laser absorption diagnostics into the infrared. Using commercially available IR gas and diode lasers we have developed quantitative measurement capabilities for C₂H₄, H₂O, CO₂, CH₄ and selected *n*-alkanes [6]. Use of these laser absorption diagnostics in shock tubes has allowed the generation of unique multi-species time-histories under near-constant-volume conditions, intended as targets for chemical kinetic modeling.

To elucidate the inner workings of the large reaction mechanisms describing *n*-hexadecane, we have applied this multi-species strategy to the measurement of several important transient species that appear during *n*-hexadecane oxidation: OH, C₂H₄, H₂O, CO₂, and CH₄. Time-history measurements of OH are extremely useful in quantifying ignition processes, as they provide critical information about the radical-pool population. Time-history measurements of ethylene, C₂H₄, provide quantitative information on the main high-temperature decomposition product and the pathways of alkanes. While others have measured stable intermediate and product species during hexadecane and diesel combustion in a jet-stirred reactor (JSR) [7], those measurements do not provide the detailed information on the short, transient time scales that are available with shock tube/laser absorption experiments.

Here we present speciation measurements during the oxidation of *n*-hexadecane over a range of

temperatures from 1165 to 1352 K, pressures near 2 atm, oxygen concentrations of 4% in argon, and equivalence ratios of 0.8–1. This is an extension of our earlier preliminary study [8] of the same fuel for a limited set of species (OH and C₂H₄) that was performed at higher pressures (4–7 atm) and lower oxygen content (1% in argon) and higher equivalence ratios (1.2).

Comparisons are given of these species concentration time-histories with two current large *n*-alkane mechanisms: the LLNLC16 mechanism of Westbrook et al. [1] and the Ranzi et al. C16 mechanism [9]. Comparisons of the *n*-hexadecane data are also made with the intermediate product yields for two other large *n*-alkanes: *n*-heptane and *n*-dodecane, also acquired in our laboratory.

2. Experimental setup

2.1. Aerosol shock tube facility

Experiments were performed in the Stanford 4" (10 cm) Aerosol Shock Tube [10]. This shock tube has an electro-polished stainless steel and fluoropolymer-coated aluminum driven section with length/diameter (*L/D*) ratio of 96 and used a helium-filled driver section with an *L/D* of 36 to burst 0.25 mm thick polycarbonate diaphragms (against a crossed-knife arrangement in a short square section of the shock tube). The shock tube is sealed with Viton O-rings, is operated at room temperature (i.e., without heating) and is mechanically pumped. Typically reflected shock wave experiments were performed hourly and over this time frame the ultimate shock tube pressure before filling was ~0.05 torr (because of the large liquid volume deposited into the shock tube) and the leak and outgassing rate was 0.05 torr/min.

Mixtures were made in the aerosol mixing plenum using 4% O₂ in argon carrier gas (Praxair, research grade) and a bath of *n*-hexadecane (Sigma). The aerosol is first created in a mixing tank connected to the endwall of the shock tube, using a bank of ultrasonic nebulizers, and introduced through an endwall gate valve. The aerosol is slowly pulled into the test section (by a vacuum line located near the upstream gate valve) to ensure uniformity of the test mixture. When the test volume is filled with aerosol mixture, the upstream gate valve is opened and the endwall gate valve is closed. The diaphragm at the driver section is then burst (using high-pressure helium), and an incident shock wave is sent towards the endwall; typical conditions behind the incident shock wave are in the range of 600–800 K, and 0.6 atm. As the incident shock passes through the fuel aerosol, with a typical average droplet diameter of ~4 μm [9], the fuel is rapidly evaporated and diffusively mixed. Initial gas-phase fuel concentration is measured using laser absorption

at 3.39 μm in this fully-evaporated fuel mixture behind the incident shock wave, with a typical uncertainty of approximately $\pm 2\%$. The incident shock wave is reflected from the endwall, and this reflected shock wave further heats the gaseous mixture to combustion temperatures and pressures.

Incident shock speeds were determined by measuring the incident shock arrival times using a series of 5 small-diameter piezo-electric pressure transducers (PZT) (PCB model 132) spaced at approximately 30 cm intervals over about the last meter of the driven section and recorded using a National Instruments DAQ system. Incident shock speeds were extrapolated to the end wall position and reflected shock conditions were calculated using an in-house-developed chemically frozen aerosol shock code (AEROFROSH) [11] and thermodynamic database from Kee et al. [12]. The resulting uncertainty in reflected shock temperatures over test times of 1 ms (typical for these experiments) was $< \pm 1\%$ or 13 K at $T_5 = 1300$ K. Uncertainty in the reflected shock pressure P_5 was also $< \pm 1\%$ and was confirmed with equal uncertainty using a sidewall PZT pressure measurement (Kistler model 601B1).

2.2. Laser absorption measurements

Species concentration time-history measurements were made using laser absorption.

Laser absorption of OH: OH concentration was measured using narrow-linewidth laser absorption near 306.7 nm. The chosen wavelength was the peak of the well-characterized $R_1(5)$ absorption line in the OH A-X (0, 0) band [12]. CW laser light at 613.4 nm was generated by a Spectra Physics 380 dye laser pumped by a 5 W Coherent Verdi at 532 nm. Light at 306.7 nm was generated by intracavity frequency-doubling, using a temperature-tuned AD^A crystal. The peak wavelength was set using a wavemeter and confirmed by experiments at off-center wavelengths. Common mode rejection was used to reduce laser intensity noise to $< 0.1\%$, resulting in a minimum detection sensitivity of < 1 ppm for most conditions in this work. OH concentration was calculated using Beer's law:

$$I/I_0 = \exp(-k_v P_{\text{total}} X_{\text{OH}} L) = \exp(-\alpha) \quad (1)$$

where I and I_0 are the transmitted and incident beam intensities, k_v is the line-center absorption coefficient at 306.7 nm for OH, P_{total} is the total test gas mixture pressure, X_{OH} is the OH mole fraction, and L is the pathlength, 10 cm in the current experiments; the combined quantity α is termed the absorbance. The estimated uncertainty in measured X_{OH} is $\sim 3\%$ [13].

Measurements were also performed with the laser tuned off the OH absorption line, and separately with the laser turned off, to verify that there

was no significant interfering absorption or emission. Further details of the OH laser absorption diagnostic are available elsewhere [13].

IR diode laser absorption of CO₂ and H₂O: The recent commercial availability of DFB (distributed feedback) diode lasers emitting in the wavelength range of 2.5–2.7 μm has opened up a new diagnostic window to combustion products. Using these lasers we have developed a CO₂ absorption diagnostic near 2.7 μm [14] and H₂O diagnostic near 2.5 μm [15].

Absorption measurements of CO₂ were made with a fixed-wavelength (using the R(28) transition at 2752.5 nm) direct-absorption strategy that provided a sensor bandwidth of about 1 MHz. Ability to make accurate measurements of CO₂ concentration has previously been demonstrated in CO₂–Ar mixtures over a temperature range of 300–1500 K [14]. Quantitative CO₂ concentration profiles were generated from the raw traces of fractional absorption using Beer's law and the known absorption coefficient. Minimum CO₂ detectivities are of the order of 300 ppm in the current experiments.

The detection of water has also been demonstrated previously [15], using the same DFB laser technology at wavelengths of 2.5 μm . Water concentration time-histories were measured here using the IR transition centered at 2550.96 nm within the ν_3 fundamental vibrational band. This line was selected primarily because of its favorable line strength. The line strength and broadening coefficients of this line were characterized in heated cell experiments before conducting the chemical kinetic studies in a shock tube [15]. In a typical shock tube experiment, with reflected shock temperatures and pressures of 1100 K and 2 atm, 1000 ppm of H₂O in argon over a pathlength of 14 cm gives a strong peak absorbance of approximately 7% with a typical signal-to-noise ratio (SNR) of 50–80.

In part because of the effect of temperature and pressure on the absorption coefficients for CO₂ and H₂O, an explicit time-dependent absorption coefficient based on the measured pressure and kinetically modeled temperature is used to convert CO₂ and H₂O absorbance to mole fraction. High precision measurements ($\sim \pm 5\%$) of CO₂ and H₂O are possible, if the temperature and pressure are well-established, because of the high accuracy to which the absorption coefficients for these two transitions are known. As will be noted later, temperatures and pressures in the current experiments are well-established up to the point of ignition.

IR DFG laser absorption of methane: A novel, mid-IR scanned-wavelength laser absorption diagnostic was used for time-resolved, interference-free, absorption measurement of methane concentration [16]. The scanned-wavelength diagnostic uses a differential absorption (peak minus valley) scheme that takes advantage of the spectral

structure difference between methane and the dominant interference species, *n*-hexadecane. Tunable mid-IR light was generated using a difference-frequency-generation (DFG) laser and scanned over a peak and valley ($2938.24\text{--}2938.01\text{ cm}^{-1}$) structure of methane absorption spectrum with 50 kHz scanning frequency. As the majority of this broadband interference absorption is from *n*-hexadecane, this method can be used to monitor its concentration as well.

CO_2 laser absorption of C_2H_4 : Ethylene mole fraction was monitored by taking advantage of the fortuitous overlap of the P(14) line of the CO_2 gas laser at $10.532\text{ }\mu\text{m}$ with the strong ethylene absorption band near $10.6\text{ }\mu\text{m}$ [17]. Similar to the situation with the C–H stretch absorption band near $3.39\text{ }\mu\text{m}$, there is a wide CH_2 wag absorption feature near $10.6\text{ }\mu\text{m}$ that is shared in varying (but weaker) strengths (at the P(14) line in particular) by other alkenes (e.g., ethylene, propene, butene, etc.) Over the experimental timeframe of the current experiments, absorption at $10.532\text{ }\mu\text{m}$ is dominated by ethylene absorption.

High-temperature absorption cross-sections of ethylene and related alkenes (as well as CO_2 and H_2O) and experimental details are also discussed in Pilla et al. [18].

Finally, because of the difference in ignition delay times between the simulations and experiments, relevant comparisons can best be made with the early time behavior of the simulations, the peak or plateau values of each of the measured species, and the species formation rates. Species concentration values after the ignition event (e.g., after $600\text{ }\mu\text{s}$ in the 1352 K example) are only given approximately in these experiments because of the non-constant-volume behavior of the test gas that occurs when there is large energy release. Uncertainties in the test gas temperature, because of this non-constant-volume behavior, can affect the absorption cross-sections used in the mathematical conversion of absorbance to mole fraction.

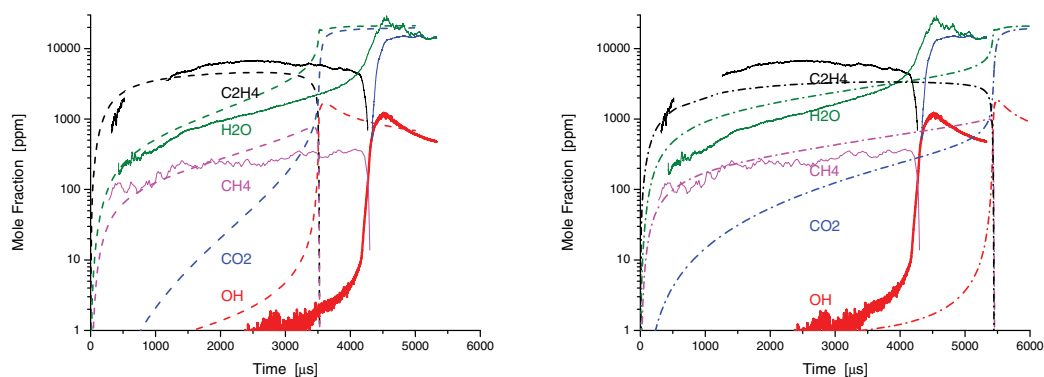
3. Results and discussion

Figures 4–9 show measured species time-histories for three temperatures (1165 , 1247 , and 1352 K) during *n*-hexadecane (fuel) oxidation, and simulations using the Westbrook et al. C16 LLNL mechanism and the Ranzi et al. C16 mechanism. The, C_2H_4 , CO_2 and OH time-histories provide good indicators of the ignition delay times, and H_2O provides a good measure of the rate of reaction progress in the pre-ignition interval. In all cases, the Westbrook et al. simulations of the ignition delay times are shorter than the measured values and the Ranzi et al. simulated ignition delay times are longer.

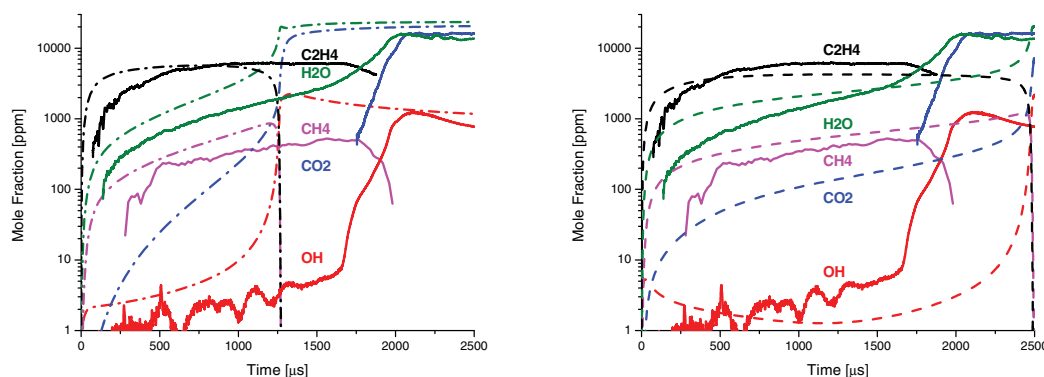
Formation rates and rise times for the intermediate and combustion products appear to be

relatively similar between the models and the experiment at 1165 K , though these times comprise only a small fraction of the entire ignition delay time. However at 1247 and 1352 K , the simulated species profiles rise significantly faster than the measured species profiles; this is particularly evident in the OH and C_2H_4 time-histories. A Rate of Production (ROP) analysis based on the LLNL mechanism (not shown here) indicates that in the case of OH, the initial OH peak is a result of a sensitive balance (i.e., a difference of two large opposing production and removal rates) between OH formation by the reaction $\text{H} + \text{O}_2$ (with a reaction rate constant that is very well-known [19]) and OH removal by the reactions of OH with *n*-hexadecane. The concentration of H-atoms feeding the $\text{H} + \text{O}_2$ reaction is determined also from a balance between formation from alkyl radical decomposition, in particular $\text{C}_2\text{H}_5 \rightarrow \text{C}_2\text{H}_4 + \text{H}$, and removal by $\text{H} + n\text{-hexadecane}$. The alkyl radical concentration is formed directly from fuel decomposition pathways. The measured time of formation for the first plateau of OH at 1352 K is approximately $100\text{ }\mu\text{s}$. The slower measured formation rate of OH must therefore be related to a faster removal rate by the reaction of OH + *n*-hexadecane, or a slower formation rate of H-atoms in the experiment (either by a slower alkane decomposition rate, by a slower alkyl decomposition rate, or a scavenging of H-atoms by reaction with fuel or intermediate fuel decomposition products). No evidence of the initial sharp OH formation peak seen in the simulations at the two higher temperatures is seen in the measurements. However, it is worth noting that in simulations of OH time-histories during *n*-dodecane oxidation [6] using the same LLNL C16 large alkane mechanism, the initial OH formation rate was captured significantly better and an initial sharp OH formation peak was seen in both the data and simulation. At longer times, after the disappearance of the initial fuel concentration, the OH level is controlled mainly by a trade-off between formation by $\text{H} + \text{O}_2$ and removal by $\text{OH} + \text{C}_2\text{H}_4$ and $\text{OH} + \text{CH}_2\text{O}$.

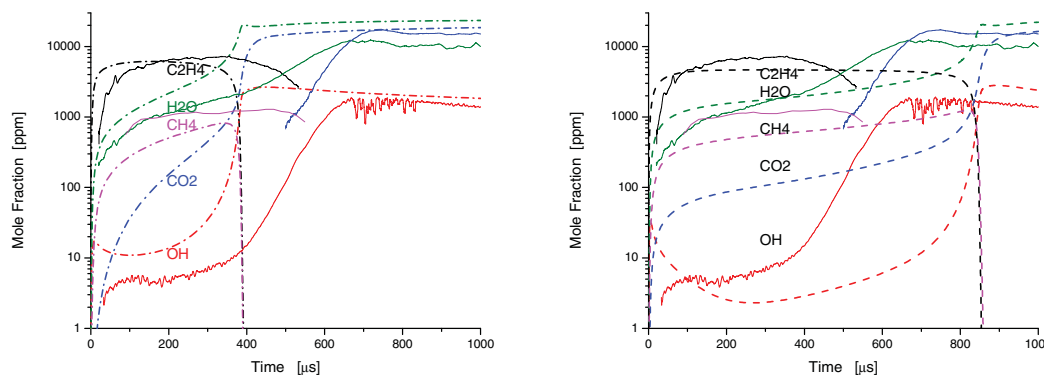
When the fuel decomposition is substantially complete, signaled by the formation of a plateau of the major alkene intermediate C_2H_4 , an OH plateau is also formed. This plateau level places a constraint on the competition between OH formation (via $\text{H} + \text{O}_2$) and OH removal by OH + alkenes (H-abstraction), the major reactive intermediate products. In the Westbrook et al. model, the plateau level is higher than the experiment and the ignition delay time is shorter; in the case of the Ranzi et al. model, the plateau level is lower than the experiment and the ignition delay time is longer. Accurately capturing the H-atom profile (also influenced by the $\text{H} + \text{fuel}$ and $\text{H} + \text{alkene}$ reactions) and implementation of accurate OH + alkene rate constants are both necessary to achieve a proper determination of the



Figs. 4 and 5. OH, H₂O, CH₄, CO₂, and C₂H₄ species time-histories during *n*-hexadecane oxidation behind reflected shock waves. Initial conditions: 1165 K, 2.08 atm, 1290 ppm C₁₆H₃₄/4% O₂/Ar, $\Phi = 0.79$. Simulations using the LLNL C16 mechanism (Fig. 4) and Ranzi et al. (Fig. 5).



Figs. 6 and 7. OH, H₂O, CH₄, CO₂, and C₂H₄ species time-histories during *n*-hexadecane oxidation behind reflected shock waves. Initial conditions: 1247 K, 1.83 atm, 1500 ppm C₁₆H₃₄/4% O₂/Ar, $\Phi = 0.92$. Simulations using the LLNL C16 mechanism (Fig. 6) and Ranzi et al. (Fig. 7).



Figs. 8 and 9. OH, H₂O, CH₄, CO₂, and C₂H₄ species time-histories during *n*-hexadecane oxidation behind reflected shock waves. Initial conditions left frame: 1352 K, 1.71 atm, 1565 ppm C₁₆H₃₄/4% O₂/Ar, $\Phi = 0.96$. Simulations using the LLNL C16 mechanism (Fig. 8) and Ranzi et al., (Fig. 9).

ignition delay time consistent with the measured time-history profiles.

The measured plateau level of C₂H₄ (~5.2 C₂H₄ formed per C₁₆H₃₄ at 1165 K, i.e., 65%

conversion of carbon atoms to C₂H₄, and ~4.6 C₂H₄ formed at 1352 K, i.e., 48% conversion to C₂H₄) place constraints on the fuel decomposition pathways. In both the Westbrook et al., and the

Ranzi et al. simulations, the plateau values of C_2H_4 are generally smaller than the measured values. Thus, other intermediate products, including propene (not measured here) and methyl radicals (which convert to methane that is measured here), should have larger predicted values. At 1165 K, the methane yields are approximately correct for both models over the first 2 ms, but at 1247–1352 K, both models do not accurately predict the methane yields (factor of 2 variation). Re-evaluations and measurements of the rate constants and branching ratios for the decomposition pathways for *n*-hexadecane and for the reactions of *n*-hexadecane with OH and H are needed to resolve these differences.

In the earlier preliminary study [8] of *n*-hexadecane oxidation using similar methodology, the measured C_2H_4 plateau levels were found to be smaller than the LLNL simulated values in all cases. In the present study, the measured C_2H_4 time-histories are smaller than the simulations during the first several hundred μ s, and this is consistent with the fact that the fuel decomposition rates in the mechanism are faster than those observed in both experiments. The earlier preliminary experiments were performed with significantly less fuel (typically 500 ppm) than the current study and at higher pressures (4–7 atm), lower oxygen content (1% in argon) and higher equivalence ratios (1.2). At the lower pressures and higher fuel concentration of the current study, the LLNL model under-estimates the final C_2H_4 yields; thus at these different conditions, the LLNL model shows either less production of C_2H_4 through fuel decomposition, or more removal of C_2H_4 through radical reactions than measured.

3.1. Comparison with smaller *n*-alkanes

As noted above, in the previous *n*-dodecane oxidation study, the early-time simulated OH profiles using the LLNL C16 mechanism approximately match the measured OH profiles [5]. However, in the current *n*-hexadecane oxidation experiments, the early-time simulated OH profiles using the same LLNL C16 mechanism poorly capture the measured OH profiles. This difference may be related to the fuel decomposition rates and branching ratios used for *n*-hexadecane. The strong predicted similarity in the species time-histories for different large *n*-alkanes (see Fig. 3) can also be tested by a comparison of the intermediate product yields of ethylene for these fuels. Representative experimental data for the major intermediate fuel decomposition product, ethylene, are shown in Fig. 10 for *n*-heptane [20], *n*-dodecane [6] and the current *n*-hexadecane data.

In the experiments, approximately 63% of the fuel carbon is converted to ethylene before ignition for *n*-heptane; for *n*-dodecane we observed 50%, and for *n*-hexadecane 61%. The LLNL C16

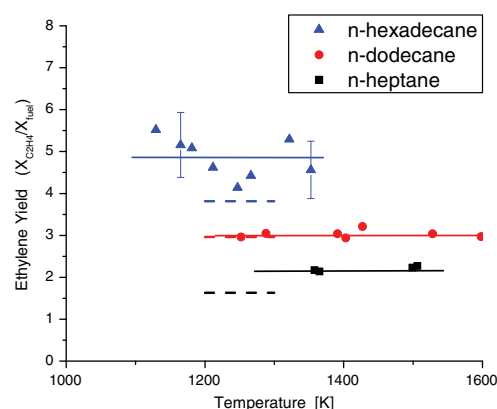


Fig. 10. Ethylene yields for large *n*-alkanes: *n*-heptane, *n*-dodecane and *n*-hexadecane. Low concentration, high-temperature oxidation and pyrolysis experiments combined. Typical mixtures: 2 atm, 300–1500 ppm fuel in argon or 4% O_2 /argon, $\Phi = 1$. Solid lines, best fit to data; dashed lines: LLNL C16 model simulations.

model predicts yields of 1.6 C_2H_4 per C_7H_{16} molecule, 3.0 C_2H_4 for $C_{12}H_{26}$ and 3.8 C_2H_4 for $C_{16}H_{34}$ near the conditions of Fig. 10, which are equivalent to 47–50% conversion to ethylene for the three fuels. While the LLNL C16 model is in good agreement with the ethylene yields for *n*-dodecane, it under-predicts the yields significantly for *n*-hexadecane (based on the average value over the measured temperature range), and thus may also not predict the other major decomposition products accurately. The simple hierarchical extension of the smaller *n*-alkane mechanism to form an *n*-hexadecane mechanism, while capturing many of the trends of the multi-species time-history data, thus leads to some inaccuracies in prediction for large carbon number alkanes.

4. Conclusion

Multi-species time-histories were measured during *n*-hexadecane oxidation. Measurements were performed behind reflected shock waves in an aerosol shock tube using high-sensitivity laser absorption, providing species time-histories for OH, C_2H_4 , CH_4 , H_2O , and CO_2 . A comparison of these measurements with simulations using hierarchically-based models finds significant differences in the time-history profiles of species and the levels of reaction products formed before ignition. Many of these differences can be attributed to uncertainties in the *n*-hexadecane decomposition pathways and reaction rate constants and reaction rate constants of OH and H with *n*-hexadecane. Measurements of these reaction rate constants are needed. The kinetic target data

assembled here should help provide stronger constraints for the testing and refinement of large *n*-alkane reaction mechanisms.

Acknowledgements

This work was supported by the Army Research Office under Contract Number W911NF-10-1-0125 with Dr. Ralph Anthenien as technical monitor.

Appendix A. Supplementary data

Supplementary data associated with this article can be found, in the online version, at <http://dx.doi.org/10.1016/j.proci.2012.06.014>.

References

- [1] C.K. Westbrook, W.J. Pitz, O. Herbinet, H.J. Curran, E.J. Silke, *Combust. Flame* 156 (2009) 181–199, available at http://www-pls.llnl.gov/?url=science_and_technology-chemistry-combustion.
- [2] S.S. Vasu, D.F. Davidson, Z. Hong, V. Vasudevan, R.K. Hanson, *Proc. Combust. Inst.* 32 (2009) 173–180.
- [3] D.R. Haylett, D.F. Davidson, R.K. Hanson, *Combust. Flame* 159 (2012) 552–561.
- [4] H.-P.S. Shen, J. Steinberg, J. Vanderover, M.A. Oehlschlaeger, *Energy Fuels* 23 (2009) 2482–2489.
- [5] D.F. Davidson, R.K. Hanson, in: G. Ben-Dor, O. Igra, T. Elperin, (Eds.), *Handbook of Shock Waves*, Vol. 1, Academic Press, San Diego, 2001 (Chapter 5.2).
- [6] D.F. Davidson, Z. Hong, G.L. Pilla, A. Farooq, R.D. Cook, R.K. Hanson, *Proc. Combust. Inst.* 33 (2011) 151–157.
- [7] A. Ristori, P. Dagaut, M. Cathonnet, *Combust. Flame* 125 (2001) 1128–1137.
- [8] D.R. Haylett, R.D. Cook, D.F. Davidson, R.K. Hanson, *Proc. Combust. Inst.* 33 (2011) 167–173.
- [9] E. Ranzi, M. Dente, A. Goldaniga, G. Bozzano, T. Faravelli, *Prog. Energy Combust. Sci.* 27 (2001) 99–139; see also E. Ranzi, A. Frassoldati, S. Granata, T. Faravelli, *Ind. Eng. Chem. Res.* 44 (2005) 5170–5183, available at <http://creckmodeling.chem.polimi.it/kinetic.html>.
- [10] S.S. Vasu, unpublished, Stanford University, 2009.
- [11] D.R. Haylett, P.P. Lappas, D.F. Davidson, R.K. Hanson, *Proc. Combust. Inst.* 32 (2009) 477–484; see also, D.R. Haylett, D.F. Davidson, R.K. Hanson, *J. Shock Waves*, in press; see also D.F. Davidson, D.R. Haylett, R.K. Hanson, *Combust. Flame* 155 (2008) 108–117.
- [12] R.J. Kee, F.M. Rupley, J.A. Miller, *The Chemkin Thermodynamic Data Base*, Report No. SAND-87-8215B, Sandia National Labs., Livermore, CA, USA.
- [13] J.T. Herbon, R.K. Hanson, D.M. Golden, C.T. Bowman, *Proc. Combust. Inst.* 29 (2002) 1201–1208.
- [14] A. Farooq, D.F. Davidson, R.K. Hanson, L.K. Huynh, A. Violi, *Proc. Combust. Inst.* 32 (2009) 247–253.
- [15] A. Farooq, J.B. Jeffries, R.K. Hanson, *Meas. Sci. Technol.* 19 (2008) 075604, 11pp.
- [16] S.H. Pyun, J. Cho, D.F. Davidson, R.K. Hanson, *Meas. Sci. Technol.* 22 (2011) 025303, 9pp.
- [17] W. Ren, D.F. Davidson, R.K. Hanson, *Int. J. Chem. Kinet.*, doi:10.1002/kin.20599.
- [18] G.L. Pilla, D.F. Davidson, R.K. Hanson, *Proc. Combust. Inst.* 33 (2011) 333–340.
- [19] Z. Hong, D.F. Davidson, R.K. Hanson, *Proc. Combust. Inst.* 33 (2011) 309–316.
- [20] D.F. Davidson, Z. Hong, G.L. Pilla, A. Farooq, R.D. Cook, R.K. Hanson, *Combust. Flame* 157 (2010) 1899–1905.

Second-generation aerosol shock tube: an improved design

D. R. Haylett · D. F. Davidson · R. K. Hanson

Received: 5 November 2009 / Revised: 20 May 2012 / Accepted: 21 May 2012 / Published online: 5 June 2012
© Springer-Verlag 2012

Abstract An improved, second-generation aerosol shock tube (AST II) has been developed for the study of the chemical kinetics of low-vapor-pressure fuels. These improvements enable a wider range of fuel concentrations and enhanced spatial uniformity relative to our initial aerosol shock tube (AST I). In addition, the design of AST II limits the aerosol loading zone in the shock tube to a fixed region (1.2 m in length adjacent to the shock tube endwall). AST II achieves these improvements using a separate holding tank to prepare the aerosol mixture and a slightly under-pressure dump tank to carefully pull the aerosol mixture into the tube in a plug-flow. This filling method is capable of producing room temperature test gas mixtures of *n*-dodecane with equivalence ratios of up to 3.0 in 21 % O₂, three times the loading achievable in the earlier AST I that used a flow-through strategy. Improvements in aerosol uniformity were quantified by measuring the liquid volume concentration at multiple locations in the shock tube. The measurements made over a length of 1.1 m of shock tube indicate that the AST II method of filling produces non-uniformities in liquid volume concentration of less than 2 %, whereas in the AST I method of filling the non-uniformities reached 16 %. The improved uniformity can also be seen in measurement of gas-phase fuel concentration behind the incident shock wave after the liquid droplets have evaporated. Significant reduction in the scatter of ignition delay times measured using AST II have also been achieved, confirming the importance of uniform

loading of the aerosol in making high-quality combustion measurements.

Keywords Aerosol · Shock tube · Combustion · Low-vapor pressure · Dodecane · Ignition delay times

1 Introduction

Although shock tubes are normally used to study purely gas-phase phenomena, they have also been used to study aerosols [1–11]. The primary challenge, however, in studying aerosols in shock tubes is in achieving a spatially uniform distribution of aerosol test mixture. A spatially non-uniform aerosol mixture can degrade the quality of the shock tube data; in earlier studies [1–11], non uniformity in the spatial distribution of the aerosol tended to limit the accuracy of the measurements and the determination of incident and reflected shock test conditions.

The conventional gas-driven shock tube is a proven device for the study of gas-phase chemical kinetics [12]. Most practical fuels, however, such as gasoline, jet fuel, and diesel fuel, are liquid at room temperature and have many constituent components that have very low vapor pressures. This prevents the creation of high-concentration gas-phase mixtures in a shock tube at room temperature. Heating the mixing assembly and the shock tubes can be used to generate higher fuel loading by increasing the vapor pressure of the fuel [13]. However, uneven heating can cause uniformity problems, and at high heating temperatures the fuel may begin to decompose. Perhaps more importantly, fractional distillation can occur when heating fuels with multiple components, resulting in a gas-phase composition that differs from the liquid-phase composition. An alternative approach, which avoids these complications, is to fill the shock tube with a liquid fuel

Communicated by K. Takayama.

D. R. Haylett (✉) · D. F. Davidson · R. K. Hanson
Mechanical Engineering Department,
Stanford University, Stanford, CA 94305, USA
e-mail: danhaylett@gmail.com
URL: <http://hanson.stanford.edu>

aerosol. If the liquid droplets are small enough (i.e. micron-sized), they evaporate quickly behind the incident shock and then the reflected shock wave travels through a completely uniform, entirely gas-phase mixture of fuel. This was the strategy advanced in our work to develop AST I, as demonstrated in previous studies for *n*-dodecane, JP-7, and even diesel fuel [1,2].

The uniformity of the final (post-evaporation) gas mixture is highly dependent on the spatial uniformity of the initial aerosol concentration. High levels of uniformity are easily achieved in gaseous mixtures because gases occupy the entire volume. However, an aerosol/gas mixture does not behave in this ideal manner. During filling the gas tends to accelerate faster than liquid droplets, leaving the droplets behind and thus creating an spatially non-uniform aerosol loading. Smaller droplets will track the gas flow better, but small diameters render high fuel loadings difficult. A balance must be met between the benefit of high fuel loadings as gained from using larger droplets and the benefit gained by having smaller droplets which track the gas-phase flow and more easily form uniform spatial distributions. Previous work has found this balance in droplets created by ultrasonic nebulizers with mass mean diameters of around 4–5 μm [1,2].

Other researchers have also been concerned with filling a tube with aerosol. Some have used a direct injection aerosol filling strategy. One such method is to use a point source or sources where fuel injectors spray the fuel directly into the shock tube either prior to arrival of the incident shock, after the incident shock or after the reflected shock [4–8]. However, these methods produce extremely non-uniform conditions due to the fact that the spray comes out in a cone pattern and there are regions in the tube that are not filled completely. Another method is to prepare a mixture of aerosol in a separate volume, after which the aerosol mixture can be expanded into the shock tube through a tube connecting the two volumes with a valve to control the filling process [9–11]. These methods are better suited for smaller particle sizes, on the order of microns, because the high acceleration of the gas at the small area orifice will result in significant lagging of larger diameter particles. No quantification of the spatial uniformity was found in the studies discussed above; however, in [11] a uniformity of around 20 % rms was extracted from time-resolved drum-camera measurements.

There also have been a number of studies in which a uniform mixture of aerosol is created in a continuous flow scheme. In these schemes the aerosol is generated in a moving stream of gas and carried with the gas flow. The gas flow is made to pass turbulence-generating structures to mix the aerosol; this approach is commonly used in aerosol wind tunnels. In one study, Ref. [14], non uniformities as low as 11 % over a 30×30 cm cross-section of the wind tunnel for aerodynamic droplet sizes of 10 μm were reported. Using a similar technique, Brown was able to achieve ± 10 % variation

in aerosol concentration [15]. At very low pressures of 1–10 torr, other researchers have tried with partial success to minimize spatial non-uniformities [16,17].

These continuous-flow filling techniques have also been used in shock tubes. For example, the first-generation aerosol shock tube, built in our laboratory, used a continuous-flow filling technique [1,2,18]. In this facility, the aerosol is created with an ultrasonic disk nebulizer submersed in a liquid fuel pool. A continuous flow of gas is established over the nebulizer, into a manifold, through the shock tube endwall, through the entire length of the shock tube driven section, and into a mechanical pump. The aerosol carried by this flow of gas into the manifold is accelerated through a series of slightly opened poppet valves in the shock tube endwall. The narrow passages of the poppet valves create turbulence which mixes the aerosol, creating a uniform aerosol near the endwall. As the mixture flows further away from the endwall the turbulence dissipates and the aerosol tends to settle to the bottom of the tube resulting in non-uniformities. The uniformity has been measured using a light sheet and imaging the scattering at 90° . The best uniformities seen with this method (variations of ± 24 %) were found at the greatest observation distance from the shock tube end wall (45 cm) in the study. Results from gas-phase absorption of the fuel behind the incident shock indicate that this non-uniformity is lessened by the process of evaporation and diffusion, because variations of only ± 1.7 % were reported using the same filling techniques [1].

The goal of the current study is to develop a new method to introduce aerosol into the shock tube, with higher spatial uniformity (particularly over the last meter of shock tube length nearest the endwall), and with the flexibility to fill the shock tube with a wider range aerosol loadings.

2 Aerosol shock tube generation II

2.1 Experimental apparatus

A simplified schematic of the experimental setup is shown below in Fig. 1a. The schematic shows a cross section of the shock tube as viewed from the side. The driver section of the shock tube is separated from the driven section (8.4 m long and 10 cm square cross-section) by a thin polycarbonate diaphragm. The test section (1.2 m long and 10 cm square cross-section), which contains the aerosol, is separated from the rest of the driven section by a gate valve. The gate valve was specially designed to make a smooth interior when opened, and when closed restricts the aerosol from filling the entire driven section of the shock tube. Another gate valve at the end of the test section acts as the endwall when closed. When open, the endwall gate valve allows aerosol to flow into the test section from the aerosol mixing plenum (50 cm long and

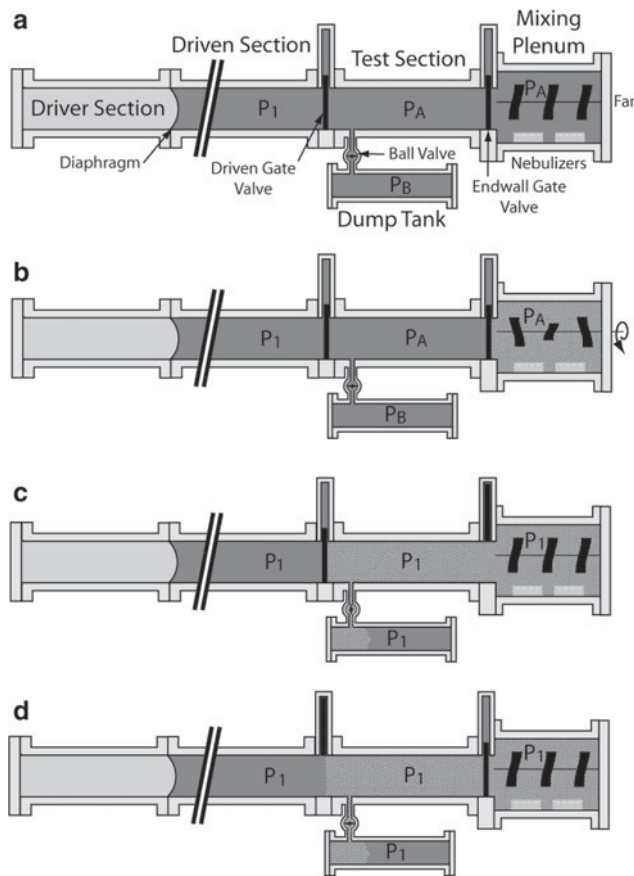


Fig. 1 **a** Diagram illustrating components of AST II and initial pressures set for operation. **b** Aerosol mixture being prepared in the mixing plenum. **c** Endwall gate valve and ball valve opened and aerosol mixture expanded into the test section. **d** Endwall gate valve and ball valve closed and the driven gate valve opened; the shock tube is ready for initiation of the shock wave

24 cm diameter). The 83-l dump tank is connected through a 5.5-mm orifice and ball valve to the test section and provides expansion volume as the aerosol is pulled into the test section.

The procedure for filling the shock tube in four steps is shown in Fig. 1a–d. First, the gas pressures in all volumes are set (with all valves closed) with a mixture of oxidizer and diluent. The aerosol mixing plenum and the shock tube test section are set to pressure P_A . The pressure P_B in the dump tank is set lower than P_A . The pressure in the rest of the driven section is set to the final desired pressure P_1 such that when the ball valve to the dump tank is opened and the pressures in the other volumes equilibrate, all pressures are equal to P_1 (Fig. 1a).

Second, the aerosol mixture is created. Inside the aerosol mixing tank a fan is turned on that mixes the entire volume. The fan rotates at approximately 100 rpm and has six individual blades equally spaced along the axis of rotation with an overall blade diameter of 12.5 cm. An ultrasonic nebulizer

array is then turned on generating liquid droplets which are quickly caught up in the mixed flow. The fan and nebulizers are left on until the liquid loading in the mixed gas reaches the desired level. Then the nebulizers are turned off (Fig. 1b). Some settling of large drops may then occur.

Third, the aerosol mixture is transferred into the test section of the shock tube. First, the endwall gate valve is opened, and because the pressure difference across this valve is zero, there will be no flow. Immediately following this, the ball valve is opened and gas begins to flow from the test section into the dump tank. As gas from the test section flows from the test section into the dump tank the mixture of aerosol is pulled in a plug flow into the test section. The pressures are set such that the dividing surface between the aerosol mixture and the non-aerosol gas propagates well past the ball valve into the dump tank (Fig. 1c).

Finally, the pressures in all the volumes equilibrate to a value such that there is no pressure difference across the driven section gate valve. This valve can then be opened without any resulting flow; the endwall gate valve and ball valve are then closed. The result is a smooth-walled shock tube with a spatially uniform aerosol near the endwall (Fig. 1d). The shock wave experiment can then be initiated, typically within a few seconds.

2.2 Calculation of loading pressures

The initial pressures in the tanks have to be set such that once equilibrated, the desired final pressure in the shock tube is reached. This final pressure, P_1 , is the pressure that the incident shock wave will propagate into and is used in calculating the conditions behind the reflected shock wave. Using a simplified model for the expansion we can assume that the expansion of ideal gases is isentropic and arrive at equations for setting the initial pressures in the dump tank, P_B , and the aerosol mixing plenum and test section, P_A , and the final pressure after expansion P_1 .

$$P_B = ((V_B - V') / V_B)^\gamma P_1 \quad (1a)$$

$$P_A = (P_f (V_A + V_B) - P_B V_B) / V_A \quad (1b)$$

The volume V' is the displaced volume, effectively the increase in volume of the plug of aerosol as it expands into the shock tube. This volume can be considered a non-dimensional number that represents the number of test section volumes to be filled.

$$X = V' / V_{TS} \quad (2)$$

where V_{TS} is the volume of the test section. To just fill the entire test section, X would equal 1, in practice, this fill parameter is made slightly larger (~ 1.5) to ensure complete filling. Using these equations, the measured final pressure is typically within 2–5 % of the expected value, and the volume

change is represented with sufficient accuracy using these equations.

3 Results

Three aspects of the AST II aerosol loading scheme performance are discussed: first, the behavior of the nebulizers; second, the spatial uniformity achieved in the aerosol mixing plenum; and third, the spatial uniformity in the filled shock tube volume.

3.1 Nebulizer performance

The effectiveness of the AST II method of loading the shock tube with aerosol in a spatially uniform manner over a wide range of volumetric concentrations depends strongly on the size of the liquid droplets that are used. A high liquid-volume fraction can be achieved by increasing the number of droplets or the size of droplets. Because volume is strongly dependent on diameter, it is advantageous to use larger diameter droplets. However, larger droplets settle faster and lag in gas flows. So a balance must be struck while considering the limitations of the aerosol generators. The ultrasonic ceramic-disk nebulizers are ideal for this purpose because they work even with viscous fuels such as diesel (DF-2) and bio-diesel surrogates such as methyl decanoate, and they are capable of producing high liquid volume fractions with sufficiently small diameters that to track the gas flows that occur with this filling method. In order to ensure consistent results the droplet size distributions of nebulized aerosols were measured for various liquids.

The nebulizer was operated in a tube with an inner diameter of 12 cm (in liquid depths above the ceramic-disk of 2.5–4.0 cm) and the droplets were entrained in a flow that went from the sidewall of the tube and out of the top (see Fig. 2a). Aerosol size distributions were measured using a Malvern Spraytec (Model RTS5214). Figure 2b shows a plot of the droplet size distribution for several liquids: water, *n*-dodecane, and diesel (DF-2) fuel. The flow rates were low

to keep with the low velocities encountered when filling the shock tube. The size distributions were found to be nearly the same for all three liquids. The mass-averaged size was between 4–5 μm . The Stokes settling time for this droplet size is approximately 1 min.

3.2 Mixing tank loading uniformity

Spatial uniformity and knowledge of loading levels in the mixing tank are of crucial importance. This can be quantified using laser extinction if we take advantage of our measured droplet size distribution. The concentration of the aerosol can be related to the attenuation of a monochromatic laser beam using Mie theory. The theory provides that the extinction ($-\ln(I/I_0)$) is given by this equation [19]

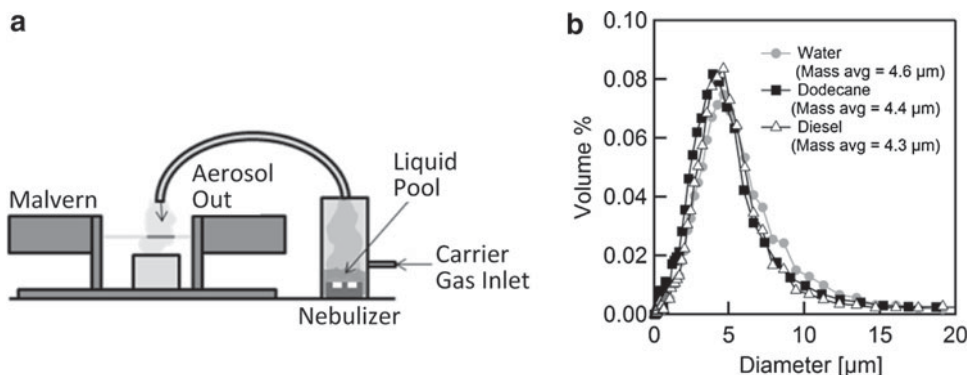
$$-\ln \frac{I}{I_0} = C_V \frac{\int_0^\infty Q_{\text{ext}}(D, n(\lambda)) f(D) \frac{\pi}{4} D^2 L dD}{\int_0^\infty f(D) \frac{4\pi}{3} D^3 dD} = 0.31 \pm 0.01 [\text{m}^{-1}] L [\text{m}] C_V [\text{ppmv}] \quad (3)$$

where the I is the intensity of the light that is transmitted, I_0 is the incident intensity, L is the path length, C_V is the liquid volume concentration, Q_{ext} is the Mie coefficient which depends on the droplet diameter (D) and the index of refraction which is dependent on the wavelength of light (λ), and $f(D)$ is the fractional size distribution. These integrals can be computed for the measured $f(D)$ shown above (Fig. 2b) and theoretical values for Q_{ext} . Because the size distributions are similar and the indices of refraction are nearly the same ($n = 1.33$ – 1.42) for the liquids used in this study, the integrals can be simplified as shown in Eq. 3.

The laser setup (shown in Fig. 3) on the mixing plenum consisted of two lasers 30 cm apart which were sent across the center of the plenum in a horizontal plane ($L = 24.2$ cm). The windows were heated ($\sim 40^\circ\text{C}$) to avoid condensation. Figure 4 below shows a typical test result.

Large variations are seen in the concentration signal while the nebulizer is on as the jets above the nebulizer disk steer the laser beams away from the detectors. The concentration rises quickly while the nebulizer is on; then once the nebulizer is

Fig. 2 **a** Experimental setup for measuring droplet size distributions. **b** Droplet size distributions (volume %) for water, *n*-dodecane, and diesel



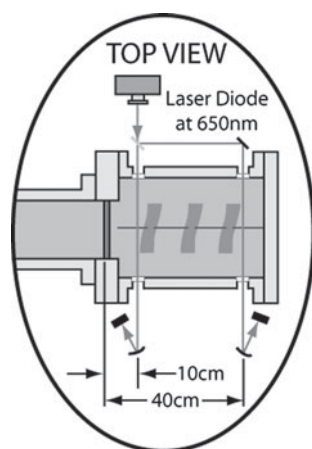


Fig. 3 Shows the optical setup on the mixing plenum to measure the uniformity and the loading

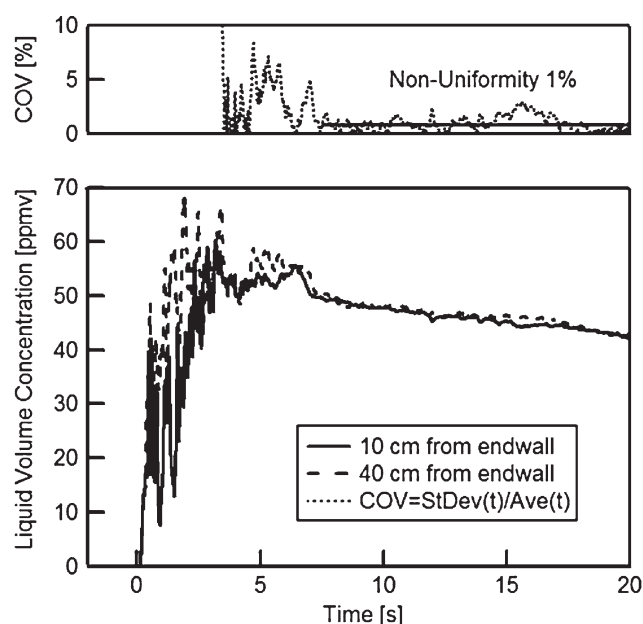


Fig. 4 Uniformity in tank: water aerosol. Two lasers at 10 and 40 cm from the endwall. The discrepancy between the two measurements indicate the magnitude of the non-uniformities present in the mixture at a particular time. The coefficient of variation ($COV = StDev(t)/Ave(t)$) is plotted as a function of time

turned off (at 4 s) these variations are reduced. When the fan is turned off (at 6 s) the variations are reduced further, and we see a very slow drop in the concentration (around 1 %/s). This is due to the larger droplets settling. This effect is less evident in actual experiments because the fill happens directly after the fan turns off. The coefficient of variation (COV) for these measurements shows that the non-uniformity in the tank is around 1 %. No strong dependence on fan speed (near the nominal value of 100 rpm) was seen.

Figure 5 shows the effects of leaving the nebulizer running for different amounts of time and the range of achievable

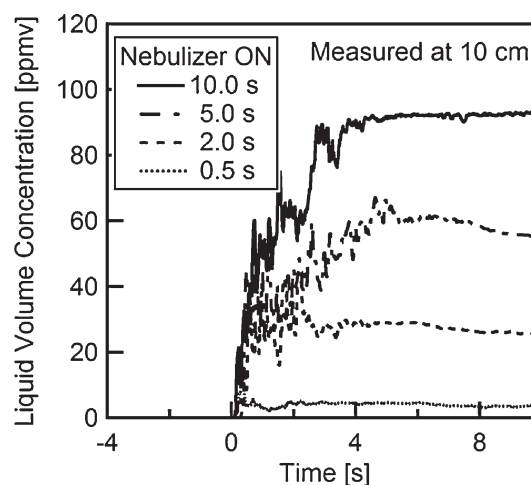


Fig. 5 Filling the tank to different concentrations: water aerosol. Various curves represent different lengths of time that the nebulizer and mixing fan was turned on

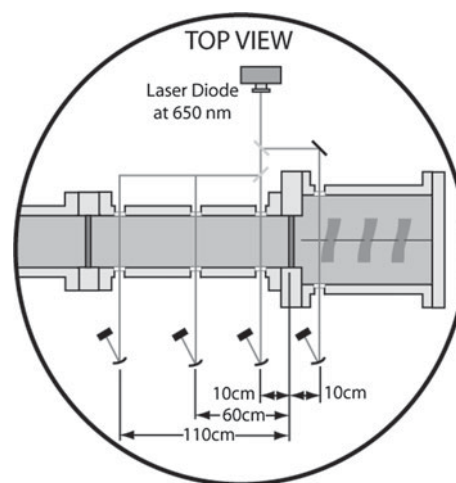


Fig. 6 Optical Setup for measuring non-uniformities in AST II method of filling

concentrations (1–100 ppmv). The AST II configuration significantly extends the concentration range beyond that which was previously achieved with the AST I method of filling the shock tube (5–20 ppmv).

3.3 Shock tube loading uniformity

Studies of shock tube loading uniformity were performed using a Plexiglass mock tube to aid in visualization. Loading in the mock tube was studied using three lasers stationed at different distances away from the endwall (10, 60, 110 cm) crossing the tube at its mid section. The windows were heated ($\sim 40^\circ\text{C}$) to avoid condensation. See Fig. 6 for the experimental setup and Fig. 7 for the results of a typical filling experiment using the AST II method.

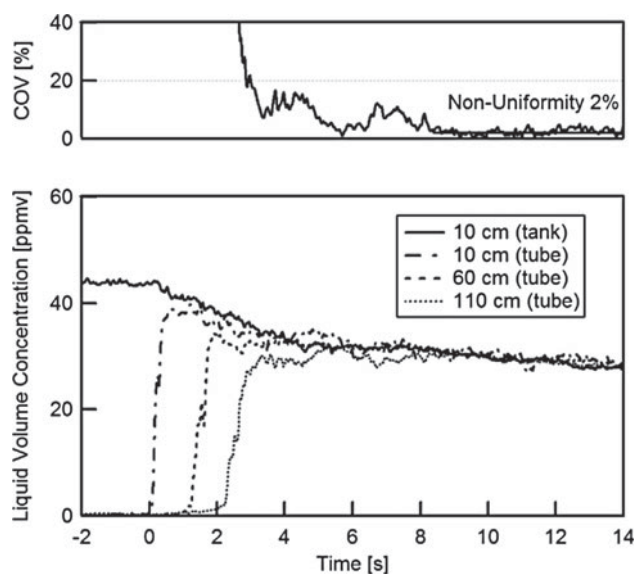
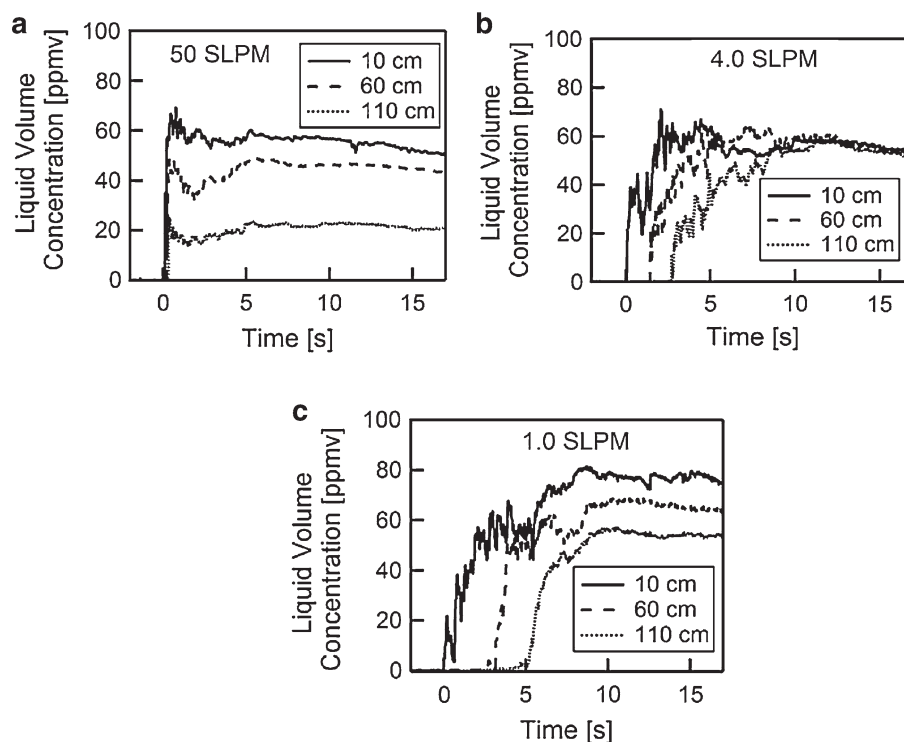


Fig. 7 Plot of laser extinction measurements at three locations along the tube and the resulting coefficient of variation: water aerosol. AST II generates non-uniformities much smaller than AST I in this case 2 %

This filling experiment was conducted with a water aerosol using loading pressures of $P_A = 759$ torr, $P_B = 326$ torr, $P_f = 460$ torr, and $X = 1.5$. The mixing plenum filling time sequence was as follows: gas flow and fan in the mixing plenum turned on at -10 s, nebulizer is turned on at -8 s and turned off at -5 s, fan turned off at -3 s. This filling sequence achieved an aerosol liquid loading of 44 ppmv

Fig. 8 These plots show measurements of aerosol concentration at three locations while filling the shock tube using the AST II filling method: **a** 50 slpm fill rate, **b** 4.0 slpm fill rate, **c** 1.0 slpm fill rate. The flow rate was varied by using various diameter orifices



(see solid black curve). The mock tube filling sequence was as follows (same time scale): ball valve to the dump tank and gate valve to mixing plenum opened at 0 s, the aerosol contact surface crosses the first laser almost immediately, the second laser registers an increase in the aerosol concentration at 1 s, and the third laser registers an increase at 2.5 s. The liquid volume concentrations decrease between 0 and 4 s due to the expansion of the mixture; once the pressures equalize at 4 s the concentrations at all three laser measurement locations are very similar in magnitude and decrease at a slow rate due to settling. The COV time-history indicates that the non-uniformities remain less than 2 % after filling. An identical set of measurements was made using the AST I “flow-through” method of filling and non-uniformities were significantly higher in all cases and typically around 16 %.

In order to minimize the nonuniformity using the AST II, one very important parameter, the plug flow rate, must also be optimized. The next set of plots in Figs. 8a–c and 9 show the effect of varying the fill rate.

In Fig. 8a the flow rate is high (50 slpm) and the aerosol takes only 0.2 s to fill the test section; large differences in the aerosol concentration are seen at the three laser measurement locations. This variation is likely due to the separation of the liquid droplets from the bulk gas at high flow velocities. In Fig. 8b the test section is filled in 2.7 s (4.0 slpm) and the aerosol is much more uniform. At significantly slower flow rates (1.0 slpm), as in Fig. 8c, the aerosol again becomes less uniform; droplets near the aerosol contact surface evaporatively cool and settle, beginning a “river-like” flow. At these filling

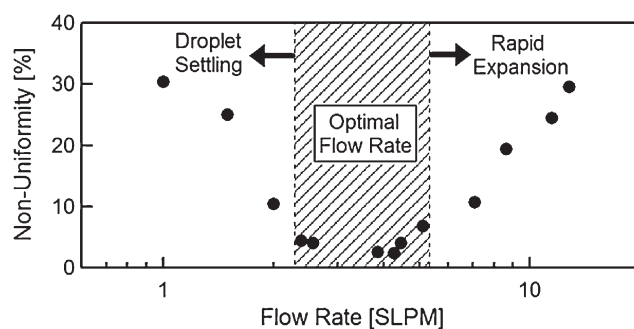


Fig. 9 Illustrates the relationship between the resulting non-uniformity to the flow rate with which the tube was filled. The flow rate was varied by using various diameter orifices. The optimal flow rate range is between 2 and 5 slpm (gas velocity ~ 45 cm/s)

rates, the aerosol flow is not an ideal plug flow and occupies only the bottom half of the tube's cross-section. The region of uniformity occurs when the flow rate is between 2 and 5 slpm or at velocities between 30 and 60 cm/s. The optimal flow rate is obtained by venting the shock tube test section (or mock tube in the visualization studies) through a throat or orifice just before the ball valve to the dump tank. The throat that was chosen to produce a velocity in the test section of 45 cm/s has an orifice diameter of 5.5 mm. Figure 9 shows many filling experiments where the flow rate was varied by opening the ball valve to different angles.

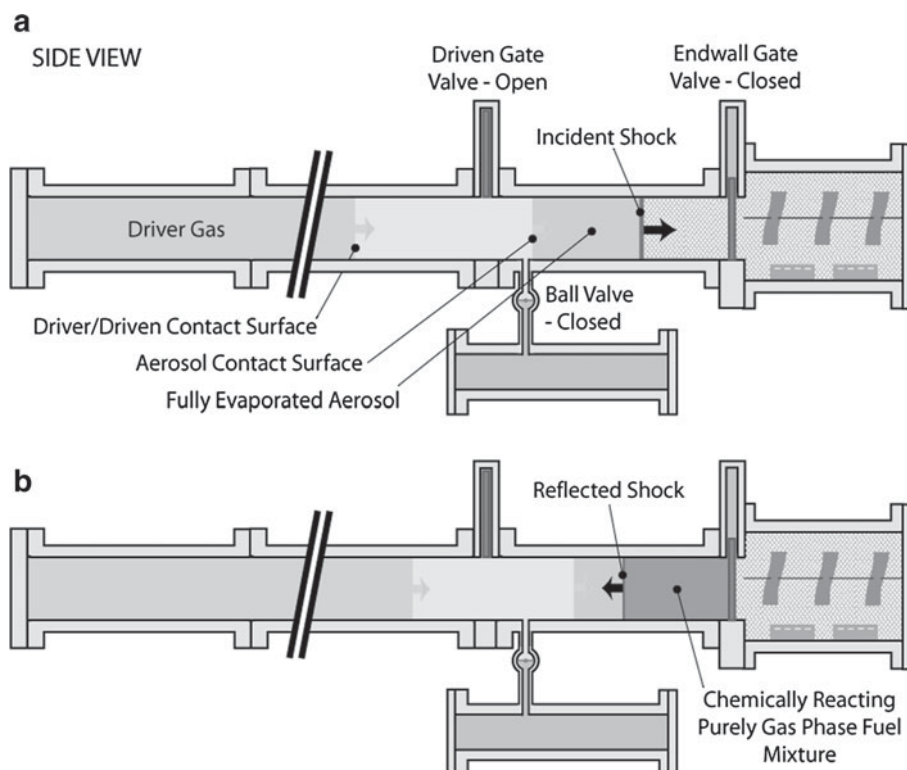
4 Shock wave experiments

4.1 Fuel loading uniformity

After the shock tube filling is complete, a shock wave is initiated (see Fig. 10a, b). The incident shock wave propagates through the driven section of the shock tube into the aerosol-filled test section. For these experiments a fuel aerosol (e.g. dodecane, diesel fuel, etc.) is used to study the chemical kinetics of that particular fuel. When the shock passes through the aerosol it quickly accelerates and evaporates the fuel. The evaporated fuel mixture then flows toward the endwall behind the incident shock (Fig. 10a). The temperature and pressure in this region is typically calculated using the measured shock speed. In the presence of vaporizing fuel droplets, the calculation requires additional thermodynamic information about the phase change of the fuel. This technique for calculating temperature has been experimentally verified in the AST by laser absorption [20].

Once the shock wave reaches the endwall the shock reflects, stagnating the evaporated fuel mixture, together with associated heating and compression (Fig. 10b). At the elevated temperatures in this region the fuel and oxidizer may undergo auto-ignition. This process can be monitored allowing extraction of important reaction rate parameters. The entire shock process is shown schematically in Fig. 11 below on an $X-T$ diagram.

Fig. 10 **a** Schematic showing incident shock propagation and **b** then subsequent reflected shock propagation



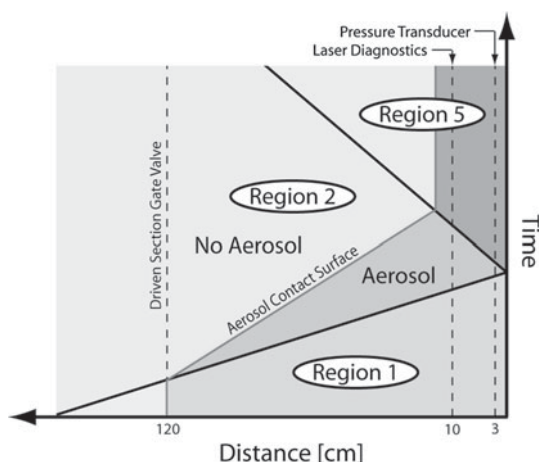


Fig. 11 X - T diagram showing the incident and reflected shocks. The aerosol contact surface describes the boundary between the aerosol mixture and the rest of the driven section

Post-evaporation gas-phase uniformity in the test gas mixture using the new aerosol loading strategy was measured using laser absorption in region 2. In region 2 the fluid is flowing toward the endwall and a time-resolved laser measurement at a single location gives information about all of the fluid elements that pass the laser. Figure 12 below shows the optical setup used in these measurements.

Shown in Fig. 13a–c, are extinction measurements ($-\ln(I/I_0)$ where I_0 is the incident laser light intensity and I is the intensity after being attenuated through the shock tube) for experiments in the shock tube. At this measurement location (10 cm) two laser beams with different wavelengths were pitched through the shock tube. The visible, 650 nm laser beam was attenuated solely by Mie scattering when there are liquid droplets present. The mid-infrared 3.39 μm

laser beam was also attenuated by Mie scattering, but in addition is resonant with the C–H stretch vibrational mode found in hydrocarbons in the mixture. The visible beam provides information on the aerosol loading and confirms when the aerosol is fully evaporated (i.e. no attenuation of 650 nm at $\sim 100 \mu\text{s}$). The mid-infrared beam provides purely gas-phase fuel concentration after the aerosol is fully evaporated. This is done using a method described in Davidson et al. [1].

Figure 13a–c shows these laser extinction measurements in regions 1, 2, and 5. Before the arrival of the shock wave, in region 1, there is no change in the extinction ($-\ln(I/I_0)$) of both wavelengths because the aerosol is stagnant. After the incident shock arrives, the mixture is compressed and the extinction rises. In the 650-nm measurement the signal quickly reaches a peak and falls to zero due to the rapid evaporation behind the incident shock. The 3.39 μm measurement falls due to evaporation as well, but then asymptotes to a steady plateau value. This plateau value of the gas-phase absorption is used to calculate the fuel concentration. This measurement also indicates that the test gas mixture passing the measurement location had very uniform fuel loading for all three tests shown here ($< 1\%$ variation). This is a significant improvement over the results obtained using the AST I filling method where the nonuniformities were typically $> 5\%$ and never better than 1.7% [1]. At the arrival of the reflected shock the mixture is further compressed. As a result the attenuation increases as seen in Fig. 13a. A Schlieren spike is also seen in the laser measurements, where the beam is temporarily steered off the detector because of the passage of the reflected shock. In Fig. 13b the increased attenuation is not seen after the reflected shock, and in Fig. 13c the attenuation even falls prior to the arrival of the reflected shock. This is due to the arrival of the aerosol contact surface at the measurement location.

Fig. 12 Diagnostics used in aerosol tube experiments. Pressure measurements are used to measure shock speed and ignition time. 650 nm can be used to measure liquid aerosol concentration. 3.39 μm is resonant with the CH stretch vibrational band and can be used to measure gas phase concentration after the fuel has evaporated

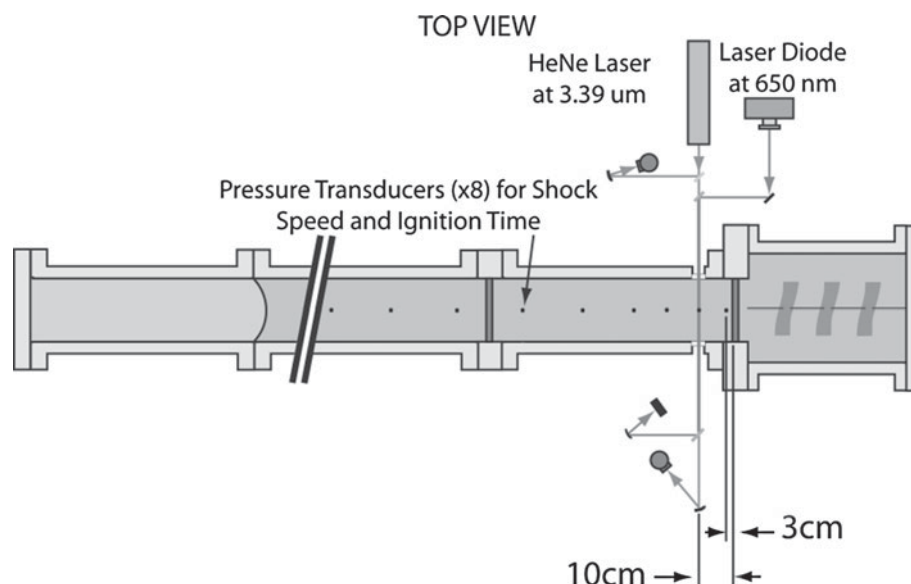


Fig. 13 Three shock experiments highlighting region 2 post-evaporation uniformity for a range of fuel loadings all with *n*-dodecane in 21 % O₂/Ar.

a Conditions: X_f (*n*-dodecane mole fraction) = 0.00680,

$T_2 = 617$ K, $P_2 = 1.11$ atm,

$T_5 = 993$ K, $P_5 = 4.23$ atm.

b Conditions:

$X_f = 0.0100$, $T_2 = 584$ K,

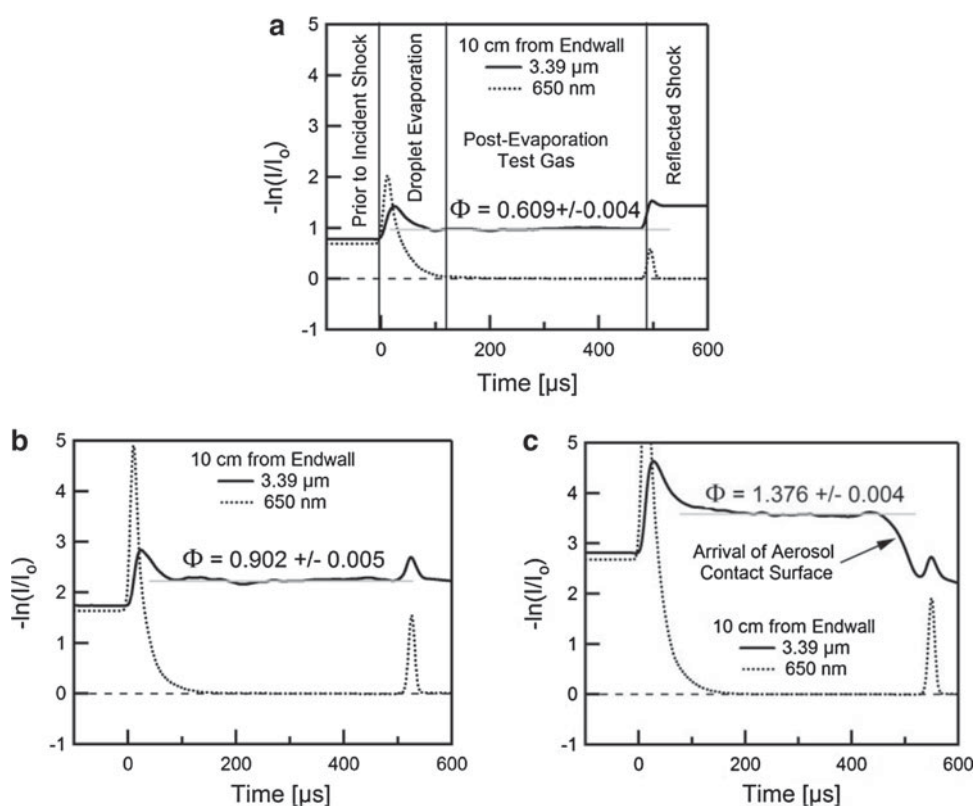
$P_2 = 1.64$ atm, $T_5 = 921$ K,

$P_5 = 6.25$ atm. **c** Conditions:

$X_f = 0.0150$, $T_2 = 534$ K,

$P_2 = 1.62$ atm, $T_5 = 838$ K,

$P_5 = 6.26$ atm



4.2 Ignition delay time measurements

As an example application and demonstration of this new facility to study combustion chemistry phenomena, autoignition delay times in *n*-dodecane/O₂/argon mixtures were measured. Ignition delay time measurements are used to describe the global performance of fuel/oxidizer mixtures. The ignition delay time is the length of time that a mixture, at a given initial pressure and temperature (typically under constant volume and energy constraints), will take to ignite; measurements can be made directly from real-time pressure profiles. Conditions behind reflected shock waves in shock tube experiments can very closely approach constant volume and internal energy conditions and provide a method to directly study the chemistry of high-temperature combustion processes without the influence of other flow processes (such as mass transport or heat conduction.) Representative *n*-dodecane ignition delay time pressure measurements are shown in Fig. 14 for various temperatures. These AST II measurements are compared with previous measurements using AST I [1] in Fig. 15.

The new aerosol filling method produces reduced scatter. The AST II points are slightly shifted to shorter ignition times while the activation energy is preserved. A comparison analysis of the AST I data shows evidence of larger nonuniformity of fuel loading, suggesting that a significant portion

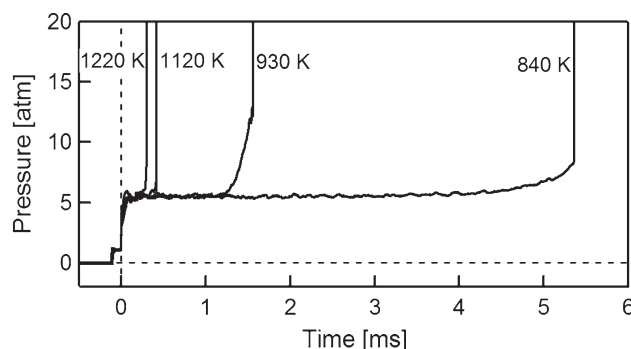


Fig. 14 *n*-Dodecane/21 % O₂/balance argon, $\Phi = 0.5$, ignition delay time measurements. Plot shows pressure at 3 cm from the endwall for four different experiments over a wide range of temperatures. The ignition time is the time between the arrival of the reflected shock and the peak in the pressure trace. Initial reflected shock pressures 5 atm

of the measurement difference was due to non-uniformities in the initial aerosol mixture. The new filling method produces a more uniform initial aerosol mixture and significantly reduces the scatter in the combustion measurements that were made.

Using the AST II, ignition delay time measurements for *n*-dodecane mixtures are possible over a wider range of equivalence ratios. Representative data are shown in Fig. 16. These represent the first rich *n*-dodecane ignition delay time

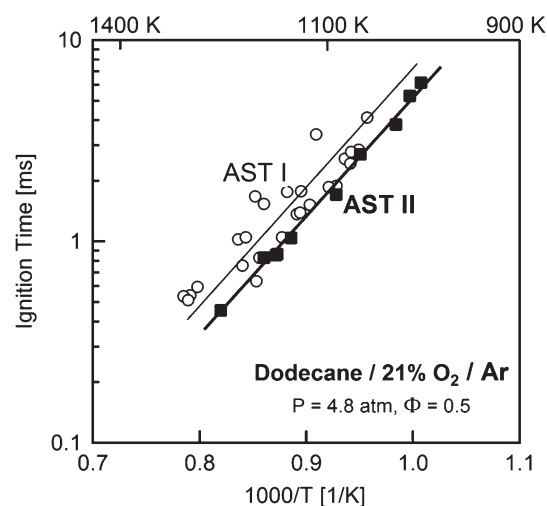


Fig. 15 Shows ignition delay times for AST I [1] and AST II. AST II data shows significantly reduced scatter and slightly lower mean values than AST I data. Pressure and Φ (equivalence ratio) were normalized to 4.8 atm and $\Phi = 0.5$ using P^{-1} and Φ^{-1} dependences, respectively

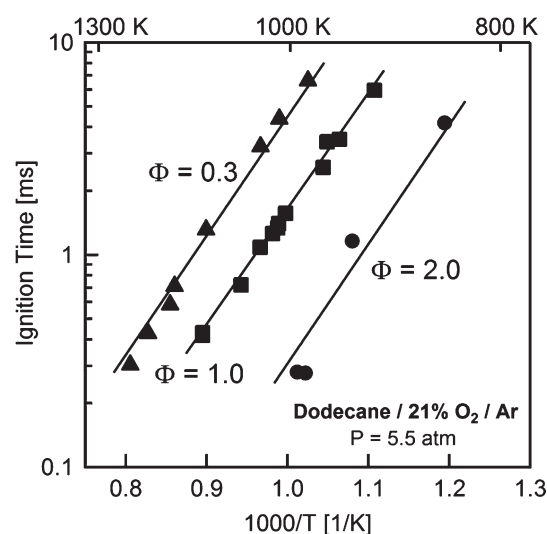


Fig. 16 *n*-Dodecane/21 % O_2 /argon ignition delay times: $\Phi = 0.3$ – 2.0 . P pressure and Φ were normalized using P^{-1} and Φ^{-1} dependences, respectively

measurements made using an aerosol loading strategy. These measurements provide a direct test of current *n*-dodecane oxidation mechanisms [21].

5 Conclusions

A second-generation aerosol shock tube has been developed. Three improvements over the previous design were demonstrated. The new method now constrains the amount of shock tube that is filled with aerosol, produces a much more uniform aerosol, and allows filling the shock tube with much higher

concentrations of fuel. These improvements will enable more accurate measurements of combustion chemistry processes, particularly as are needed for practical low-vapor-pressure fuels.

Acknowledgments This work was supported by the Army Research Office with Dr. Ralph A. Anthenien as technical monitor.

References

- Davidson, D.F., Haylett, D.R., Hanson, R.K.: Development of an aerosol shock tube for kinetic studies of low-vapor-pressure fuels. *Combust. Flame* **155**(1–2), 108–117 (2008)
- Haylett, D.R., Lappas, P.P., Davidson, D.F., Hanson, R.K.: Application of an aerosol shock tube to the measurement of diesel ignition delay times. *Proc. Combust. Inst.* **32**, 477–484 (2009)
- Roth, P.: The shock tube technique applied to study aerosol rate processes. *Shock Waves* **1**, 73–82 (1991)
- Cadman, P.: Shock tube combustion of liquid hydrocarbon sprays of toluene. *Phys. Chem. Chem. Phys.* **3**, 4301–4309 (2001)
- Rotavera, B., Amadio, A., Antonovski, V., Petersen, E.: New approaches for fundamental rocket injector studies using a shock tube. In: 42nd AIAA/ASME/SAE/ASEE Joint Propulsion Conference & Exhibit, 9–12 July 2006
- Petersen, E.L., Rickard, M.J.A., Crofton, M.W., Abbey, E.D., Traum, M.J., Kalitan, D.M.: A facility for gas- and condensed-phase measurements behind shock waves. *Meas. Sci. Technol.* **16**, 1716–1729 (2005)
- Servaites, J., Krier, H., Melcher, J.C., Burton, R.L.: Ignition and combustion of aluminum particles in shocked $H_2O/O_2/Ar$ and $CO_2/O_2/Ar$ mixtures. *Combust. Flame* **125**(1–2), 1040–1054 (2001)
- Bazyn, T., Glumac, N., Krier, H., Ward, T.S., Schoenitz, M., Dreizin, E.L.: Reflected shock ignition and combustion of aluminum and nanocomposite thermite powders. *Combust. Sci. Technol.* **179**(3), 457–476 (2007)
- Glumac, N., Krier, H., Bazyn, T., Eyer, R.: Temperature measurements of aluminum particles burning in carbon dioxide. *Combust. Sci. Technol.* **177**(3), 485–511 (2005)
- Kalitan, D.M., Petersen, E.L.: A shock-tube study of aluminum oxidation at elevated temperatures. In: 42nd AIAA/ASME/SAE/ASEE Joint Propulsion Conference & Exhibit, 9–12 July 2006
- Falk, T.J.: Evaporation of submicron platinum particles in a shock tube. *J. Chem. Phys.* **48**, 3305 (1968)
- Davidson, D.F., Hanson, R.K.: Interpreting shock tube ignition data. *Int. J. Chem. Kinet.* **36**(9), 510–523 (2004)
- Vasu, S.S., Davidson, D.F., Hong, Z., Vasudevan, V., Hanson, R.K.: *n*-Dodecane oxidation at high-pressures: measurements of ignition delay times and OH concentration time-histories. *Proc. Combust. Inst.* **32**(1), 173–180 (2009)
- Inhalation Toxicology Research Institute Annual Report 1995–1996: ITRI-148, prepared for the U.S. Department of Energy under Contract DE AC04 76EV01013, Albuquerque, NM, December 1996
- Brown, J.R.: Low-speed, low-cost wind tunnel. *The Engineer*, 481–483, 31 March 1967
- Bae, G.-N., Kinney, P.D., Liu, B.Y.H., Pui, D.Y.H.: Investigation of aerosol spatial distributions downstream of a critical orifice at low pressure. *Aerosol Sci. Technol.* **28**(6), 479–488 (1998)
- Sato, S., Chen, D.-R., Pui, D.Y.H.: A novel method for producing spatially uniform aerosols in a low pressure environment. *Aerosol Sci. Technol.* **36**(2), 145–153 (2002)

18. Hanson, T.C.: The development of a facility and diagnostics for studying shock-induced behavior in micron-sized aerosols. Stanford Thesis, Dec 2005
19. van de Hulst, H.C.: Light Scattering by Small Particles. Wiley, New York (1957)
20. Ren, W., Jeffries, J., Hanson, R.: Temperature sensing in shock-heated evaporating aerosol using wavelength-modulation absorption spectroscopy of CO₂ near 2.7 μ m. Meas. Sci. Technol. **21**, 105603 (2010)
21. Sirjean, B., Dames, E., Sheen, D.A., You, X.-Q., Sung, C., Holley, A.T., Egolfopoulos, F.N., Wang, H., Vasu, S.S., Davidson, D.F., Hanson, R.K., Pitsch, H., Bowman, C.T., Kelley, A., Law, C.K., Tsang, W., Cernansky, N.P., Miller, D.L., Violi, A., Lindstedt, R.P.: A high-temperature chemical kinetic model of *n*-alkane oxidation. JetSurF version 1.0, September 15, 2009. http://melchior.usc.edu/JetSurF/Version1_0/Index.html



Ignition delay times of low-vapor-pressure fuels measured using an aerosol shock tube

Daniel R. Haylett^{a,*}, David F. Davidson^b, Ronald K. Hanson^b

^a Lawrence Livermore National Laboratory, Livermore, CA 94550, USA

^b High Temperature Gasdynamics Laboratory, Department of Mechanical Engineering, Stanford University, Stanford, CA 94305, USA

ARTICLE INFO

Article history:

Received 1 February 2011

Received in revised form 1 June 2011

Accepted 24 August 2011

Available online 23 September 2011

Keywords:

Ignition delay times

Aerosol shock tube

n-Dodecane

n-Hexadecane

Methyl decanoate

Diesel

ABSTRACT

Gas-phase ignition delay times were measured behind reflected shock waves for a wide variety of low-vapor-pressure fuels. These gas-phase measurements, without the added convolution with evaporation times, were made possible by using an aerosol shock tube. The fuels studied include three large normal alkanes, *n*-decane, *n*-dodecane and *n*-hexadecane; one large methyl ester, methyl decanoate; and several diesel fuels, DF-2, with a range of cetane indices from 42 to 55. The reflected shock conditions of the experiments covered temperatures from 838 to 1381 K, pressures from 1.71 to 8.63 atm, oxygen concentrations from 1 to 21%, and equivalence ratios from 0.1 to 2. Ignition delay times were measured using sidewall pressure, IR laser absorption by fuel at 3.39 μm , and CH^+ and OH^+ emission. Measurements are compared to previous studies using heated shock tubes and current models. Model simulations show similar trends to the current measurement except in the case of *n*-dodecane/21% O_2 /argon experiments. At higher temperatures, e.g. 1250 K, the measured ignition delay times for these mixtures are significantly longer in lean mixtures than in rich mixtures; current models predict the opposite trend. As well, the current measurements show significantly shorter ignition delay times for rich mixtures than the model predictions.

© 2011 The Combustion Institute. Published by Elsevier Inc. All rights reserved.

1. Introduction

There is a need to extend the study of purely gas-phase combustion chemistry to include low-vapor-pressure fuels. Conventional shock tubes use gas-phase mixtures and can provide, behind the reflected shock wave, ideal, nearly zero-dimensional, nearly constant-volume reactor conditions up to the time of ignition, or longer in highly dilute mixtures [1]. However, this conventional operation limits the fuels that can be easily loaded into the shock tube to gases and liquids with a sufficiently high vapor pressure. Heating the shock tube and mixing manifold can raise the vapor pressure to allow the study of heavier fuels [2], but this process can be limited by pre-test fuel decomposition or oxidation. To avoid these issues we have developed a method of injecting aerosols into the shock tube and evaporating them behind the incident shock wave, thus producing a purely gas-phase test mixture for study behind reflected shock waves [3,4]. Using this method, the range of fuels that can be studied is greatly extended, and it is now possible to investigate the ignition kinetics of practical heavy fuels that are used industrially, as well as their kinetically-simpler surrogates.

Ignition delay times are good indicators of the overall behavior of combustion reactions and are regularly used as performance benchmarks for detailed chemical mechanisms. Validation of the detailed chemical mechanisms is very important, because these mechanisms are obliged to use many reactions and rate constants that are only estimated or theoretically predicted and not derived directly from experiment. For large fuel molecules (which typically have low vapor pressures), the number of species that are formed during decomposition and oxidation can be very large. For example, a Lawrence Livermore National Labs (LLNL) chemical mechanism for alkanes up to *n*-hexadecane ($\text{C}_{16}\text{H}_{34}$) contains over 2000 species and over 8000 reactions [5]. Ignition delay times provide useful targets and some constraint on the modeling of these complex systems.

Much work is still needed to fully understand the combustion of large fuel molecules, because of the increased complexity of their detailed mechanisms and the added difficulty in performing experiments with these fuels [18]. This is unfortunate, because most of the devices that utilize combustion are powered by low-vapor-pressure fuels including diesel and bio-diesel fuels, and rocket and jet fuels. Many new mechanisms have been developed recently [5–9,25,28], but more experimental validation targets are required for these fuels and their surrogates [27]. To help address this need, we have initiated studies of a variety of low-vapor-pressure fuels

* Corresponding author.

E-mail address: danhaylett@gmail.com (D.R. Haylett).

using an aerosol shock tube methodology, providing in many cases, the first purely gas-phase shock tube ignition delay time measurements for these fuels.

2. Low-vapor-pressure fuels

Fuels used in combustion devices are rarely composed of a pure single component, and in order to model a real, multi-component fuel, single- or multi-component surrogate mixtures are often employed [10,27]. This motivates the study of various types of pure fuels that display characteristics similar to real fuels, in addition to the study of the real fuels themselves. Because fuels such as jet fuel, diesel, and bio-diesel are non-volatile, the surrogate components that best represent these fuels also have low-vapor-pressures, and the aerosol shock tube is well suited for the study of these fuels. Here we focus on *n*-alkanes, which can make up a significant fraction of distillate diesel fuels themselves, and methyl decanoate as a large methyl ester that is structurally related to bio-diesel.

2.1. *n*-Decane

There have been many ignition delay time studies of *n*-decane [11–14,24,26]. This is in part because its vapor pressure at room temperature is near 1.4 torr, which generally is sufficient to make a purely gas-phase mixture at relevant mixture fractions, with the exception of experiments at high pressures. *n*-Decane ($C_{10}H_{22}$) has been commonly used as the alkane representation for jet fuel-relevant surrogates, but has also been used for diesel [13] and bio-diesel [8] comparisons.

2.2. *n*-Dodecane

Less abundant are ignition delay time studies focused on *n*-dodecane [11,15]. The vapor-pressure at room temperature of *n*-dodecane is only 0.13 torr. This limits the fuel loadings that can be achieved, and hence heating is usually necessary to perform shock tube experiments. *n*-Dodecane ($C_{12}H_{26}$) has also been used as the alkane component in jet fuel surrogates.

2.3. *n*-Hexadecane

There are very few studies on the purely gas-phase oxidation of *n*-hexadecane [6,16,17] because its vapor pressure at room tem-

perature is only 1.4 mtorr. *n*-Hexadecane (cetane) is a major alkane constituent of diesel fuel, and appears to be very important in influencing its behavior upon oxidation. Also, *n*-hexadecane ($C_{16}H_{34}$) is one of the species that is used in the definition of the cetane number scale to characterize the combustion characteristics of diesel fuel. By definition *n*-hexadecane has a cetane number of 100.

2.4. Methyl decanoate

The authors are unaware of any purely gas-phase shock tube studies of methyl decanoate, despite the fact that it is a important surrogate fuel for the study of methyl ester based bio-diesels. A detailed mechanism has been developed at LLNL that predicts the behavior of methyl decanoate oxidation [8].

2.5. Diesel (DF-2)

Diesel fuel is a low-volatility distillate fuel widely used in combustion devices. Heated shock tubes have been used recently in the past to study diesel ignition [19,20], but with a distillation curve that extends up to 350 °C (623 K), it can be a very difficult task to get all of the heavier components of the fuel mixture into the shock tube. Here we examine several different diesel fuel samples to show how variability in composition and cetane index affect ignition delay times.

3. Experimental setup

Our current aerosol shock tube methodology is described in Haylett et al. [3,4]. The aerosol shock tube and supporting diagnostics are shown in Fig. 1. A series of fast-response pressure sensors are used for measuring the incident shock speed. A mid-IR (3.39 μ m) laser and a visible (660–670 nm) laser are used for measuring fuel loading. A Kistler 601B piezo-electric transducer located near the endwall (3 cm) is used as the primary measure of ignition delay time. CH^* (at 431 nm) and OH^* (at 306 nm) are both detected through sidewall windows located near the endwall, also to provide ignition delay data.

The aerosol is first created in a mixing tank connected to the endwall of the shock tube, using a bank of ultrasonic nebulizers, and introduced through an endwall gate valve. The aerosol is slowly pulled into the test section (by a vacuum line located near the upstream gate valve) to ensure uniformity of the test mixture.

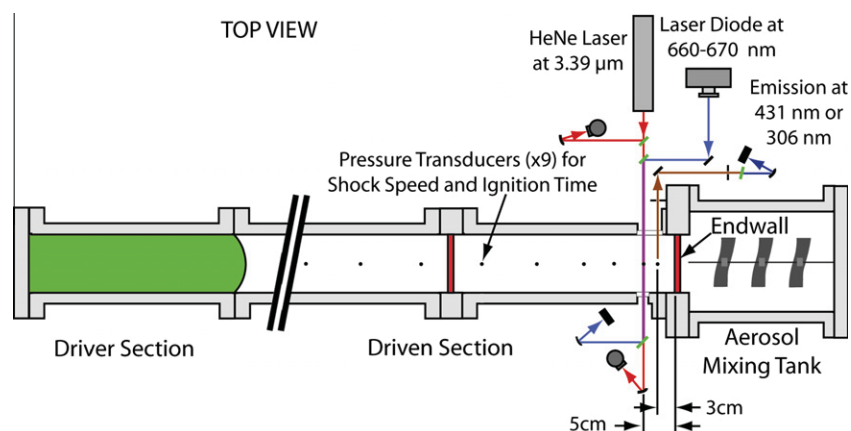


Fig. 1. Schematic of aerosol shock tube with pressure, emission, and laser diagnostics. The pressure sensors are used for shock speed measurement and ignition delay time determination, the mid-IR HeNe laser is used for absorption-based fuel measurements, the visible laser diode is used for droplet scattering measurements, and the emission measurement is used to measure ignition delay time. Sliding gate valves are shown in red as the shock tube end wall and 1 m from the end of the end wall. (For interpretation of the references to colour in this figure legend, the reader is referred to the web version of this article.)

When the test volume is filled with aerosol mixture, the upstream gate valve is opened and the endwall gate valve is closed. The diaphragm at the driver section is then burst (using high-pressure helium/nitrogen mixtures), and an incident shock wave is sent towards the endwall. As the incident shock passes through the fuel aerosol, with a typical average droplet diameter of $\sim 4\ \mu\text{m}$ [4], the fuel is rapidly evaporated and diffusively mixed. The incident shock wave is reflected from the endwall, and this reflected shock wave further heats the gaseous mixture to combustion temperatures and pressures.

The ignition delay time can be defined by the time between the arrival of the reflected shock wave at the pressure sensor (located 3 cm from the endwall) and the time at which the pressure begins its rapid rise associated with ignition. This definition of ignition delay time exhibited the most consistency and proved to be the most reliable for these experiments. Ignition delay times determined from laser absorption measurements (at $3.39\ \mu\text{m}$) of fuel consumption and emission measurements of CH^* and OH^* , while consistent with the pressure measurements, exhibited larger scatter and were used only to confirm the values derived from the pressure measurements.

4. Results

Typical experimental data are shown below in Fig. 2. The top frame shows 670 nm laser extinction (1), pressure (2), and CH^* emission (3) all located 3 cm from the endwall. The bottom frame shows $3.39\ \mu\text{m}$ laser absorption (combined with Mie scattering from droplets, when droplets are present) by fuel (4), and 660 nm laser extinction (5), both located 5 cm from the endwall.

Complete evaporation of the aerosol droplets behind the incident shock wave is evident from the 660 and 670 nm laser extinction traces, which show zero extinction (at $-20\ \mu\text{s}$ in the upper frame and at $-60\ \mu\text{s}$ in the lower frame) before the arrival of the

reflected shock wave. This wavelength range was selected as it does not overlap with any absorption feature of the fuel (DF-2 in this case), and responds only to Mie scattering by droplets. Spikes in the laser signals at $0\ \mu\text{s}$ (upper frame) and $100\ \mu\text{s}$ (lower frame) are a result of beam steering off the detectors due to the transiting shock wave.

The $3.39\ \mu\text{m}$ laser absorption measurement of fuel (4) in the lower frame verifies that the fuel concentration that passes the window at 5 cm is uniform. This is evident from the constant absorbance by fuel vapor seen from -60 to $100\ \mu\text{s}$ after the complete evaporation of the aerosol droplets. The test gas mixture that passes the 5 cm observation station will stagnate behind the reflected shock wave at the 3 cm observation station. Thus, the fuel concentration of the fluid elements that are stagnated behind the reflected shock wave will also be uniform and can be known from a fuel measurement made prior to arrival of the reflected shock. This uniformity is very important to making quality measurements using an aerosol shock tube [4].

The pressure profile (2) in the upper frame shows classic shock tube behavior (see Supplemental File for representative pressure traces for each fuel). At times before $-80\ \mu\text{s}$, the pressure is given by the pre-shock fill pressure; from -80 to $0\ \mu\text{s}$, the pressure behind the incident shock wave is recorded; after $0\ \mu\text{s}$, the reflected shock region pressure is recorded. At $280\ \mu\text{s}$ the rapid rise in pressure signifies ignition (more specifically the point of maximum slope), then combustion waves cause rapid fluctuations. This is coincident with the rise in CH^* emission (3) and slightly delayed (at $300\ \mu\text{s}$ at the 5 cm location in the lower frame) by complete consumption of fuel. The ignition delay times and conditions are listed in Appendix 1.

4.1. *n*-Decane

Because *n*-decane has a higher vapor pressure at room temperature only a sparse aerosol is needed to create a stoichiometric mixture. The fraction of fuel in the final evaporated mixture that comes from the liquid droplets as compared to the amount in the saturated bath gas is small; hence, *n*-decane represents one of the most volatile fuels that can be used with the aerosol shock tube methodology. Figure 3 shows representative data taken with the aerosol shock tube at 5 atm.

Also shown are the Olchanski and Burcat measurements of [25] high-temperature ignition delay times for *n*-decane in 23% O_2 in argon, obtained in a heated shock tube. Their ignition delay time correlation can be rearranged to represent the dependence on the variables P and Φ for constant O_2 mole fraction as

$$\tau \sim P^{-0.625} \Phi^{0.06}$$

Also shown in Fig. 3 are the recent heated shock tube data at higher pressures (nominal values of 11 and 40 atm) published by Shen et al. [11]. The expected trend with pressure is apparent, and these data exhibit negative temperature coefficient behavior at high pressures and low temperatures.

Both of the previous studies utilized a heated shock tube (100°C or $373\ \text{K}$ in [25]; up to 160°C or $433\ \text{K}$ in [11]). Because *n*-decane has a relatively high vapor pressure, only moderate shock tube temperatures are required to generate sufficient fuel loading for equivalence ratios of unity. As a result, pre-test decomposition or oxidation is likely not a problem and thus the agreement between the previous *n*-decane data and the aerosol shock tube data at 5 atm provides additional confidence in the aerosol shock tube methodology. As less volatile fuels are used, the heated shock tube must operate at higher temperatures and becomes more susceptible to pre-test decomposition, whereas the aerosol shock tube does not suffer from this uncertainty.

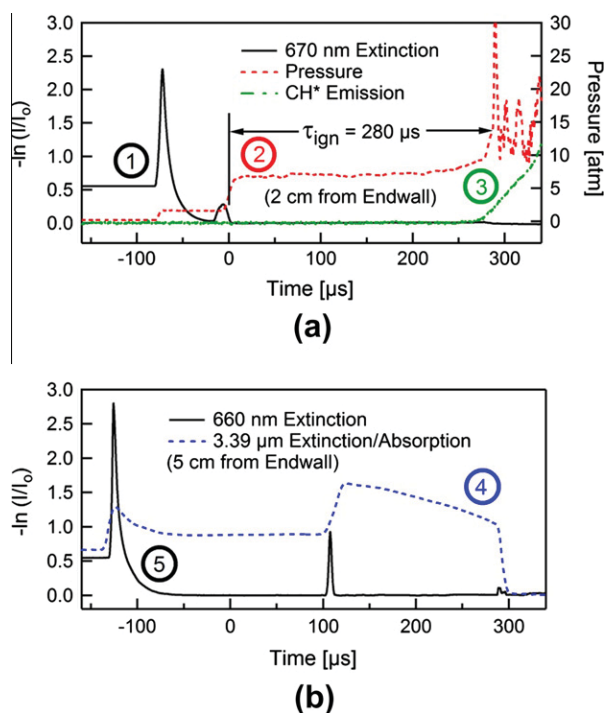


Fig. 2. Example of an ignition delay time measurement. This example was done with a DF-2 (CI 43)/21% O_2 /argon mixture with $\Phi = 0.48$, $T = 1197\ \text{K}$, and $P = 7.21\ \text{atm}$. The diagnostics in the upper frame are located 3 cm from the endwall, and in the lower frame are 5 cm from the end wall: (1) Mie scattering extinction, (2) pressure, (3) CH^* emission, (4) fuel absorption plus scattering, and (5) extinction by Mie scattering.

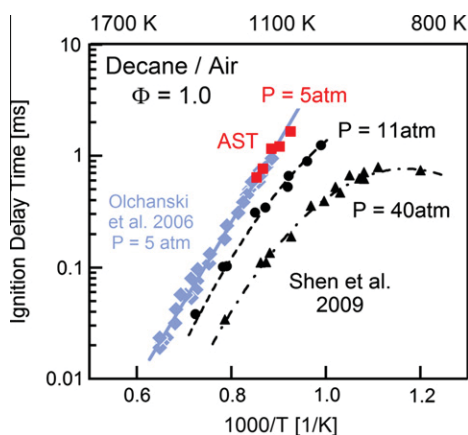


Fig. 3. *n*-Decane/air ignition delay times for various pressures. Current data: red squares; Olchanski and Burcat [25]: blue diamonds; Shen et al. [11]: black circles and triangles. All data scaled using the Olchanski and Burcat correlation [25]. All lines and curves represent simple fits to the data. (For interpretation of the references to colour in this figure legend, the reader is referred to the web version of this article.)

4.2. *n*-Dodecane

Ignition delay times for *n*-dodecane/air and *n*-dodecane/21% O₂/argon are shown in Fig. 4a and b. A pressure scaling of $P^{-0.89}$ is found for the air experiments (for all data except the Shen et al. 40 atm air data at the lowest temperatures), and a scaling of $P^{-0.86}$ is found for the 21% O₂/Ar experiments. Similarly, (though not presented here), only small variations of a few percent in the ignition delay times are seen with a change in diluents; this is consistent with simulations using the Westbrook et al. (LLNL) [5] or the Wang et al. (JetSurF 2.0) [28] models.

Figure 5 shows the variation of ignition delay time with equivalence ratio for *n*-dodecane. Over the limited Φ ratio range of 0.3–1.3, the data roughly follow a scaling of $\Phi^{-1.5}$. This dependence on equivalence ratio is also shown in Fig. 6a and b. At high temperatures (Fig. 6a) there are major differences between the data and the predictions of the detailed mechanisms of Westbrook et al. (LLNL) [5] and that of Wang et al. (JetSurF 2.0) [28]. At lower temperatures (Fig. 6b) the data and predictions give the same trend, but deviate at high equivalence ratio.

The dependence on equivalence ratio, when the oxygen mole fraction is fixed, is a direct result of changing the fuel mole fraction. At all temperatures studied, the measured ignition delay times are

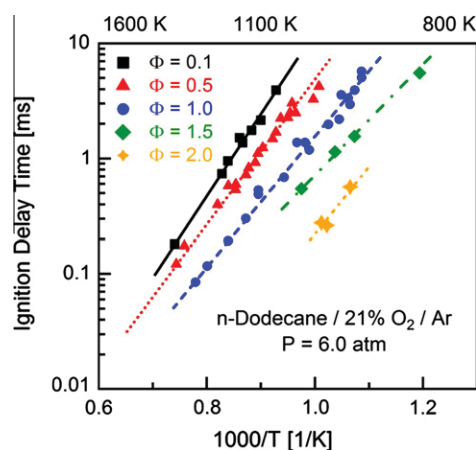


Fig. 5. Variation of *n*-dodecane/21% O₂/Ar ignition delay time with equivalence ratio; pressure is scaled to 6.0 atm (4.01–8.63 atm). All lines represent fits to the data.

reduced for higher equivalence ratios. The models capture this trend at lower temperatures (i.e. 1000 K), however, at higher temperatures (i.e. 1250 K), the models predict that higher fuel concentrations result in a longer ignition delay time. This trend in ignition delay time with equivalence ratio has also been observed in experiments with smaller fuels (e.g. *n*-butane) [22]. This behavior may be a result of increased radical scavenging by fuel decomposition product molecules in the simulation (e.g. OH + alkenes), or reduced production of radicals at higher temperatures as a result of less branching to fuel decomposition channels that generate H-atoms).

4.3. *n*-Hexadecane

n-Hexadecane has a very low vapor pressure and is well-suited for aerosol shock tube studies. Representative measurements are shown in Fig. 7a–c. Because of the high temperatures needed to achieve significant fuel loading, *n*-hexadecane is near the practical limit for long-chain *n*-alkanes experiments in heated shock tubes. One group, Penyazkov and coworkers [17] has attempted experiments with this fuel using a shock tube heated to 100 °C (373 K); their results are also shown in Fig. 7a.

Figure 7a presents the trend of ignition delay time with varying oxygen concentration (for the 1% and 4% O₂ in argon data of the present study, $\tau \sim X_{O_2}^{-0.54}$). The Penyazkov et al. data (21% O₂ in N₂) are not consistent with this trend. Simulations of these exper-

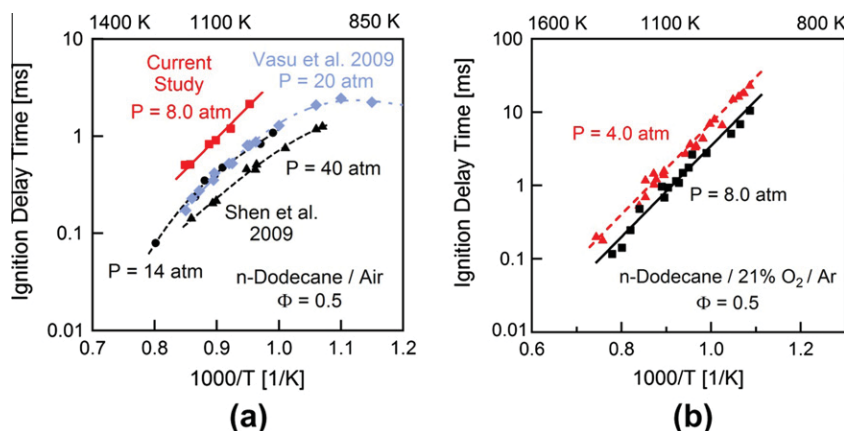


Fig. 4. (a) *n*-Dodecane/air ignition delay times for fuel-lean mixtures ($\Phi = 0.5$) at various pressures. Current data: red squares; Vasu et al. [15]: blue diamonds; Shen et al. [11]: black circles and triangles. (b) *n*-dodecane/21% O₂/Ar ignition delay times for fuel-lean mixtures ($\Phi = 0.5$) at various pressures. Current study 4 atm: red triangles; 8 atm: black squares. All lines represent fits to the data. (For interpretation of the references to color in this figure legend, the reader is referred to the web version of this article.)

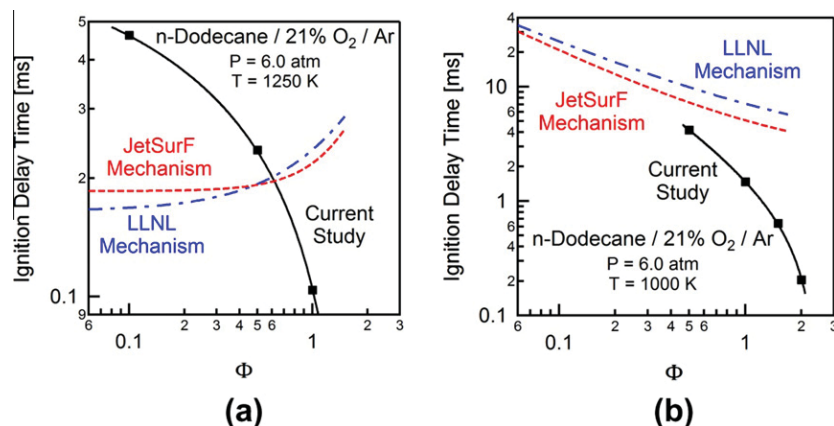


Fig. 6. (a) Equivalence ratio dependence of the ignition delay times for *n*-dodecane at high temperatures (1250 K). (b) A similar comparison at lower temperatures (1000 K).

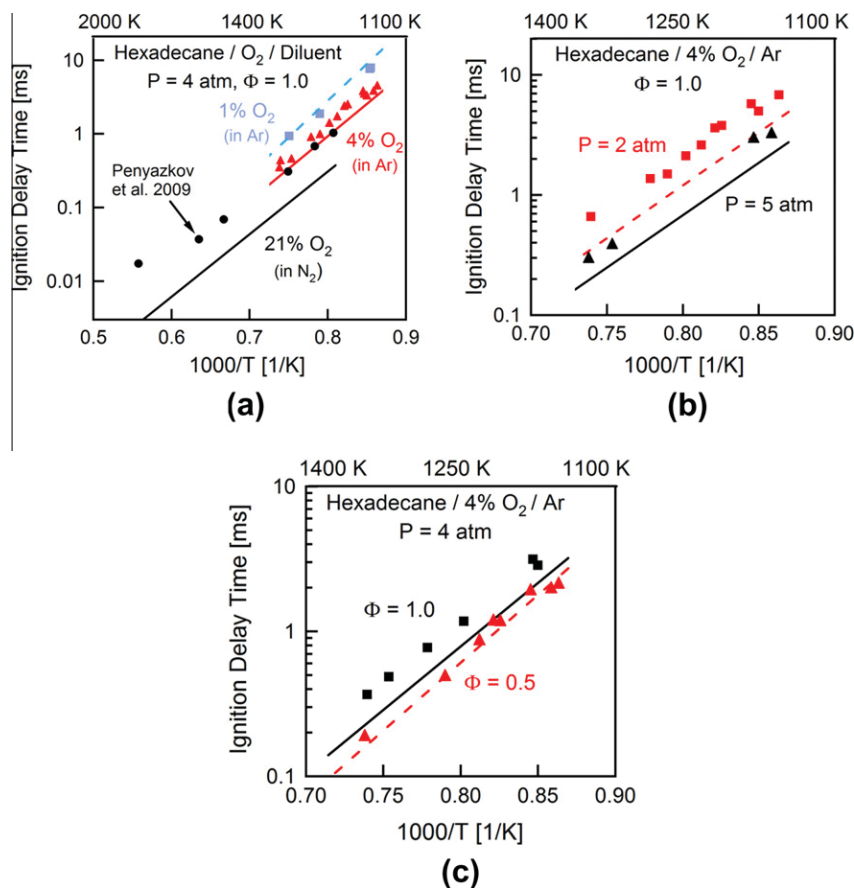


Fig. 7. (a) Comparison of *n*-hexadecane ignition delay times at 4 atm and equivalence ratio of 1.0 for various oxygen concentrations. Heated shock tube data by Penyakzov and coworkers [17] (21% O_2 in N_2) are also shown. (b) Ignition delay time variation with pressure for stoichiometric *n*-hexadecane/4% O_2 /Ar mixtures. (c) Ignition delay time variation with equivalence ratio at 4 atm for *n*-hexadecane/4% O_2 /Ar mixtures. All lines represent the Westbrook et al. model [5].

iments using the LLNL C16 mechanism [5] (which demonstrates a $X_{O_2}^{-0.74}$ scaling) suggest that the ignition delay times for the 21% O_2 in N_2 (models show that diluent makes only a few percent difference) experiments would be expected to be approximately one third of that found in the 4% O_2 in argon experiments, whereas a reduction of only $\sim 33\%$ is seen in the data. This difference may in part be attributed to fuel decomposition or oxidation to more stable components as the heated shock tube in the study was kept

at 100 °C (373 K) and the mixing tank kept at 200 °C (473 K), with mixtures kept in the mixing tank for between 3 and 4 h.

Figure 7b and c shows the variation of *n*-hexadecane ignition delay times with pressure and equivalence ratio. For fixed oxygen concentration, the measured ignition delay times scale as $P^{-0.73}$, and at 4 atm, scale as $\Phi^{0.82}$. Both of these are consistent with the LLNL C16 mechanism predictions of $P^{-0.70}$ and $\Phi^{0.55}$, though the model scaling with equivalence ratio is less satisfactory.

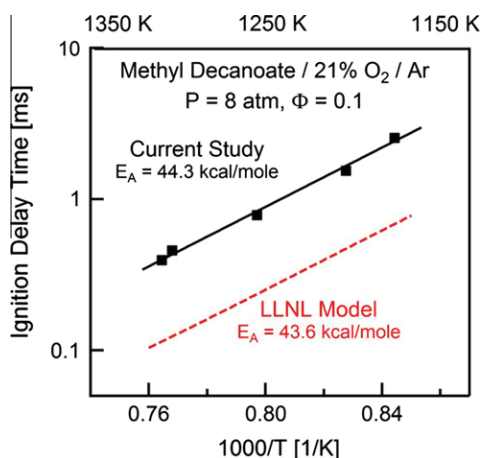


Fig. 8. Methyl Decanoate ignition delay times: experiment and simulation. Squares and solid line: current study; dotted line: simulation using the LLNL mechanism by Herbinet et al. [8].

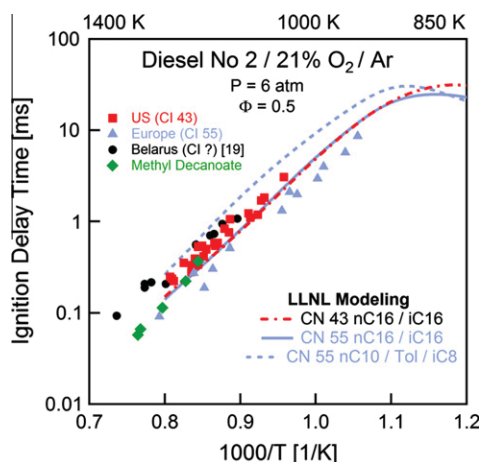


Fig. 9. Diesel ignition delay times for three different diesel fuels compared with simulations using the LLNL mechanism for various surrogate mixtures. All mixtures have an oxygen concentration of 21% with $P = 6$ atm and $\Phi = 0.5$. Colored, square symbols indicate data taken with aerosol shock tube; black circles represent data taken in a heated shock tube by Penyakzov et al. [19]. (For interpretation of the references to color in this figure legend, the reader is referred to the web version of this article.)

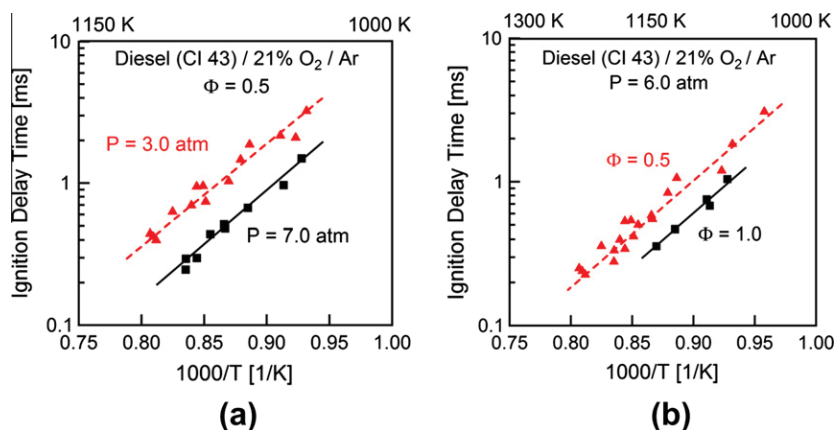


Fig. 10. Variation of ignition delay time with pressure ($\Phi = 0.5$) and equivalence ratio ($P = 6$ atm) for mixtures consisting of DF-2 (CI 43)/21% O_2 /Ar. All lines represent fits to the data.

4.4. Methyl decanoate

Methyl decanoate has a low vapor pressure (37 mtorr), and hence is also an ideal candidate for measurements in the aerosol shock tube. Figure 8 presents measured ignition delay times for methyl decanoate and simulations using the Herbinet et al. model [8]. These initial experiments were performed at a low equivalence ratio.

The experiments have longer ignition delay times than the LLNL model simulations [8], by a factor of 2.5, however, the measured activation energy (44.3 kcal/mol) is in close agreement with the LLNL model value (43.6 kcal/mol). The small pressure range of the experiments (7.8–8.0 atm) precluded determining a pressure dependence and so we were unable to confirm the strong variation with pressure ($\tau \sim P^{-1.32}$) predicted by the model. Over the range of lean equivalence ratios studied, $\Phi = 0.08$ –0.17, the ignition delay times scaled as $\Phi^{-1.2 \pm 0.05}$. This is in contrast to the model's predicted scaling of Φ^{-4} at these extreme equivalence ratios.

4.5. Diesel

Diesel fuel contains very heavy components and is thus an ideal fuel to be tested in the aerosol shock tube. We have tested a variety of diesel fuels with varying cetane index and oxygen concentration. Representative ignition delay times are shown in Fig. 9.

This figure shows data from three different diesel fuel mixtures. The US diesel sample has a cetane index of 43 calculated (ASTM D976) using its density of 0.86 g/cc (at 15 °C) and a distillation D86 at 50% of 265.9 °C, and was provided to our laboratory from the US Army Research Office. The European diesel sample has a higher estimated cetane index of 55. Although the ignition delay time difference between varying cetane indices is small, the larger cetane index diesel data exhibit shorter ignition delay times. These measurements were both made in the aerosol shock tube. Data from the Belarus diesel sample has an unknown cetane index and comes from the measurements by Penyakzov et al. [19] using a heated shock tube.

Also shown on this plot are simulations by Westbrook et al. (LLNL) [personal communication 2010] using three different surrogate blends with theoretically calculated cetane indices. These surrogates are comprised of either *n*-hexadecane and iso-cetane, or *n*-decane, toluene and iso-octane. The three-component CI-55 surrogate slightly overpredicts the ignition delay times of the CI = 55 European diesel fuel. The two-component surrogates employ larger molecules that more closely match the molecular weight of diesel fuel, and are based on primary reference fuel,

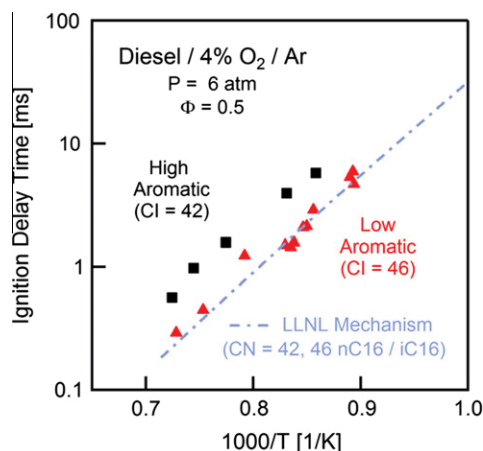


Fig. 11. Variation in ignition delay time with aromatic content of diesel fuel. Oxygen concentrations of 4% were used with Ar as the diluent. $P = 6$ atm and $\Phi = 0.5$. Results were compared to mixtures of n -hexadecane and iso-cetane (CN 42, 46) using LLNL mechanisms [5,7].

PRF, components. Simulations with these surrogates more closely match the experimental data.

The US diesel was also tested over a range of pressures and equivalence ratios. Figure 10a and b shows how these variations effect the ignition delay time.

As pressure increases the ignition delay time decreases following a scaling of $P^{-0.82}$. A decrease in ignition delay is also apparent if we increase the equivalence ratio (while holding oxygen concentration constant) following a scaling of $\Phi^{-0.70}$. An overall correlation for this fuel with 21% O_2 in argon is given by:

$$\tau[s] = 2.64 \times 10^{-8} P[\text{atm}]^{-0.82} \Phi^{-0.70} e^{24980[\text{cal/mole}]/RT}$$

We also measured ignition delay times for two other diesel fuels, this time at lower oxygen concentration. The results are shown below in Fig. 11.

The two diesel blends were chosen to bracket the large variation in aromatic content allowed by the US EPA. The higher-aromatic diesel has a general composition of: saturates 44.2%, aromatics 38.8%, and olefins 17%; whereas the lower-aromatic diesel has a composition: saturates 81%, aromatics 16.2%, and olefins 2.7%. No significant difference was seen in the PRF surrogate (using only cetane and iso-cetane as components) model for the two ce-

tane index cases. The simulations approximately capture the lower aromatic fraction fuel ignition delay times, but the higher aromatic fuel shows a larger discrepancy, implying that this simple mixture is not sufficient to capture the ignition behavior. The agreement may improve by using a mixture which sufficiently captures the aromatic chemistry that is affecting the ignition delay times.

5. Conclusions

This paper demonstrates the capabilities of aerosol shock tubes to investigate ignition delay times for many low-vapor-pressure fuels. The data obtained provide useful kinetic targets for testing the overall behavior of detailed mechanisms for pure and practical fuels. Correlations are provided, which are meant to capture rough trends in the data for ease of comparison.

Several important conclusions can be derived from these new data. Perhaps the most important is that n -dodecane ignition delay times for mixtures with 21% O_2 exhibit a negative power law dependence with equivalence ratio at high temperatures, whereas the LLNL [11] and JetSurF [28] models both predict a positive exponent. We believe that current n -dodecane mechanisms may require more than just minor modification to capture this behavior accurately.

To our knowledge, this study provides the first shock tube ignition delay time data for methyl decanoate and the first aerosol shock tube measurements for n -hexadecane. The n -hexadecane data reveals oxygen concentration dependence, pressure dependence and equivalence ratio dependence; the methyl decanoate data provide temperature and equivalence ratio dependences, and provide targets for the validation of large n -alkane and methyl ester (i.e. bio-diesel) reaction mechanisms.

This study also provides gas-phase ignition delay times for several types of diesel fuel and the variation of ignition delay time with cetane index, pressure, equivalence ratio, and aromatic content. These data provide a fundamental database for the testing and refinement of diesel surrogate mechanisms.

Acknowledgments

The authors would like to acknowledge the continued support of the Army Research Office for this work with Dr. Ralph Anthenien Jr. as contract monitor. We would also like to thank Dr. Westbrook and the LLNL Combustion Chemistry Group for supplying the PRF mechanism simulation results.

Appendix A

Conditions and ignition delay times.

No	Fuel	Diluent	X_O2 (nd)	X_fuel (nd)	T_5 (K)	P_5 (atm)	phi (nd)	Ign time (ms)
1	<i>n</i> -Decane	N2	0.21	0.014395	1081	5.14	1.06	1.696
2		N2	0.21	0.014940	1131	4.87	1.10	1.252
3		N2	0.21	0.018953	1154	5.15	1.40	0.921
4		N2	0.21	0.014720	1109	4.56	1.09	1.358
5		N2	0.21	0.025666	1173	4.93	1.89	0.950
6	<i>n</i> -Dodecane	N2	0.21	0.006844	1127	6.12	0.60	0.797
7		N2	0.21	0.009365	1050	7.88	0.82	1.034
8		N2	0.21	0.007871	1084	8.02	0.69	0.738
9		N2	0.21	0.006885	1114	8.50	0.61	0.640
10		N2	0.21	0.009497	1179	8.53	0.84	0.220
11		N2	0.21	0.010246	1167	7.88	0.90	0.215
12	<i>n</i> -Dodecane	Ar	0.21	0.007339	1168	6.37	0.65	0.484
13		Ar	0.21	0.001860	1209	4.64	0.16	0.926
14		Ar	0.21	0.002534	1163	4.93	0.22	1.800
15		Ar	0.21	0.003437	1192	5.06	0.30	1.110
16		Ar	0.21	0.002074	1078	4.00	0.18	5.605
17		Ar	0.21	0.004056	976	4.87	0.36	6.220

Appendix A (continued)

No	Fuel	Diluent	X_O2 (nd)	X_fuel (nd)	T_5 (K)	P_5 (atm)	phi (nd)	Ign time (ms)
18		Ar	0.21	0.009297	903	5.00	0.82	7.825
19		Ar	0.21	0.003488	1241	4.79	0.31	0.337
20		Ar	0.21	0.002064	1351	4.51	0.18	0.233
21		Ar	0.21	0.021380	979	5.04	1.88	0.306
22		Ar	0.21	0.016590	1025	6.06	1.46	0.543
23		Ar	0.21	0.019896	988	6.46	1.75	0.260
24		Ar	0.21	0.001905	1112	5.65	0.17	2.281
25		Ar	0.21	0.015036	838	6.26	1.32	5.352
26		Ar	0.21	0.018020	939	6.31	1.59	0.544
27		Ar	0.21	0.012890	964	5.82	1.14	1.175
28		Ar	0.21	0.014940	932	6.01	1.32	1.559
29		Ar	0.21	0.000558	1156	5.34	0.05	1.526
30		Ar	0.21	0.000662	1134	5.20	0.06	2.006
31		Ar	0.21	0.005336	1172	6.19	0.47	0.524
32		Ar	0.21	0.005890	1191	6.40	0.52	0.550
33		Ar	0.21	0.007572	1249	6.23	0.67	0.114
34		Ar	0.21	0.008276	1284	6.42	0.73	0.080
35		Ar	0.21	0.005649	1053	6.56	0.50	2.105
36		Ar	0.21	0.006098	1045	6.71	0.54	2.753
37		Ar	0.21	0.005160	1068	6.40	0.45	2.126
38		Ar	0.21	0.005023	1078	6.32	0.44	1.624
39		Ar	0.21	0.005655	1086	6.32	0.50	1.422
40		Ar	0.21	0.005533	1107	6.25	0.49	1.200
41		Ar	0.21	0.005678	1118	6.18	0.50	1.081
42		Ar	0.21	0.005760	1140	6.07	0.51	0.820
43		Ar	0.21	0.006297	1345	5.92	0.55	0.123
44		Ar	0.21	0.004595	1319	5.78	0.40	0.181
45		Ar	0.21	0.007901	1117	8.09	0.70	0.412
46		Ar	0.21	0.006972	1124	8.24	0.61	0.702
47		Ar	0.21	0.006795	993	4.23	0.60	5.732
48		Ar	0.21	0.012310	921	4.86	1.08	6.085
49		Ar	0.21	0.012800	943	5.21	1.13	3.804
50		Ar	0.21	0.012400	932	4.98	1.09	4.627
51		Ar	0.21	0.011580	954	5.05	1.02	4.169
52		Ar	0.21	0.011158	1061	4.10	0.98	0.959
53		Ar	0.21	0.009624	1019	4.36	0.85	1.828
54		Ar	0.21	0.010003	976	4.49	0.88	2.555
55		Ar	0.21	0.008750	1192	4.57	0.77	0.246
56		Ar	0.21	0.008929	1118	4.88	0.79	0.587
57		Ar	0.21	0.005656	1146	4.01	0.50	1.027
58		Ar	0.21	0.008300	1035	4.43	0.73	1.803
59		Ar	0.21	0.007420	1003	4.68	0.65	4.081
60		Ar	0.21	0.012760	1147	4.97	1.12	0.357
61		Ar	0.21	0.004879	1220	8.63	0.43	0.292
62		Ar	0.21	0.007078	1172	5.33	0.62	0.663
63		Ar	0.21	0.011790	1011	6.57	1.04	1.100
64		Ar	0.21	0.011660	940	7.00	1.03	2.599
65		Ar	0.21	0.011690	958	6.57	1.03	2.041
66		Ar	0.21	0.009985	921	6.25	0.88	5.556
67		Ar	0.21	0.005463	1037	5.69	0.48	2.607
68		Ar	0.21	0.005734	1049	5.76	0.51	2.581
69	n-Hexadecane	Ar	0.01	0.000497	1267	6.54	1.22	1.902
70		Ar	0.01	0.000312	1172	4.44	0.76	4.577
71		Ar	0.01	0.000326	1170	4.60	0.80	5.022
72		Ar	0.01	0.000493	1333	6.77	1.21	0.917
73		Ar	0.04	0.001832	1327	6.46	1.12	0.360
74		Ar	0.04	0.001023	1355	4.19	0.63	0.212
75		Ar	0.04	0.001207	1183	2.05	0.74	4.264
76		Ar	0.04	0.000920	1159	2.06	0.56	3.870
77		Ar	0.04	0.001776	1181	2.13	1.09	5.536
78		Ar	0.04	0.001168	1266	1.94	0.72	1.122
79		Ar	0.04	0.000909	1212	1.91	0.56	2.270
80		Ar	0.04	0.001485	1247	1.83	0.91	2.060
81		Ar	0.04	0.001582	1285	1.89	0.97	1.386
82		Ar	0.04	0.001565	1353	1.71	0.96	0.708
83		Ar	0.04	0.001290	1165	2.08	0.79	4.548
84		Ar	0.04	0.001571	1177	2.03	0.96	4.778
85		Ar	0.04	0.001165	1218	1.96	0.71	2.657
86		Ar	0.04	0.001254	1231	1.86	0.77	2.137
87	Methyl decanoate	Ar	0.21	0.001610	1302	7.67	0.15	0.298
88		Ar	0.21	0.001005	1308	7.57	0.09	0.486
89		Ar	0.21	0.001789	1185	7.84	0.17	1.385
90		Ar	0.21	0.001263	1255	8.03	0.12	0.631
91		Ar	0.21	0.001823	1208	7.90	0.17	0.831

(continued on next page)

Appendix A (continued)

No	Fuel	Diluent	X_O2 (nd)	X_fuel (nd)	T_5 (K)	P_5 (atm)	phi (nd)	Ign time (ms)
92	US DF2	Ar	0.21	0.005214	1128	6.42	0.46	1.065
93		Ar	0.21	0.005305	1212	6.52	0.47	0.350
94		Ar	0.21	0.005384	1185	6.69	0.47	0.509
95		Ar	0.21	0.004445	1178	6.51	0.39	0.600
96		Ar	0.21	0.005180	1236	6.07	0.46	0.252
97		Ar	0.21	0.006430	1232	6.17	0.57	0.202
98		Ar	0.21	0.006051	1073	6.29	0.53	1.690
99		Ar	0.21	0.006093	1138	6.29	0.54	0.763
100		Ar	0.21	0.004300	1170	7.32	0.38	0.517
101		Ar	0.21	0.004600	1185	7.40	0.41	0.331
102		Ar	0.21	0.003660	1198	7.24	0.32	0.328
103		Ar	0.21	0.007700	1095	7.54	0.68	0.741
104		Ar	0.21	0.007750	1078	7.99	0.68	1.082
105		Ar	0.21	0.004410	1155	7.58	0.39	0.574
106		Ar	0.21	0.005220	1154	7.08	0.46	0.508
107		Ar	0.21	0.007560	1130	7.59	0.67	0.515
108		Ar	0.21	0.005670	1197	7.21	0.50	0.288
109		Ar	0.21	0.007340	1191	4.35	0.65	0.430
110		Ar	0.21	0.007340	1240	3.86	0.65	0.301
111		Ar	0.21	0.008297	1098	4.33	0.73	1.232
112		Ar	0.21	0.006243	1175	4.06	0.55	0.542
113		Ar	0.21	0.007027	1044	4.27	0.62	3.510
114		Ar	0.21	0.015770	1150	2.33	1.39	0.620
115		Ar	0.21	0.007223	1084	4.68	0.64	1.233
116	Europe DF2	Ar	0.21	0.001976	1261	7.28	0.18	0.160
117		Ar	0.21	0.001796	1193	7.39	0.17	0.493
118		Ar	0.21	0.001954	1174	3.50	0.18	0.601
119		Ar	0.21	0.002040	1158	3.78	0.19	0.881
120		Ar	0.21	0.002456	1129	4.02	0.23	1.232
121		Ar	0.21	0.002642	1047	3.73	0.24	3.240
122		Ar	0.21	0.002633	998	4.55	0.24	6.228
123		Ar	0.21	0.003437	990	4.32	0.32	7.125
124		Ar	0.21	0.002616	962	4.83	0.24	11.400
125		Ar	0.21	0.002505	1036	5.24	0.23	4.067
126		Ar	0.21	0.002376	1025	4.96	0.22	4.116
127		Ar	0.21	0.004143	947	4.82	0.38	12.544
128	Low aromatic DF2	Ar	0.04	0.001380	1373	6.33	0.61	0.243
129		Ar	0.04	0.001279	1327	6.10	0.57	0.402
130		Ar	0.04	0.001462	1263	6.77	0.65	0.931
131		Ar	0.04	0.001156	1206	6.88	0.51	1.317
132		Ar	0.04	0.001228	1198	6.69	0.54	1.251
133		Ar	0.04	0.001198	1193	6.60	0.53	1.400
134		Ar	0.04	0.001713	1182	6.76	0.76	1.406
135		Ar	0.04	0.001009	1177	6.61	0.45	2.116
136		Ar	0.04	0.001705	1168	6.54	0.76	2.007
137		Ar	0.04	0.001761	1119	4.63	0.78	4.251
138		Ar	0.04	0.001947	1124	4.06	0.86	5.040
139		Ar	0.04	0.001772	1120	4.11	0.79	5.866
140	High aromatic DF2	Ar	0.04	0.000971	1381	5.88	0.43	0.641
141		Ar	0.04	0.001666	1344	6.15	0.74	0.731
142		Ar	0.04	0.002368	1291	5.50	1.05	1.013
143		Ar	0.04	0.003173	1203	2.05	1.41	4.621
144		Ar	0.04	0.005303	1166	2.09	2.35	4.644

Appendix B. Supplementary material

Supplementary data associated with this article can be found, in the online version, at doi:10.1016/j.combustflame.2011.08.021.

References

- [1] D.F. Davidson, R.K. Hanson, *Int. J. Chem. Kinet.* 36 (9) (2004) 510–523.
- [2] S.S. Vasu, D.F. Davidson, Z. Hong, V. Vasudevan, R.K. Hanson, *Proc. Combust. Inst.* 32 (1) (2009) 173–180.
- [3] D.R. Haylett, D.F. Davidson, R.K. Hanson, Second-generation aerosol shock tube: an improved design, *Shock Waves*, in press.
- [4] D.F. Davidson, D.R. Haylett, R.K. Hanson, *Combust. Flame* 155 (1–2) (2008) 108–117.
- [5] C.K. Westbrook, W.J. Pitz, O. Herbinet, H.J. Curran, E.J. Silke, *Combust. Flame* 156 (1) (2009) 181–199.
- [6] A. Ristori, P. Dagaut, M. Cathonnet, *Combust. Flame* 125 (3) (2001) 1128–1137.
- [7] M.A. Oehlschlaeger, J. Steinberg, C.K. Westbrook, W.J. Pitz, *Combust. Flame* 156 (11) (2009) 2165–2172.
- [8] O. Herbinet, W.J. Pitz, C.K. Westbrook, *Combust. Flame* 154 (3) (2008) 507–528.
- [9] O. Herbinet, W.J. Pitz, C.K. Westbrook, *Combust. Flame* 157 (5) (2010) 893–908.
- [10] W.J. Pitz, C.J. Mueller, *Prog. Energy Combust. Sci.* 37 (2011) 330–350.
- [11] H.S. Shen, J. Steinberg, J. Vanderover, M.A. Oehlschlaeger, *Energy Fuels* 23 (2009) 2482–2489.
- [12] G. Bikas, N. Peters, *Combust. Flame* 126 (1–2) (2001) 1456–1475.
- [13] U. Pfahl, K. Fieweger, G. Adomeit, *Symp. Int. Combust.* 26 (1) (1996) 781–789.
- [14] U. Pfahl, K. Fieweger, G. Adomeit, Shock tube Investigation of Ignition Delay Times of Multicomponent Fuel/Air-Mixtures Under Engine Relevant Conditions, Final Report, Subprogramme FK.4, IDEA-EFFECT, 1996.
- [15] S.S. Vasu, D.F. Davidson, R.K. Hanson, *Shock Waves (Part IV)* (2009) 293–298.
- [16] D.R. Haylett, R.D. Cook, D.F. Davidson, R.K. Hanson 33(1) (2011) 167–173.
- [17] M. Assad, V.V. Leschevich, O.G. Penyazkov, K.L. Sevrout, V.E. Tangirala, N.D. Joshi, Autoignitions of n-hexadecane and heptamethylnonane at high temperatures, in: G.D. Roy, S.M. Frolov, A.M. Starik (Eds.), *Nonequilibrium*

- Phenomena: Plasma, Combustion, Atmosphere, Torus Press Ltd., Moscow, pp. 210–220.
- [18] S. Wang, B.C. Fan, Y.Z. He, J.P. Cui, Shock Waves (Part IX) (2009) 775–780.
- [19] O.G. Penyazkov, K.L. Sevrout, V. Tangirala, N. Joshi, Autoignitions of diesel fuel/air mixtures behind reflected shock waves, in: Proceedings of the 4th European Combustion Meeting, April 14–17, Vienna, Austria, 2009, 6 p.
- [20] V.V. Leschevich, O.G. Penyazkov, K.L. Sevrout, V.E. Tangirala, N.D. Joshi, Auto-ignition of Diesel fuel at high temperatures and pressures, in: Proceedings of the 22nd International Colloquium on Dynamics of Explosions and Reactive Systems, July 26–31, Minsk, Belarus, 2009, 4p.
- [22] D. Healy, N.S. Donato, C.J. Aul, E.L. Petersen, C.M. Zinner, G. Bourque, H.J. Curran, Combust. Flame 157 (8) (2010) 1526–1539.
- [24] X. You, F.N. Egolfopoulos, H. Wang, Proc. Combust. Inst. 32 (1) (2009) 403–410.
- [25] E. Olchanski, A. Burcat, Int. J. Chem. Kinet. 38 (12) (2006) 703–713.
- [26] J.T. Farrell, N.P. Cernansky, F.L. Dryer, D.G. Friend, C.A. Hergart, C.K. Law, R.M. McDavid, C.J. Mueller, A.K. Patel, H. Pitsch, SAE Paper 2007-01-0201, 2007 SAE World Congress, Detroit, MI, 2007.
- [27] B. Akih-Kumgeh, J.M. Bergthorson, Energy Fuels 24 (4) (2010) 2439–2448.
- [28] H. Wang, E. Dames, B. Sirjean, D.A. Sheen, R. Tangko, A. Violi, J.Y.W. Lai, F.N. Egolfopoulos, D.F. Davidson, R.K. Hanson, C.T. Bowman, C.K. Law, W. Tsang, N.P. Cernansky, D.L. Miller, R.P. Lindstedt, A high-temperature chemical kinetic model of *n*-alkane (up to *n*-dodecane), cyclohexane, and methyl-, ethyl-, *n*-propyl and *n*-butyl-cyclohexane oxidation at high temperatures, JetSurF version 2.0, September 19, 2010. <<http://melchior.usc.edu/JetSurF/JetSurF2.0>>.

8th U. S. National Combustion Meeting
Organized by the Western States Section of the Combustion Institute
and hosted by the University of Utah
May 19-22, 2013

Ignition delay times of very-low-vapor-pressure biodiesel surrogates behind reflected shock waves

Matthew F. Campbell David F. Davidson Ronald K. Hanson

Department of Mechanical Engineering, Stanford University, Stanford CA 94405 USA

Ignition delay times for five low-vapor-pressure biodiesel surrogates were measured behind reflected shock waves, using an aerosol shock tube. These fuels included methyl decanoate ($C_{11}H_{22}O_2$, CAS: 110-42-9), methyl laurate ($C_{13}H_{26}O_2$, CAS: 111-82-0), methyl myristate ($C_{15}H_{30}O_2$, CAS: 124-10-7), and methyl palmitate ($C_{17}H_{34}O_2$, CAS: 112-39-0), all of which have a fully saturated alkane chemical structure. This study also examined a methyl oleate ($C_{19}H_{36}O_2$, CAS: 112-62-9) / Fatty Acid Methyl Ester (FAME) blend. Experiments were conducted in 4% oxygen/argon mixtures with the exception of methyl decanoate which was studied in 1% and 21% oxygen/argon blends. Reflected shock conditions covered temperatures from 1026 to 1388 K, at pressures of 3.5 and 7.0 atm, and equivalence ratios from 0.3 to 1.4. Arrhenius expressions describing the experimental ignition delay time data are given and compared to those derived from applicable mechanisms available in the literature. Graphical comparisons between experimental data and mechanism predictions are also provided. Experiments of methyl laurate, methyl myristate, and methyl palmitate represent the first shock tube ignition delay time measurements for these fuels. Finally, experiments with methyl palmitate represent, to the authors' knowledge, the first neat fuel/oxidizer/diluent gas-phase experiments involving a fuel which is a waxy solid at room temperature.

1. Introduction

In light of the finite supply of fossil fuels and recent concerns about the impact of combustion engine emissions, a search has begun for alternative energy resources. Such fuels would ideally have characteristics such as a high-energy-density, lower pollutant (hydrocarbon, soot, nitrogen oxide, etc.) emissions, the ability to be produced and refined geographically close to the location of consumption, and the ability to be consumed using currently existing infrastructure. With the exception of lower nitrogen oxide emissions, biodiesel fuel realizes all of these qualities and as such has become a leading candidate to blend with, supplement, or completely replace traditional fossil diesel fuel [Knothe 2010, Demirbas 2007, Demirbas 2009, Schönborn 2009]. In order to achieve this, however, a comprehensive understanding of biodiesel oxidation chemistry is necessary. One key component of such an understanding is a fuel's ignition delay time at elevated temperatures and pressures.

This study measured ignition delay times for several biodiesel surrogate molecules behind reflected shock waves using an aerosol shock tube. Biodiesel fuel is composed of Fatty Acid Methyl Esters (FAMES), the actual fuel mixture having only five such components: methyl palmitate (MP, $C_{17}H_{34}O_2$), methyl stearate (MS, $C_{19}H_{38}O_2$), methyl oleate (MO, $C_{19}H_{36}O_2$), methyl linoleate (ML, $C_{19}H_{34}O_2$), and methyl linolenate (MLN, $C_{19}H_{32}O_2$). Neat MO and ML were studied in another work [Campbell 2012]. MP and MS are fully saturated molecules, having no double bonds in their normal-alkane-like carbon chain; at room temperature they are waxy solids and normally they are found dissolved into the other three biodiesel components. Other saturated FAMES can be formed by varying the carbon chain length; three such molecules covered in this study are methyl decanoate (MD, $C_{11}H_{22}O_2$), methyl laurate (MLA, $C_{13}H_{26}O_2$), and methyl myristate (MM, $C_{15}H_{30}O_2$). Studying ignition delay times of smaller surrogate compounds can elucidate the chemistry of these molecules' larger counterparts.

2. Previous Studies

Methyl Decanoate

Of the surrogate fuels examined in this study, methyl decanoate (MD) has been the subject of the majority of research efforts to date. This is because its vapor pressure at 315 K (186 mTorr) makes it experimentally accessible using traditional techniques [Yuan 2005]; its melting point is 260 K [Knothe 2008] (more fuel property information can be found in Table 1). Moreover, it is the largest component in cuphea biodiesel (65% by mass), hailed for its beneficial combustion properties [Knothe 2009]. Previous studies of MD include microgravity experimentation [Vaughn 2006, Marchese 2011, Liu 2013], motored engine studies [Szybist 2007], pre- and non-pre-mixed flame examinations [Seshadri 2009, Sarathy 2010, Diévert 2011, Wang 2011, Feng 2012, Diévert 2013], pyrolysis studies [Pyl 2012], and jet-stirred reactor analyses [Glaude 2010, Herbinet 2011a]. Shock tube studies were performed by Wang and Oehlschlaeger, who worked at pressures of 15-16 atm in 21% O₂/N₂ mixtures with lean, stoichiometric, and rich equivalence ratios [Wang 2012]; Haylett et al., who worked at a pressure of 8 atm in 21% O₂/Ar mixtures with very lean equivalence ratios [Haylett 2012a]; and Li et al., who examined methyl decanoate autoignition at engine exhaust gas recirculation (EGR) conditions in air [Li 2012]. Other researchers have conducted modeling studies [Herbinet 2008, Hoffman 2009, Herbinet 2010, Luo 2010, Herbinet 2011b, Diévert 2012, Grana 2012, Luo 2012], and some of the experimental papers also include sections concerning mechanism development or reduction [Marchese 2011, Seshadri 2009, Sarathy 2010, Diévert 2011]. A summary of kinetic mechanisms designed for the fuels explored in this study is given in Table 2.

Table 1: Physical property information for the fuels investigated in this study [Yuan 2005, Knothe 2008].

Fuel	Molecular formula	Molecular weight [g/mol]	Vapor pressure (315 K) [Torr]	Melting point (1 atm) [K]
Methyl decanoate	C ₁₁ H ₂₂ O ₂	186.3	186x10 ⁻³	260
Methyl laurate	C ₁₃ H ₂₆ O ₂	214.3	21x10 ⁻³	278
Methyl myristate	C ₁₅ H ₃₀ O ₂	242.4	3x10 ⁻³	292
Methyl palmitate	C ₁₇ H ₃₄ O ₂	270.5	327x10 ⁻⁶	304
Methyl oleate	C ₁₉ H ₃₆ O ₂	296.5	97x10 ⁻⁶	254

Methyl Laurate

Methyl laurate (MLA) has been studied by far fewer researchers. Its vapor pressure at 315 K is 21 mTorr [Yuan 2005] and its melting point is 278 K [Knothe 2008]. Vaughn et al. [Vaughn 2006] and Marchese et al. [Marchese 2011] studied MLA droplets in microgravity environments, Schönborn et al. examined it in an engine study [Schönborn 2009], and Herbinet et al. [Herbinet 2011b] developed a kinetic mechanism for this fuel using an automatic compilation program known as EXGAS.

Methyl Myristate

Methyl myristate (MM) has also been relatively untouched in the literature. Its vapor pressure at 315 K is 3 milli-Torr [Yuan 2005] and its melting point is 292 K [Knothe 2005]. One motored engine study [Schönborn 2009] and one modeling study [Herbinet 2011b] have addressed this fuel.

Methyl Palmitate

Despite being one of the five primary components of real biodiesel blends, to the authors' knowledge, methyl palmitate (MP) has been the subject of only two experimental kinetic studies and two kinetic modeling studies. Its low vapor pressure (327 μTorr at 315 K) [Yuan 2005] and its high melting point (304 K) [Knothe 2005] make it inaccessible to typical gas-phase experimental techniques. Schönborn et al. studied MP in an engine using PID-controlled heaters to melt this waxy fuel [Schönborn 2009], and Hakka et al. dissolved MP in *n*-decane (at a mol:mol ratio of 26:74) in order to examine it using a jet-stirred reactor [Hakka 2009]. The two modeling studies of this methyl ester are Herbinet et al. [Herbinet 2011b] and Westbrook et al. [Westbrook 2011].

Table 2: Studies which have developed or modified kinetic mechanisms for the fuels examined in this study.

Fuel	Authors	Year	Design
Methyl decanoate	Herbinet et al.	2008	Detailed chemical kinetic mechanism
	Seshadri et al.	2009	Skeletal mechanism
	Glaude et al.	2010	EXGAS automatically-generated mechanism
	Herbinet et al.	2010	Modifications for monounsaturated variants of MD
	Luo et al.	2010	Skeletal mechanism
	Herbinet et al.	2011a	EXGAS automatically-generated mechanism
	Herbinet et al.	2011b	EXGAS automatically-generated mechanism
	Sarathy et al.	2011	Detailed chemical kinetic mechanism and skeletal mechanism
	Diévar et al.	2012	Detailed chemical kinetic mechanism
	Grana et al.	2012	Lumped kinetic mechanism
	Luo et al.	2012	Skeletal mechanism
Methyl laurate	Herbinet et al.	2011b	EXGAS automatically-generated mechanism
Methyl myristate	Herbinet et al.	2011b	EXGAS automatically-generated mechanism
Methyl palmitate	Herbinet et al.	2011b	EXGAS automatically-generated mechanism
	Westbrook et al.	2011	Detailed chemical kinetic mechanism
Methyl oleate	Naik et al.	2011	Detailed chemical kinetic mechanism
	Westbrook et al.	2011	Detailed chemical kinetic mechanism
	Westbrook et al.	2013	Detailed chemical kinetic mechanism
	Campbell et al.	2013	Updates to thermochemistry in Westbrook 2011 mechanism
	Saggese et al.	2013	Lumped kinetic mechanism

Methyl Oleate

Methyl oleate (MO) has been the subject of multiple studies. Its vapor pressure at 315 K is 97 μ Torr [Yuan 2005] and its melting point is 254 K [Knothe 2008]. Early work from the food industry is summarized by Porter et al. [Porter 1995]. More recent work includes tubular reactor studies [Archambault 1998, Archambault 1999], cetane number determination work [Knothe 2003], microgravity experimentation [Vaughn 2006, Marchese 2011], a motored engine study [Schönborn 2009], a jet-stirred reactor analysis [Bax 2010], an aerosol shock tube study [Campbell 2013], and kinetic modeling [Naik 2011, Westbrook 2011, Westbrook 2013, Saggese 2013].

Summary of Previous Studies

The literature review above demonstrates that a solid base of research in the area of large biodiesel surrogates has been established. However, key pieces of information which are necessary to improve kinetic mechanism accuracy are still lacking. In the case of MD, shock tube studies at oxygen contents other than 21% are needed. For ML, MM, and MP, no shock tube data is currently available. Finally, for MO, shock tube data demonstrating the effect of blending this methyl ester with other FAMES would provide direct information on methyl ester blends. The current study has sought to explore these research problems.

3. Experimental Setup

Aerosol Shock Tube

Ignition delay times were measured behind reflected shocks in a second-generation aerosol shock tube. Details of this facility and the associated optical diagnostics are available elsewhere [Davidson 2008, Haylett 2012a, Haylett 2012b, Campbell 2013], so only a brief overview will be given here. The aerosol shock tube consists of a driver section filled with high-pressure helium separated by a polycarbonate diaphragm from a low-pressure mixture of bath gas (1%, 4%, or 21% oxygen in argon; gas/fuel supplier and purity information can be found in Table 1). Nebulizers (Ocean Mist DK12NS) in a tank adjacent to the endwall produce a mixture of fuel droplets and bath gas, and the mixture is introduced

into the last 1.3 meters of the shock tube via a sliding endwall gate valve. An incident shock wave, generated upon bursting of the diaphragm, propagates through the aerosol mixture and evaporates the droplets, producing a uniform gas-phase fuel-oxidizer-diluent mixture. The size of the droplets follows a log-normal distribution with an approximate 2.5 μm number median diameter; this small size allows the droplets to evaporate quickly. When the incident shock reaches the endwall, it reflects back into the gas, stagnating the flow, and rapidly producing the high temperatures needed for the ignition experiment.

Table 3: Gas/fuel purity information, as determined by the supplier. The methyl oleate blend (MOB) is a mixture, obtained and used as-supplied from Sigma-Aldrich, which consists of about 70% (by mole) methyl oleate, along with about 30% other FAME components. Fuels were subjected to mechanical pumping to remove dissolved oxygen but were otherwise used as-is without further purification.

Component	Supplier	Purity
Helium	Praxair	99.99%
1% Oxygen in argon	Praxair	99.99+%
4% Oxygen in argon	Praxair	99.99+%
21% Oxygen in argon	Praxair	99.99+%
Methyl decanoate (MD)	Sigma-Aldrich	99.4%
Methyl laurate (MLA)	Sigma-Aldrich	99.1%
Methyl myristate (MM)	Sigma-Aldrich	99.6%
Methyl palmitate (MP)	Sigma-Aldrich	99.4%
Methyl oleate blend (MOB)	Sigma-Aldrich	~70% MO, ~30% other FAMEs

Spectroscopic measurements of fuel concentration and droplet scattering were made using a 3.39 μm helium-neon laser and a 650 nm diode laser, respectively; through sidewall windows located 3.6 cm from the endwall. In order to increase nebulizer output, the liquid fuels were heated to 40 C prior to nebulization; such mild heating is not known to induce premature fuel decomposition [Dantas 2007]. Test gas temperature, pressure, and equivalence ratio were computed using an in-house code described in [Davidson 2008] with thermodynamic data taken from the Westbrook et al. mechanism [Westbrook 2011]. Absorption cross section values for the fuels examined in this study at 3.39 μm , necessary for the quantitative Beer’s Law-based fuel mole fraction measurement, were estimated with an uncertainty of approximately $\pm 10\%$ based on published data for smaller normal alkanes and methyl esters [Sharpe 2004].

For shocks involving MLA, MM, and MP, a driver insert, constructed according to the method of Hong et al. [Hong 2009], was used to mitigate the non-ideal pressure rise following the reflected shock wave. The resulting non-reactive (no fuel) pressure trace showed an increase of about 2%/ms at 7.0 atm and 1%/ms at 3.5 atm. This residual non-ideal pressure rise in the presence of the driver insert may be related to flow variations generated by the circular-to-square transition incorporated in this shock tube near its end section.

Ignition Measurement

Ignition was measured by observing excited OH radical (OH*) emission at 306 nm using a silicon photo-detector and UG-5 Schott glass band-pass filter positioned at 3.6 cm from the endwall. Ignition delay time was defined as the time from the arrival of the reflected shock (marked by either the peak or the 50%-rise point of the helium-neon laser Schlieren spike) to the point where the maximum slope of the OH* emission trace was extrapolated to the OH* baseline (zero) value. This time was confirmed by sidewall pressure measurements (Kistler Model 603B1) and by helium-neon fuel absorption data. Ignition delay time data are plotted in Arrhenius form, where best-fit (residual) uncertainties are typically $\pm 15\%$. This error margin is largely due to a $\pm 1.5\%$ uncertainty in individual temperature determinations.

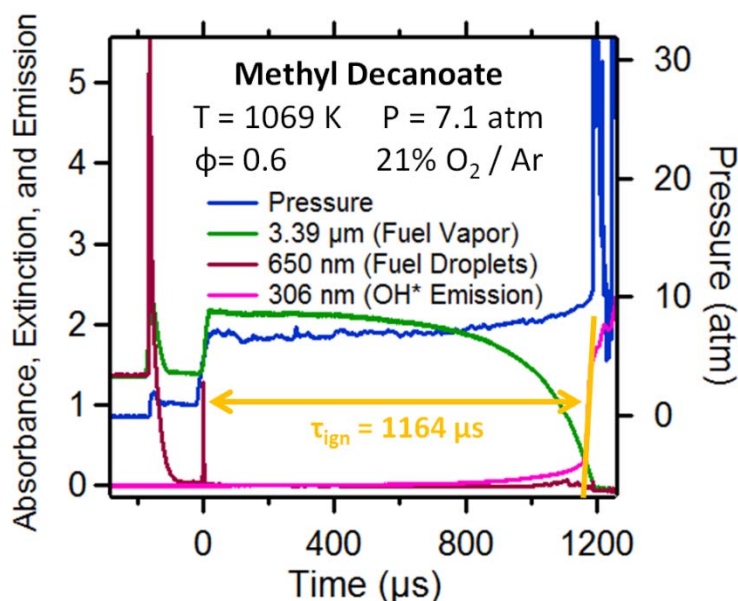


Figure 1: Example methyl decanoate ignition delay time data. Reflected shock initial conditions: 1069 K, 7.1 atm, 21% O₂ in Argon, $\phi=0.6$, $t_{\text{ign}} = 1164 \mu\text{s}$.

An example ignition delay time measurement is given in Figure 1. Following the incident shock, the droplets rapidly evaporate, as confirmed by the 650 nm laser trace, which shows the extinction dropping to zero at approximately 50 μs before arrival of the reflected shock. The 3.39 μm signal also decreases while evaporation is taking place, because in this intermediate time the laser is both scattered by aerosol droplets and absorbed by evaporated fuel molecules. At typical post-incident-shock temperatures and pressures (700 K / 1.7 atm), the timescale of fuel decomposition is much longer than the particle time (time between shock waves as experienced by individual molecules, typically 400 μs), thus fuel molecules enter the post-reflected-shock region intact. After evaporation is complete, the 3.39 μm signal shows a uniform purely gas-phase fuel mixture as these post-incident-shock gases flow past the observation window. Typical variation in 3.39 μm signal following complete evaporation is 2%, representing 2% non-uniformity in initial gas-phase fuel concentration. When the reflected shock arrives, at time zero, the pressure undergoes a step-change and the fuel begins to decompose. Ultimately, the fuel concentration drops to zero as the OH* radical light emission at 306 nm and pressure rise exponentially, marking the ignition event.

4. Kinetic Modeling

Ignition delay times were simulated using Chemkin-II (for EXGAS mechanisms) and Chemkin-Pro [Reaction Design 2010] (for all other mechanisms) by extrapolating the maximum gradient in the OH-radical concentration to the baseline (pre-ignition) value. Simulations did not include the experimental non-ideal pressure rise; however, at high temperatures this small increase has little effect on ignition delay, as illustrated in the recent methyl decanoate experiments/modeling of Wang and Oehlschlaeger [Wang 2012].

Results for MD were simulated using three mechanisms: Herbinet et al. [Herbinet 2008], Glaude et al. [Glaude 2010], and Diévert et al. [Diévert 2012]. These mechanisms are described and compared extensively in Li et al. [Li 2012]. Ignition delay times for MLA, MM, and MP were simulated using the Herbinet et al. [Herbinet 2011b] mechanism, which was automatically generated using the EXGAS software package and validated against methyl palmitate jet-stirred reactor experiments [Hakka 2009]. Data for MP were also simulated using the Westbrook et al. [Westbrook 2011] mechanism, which included thermochemistry updates as suggested by Campbell et al. [Campbell 2013]. Finally, results for the MOB were simulated using the updated Westbrook et al. [Westbrook 2011, Campbell 2013] mechanism.

5. Results and Discussion

Methyl Decanoate

Ignition delay times for methyl decanoate were measured at a pressure of 7 atm in 1% and 21% oxygen/argon bath gas at equivalence ratios ranging from 0.29 to 0.81 and at temperatures ranging from 1026 to 1388 K. Using these results, Arrhenius expressions in the form

$$\tau_{ign} = A \exp\left(\frac{E_A}{RT}\right)$$

were determined from the experimental data for the 1% and 21% oxygen/argon/MD mixtures. In this expression, τ_{ign} is the ignition delay time in ms, A is the A-factor [ms], E_A is the activation energy [kcal/mol], R is the ideal gas constant [kcal/mol-K], and T is the temperature of the experiment [K]. Likewise, Arrhenius parameters were also determined based on ignition delay times simulated using the Herbinet et al. [Herbinet 2008], Glaude et al. [Glaude 2010], and Diévert et al. [Diévert 2012] mechanisms for 1% and 21% oxygen/argon/MD mixtures at the conditions of this study. Finally, data from Wang and Oehlschlaeger [Wang 2012], which were obtained using a high pressure shock tube at 15-16 atm in 21% oxygen/nitrogen/MD mixtures, were scaled to 7 atm using a simple $\tau_{ign} \sim P^{-1}$ rule; an Arrhenius expression for this scaled data set has also been determined. The Arrhenius parameters mentioned above, along with the Arrhenius data determined by both mechanism and experiment for the other fuels pertinent to this study, are listed in Table 4.

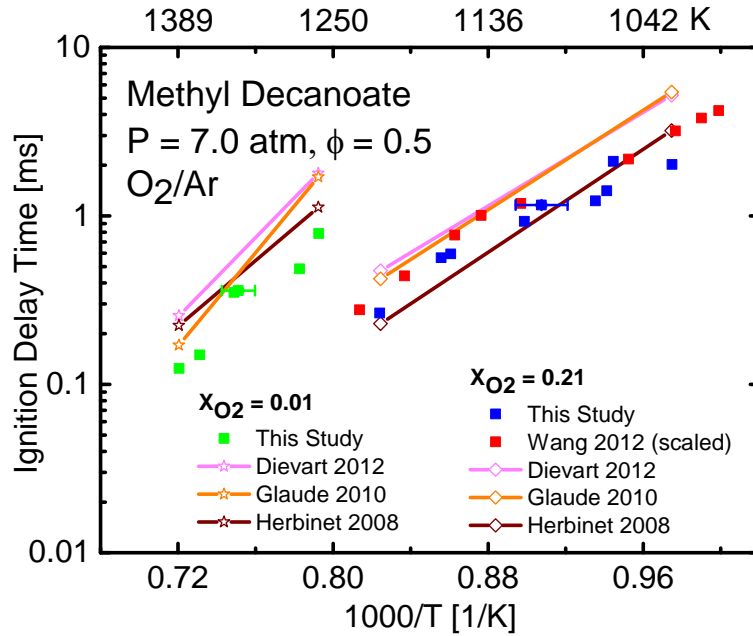


Figure 2: Methyl decanoate ignition delay times at $\phi=0.5$ and 7 atm for oxygen mole fractions of 0.01 and 0.21 in argon. Solid lines are predictions by Diévert et al. [Diévert 2012], Glaude et al. [Glaude 2010], and Herbinet et al. [Herbinet 2008] mechanisms. Data from Wang and Oehlschlaeger [Wang 2012] were taken in air at 15-16 atm and have been scaled to 7 atm using a simple $\tau_{ign} \sim P^{-1}$ rule.

Ignition delay time data measured in this study for methyl decanoate are plotted in Arrhenius form in Figure 2. Small corrections to ignition delay times have been applied to normalize individual points to common pressure and equivalence ratio values in this and all subsequent figures. Noteworthy is the negative oxygen mole fraction scaling shown on the plot; as oxygen content increases, ignition delay times decrease. Moreover, activation energy, visible in the slope ($\frac{d\tau_{ign}}{dT}$) of the data points and numerically in Table 2, decreases as oxygen content increases.

Also shown in this figure are the 21% oxygen/nitrogen/MD data from Wang and Oehlschlaeger [Wang 2012] which again have been scaled from their original 15-16 atm pressures to a common pressure of 7 atm using a simple $\tau_{ign} \sim P^{-1}$ rule. Notice the similarity, given experimental uncertainty, in ignition delay times and activation energy between the scaled Wang and Oehlschlaeger data and the 21% oxygen/argon/MD data presented in the current study. This gives confidence to the aerosol shock tube technique and helps validate comparisons between the two shock tube facilities. As expected, the diluent of the experiment (nitrogen vs. argon) has little effect on the measured ignition delay times; however, a slightly shorter ignition delay time in the argon-diluted data is observable.

Table 4: Best-fit Arrhenius parameters for fuels examined in this study. Comparisons are also given, where appropriate, with predictions from Diévert et al. [Diévert 2012], Glaude et al. [Glaude 2010], Herbinet et al. [Herbinet 2008], Herbinet et al. [Herbinet 2011b], and updated Westbrook et al. [Westbrook 2011, Campbell 2013] mechanisms. Arrhenius information is given as well for the scaled methyl decanoate data of Wang and Oehlschlaeger [Wang 2012], together with pure methyl oleate data taken by Campbell et al. [Campbell 2013]. $\tau_{ign} = A \exp\left(\frac{E_A}{RT}\right)$.

Fuel	Data Set	Pressure (atm)	Equivalence Ratio	X _{O2}	A Factor (ms)	E _A (kcal/mol)
MD	This Study	7.0	0.5	0.01	4.95x10 ⁻⁹	47.3
MD	Herbinet 2008	7.0	0.5	0.01	2.10x10 ⁻⁸	44.6
MD	Glaude 2010	7.0	0.5	0.01	1.70x10 ⁻¹¹	63.5
MD	Diévert 2012	7.0	0.5	0.01	8.70x10 ⁻¹⁰	53.8
MD	This Study	7.0	0.5	0.21	7.11x10 ⁻⁶	25.9
MD	Wang 2012 (in air; scaled)	7.0	0.5	0.21	2.27x10 ⁻⁶	28.9
MD	Herbinet 2008	7.0	0.5	0.21	1.18x10 ⁻⁷	34.9
MD	Glaude 2010	7.0	0.5	0.21	3.48x10 ⁻⁷	33.8
MD	Diévert 2012	7.0	0.5	0.21	9.02x10 ⁻⁷	31.7
MLA	This Study	3.5	1.25	0.04	2.71x10 ⁻⁸	43.2
MLA	Herbinet 2011	3.5	1.25	0.04	7.53x10 ⁻⁹	49.3
MLA	This Study	7.0	0.75	0.04	4.74x10 ⁻⁸	40.8
MLA	Herbinet 2011	7.0	0.75	0.04	3.56x10 ⁻⁹	48.6
MLA	This Study	7.0	1.25	0.04	2.95x10 ⁻⁶	30.9
MLA	Herbinet 2011	7.0	1.25	0.04	6.37x10 ⁻⁸	42.3
MM	This Study	3.5	0.75	0.04	1.32x10 ⁻⁸	44.2
MM	Herbinet 2011	3.5	0.75	0.04	3.12x10 ⁻⁹	50.1
MM	This Study	7.0	0.75	0.04	1.57x10 ⁻⁸	43.1
MM	Herbinet 2011	7.0	0.75	0.04	4.81x10 ⁻⁹	47.9
MM	This Study	7.0	1.25	0.04	5.26x10 ⁻⁷	34.9
MM	Herbinet 2011	7.0	1.25	0.04	9.99x10 ⁻⁸	41.3
MP	This Study	3.5	0.75	0.04	4.14x10 ⁻¹⁰	52.4
MP	Herbinet 2011	3.5	0.75	0.04	3.67x10 ⁻⁹	49.9
MP	Westbrook 2011	3.5	0.75	0.04	2.46x10 ⁻⁸	41.8
MP	This Study	7.0	0.325	0.04	3.29x10 ⁻⁷	35.1
MP	Herbinet 2011	7.0	0.325	0.04	2.99x10 ⁻¹⁰	53.6
MP	Westbrook 2011	7.0	0.325	0.04	3.12x10 ⁻⁹	46.0
MOB	This Study	7.0	0.75	0.04	3.42x10 ⁻⁷	35.6
MO	Campbell 2013 (pure MO)	7.0	0.75	0.04	7.32x10 ⁻⁷	33.5
MO	Westbrook 2011 (pure MO)	7.0	0.75	0.04	2.40x10 ⁻⁸	41.8
MOB	This Study	7.0	1.25	0.04	2.60x10 ⁻⁶	30.7
MO	Campbell 2013 (pure MO)	7.0	1.25	0.04	9.37x10 ⁻⁸	38.1
MO	Westbrook 2011 (pure MO)	7.0	1.25	0.04	4.89x10 ⁻⁸	40.2

Ignition delay time predictions made using the mechanisms of Herbinet et al. [Herbinet 2008], Glaude et al. [Glaude 2010], and Diévert et al. [Diévert 2012] have also been plotted in Figure 2 in solid lines. First, observe the 1% oxygen/argon/MD mixture data. At low temperatures, the Herbinet mechanism predictions are most accurate; however, at higher temperatures, those based on the Glaude mechanism do a better job. For all temperatures, the Diévert mechanism's predictions are too slow by an approximate factor of two. In terms of activation energy, the Herbinet mechanism underpredicts the experimental value of 47.3 kcal/mol by 2.7 kcal/mol, and the Glaude and Diévert mechanisms overpredict this value by 16.2 and 6.5 kcal/mol respectively.

Next, observe the data 21% oxygen/argon/MD mixture data. At these conditions, all of the mechanisms do a reasonable job at simulating the experimental data. In particular, the Herbinet mechanism underpredicts ignition delay times at high temperatures but reproduces them well at low temperatures. Conversely, the Glaude and Diévert mechanisms overpredict ignition delay times at low temperatures but do a good job at high temperatures. All three mechanisms give similar activation energies, which are higher than the experimental data by between 5.8 and 9.0 kcal/mol. Finally, notice that, true to the experimental data presented here, all of the mechanisms predict a decrease in ignition delay time and activation energy as oxygen content increases.

Methyl Laurate

Ignition delay times for methyl laurate were measured at pressures of 3.5 and 7 atm in 4% oxygen/argon bath gas at equivalence ratios ranging from 0.67 to 1.44 and at temperatures ranging from 1163 to 1354 K. Results are displayed in Figure 3. First observe the data at a common pressure of 7 atm. For these data, at high temperatures, positive equivalence ratio scaling is evident, in which an increase in equivalence ratio results in an increase in ignition delay time. However, notice that at low temperatures, the data seem to be insensitive to equivalence ratio. Such a trend was seen in the neat methyl oleate and methyl linoleate/4% oxygen/argon mixtures studied by Campbell et al. [Campbell 2013]. Furthermore, activation energy decreases with increasing equivalence ratio, a trend also observed by Campbell et al. Next observe the data at a common equivalence ratio of $\phi=0.75$. Within this subset of the data, negative pressure scaling is evident; as pressure increases, ignition delay time decreases. In addition, activation energy decreases with increasing pressure.

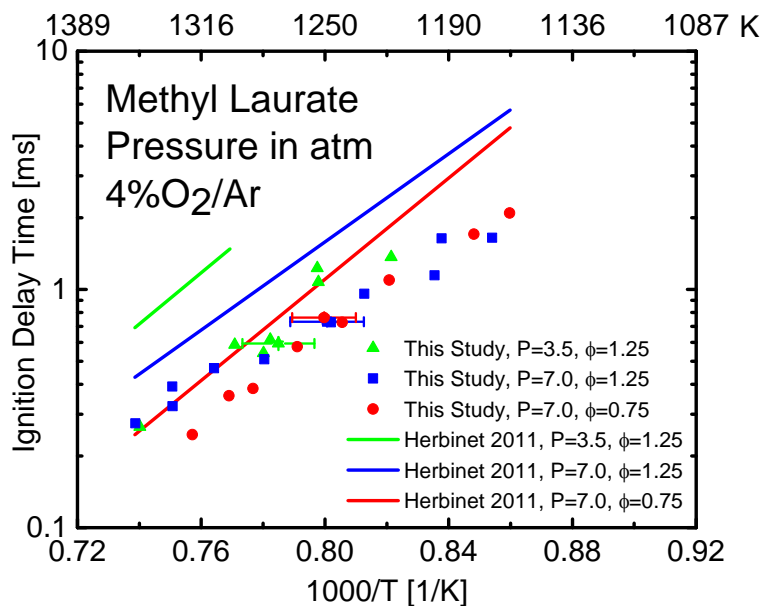


Figure 3: Methyl laurate ignition delay times taken in 4% oxygen/argon mixtures. Comparison is given with the Herbinet et al. mechanism [Herbinet 2011b], shown in solid lines.

Ignition delay time predictions calculated using the Herbinet et al. mechanism [Herbinet 2011b] are also shown in Figure 3. Notice that the Herbinet mechanism generally overpredicts ignition delay times; its predictions at 3.5 atm are too long by an approximate factor of two. However, for the higher-temperature data at 7 atm, the mechanism predictions are closer to the experimental results. The mechanism seems to accurately capture the positive equivalence ratio scaling and negative pressure scaling. Focusing on the predictions at 7 atm, we observe that the mechanism emulates the experimentally-seen low-temperature equivalence ratio independence. Finally, while the mechanism overpredicts

activation energy values by 6.1 to 11.4 kcal/mol, it correctly predicts that activation energy decreases with increasing equivalence ratio and decreases with increasing pressure.

Methyl Myristate

Ignition delay times for methyl myristate were measured at pressures of 3.5 and 7 atm in 4% oxygen/argon bath gas at equivalence ratios ranging from 0.54 to 1.35 and at temperatures ranging from 1162 to 1357 K. The results, displayed in Figure 4, show striking resemblance to those of methyl laurate. Similar to ML, the MM data display positive equivalence ratio scaling (observable at high temperatures) and negative pressure scaling. Also similar to ML, the MM data show insensitivity to equivalence ratio at low temperatures. Finally, like the ML data, the MM activation energy decreases with increasing equivalence ratio and decreases with increasing pressure.

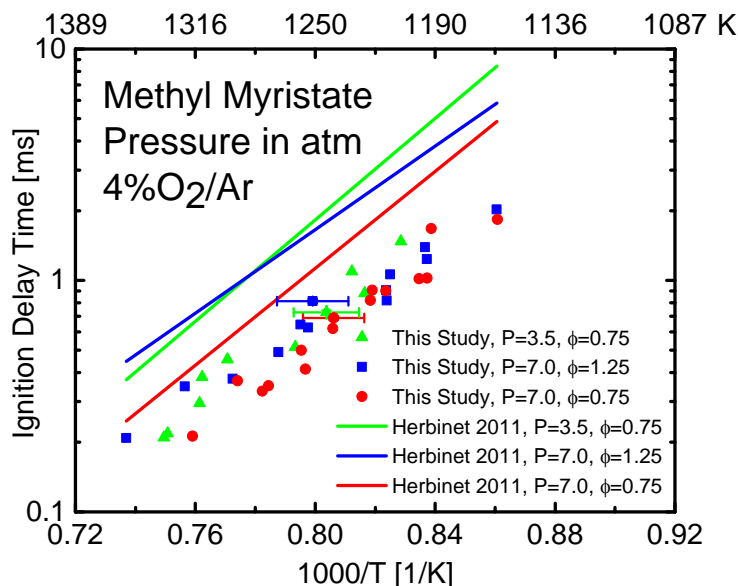


Figure 4: Methyl myristate ignition delay times taken in 4% oxygen/argon mixtures. Comparison is given with the Herbinet et al. mechanism [Herbinet 2011b], shown in solid lines.

Comparisons with the methyl myristate mechanism of Herbinet et al. [Herbinet 2011b] are also shown in Figure 4. At all temperatures studied the Herbinet mechanism overpredicts ignition delay time data by a factor of approximately two. As in the ML mechanism predictions, the MM mechanism seems to capture the positive equivalence ratio scaling and negative pressure scaling accurately. In addition, the mechanism correctly captures the equivalence ratio independence shown in the MM data at low temperatures. Finally, while the MM mechanism overpredicts activation energy by between 4.8 and 6.4 kcal/mol, it accurately predicts the trend that activation energy decreases with increasing equivalence ratio and with increasing pressure.

Methyl Palmitate

Ignition delay times for methyl palmitate were measured at pressures of 3.5 and 7 atm in 4% oxygen/argon bath gas at equivalence ratios ranging from 0.27 to 0.81 and at temperatures ranging from 1180 to 1311 K. Results are displayed in Figure 5. While the two sets of data displayed have neither pressure nor equivalence ratio in common, several important comparisons can nevertheless still be made. Observe that ignition delay times taken at lower pressure and higher equivalence ratio are longer than those taken at higher pressure and lower equivalence ratio; however, a convergence of the two trends can be seen at high temperatures. Furthermore, the activation energy is higher for the high pressure/low equivalence ratio data than for the low pressure/high equivalence ratio data.

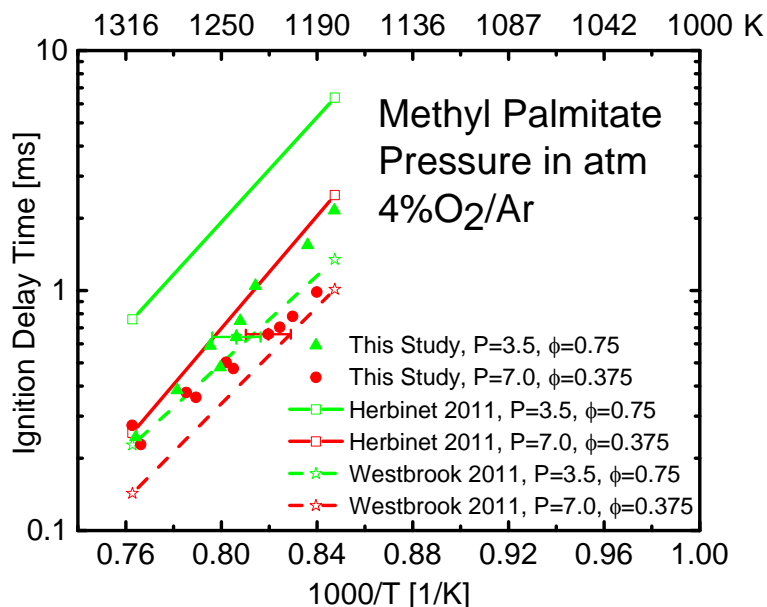


Figure 5: Methyl palmitate ignition delay times taken in 4% oxygen/argon mixtures. Comparison is given with the Herbinet et al. [Herbinet 2011b] and updated Westbrook et al. [Westbrook 2011, Campbell 2013] mechanisms, shown in solid lines.

Comparisons are given in Figure 5 with predictions from the Herbinet et al. [Herbinet 2011b] and updated Westbrook et al. [Westbrook 2011, Campbell 2013] mechanisms. Several general observations can be made upon initial examination. First, both mechanisms correctly predict that the data taken at low pressure and high equivalence ratio should have longer ignition delay times than those taken at high pressure and low equivalence ratio. However, contrary to experimental data, both mechanisms predict that activation energy should be lower for the low pressure/high equivalence ratio data rather than for the high pressure/low equivalence ratio data. Moreover, neither mechanism captures the convergence of the two trend lines at high temperatures.

More observations can be made by examining the 3.5 atm data alone. At all temperatures studied, the Herbinet mechanism overpredicts ignition delay times by an approximate factor of four. In contrast, the updated Westbrook mechanism predicts ignition delay times correctly at high temperatures, but underpredicts them by approximately two at lower temperatures. Finally, the activation energy predicted by the Herbinet mechanism is within 2.5 kcal/mol of the experimental value of 52.4 kcal/mol; however, that predicted by the Westbrook mechanism is too low by 10.6 kcal/mol.

Observations may also be made by focusing solely on the 7 atm data. At high temperatures, the Herbinet mechanism accurately captures ignition delay time data; however, at lower temperatures its predictions are too large. In contrast, the Westbrook mechanism underpredicts ignition delay times at high temperatures, but correctly simulates them at low temperatures. Finally, both the Herbinet and Westbrook mechanisms overpredict the experimentally-determined activation energy.

Methyl Oleate / FAME Blend

Ignition delay times for the methyl oleate / FAME blend were measured at a pressure of 7 atm in 4% oxygen/argon bath gas at equivalence ratios ranging from 0.32 to 1.42 and at temperatures ranging from 1141 to 1360 K. These results are displayed in Figure 6. In addition to these data, ignition delay times for pure methyl oleate at the same conditions, obtained by Campbell et al. [Campbell 2013] are also shown. There are multiple noteworthy attributes of this comparison. First, both of the MO and MOB data sets show positive equivalence ratio scaling. Moreover, for both MO and MOB, a region at low temperatures exists wherein the sensitivity of ignition delay time to equivalence ratio vanishes. By comparing ignition delay time values between the MO and MOB data sets, it can be seen that the MOB may have slightly reduced reactivity as compared to the pure MO; however, the uncertainty in the data sets makes this difficult to confirm. Finally, close comparison reveals that activation energy increases with equivalence ratio in the pure MO data set, whereas activation decreases with equivalence ratio in the MOB data. Overall, it appears that the 30% non-MO components in the MOB did not appear to significantly affect reactivity of the blend.

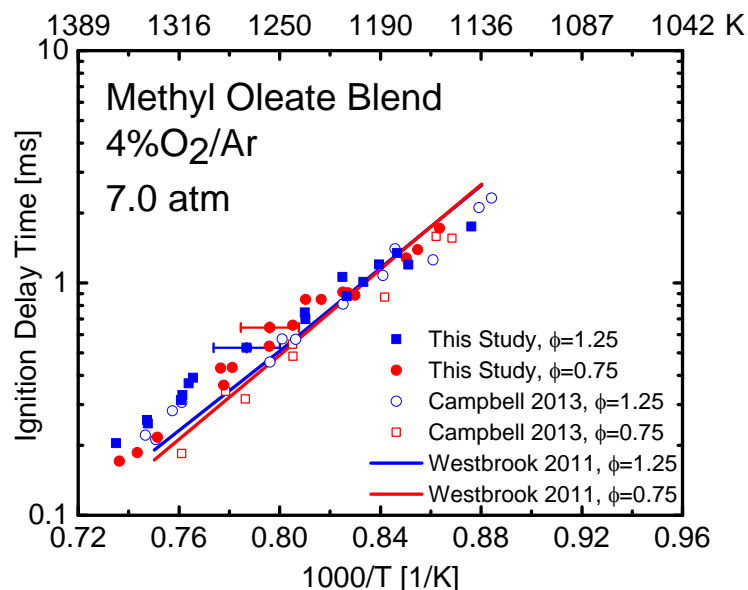


Figure 6: Methyl oleate / FAME blend ignition delay times taken in 4% oxygen/argon mixtures. Comparison is given with neat methyl oleate ignition delay times simulated using the updated Westbrook et al. [Westbrook 2011, Campbell 2013] mechanism, shown in solid lines. Ignition delay times for pure methyl oleate taken by Campbell et al. [Campbell 2013] are also shown as hollow symbols for comparison.

Comparisons of the MO and MOB experimental data to simulations of pure MO ignition delay times performed using the updated Westbrook model [Westbrook 2011, Campbell 2013] reveal further insight. In general, the updated Westbrook mechanism correctly predicts ignition delay times for both the pure MO and the MOB. However, it appears that the mechanism slightly underpredicts data at an equivalence ratio of $\phi=1.25$ at high temperatures, and tends to overpredict values at all equivalence ratios at low temperatures. The mechanism successfully predicts the experimentally-observed low-temperature equivalence ratio-independent region. At both equivalence ratios, activation energy values predicted by the Herbinet mechanism for pure MO are higher than the experimentally determined pure MO and MOB activation energy values. Finally, the mechanism predicts that activation energy for pure MO ignition should decrease as equivalence ratio increases; this is contrary to the experimental results for pure MO but in agreement with the experimental MOB results.

Fuel Comparisons

A comparison between the ignition delay time results for MLA and MM at a pressure of 7 atm and equivalence ratios of $\phi=0.75$ and $\phi=1.25$ is given in Figure 7. This comparison is insightful because it helps elucidate the effect of carbon chain length on ignition delay time; the structures of MLA and MM are identical except that the carbon chain length of MLA is 12, whereas that of MM is 14. First observe the data points for MLA and MM which occur at an equivalence ratio of $\phi=0.75$. A comparison between these two sets of data reveals that ignition delay time decreases as carbon chain length increases from MLA to MM. This effect is most pronounced at high temperatures, and is less apparent as temperature decreases. Furthermore, activation energy increases as the chain length increases from MLA to MM. A comparison of these two fuels at an equivalence ratio of $\phi=1.25$ reveals identical conclusions; ignition delay time decreases and activation energy increases as carbon chain length increases from MLA to MM. Finally, for both MLA and MM, activation energy decreases by about 9 kcal/mol as equivalence ratio increases from $\phi=0.75$ to $\phi=1.25$.

Ignition delay times simulated using the Herbinet et al. [Herbinet 2011b] mechanism are also shown in Figure 7. Again, several conclusions may be drawn by examining this plot. Most notably, the mechanism does not capture the increase in reactivity with carbon chain length; in fact, it seems to predict a slight decrease in reactivity as carbon chain length increases from MLA to MM. Moreover, the mechanism incorrectly predicts that the activation energy will slightly decrease as carbon chain length increases from MLA to MM. Finally, the mechanism correctly predicts that the activation energy decreases for both MLA and MM as equivalence ratio increases from $\phi=0.75$ to $\phi=1.25$; however, it underpredicts the magnitude of this decrease by about 3 kcal/mol.

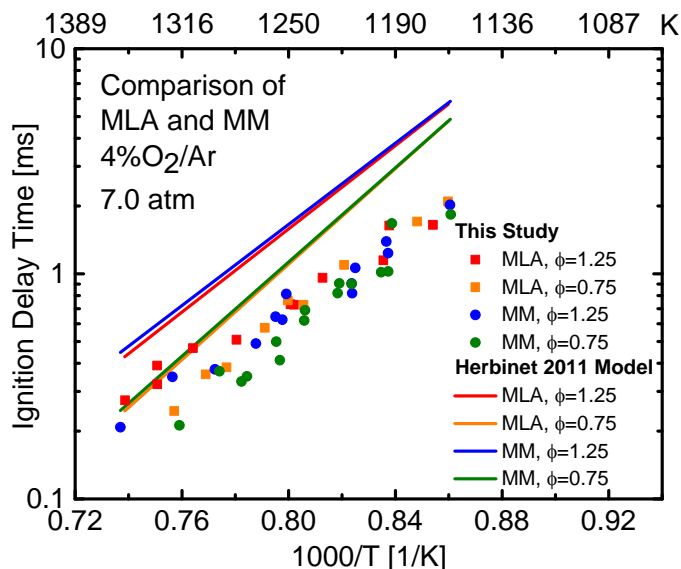


Figure 7: Comparison of methyl laurate and methyl myristate ignition delay times at 7 atm and equivalence ratios of $\phi=0.75$ and $\phi=1.25$, together with simulations performed using the Herbinet et al. [Herbinet 2011b] mechanism.

A comparison between the ignition delay time results for MM and MP at a pressure of 3.5 atm and an equivalence ratio of $\phi=0.75$ is given in Figure 8. This graph helps further emphasize the effect of carbon chain length on reactivity; MM has a carbon chain length of 14 and MP has a carbon chain length of 16. Similar to the MLA-MM comparison, this figure shows that reactivity increases (ignition delay time decreases) as carbon chain length increases from MM to MP. Moreover, in the same way this change is more pronounced at high temperatures and less noticeable as temperature decreases. Finally, the data again show that activation energy increases as carbon chain length increases.

Figure 8 also includes ignition delay time predictions performed using the Herbinet et al. [Herbinet 2011b] mechanism. As in the MLA-MM comparison, the mechanism fails to capture the increase in reactivity as chain length increases from MM to MP, and in fact a slight reduction in reactivity can be seen. Furthermore, despite the increase in chain length from MM to MP, the mechanism predicts that activation energy is nearly constant at about 50 kcal/mol.

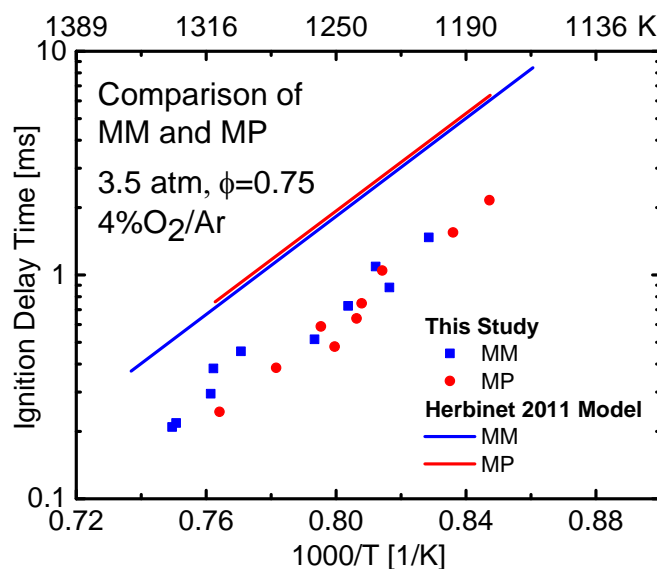


Figure 8: Comparison of methyl myristate and methyl palmitate ignition delay times at 3.5 atm and $\phi=0.75$, together with simulations performed using the Herbinet et al. [Herbinet 2011b] mechanism.

6. Conclusions

The first methyl decanoate ignition delay time data in 1% oxygen/argon bath gas mixtures have been reported at 7 atm and an equivalence ratio of $\phi=0.5$ at temperatures between 1262 and 1388 K, showing that available mechanisms generally overpredict ignition delay times at these conditions. Methyl decanoate ignition delay time data in 21% oxygen/argon bath gas mixtures have been found to compare favorably with existing mechanisms, and moreover good agreement was found with scaled data from Wang and Oehlschlaeger [Wang 2012]. The first shock tube ignition delay time measurements for neat methyl laurate, methyl myristate, and methyl palmitate have been reported at pressures of 3.5 and 7 atm, equivalence ratios ranging from $\phi=0.27$ to $\phi=1.44$, and temperatures ranging from 1162 to 1357 K. Comparisons with available mechanisms at these conditions show reasonable agreement of activation energy values, though in general simulated ignition delay times are too long. Furthermore, comparisons between these three fuels at common pressure and equivalence ratio conditions show that activation energy increases and ignition delay time decreases as carbon chain length increases. Methyl oleate has been studied in a blend of other FAMES, showing that the presence of the 30% other FAMES had little effect on reactivity. Finally, these data provide targets for the validation of reduced kinetic mechanisms for these surrogates, or for future improvements to detailed mechanisms for biodiesel fuels.

Acknowledgements

This work was supported by the Combustion Energy Frontier Research Center funded by the U.S. Department of Energy, Office of Basic Energy Sciences under Award Number DE-SC0001198. The development of the aerosol shock tube facility was supported by the Army Research Office. MFC is supported by a National Defense Science and Engineering Graduate (NDSEG) Fellowship, 32 CFR 168a. The authors are grateful to Professor Oliver Herbinet for his help in running the MLA, MM, and MP simulations, and also express their thanks to Dr. Charlie Westbrook for his assistance in the modeling of MP and MO.

References

1. D. Archambault, F. Billaud, *Indust. Crops and Prod.* 7 (1998) 329-334.
2. D. Archambault, F. Billaud, *J. Chim. Phys* 96 (1999) 778-796.
3. S. Bax, M.H. Hakka, P. Glaude, O. Herbinet, F. Battin-Leclerc, *Combust. Flame* 157 (2010) 1220-1229.
4. M.F. Campbell, D.F. Davidson, R.K. Hanson, and C.K. Westbrook, *Proc. Combust. Inst.* 34 (2013) 419-425.
5. D.F. Davidson, D.R. Haylett, R.K. Hanson, *Combust. Flame* 1-2 (2008) 108-117.
6. A. Demirbas, *Energy Conv. Manag.* 50 (2009) 14-34.
7. A. Demirbas, *Energy Policy* 35 (2007) 4661-4670.
8. M.B. Dantas, M.M. Conceicao, V.J. Fernandes Jr., N.A. Santos, R. Rosenhaim, A.L.B. Marques, I.M.G. Santos, A.G. Souza, *J. Therm. Anal. Calorim.* 87 (2007) 835-839.
9. P. Diévert, S.H. Won, J. Gong, S. Dooley, Y. Ju, *Proc. Combust. Inst.* 34 (2013) 821-829.
10. P. Diévert, S.H. Won, M. Uddi, S. Dooley, F.L. Dryer, Y. Ju, 2011 AIAA Aerospace Sciences Meeting (2011).
11. P. Diévert, S.H. Won, S. Dooley, F.L. Dryer, Y. Ju, *Combust. Flame* 159 (2011) 1793-1805.
12. Q. Feng, A. Jalali, A.M. Fincham, Y.L. Wang, T.T. Tsotsis, F.N. Egolfopoulos, *Combust. Flame* 159 (2012) 1876-1893.
13. P.A. Glaude, O. Herbinet, S. Bax, J. Biet, V. Warth, F. Battin-Leclerc, *Combust. Flame* 157 (2010) 2035-2050.
14. R. Grana, A. Frassoldati, C. Saggese, T. Faravelli, E. Ransi, *Combust. Flame* 159 (2012) 2280-2294.
15. M.H. Hakka, P.A. Glaude, O. Herbinet, F. Battin-Leclerc, *Combust. Flame* 156 (2009) 2129-2144.
16. (a) D.R. Haylett, D.F. Davidson, R.K. Hanson, *Combust. Flame* 159 (2012) 552-561.
17. (b) D.R. Haylett, D.F. Davidson, R.K. Hanson, *Shock Waves* 22 (2012) 483-493.
18. O. Herbinet, W.J. Pitz, C.K. Westbrook, *Combust. Flame* 154 (2008), 507-528.
19. O. Herbinet, W.J. Pitz, C.K. Westbrook, *Combust. Flame* 157 (2010), 893-908.
20. (a) O. Herbinet, P.A. Glaude, V. Warth, F. Battin-Leclerc, *Combust. Flame* 158 (2011) 1288-1300.
21. (b) O. Herbinet, J. Biet, M.H. Hakka, V. Warth, P.A. Glaude, A. Nicolle, F. Battin-Leclerc, *Proc. Combust. Inst.* 33 (2011) 391-398.
22. S.R. Hoffman, J. Abraham, *Fuel* 88 (2009) 1099-1108.
23. Z. Hong, G.A. Pang, S.S. Vasu, D.F. Davidson, R.K. Hanson, *Shock Waves* 19 (2009) 113-123.
24. G. Knothe, A.C. Matheus, T. W. Ryan III, *Fuel* 82 (2003) 971-975.
25. G. Knothe, *Energy Fuels* 22 (2008) 1358-1364.

26. G. Knothe, *Fuel Proc. Technol.* 86 (2005) 1059-1070.
27. G. Knothe, *Prog. Energy Combust. Sci.* 36 (2010) 364-373.
28. G. Knothe, S.C. Cermak, R.L. Evangelista, *Energy Fuels* 23 (2009), 1743-1747.
29. Z. Li, W. Wang, Z. Huang, M.A. Oehlschlaeger, *Energy Fuels* 26 (2012) 4887-4895.
30. Y.C. Liu, T. Farouk, A.J. Savas, F.L. Dryer, C.T. Avedisian, *Combust. Flame* 160 (2013) 641-655.
31. Z. Luo, M. Plomer, T. Lu, S. Som, D.E. Longman, S.M. Sarathy, W.J. Pitz, *Fuel* 99 (2012) 143-153.
32. Z. Luo, T. Lu, M.J. Maciaszek, S. Som, D.E. Longman, *Energy Fuels* (2010) 6283-6293.
33. A.J. Marchese, T.L. Vaughn, K. Kroenlein, F.L. Dryer, *Proc. Combust. Inst.* 33 (2011) 2021-2030.
34. C.V. Naik, C.K. Westbrook, O. Herbinet, W.J. Pitz, M. Mehl, *Proc. Combust. Inst.* 33 (2011) 383-389.
35. N.A. Porter, S.E. Caldwell, K.A. Mills, *Lipids* 30 (1995) 277-290.
36. S.P. Pyl, K.M. Van Geem, P. Puimege, M.K. Sabbe, M.F. Reyniers, G.B. Marin, *Energy* 43 (2012) 146-160.
37. Reaction Design CHEMKIN-PRO, Reaction Design, 2010.
38. C. Saggese, A. Frassoldati, A. Cuoci, T. Faravelli, E. Ranzi, *Proc. Combust. Inst.* 34 (2013) 427-434.
39. S.M. Sarathy, M.J. Thomson, W.J. Pitz, T. Lu, *Proc. Combust. Inst.* 33 (2011) 399-405.
40. A. Schönborn, N. Ladommatos, J. Williams, R. Allan, J. Rogerson, *Combust. Flame* 156 (2009) 1396-1412.
41. K. Seshadri, T. Lu, O. Herbinet, S. Humer, U. Niemann, W.J. Pitz, R. Seiser, C.K. Law, *Proc. Combust. Inst.* 32 (2009) 1067-1074.
42. S.W. Sharpe, T.J. Johnson, R.L. Sams, P.M. Chu, G.C. Rhoderick, P.A. Johnson, *Appl. Spectrosc.* 58 (2004) 36-45.
43. J.P. Szybist, A.L. Boehman, D.C. Haworth, H. Koga, *Combust. Flame* 149 (2007) 112-128.
44. T. Vaughn, M. Hammill, M. Harris, A. Marchese, SAE Technical Paper 2006-01-3302, (2006).
45. W. Wang, M.A. Oehlschlaeger, *Combust. Flame* 159 (2012) 476-481.
46. Y.L. Wang, Q. Feng, F.N. Egolfopoulos, T.T. Tsotsis, *Combust. Flame* 158 (2011) 1507-1519.
47. C.K. Westbrook, C.V. Naik, O. Herbinet, W.J. Pitz, M. Mehl, S.M. Sarathy, H.J. Curran, *Combust. Flame* 158 (2011) 742-755.
48. C.K. Westbrook, W.J. Pitz, S.M. Sarathy, M. Mehl, *Proc. Combust. Inst.* 34 (2013) 3049-3056.
49. W. Yuan, A.C. Hansen, Q. Zhang, *Fuel* 84 (2005) 943-950.